Linking microbes and climate:
Insights into the marine oxygen and nitrogen cycles with microbial metabolic functional types

by

Emily Juliette Zakem

Submitted to the Department of Earth, Atmospheric, and Planetary Science in partial
fulfillment of the requirements for the degree of

Doctor of Philosophy

at the

MASSACHUSETTS INSTITUTE OF TECHNOLOGY

June 2017

Signature redacted

Signature of Author: ____________________
Department of Earth, Atmospheric, and Planetary Science
April 7, 2017

Signature redacted

Certified by: ____________________
Michael J. Follows
Professor of Oceanography
Thesis Supervisor

Signature redacted

Accepted by: ____________________
Robert D. van der Hilst
Schlumberger Professor of Earth and Planetary Sciences
Head of Department

Linking microbes and climate:
Insights into the marine oxygen and nitrogen cycles with microbial metabolic functional types

by

Emily Juliette Zakem

Submitted to the Department of Earth, Atmospheric, and Planetary Science
on April 7, 2017 in partial fulfillment of the requirements for the degree of
Doctor of Philosophy

Abstract

This thesis posits that understanding the controls on microbially-mediated marine biogeochemical cycling requires a mechanistic description of microbial activity in biogeochemical models. In the work here, the diverse microbial community is resolved using metabolic functional types, which represent metabolisms as a function of their underlying redox chemistry and physiology.

In Chapter 2, I use a simple model to predict the limiting oxygen concentration of aerobic microbial growth in an ecosystem. This limiting concentration is in the nanomolar range for much of the parameter space that describes microbial activity in marine environments, and so anticipates the recent measurements of oxygen to nanomolar concentrations or lower in anoxic zones. Anaerobic metabolisms should become favorable at this limiting concentration. The model provides a parameterization for dynamic oxygen depletion and limitation, without a prescribed critical oxygen concentration.

In Chapter 3, I extend the above analysis to determine the full set of conditions required for favorable anaerobic metabolism. Resource ratio theory is used to explain the competitive exclusion of anaerobic metabolisms in oxygenated environments as well as the stable coexistence of aerobic and anaerobic metabolisms when oxygen is limiting. The onset of this coexistence is a function of the relative availability of oxygen and a mutually required substrate. Results hypothesize the likelihood of coexisting aerobic and anaerobic metabolisms at limiting oxygen concentrations, which is consistent with observations. These dynamics are demonstrated in an idealized oxygen minimum zone model.

In Chapter 4, I use a mechanistic description of nitrification to explain the location and intensity of the primary nitrite maximum. First, competition with phytoplankton excludes nitrification from the sunlit layer of the ocean, resulting in peak nitrification at depth, as widely observed. Second, differences in the metabolisms of the microbial clades responsible for the two steps of nitrification explain why nitrite accumulates consistently as an intermediate. The model provides a dynamic resolution of nitrification in the ocean. It predicts that nitrification is favorable in sunlit waters where phytoplankton growth is limited by light or by a substrate other than reduced inorganic nitrogen.

Thesis Supervisor: Michael J. Follows
Title: Professor of Oceanography

Acknowledgements

I would most like to thank my advisor, Mick Follows, for guiding me through the process of becoming a scientist with such consistent support and enthusiasm.

I would also like to thank:

My thesis committee – Penny Chisholm, Amala Mahadevan, Martin Polz, and Dan Repeta – for their ongoing support. Amala Mahadevan especially for guidance with the development of the 2D model in Chapter 3. Stephanie Dutkiewicz and Oliver Jahn for incredible support, advice, modeling assistance, and helpful discussions. Andrew Babbin for chairing the defense, and for very helpful discussions about nitrogen cycling and microbial metabolisms. Members of NEMO Cruise 1417, and especially Brenner Wai for collecting the samples for the *amoA* measurements, as well as Matt Mills, Irina Shilova, and Gert van Dijken for support with shipboard measurements for Chapter 4. Alia Al-Haj, Wally Fulweiler, and other members of Wally's group for their generous assistance with preparation for the cruise and post-cruise laboratory analysis, and overall willingness to help me learn how to collect data from the ocean. Silvia Newell for meeting with me at the last minute on her last day in Boston about cruise measurements and connecting me with Wally Fulweiler. Elise Heiss for crucial guidance with measurement strategy. Students, post-docs, and other faculty and researchers for helpful discussions and contributions, especially Cael Barry, Rogier Braakman, Raf Ferrari, Glenn Flierl, Chris Follet, Keisuke Inomura, Jonathan Lauderdale, Anne-Willem Omta, Deepa Rao (also for the O'Keefe quote), David Talmy, and Darcy Taniguchi. The excellent administrative staff in the department who are so critical to making science happen, and especially Christine Maglio, Darius Inniss Collazo, and Roberta Allard for assistance and support over the years. The Simons Foundation, the Gordon and Betty Moore Foundation, and NSF for support of the research.

And of course, my parents, sisters, friends, and family for everything. J especially for everything.

"Nothing is less real than realism. It is only by selection, by elimination, by emphasis, that we get at the real meaning of things."

–Georgia O'Keeffe

Contents

Chapter 1

Introduction

1.1 Overview

Global biogeochemical cycles are mediated by the metabolisms of small living organisms. Microorganisms – or, microbes, defined operationally as living organisms too small to see with the naked eye – control significant portions of the fluxes of oxygen, carbon, and nitrogen between ocean, atmosphere, and land. Microbes produce half of the atmosphere's oxygen supply, with land-based plants responsible for the other half, and are responsible for almost all of the heterotrophic activity of both ocean and land. Understanding the controls on these fluxes, and thus the microbial activities that allow larger organisms to eat, breathe, and otherwise survive on planet earth, is an overarching goal. Since parts of these biogeochemical cycles involve elements relevant to the climate system, such as carbon dioxide and nitrous oxide, understanding how microbes operate at large scales is also important for understanding how biogeochemical cycles and the climate system change over time.

This thesis aims to expand knowledge about the controls on biogeochemical cycling in the ocean. It hypothesizes that the activity of microbes within an ecosystem is sufficiently predictable to provide insight into the formation of large-scale features, such as anoxic oxygen minimum zones and patterns of nitrification. The predictability results from an assumption that much of the large-scale function of the microbial community can be understood by reducing that activity to its underlying chemistry and to the physiology of a microbial cell. The interactions of diverse microbial populations with each other and the environment results in the geochemical distributions that we observe. With mechanistic description of microbial growth and respiration, simple modeling provides new insights into these distributions, with connections to rates of microbial activity and the biogeography of the microbial communities.

1.2 Microbial ecosystems as diverse, complex, and predictable

This thesis aims to understand the impacts of microbial activity on marine biogeochemical cycles. First, how certain are we that this understanding is even a reasonable goal? How do we know that microbial activity should impact ecosystems in ways that are consistent and that we expect will continue over time – i.e., in ways that are predictable?

Microbial systems are notoriously diverse and complex (Delong and Pace 2001). We are currently unable to predict microbial activity accurately and precisely in most environments at the level of detail that we observe the system (Widder et al. 2016). Much of the rapidly expanding sequencing data remains to be understood, particularly in natural environments (DeLong and Karl 2005; Hood et al. 2007; van der Heijden et al. 2008). Of course, the materialist perspective of science contends that all biological activity is ultimately deterministic, slave to the fundamental laws of physics. But the incredible complexity of the intermediate steps between physical laws and the biology that we observe prohibits the prediction of biological activity from 'first principles.' This is in contrast to the laws of fluid dynamics that can be used to predict much of the circulation of the atmosphere and ocean. Thus, climate models can estimate the distributions oxygen and nitrous oxide in the ocean as a function of this theoretically-predicted circulation, but must parameterize the microbial processes that form and consume them.

Even if complete prediction was possible, observations of microbial activity in natural environments are limited. Much of the microbial world remains unknown, and its unearthing has been a relatively recent phenomenon (Kirchman and Williams 2000). The majority of bacterial and archaeal species in natural environments have not been isolated in culture (Hug et al. 2016; Zinger et al. 2012). Without an ability to study most organisms in detail, can we meaningfully understand their impact on the environment?

Environmental sequencing technologies have resulted in a huge expansion of information about these uncultivated species *in situ* (Ward 2002; DeLong and Karl 2005; Armbrust and Palumbi 2015). With genetic information from over 1000 uncultivated organisms, Hug et al. (2016) have created a modified version of the tree of life, which emphasizes that the uncultivated Bacteria and Archaea contain the bulk of genetic diversity, with Eukaryotes exhibiting much lower diversity, reflecting their "comparatively recent evolution" (Hug et al. 2016). Sequencing data has provided enormous amounts of information about microbial activity – enzymatic capabilities, gene expression, metabolites, etc. – and linking this knowledge about organisms to ecosystems and the environment is progressing (Martiny et al. 2006; Green et al. 2008; Zinger et al. 2012; Barberán et al. 2014; Sunagawa et al. 2015; Widder et al. 2016). However, quantitative data is still limited, and it remains an open question of how new knowledge will be integrated into ecosystem models (Hood et al. 2007; Coles and Hood 2016).

In parallel, laboratory research is progressing our understanding of microbial ecosystem dynamics at smaller scales, and developing principles that can be extended to natural environments. For example, we have learned that the growth of *Prochlorococcus* – the most abundant primary producer in the ocean – is improved when cultivated alongside particular heterotrophs (Sher et al. 2011; Biller et al. 2016). This and similar findings has led to the perspective that the microbial community is best characterized by both positive and negative interactions at the very small scales relevant to microbial cells (Azam and Malfatti 2007).

A question arising from this emphasis on the significance of small-scale interactions is whether diverse microbial communities impact the ecosystem in consistent ways. Does diversity result in different ecosystem function for the same conditions? I.e., will microbial ecosystems in different locations respond to changes in the environment in ways that allow for the prediction of the bulk properties of that environment, such as oxygen and macronutrient distributions? How much of the small-scale detail can be bypassed?

Seemingly random processes govern microbial growth: it has been proposed that stochasticity of genetic processes leads to this 'noise' in microbial activity Elowitz et al. (2002). With extremely careful control of a laboratory system, however, Frentz et al. (2015) was able to replicate microbial activity, and provide evidence that external conditions cause the observed fluctuations, and not genetic variation. Thus, Frentz et al. (2015) concluded that microbial systems have the potential to be determined by macroscopic laws.

This thesis contends that microbial community impact as a whole, in contrast with the species composition of the community, is largely consistent. Questions about the resilience and stability of the structure of microbial community composition itself are a subject of active research (e.g. Allison and Martiny 2008). Evidence suggests that rather than creating unpredictable environments, the microbial community as a whole converges to carry out predictable biogeochemical activity. For example, Martiny et al. (2013) have shown that ecologically significant traits are phylogenetically conserved, implying a consistency of microbial control on ecosystem function. This is related to an understanding that ecological interactions have the ability to shape the diversity of microbial communities. Genetic mutations and deletions happen quickly enough to allow for horizontal gene transfer to dominate bacterial evolution (Croucher et al. 2016), implying that evolution occurs on timescales similar to ecological interactions. Thus, the microbial community at any location should be able to optimize the exploitation of available resources.

1.3 Organisms as dissipators of chemical energy

An alternative perspective to the small-scale approach to microbial ecology emphasized by Azam and Malfatti (2007), one that instead embraces bulk properties at the expense of micro-scale detail, is attempting to understand the ecosystem 'from the outside in' (Lindeman 1942; Vallino and Algar 2016). How can ecosystem function as a whole – both abiotic and biotic components – be related to the chemical gradients that organisms appropriate for energy?

For example, organic matter has a high chemical potential compared to CO_2, and a heterotrophic metabolism exploits this potential energy by respiring it (Vallino 2010). This energy is then used for cell synthesis and maintenance. The efficiency of this conversion of energy can be generally represented by the yield y of biomass with respect to organic matter substrate (del Giorgio and Cole 1998).

In one sense, it is often anticipated that organisms evolve and adapt to maximize this efficiency (Pirt 1965; del Giorgio et al. 2011). Organisms that can grow and reproduce more quickly in the environment have the potential to competitively exclude other organisms

(Hutchinson 1961; Tilman 1982). In the arms race for survival, an organism seems to benefit from a more efficient use of substrate and thus a larger y. This assumption – that an organism is best fit by maximizing its yield – has been shown to not be universally true; in some environments it appears an organism is more fit by maximizing its growth rate at the expense of an efficiency, such as in fermentation, or by utilizing organic carbon less efficiently than other elements (Pfeiffer et al. 2001; Carlson et al. 2007; Lipson 2015).

On the other hand, the Second Law of Thermodynamics requires that gradients in chemical potential be reduced over time. Respiration by living organisms increases the entropy of the environment by dissipating concentrated sources of chemical energy, e.g., converting organic matter to CO_2 (Meysman and Bruers 2007; Vallino 2010). In simple terms of the yield y, this CO_2 production is roughly $(y-1)$. From this perspective, the lower the efficiency of an organism, and thus the lower the yield, the more energy is dissipated. The respiration of organisms thus functions to carry out the reduction of chemical potential as predicted by the Second Law, which is an especially efficient mechanism given that yields are generally low in natural environments. (Average values for the open ocean and for natural environments as a whole are estimated as $y = 0.14 \pm 0.14$ and $y = 0.3$, respectively (Robinson 2008; Sinsabaugh et al. 2013).

How can we relate this seeming paradox – the explanations for both a maximum and a minimum y? With the laws of thermodynamics governing the physical world, why hasn't biology evolved so that $(y-1)$ approaches zero? (Or in other words, why is there biology?) One explanation is that an optimum amount of biomass exists to maximize the production of energy, with an optimum y to maximize the rate of overall energy dissipation by the respiration of organisms in the biotic and abiotic system as a whole (Meysman and Bruers 2007, 2010; Vallino 2010; Vallino and Algar 2016). From this maximum entropy perspective, when considering the earth as a system, biomass functions as the enzyme necessary for the optimal dispersal of incoming solar energy into more dissipate forms of chemical energy.

Taking this principle one step further, Maximum Entropy Production (MEP) theory contends that biota is able to produce more entropy in the earth system than would otherwise occur abiotically (e.g., via combustion), and that the rate at which entropy is produced is maximized when integrated over a period of time (Meysman and Bruers 2007; Dewar 2010; Meysman and Bruers 2010; Vallino 2010; Kleidon et al. 2010). In this way, Meysman and Bruers (2007) and Vallino (2010), among others, have aimed to anticipate the activity of the ecosystem as a whole from the chemical potential of available substrate, computing the free energies of the chemical reactions to estimate individual yields and rates of synthesis. This approach is not without criticism (Volk 2007; Volk and Pauluis 2010), namely because the physical theory of maximum entropy production was derived to explain the activity of gas molecules in a vaccuum, and has not yet reached consensus in the physics community (Dewar and Maritan 2014), and so the application of it to organisms in an ecosystem may be characterized as an overextension of a still-developing theory.

While MEP theory has its challenges, an intermediate organizing principle for microbial ecosystems is to focus just on the tendency for organisms to exploit the chemical potential in an environment (Vallino et al. 1996). Indeed, all organisms must acquire chemical energy from reduction-oxidation reactions to carry out their metabolisms (Madigan et al. 2013; Rittman and McCarty 2001). Theoretical microbiologists aim to calculate the free energy acquired by a redox reaction, such as the oxidation of organic matter to CO_2 with oxygen as an electron acceptor, and balance that energy yield against the energetic demands of the cell, such as cell synthesis, to energy budget for that metabolism (e.g. Heijnen and Roels 1981; Russell and Cook 1995; VanBriesen 2002; Jol et al. 2010; Roden and Jin 2011; van de Leemput et al. 2011; LaRowe et al. 2012). This is, in essence, the way that civil engineers have approached the prediction of microbial activity of bioreactors in water treatment plants (Rittman and McCarty 2001): with theoretical energy budgets of diverse metabolisms, they have anticipated the dominant metabolisms that will occur as a function of the substrates in the reactor. In relating the microbial activity to the chemical equations underlying these metabolisms, they have been able to quantitatively relate microbial growth to the rates of conversion of the substrates to the end-products. Variations of this approach have been extended to a natural aquatic environments with success Dick and Shock (2013); Algar and Vallino (2014); Preheim et al. (2016).

This thesis follows the spirit of this approach in organizing the diverse marine microbial metabolisms by their underlying redox reactions, and thus relating microbial growth to ambient nutrient concentrations. In this sense, it considers the ocean as a giant bioreactor. A difficulty is estimating the free energies of reactions in natural environments, and so the pluralistic approach here instead incorporates observed efficiencies of metabolisms and substrate yields. The theoretical approach here does not predict the rates of growth and respiration, and so observations of kinetics and bulk rates are incorporated. In the absence of comprehensive quantitative information about microbial activity, this approach provides a theoretical grounding principle for its description in the ocean, as a tangible way to build a model of the ocean in which microbially-mediated processes are represented mechanistically through growth and respiration.

1.4 Marine biogeochemistry and microbial ecology: Main links and big questions

Moving towards a general hypothesis that we can somewhat anticipate large-scale microbial function in an environment by analyzing the chemical potential of the environment, and translating that into the redox reactions fueling microbial metabolisms, we next turn to the reasons for doing so. What is it that we want to know?

The work here aims to answer questions about large-scale marine biogeochemical dynamics, with more attention to microbial process than is typical for the field. Connecting marine microbial processes with large-scale ocean circulation does require some degree of simplification of those processes. In general, more attention has been given in such models to the phytoplankton responsible for the primary production in the sunlit surface ocean, as well as their small zooplankton predators, than to smaller groups of microbes (Hood et al. 2007; Follows and Dutkiewicz 2011). Phytoplankton functional type models and their modifications have provided great insight into how environment-organism interactions set the biogeography and diversity of phytoplankton (Le Quere et al. 2005; Follows et al. 2007; Barton et al. 2010; Dunne et al. 2012; Clayton et al. 2013; Dutkiewicz et al. 2014). However, the 'other half' of production – the remineralization of organic matter back into its inorganic counterparts – is typically more crudely parameterized in biogeochemical models. For example, the 'Martin curve,' and its modifications, parameterizes remineralization of organic matter with depth with prescribed coefficients tuned to reflect observations of the particle flux from sediment traps in the deep ocean (Martin et al. 1987; Buesseler et al. 2007; Buesseler and Boyd 2009).

Zooplankton as well as heterotrophic bacteria play a significant role in this remineralization, but heterotrophic bacteria are not often represented in large models explicitly, although there are of course exceptions (Fasham et al. 1990; Le Quere et al. 2005). This lack of representation is historical, in that we have previously assembled more knowledge about phytoplankton (and zooplankton), and also practical, in that representing the growth at daily or weekly timescales below the thermocline requires integrating model equations at daily timescales for thousands of years, which has been computationally very expensive, time-consuming, and also perhaps unhelpful given the lack of comprehensive observations of activity in the dark ocean. However, as computers become faster and microbial datasets expand, microbial ecological modeling is turning towards opening up the 'black box' of remineralization (Allison and Martiny 2008; Bouskill et al. 2012; Reed et al. 2014; Bowen et al. 2014; Preheim et al. 2016).

The specific questions in this thesis involve the growth and respiration associated with organic matter remineralization and its consequences, rather than the complexities of the degradation of organic matter itself. The questions focus generally on the microbial metabolisms that have the potential to affect and be affecting by changes to the climate system. Unlike the land ecosystem, the carbon budget of the marine ecosystem as a whole is not believed to be currently changing as a result of increased atmospheric carbon dioxide or warming (IPCC 2014), since primary production in the ocean is not carbon limited. Models do predict a change in ecosystem structure on shorter timescales (Dutkiewicz et al. 2013, 2015), and long term effects of changes in temperature are anticipated (Matsumoto et al. 2007). Work here is also relevant for understanding the distributions of nitrogen, which proximally limits about half of the primary production in the surface ocean (Moore et al. 2013).

Deoxygenation and the transition to anaerobic metabolisms

First, the work here contributes to an improved understanding of the effects the projected deoxygenation of the oceans due to global warming (IPCC 2014). Deoxygenation is expected as a consequence of the decrease in solubility of oxygen in warming waters, at the approximate rate of about 5 μM less oxygen per degree temperature increase, and should lead to significant decreases in ocean oxygen content over the next century (Keeling et al. 2010). This effect takes place at the air-sea interface, where waters warm, and so will take hundreds or thousands of years to affect the oxygen in the its least ventilated areas. However, depending on the location, the oxygen minimum of the water columns in some locations may be affected by deoxygenation over the decadal timescales that govern the thermocline. In much of the tropical Pacific ocean, for example, oxygen reaches relatively low concentrations (tens of μM) that are relevant for the viability of larger animal growth and respiration (Paulmier and Ruiz-Pino 2009; Stramma et al. 2010); fish hypoxia can set in as high as 60μM (Keeling et al. 2010). Thus, deoxygenation could contract the habitat for fish and other marine animals (Deutsch et al. 2011, 2015). Given human dependency on fisheries, deoxygenation could potentially affect human society in decadal or centurial timescales (Stramma et al. 2010), and so, understanding the biogeochemical and physical interactions that control oxygen distributions is important for anticipating such changes.

The effect of deoxygenation for which the work here is directly relevant is the potential change in the rates of anaerobic activity in marine anoxic zones. Oxygen has been depleted to nanomolar concentrations or lower by aerobic respiration in these zones (Fig. 1.1) (Lam and Kuypers 2011; Ulloa et al. 2012), and an open question is whether or not further loss of oxygen will lead their expansion (Stramma et al. 2008; Gnanadesikan et al. 2012; IPCC 2014; Cabré et al. 2015; Long et al. 2016). Anaerobic processes result in denitrification – the loss of fixed nitrogen to nitrogen gas (N_2) and the potent greenhouse gas nitrous oxide (N_2O) (Devol 2008; Ward 2013). Thus, the transition from aerobic to anaerobic microbial respiration controls rates of denitrification, but this transition has not been quantitatively understood. Chapters 1 and 2 here provide insight into this transition.

Nitrification and its relationship to the biological pump

A second area of emphasis in this work, also involving the marine nitrogen cycle, is relevant for understanding the structure of marine ecosystem production and the biological pump. The biological pump refers to the increase in dissolved inorganic nutrients with depth, and is a consequence of the remineralization of exported organic matter at depth (Volk and Hoffert 1985). This sequestration of nutrients at depth leads to an enhanced storage of carbon in the ocean of roughly 100 $\mu\text{mol kg}^{-1}$ (Williams and Follows 2011). Though this is roughly only about a 5% increase of the total carbon inventory from the carbon storage due to air-sea equilibration, but globally integrated, is about three times higher than the carbon stored in the atmosphere (Williams and Follows 2011). An active area of research is to develop a more mechanistic understanding and quantification of the export production that enables this sequestration (Siegel et al. 2016).

The work here relates to the inverse of this export production, the 'new production' that occurs due to the upwelling of nutrients from depth (Dugdale and Goering 1967). The amount of organic matter exported to depth must be balanced by this new production over large time and space scales (Eppley and Peterson 1979). New production was once defined as that fueled by nitrate, the most oxidized form of dissolved inorganic nitrogen (DIN), since the bulk of primary production in the mixed layer is fueled by ammonium (Dugdale and Goering 1967). This latter 'regenerated' productivity is that which occurs due to local cycling of photosynthesis and respiration within the mixed layer, fueled by ammonium. However, observations of nitrification – the microbially-mediated oxidation of ammonium

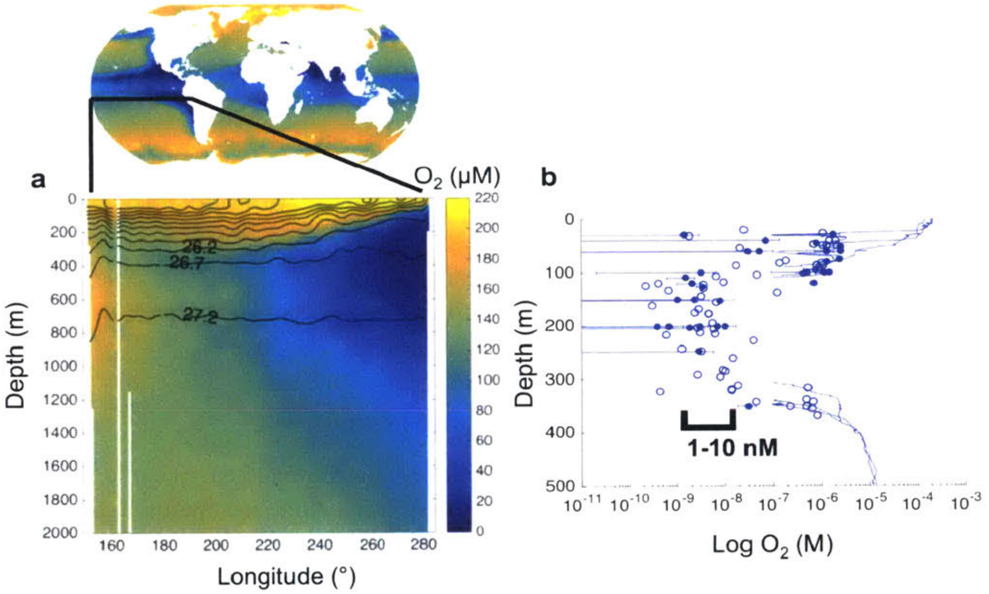

Figure 1.1: (a) Dissolved oxygen at 300m depth, and along the 10°S transect in the South Pacific Ocean (Data: WOA 2013). (b) Oxygen measured by Thamdrup et al. (2012) with the STOX (Switchable Trace amount OXygen) sensor (circles) and a STOX-calibrated conventional oxygen sensor (lines) in the Eastern South Pacific along the west coast of South America. As in Thamdrup et al. (2012), locations with multiple measurements (solid circles) include error bars (standard deviations), and locations with one measurement (open circles) have a detection limit of 10 nM. Error bars that intersect with the y-axis signify error to or below zero.

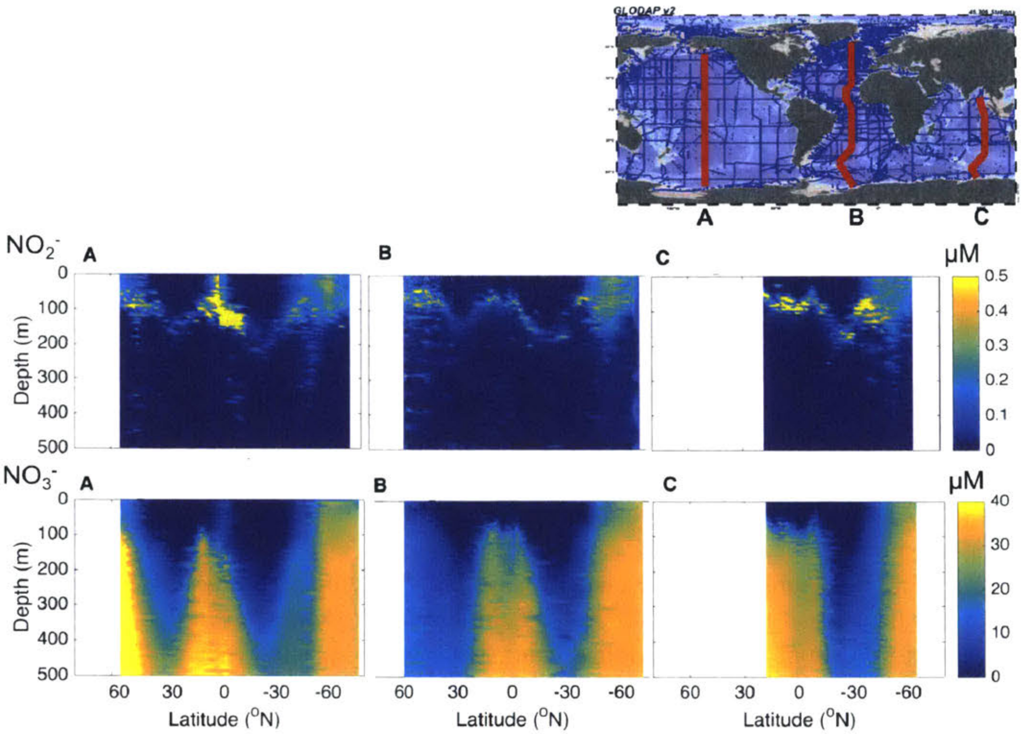

Figure 1.2: Observed nitrite and nitrate concentrations along three transects in the ocean (Data: GLODAPv2, accessed with Ocean Data View).

to nitrate – in the euphotic zone and/or mixed layer have complicated these traditional definitions (Ward 1987; Dore and Karl 1996a; Ward 2005; Clark et al. 2008; Cavagna et al. 2015; Fripiat et al. 2015). Yool et al. (2007) have demonstrated the impact of accounting for nitrification in estimates of new production.

How much nitrification occurs in the euphotic zone versus at depth, and why? Chapter 3 provides insight into the controls on nitrification in the ocean. Nitrification typically peaks at depth, just below the euphotic zone (Zafiriou et al. 1992; Dore and Karl 1996b; Ward 2008; Mackey et al. 2011; Santoro et al. 2013). Because nitrite is an intermediate product in the two-step nitrification process, understanding what forms the primary nitrite maximum (PNM) – the accumulation of nitrite at the base of the euphotic zone in stratified water columns – serves as a focusing feature for understanding nitrification more generally Fig. 1.2). Though ubiquitous in the ocean, the PNM is still not well understood (Lomas and Lipschultz 2006; Santoro et al. 2013), and Chapter 3 proposes the processes that form it.

Nitrification is also relevant to microbial feedbacks to the climate system, since the greenhouse gas N_2O is a known byproduct of nitrification in the oxygenated ocean, in addition to denitrification in anoxic zones (Ward 2008; Babbin et al. 2015). Though work here does not specifically target N_2O formation or consumption, insights on the controls on ni-

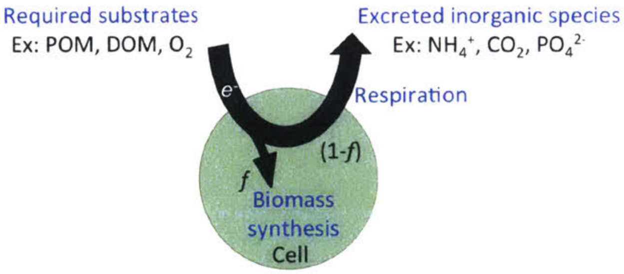

Figure 1.3: Schematic of a metabolic functional type, modeled as a function of the partitioning of electrons into the fraction f used for biomass synthesis vs. that used for respiration.

trification and denitrification are indirectly relevant for predicting marine N_2O emissions. Changes to the distribution of nitrification due to warming-induced changes in water column stratification, for example, could potentially affect the amount of N_2O that escapes the water column into the atmosphere.

The work here aims to provide a mechanistic understanding of the relationship between ocean circulation and the microbial processes that result in oxygen depletion, denitrification, and nitrification. Simple microbial ecosystem models quantitatively link growth and respiration to ocean circulation to better understand the cycling of oxygen and nitrogen in the ocean.

1.5 Approach: Microbial metabolic functional types

This work organizes the metabolisms carried out by marine microbes into metabolic functional types. The approach is inspired conceptually by the labelling of microbes as the "engines that drive biogeochemical cycles" by Falkowski et al. (2008), and practically by field of environmental biotechnology, which has long embraced the thought of microbes as engines in bioreactors (Rittman and McCarty 2001). Each functional type is defined by a particular set of redox reactions that underlies a metabolism, such as photoautotrophy, aerobic heterotrophy, all combinations of the subsets of heterotrophic denitrification, ammonia oxidation, and nitrite oxidation (Fig. 1.3).

The details of functional type development for particular metabolisms are contained within the appendices of the following chapters. Here, an overview of the strategy and general assumptions are presented. The aerobic heterotrophic functional type serves as an example for the overview, since along with photoautotrophy, it represents the dominant metabolism in the earth system.

Functional type stoichiometry

First, an equation for the stoichiometry of a metabolism is described by its underlying reactions, following the methodology of Rittman and McCarty (2001). The description consists of three half-reactions: biomass synthesis, oxidation of an electron donor, and reduction of an electron acceptor. The ratio of anabolism and catabolism is represented by the fraction f of electrons fueling cell synthesis vs. respiration for energy (Fig. 1.3). For aerobic heterotrophy, organic matter (OM) provides the elements and electrons for both the synthesis of biomass (B) and energy production, and oxygen serves as the electron acceptor, as (neglecting water and charge balance with bicarbonate for simplicity):

$$\frac{1}{d_{OM}}OM + \frac{1-f}{4}O_2 \rightarrow \frac{f}{d_B}B + \left(\frac{c_{OM}}{d_{OM}} - \frac{c_B f}{d_B}\right)CO_2 + \left(\frac{n_{OM}}{d_{OM}} - \frac{n_B f}{d_B}\right)NH_4^+ \qquad (1.1)$$

where d is the number of electron equivalents for generic organic matter composition $C_cH_hO_oN_n$ that correspond to the oxidation states of its inorganic constituents (below as $d = 4c + h - 2o - 3n$). In this formulation, the electron fraction f is assumed the same for both carbon and nitrogen utilization, but observations show that bacteria may preferentially respire carbon and utilize nitrogen more efficiently (Goldman et al. 1987). The description could account for this by including multiple values of f, one for each substrate.

Theoretically, the fractionation of electrons f can be calculated from the free energies of the redox reactions, along with estimates of the energy costs of cell synthesis and maintenance. This approach works well in some environments such as bioreactors (Rittman and McCarty 2001), but less so in natural environments: in the following chapters, the theoretical f consistently overestimates the efficiencies gathered from marine observations. One reason for the theoretical overestimate could be the underestimate of the costs of cell synthesis in oligotrophic environments, particularly if more energy is required to access nutrients at low concentrations. Another reason could be the overestimation of the free energy available in marine organic matter; the theoretical calculations are all based on an assumption of that free energy, which was assumedly tuned for water treatment plants, and so may not hold across widely varying environments. A third reason is that the assumption of the inefficiencies of energy conversion (i.e. that which is lost to heat within cells) is largely uncertain even in the bioreactor environments, and so serves as a tuneable parameter even for the theoretical calculations.

In sum, even the theoretical calculations of the electron fractionation involve uncertainty, and are tuned to match observations. This work foregoes these theoretical estimates entirely and instead assigns efficiencies inferred from observations. For example, compilations of bacterial growth yields are assigned as the yields for the aerobic heterotroph. These yields are 0.14 ± 0.14 and 0.19 ± 0.16 mol C synthesized per mol C consumed for the open and coastal ocean, respectively, which are significantly lower than theoretically predicted yields of about 0.5 for marine organic matter stoichiometry (Rittman and McCarty 2001; Robinson 2008).

For the heterotroph, this assigned organic matter yield, y_{OM}, relates to f as $y_{OM} = \frac{d_{OM}}{d_B}f$, and so $y_{OM} = f$ when assuming the same stoichiometry for both the organic matter substrate and microbial biomass. Assuming the average stoichiometry of marine organic matter ($C_{106}H_{175}O_{42}N_{16}$; Anderson 1995) for both gives a ballpark values for the heterotrophic metabolism as:

$$OM + \frac{467(1-y_{OM})}{4}O_2 \rightarrow y_{OM}B + 106(1-y_{OM})CO_2 + 16(1-y_{OM})NH_4^+ \qquad (1.2)$$

Thus, $y_{OM} \to 0$ represents the traditional biogeochemical description of organic matter remineralization where bacteria biomass is neglected as an intermediate pool. Here, the C:O ratio of remineralization implied by neglecting B is $\frac{106.4}{467} = 0.9$, which is the value of the respiratory quotient as estimated by (Williams and del Giorgio 2005).

Functional types as populations

With the stoichiometry of the metabolism determined, a functional type is then represented as a population with biomass B, as in typical ecological population models, with a differential equation describing its rate of change as a function of its growth rate μ and its loss rate L:

$$\frac{DB}{Dt} = \mu B - LB \tag{1.3}$$

where the substantial derivative D/Dt includes the diffusive flux as function of the diffusive coefficient K as $\nabla \cdot (\vec{K} \nabla B)$, and advective fluxes as functions of velocity $\vec{u}$ as $\nabla \cdot (\vec{u} B)$. The growth rate is calculated as the minimum product of the rate of uptake ρ of each required substrate and its yield, following Liebig's Law of the Minimum. For the heterotroph, either organic matter or oxygen limits the growth rate as:

$$\mu = \min[\rho_{OM} y_{OM}, \rho_{O_2} y_{O_2}] \tag{1.4}$$

Thus, an assumption here is that the yield and the growth rate are correlated with respect to any one substrate, which is often but not always the case, as discussed above.

The uptake of any substrate is then described using observed kinetic parameters when available and appropriate. The uptake of oxygen is modeled assuming a diffusive limitation; this assumption is explored at length in Chapter 2. The uptake of all other substrates, including organic matter, is described using a Michaelis-Menten saturating form, defined by a half-saturation constant and maximum uptake rate. For dissolved inorganic nitrogen, these parameters are taken from the literature. For organic matter, the uptake parameters are not represented mechanistically, but rather inversely incorporate estimates of marine bacterial growth rates (see Appendix 4.A.3).

Lastly, the loss rate L of the functional type populations is modeled as a combination of both consumption by grazers and a general linear mortality rate meant to implicitly include the losses due to viruses. Much remains unknown about these loss rates for microbial populations, though Taniguchi et al. (2014) provide useful size-based quantitative estimates. An overall value for L can be inferred from mean bacterial growth rates, since for a stable population at steady state, loss rates must balance growth rates. Bacterial growth rates at the surface vary substantially, but on average range from about 0.1 to 1 day^{-1} (Ducklow 2000), with 0.1 day^{-1} as a calculated average (Kirchman 2016). Subsurface pelagic bacterial growth rates are also on average 0.1 day^{-1} (Aristegui et al. 2009).

Benefits and limitations

In general, using these metabolic functional types to describe prokaryotic function aims to aggregate the diverse, mixed community of many species that may be carrying out that same metabolism. Such aggregation has been deemed a useful strategy for representing the biogeochemical impacts of the microbial community (Shapiro and Polz 2014), and particularly so for that of the phytoplankton community (Mutshinda et al. 2016).

However, the approach has its limitations. Perhaps most significantly, it involves a choice about which metabolisms occur within a single population, and which are dispersed among more than one population. Chapter 3 demonstrates that this choice does not always affect the overall estimates of the environment: in a model, a facultatively anaerobic population results in the same ambient nutrient concentrations and total biomass as discrete aerobic and anaerobic populations. But this not always the case: Chapter 4 makes the assumption that the two steps of nitrification are carried out by distinct populations, which is justified both with observations and theory (Costa et al. 2006; Ward 2008). If the model had assumed that the two steps occurred within a single population, it would not have predicted the accumulation of nitrite in the environment. Additionally, the versatility and mixotrophy of microbial metabolisms – nitrite oxidizers in particular – is increasingly appreciated (Qin et al. 2014; Daims et al. 2016), and including such mixotrophic lifestyles is believed to have consequences for overall ecosystem function since such lifestyles modify the fitness of populations in their environments (Ward and Follows 2016).

The population modeling approach also fails to incorporate another common characteristic of prokaryotic communities: the capacity for dormancy and survival in a starved state with little activity (Ducklow 2000). In the models here, the biomass of the microbial functional type varies linearly with the production rates. However, in real communities, a smaller fraction may be active: evidence suggests that less than 10% to more than 75% of the microbial community may be inactive (Ducklow 2000). This complicates the comparisons of modeled biomass and activity rates with observations, and may be one explanation for underestimates of biomasses or overestimates of activity rates.

While there are benefits and limitations to the metabolic functional type approach in general, the work presented in the next chapters use the approach as customized for the specific questions considered. The conclusions made in each are presented with their associated specific limitations. The work shows that representing microbial activity mechanistically and explicitly, despite these general uncertainties, is able to provide insight into the dynamics of oxygen depletion, the transition to anaerobic metabolisms, and the formation of the primary nitrite maximum.

1.6 Outline of thesis

This thesis posits that answering the following questions requires a mechanistic description of the microbial processes involved within a physical model of the environment.

Chapter 2: Why is oxygen depleted to nanomolar concentrations in marine anoxic zones?

When aerobic microbes deplete oxygen sufficiently, anaerobic metabolisms activate, driving losses of fixed nitrogen from marine oxygen minimum zones. Recently developed technology has lowered the detection limit for *in situ* oxygen measurements by three orders of magnitude, to 1–10 nM, and its deployment has revealed large regions in the ocean at or below these concentrations (Fig. 1.1). These observations imply that microbial activity is able to access oxygen at these levels, yet previous theory and observations suggested much higher critical oxygen concentrations. Simple modeling links microbial growth and respiration to the supply of oxygen in an environment, and provides an explanation for these observations. A generic aerobic metabolic functional type is considered, and results are relevant for diverse aerobic microbial populations. The model predicts the limiting concentration of oxygen for the aerobic functional type as a function of its size, its oxygen demand, its population turnover rate, and the ambient temperature. These limiting concentrations vary, but are largely in the nanomolar range, and so the model anticipates the observed nanomolar concentrations.

Chapter 3: What governs the transition from aerobic to anaerobic metabolisms in marine anoxic zones? What enables their coexistence?

The transition from aerobic to anaerobic metabolisms in the ocean is qualitatively well understood, but quantitative description is necessary for understanding how fixed nitrogen loss might change over time. What conditions allow for the favorability of anaerobic metabolisms? Observations have suggested the coexistence of aerobic and anaerobic metabolisms in low oxygen environments as well as in the laboratory. How can we explain this coexistence from an ecological perspective? Resource competition theory is used to explain the sustained coexistence of aerobic and anaerobic metabolisms, as well as a description of the threshold for the onset of favorable anaerobic metabolism. Two metabolic functional types are considered: an aerobic and an anaerobic (denitrifying) heterotroph. In Addendum 1, the interactions of four additional types are included. This set of six metabolisms represents the minimum set of metabolisms currently understood to control the rates of nitrogen loss in anoxic zones. In Addendum 2, we connect the resulting theoretical descriptions to datasets of the whole ocean, in an attempt to identify the domain of favorable anaerobic metabolisms.

The main chapter defines the transition from exclusive aerobic activity to the sustainable coexistence of aerobic and anaerobic metabolisms as a function of the relative availability of oxygen and organic matter. Addendum 1 shows that this theoretical framework can also explain the coexistence of aerobic nitrification and anaerobic ammonium oxidation (anammox). It also proposes a detailed description of the transition from multiple aerobic to multiple anaerobic functional types as a function of oxygen supply, and one of the intermediate states is compared to recent observations. Addendum 2 predicts a volume of the ocean where anaerobic activity should be steadily sustainable, although the uncertainty in the oxygen and POC flux climatologies prevent precise quantitative prediction.

Chapter 4: What forms the primary nitrite maximum?

In the stratified water columns in the ocean, a small concentration of nitrite accumulates at the base of the sunlit surface layer: the primary nitrite maximum (PNM; Fig. 1.2). We still do not understand its formation, which highlights a gap in our understanding of the controls on marine photosynthesis, which is often limited by nitrogen. A long-standing hypothesis has been that sunlight inhibits the activity of chemoautotrophic nitrifiers, the microorganisms seemingly responsible for formation of the PNM, but this fails to explain why nitrification has also been observed in sunlit waters. To date, no robust explanation exists for why the two steps of nitrification are consistently decoupled, which is required for the accumulation of nitrite as an intermediate product. Two metabolic functional types are developed that represent the two steps of nitrification. The redox chemistry and size-based assumptions of affinity differentiate the two nitrifier types, which are then included in a microbial ecosystem model to gain insight into the controls on nitrification in marine environments and the formation of the PNM. The model shows that both differences between the two nitrifying metabolisms contribute to a larger subsistence concentration of nitrite for the nitrite oxidizer than for that of ammonium for the ammonia oxidizer, and so result in an accumulation of nitrite. Subsistence concentrations also explain why nitrification peaks at depth. Phytoplankton, with lower subsistence concentrations of DIN than nitrifiers, are able to competitively exclude nitrifiers when their growth is limited by nitrogen, such as at the surface. Nitrification becomes sustainable at depth where phytoplankton are light-limited.

Finally, in the Appendix, we comment upon a way to circumvent the inherent error of the resolution of the cell quota in a population model.

Chapter 2

A theoretical basis for a nanomolar critical oxygen concentration

The work in this chapter is based upon the following publication: Zakem, E. J., and M. J. Follows. 2016. A theoretical basis for a nanomolar critical oxygen concentration. *Limnolology and Oceanography*.

2.1 Overview

When aerobic microbes deplete oxygen sufficiently, anaerobic metabolisms activate, driving losses of fixed nitrogen from marine oxygen minimum zones. Biogeochemical models commonly prescribe a 1–10 μM critical oxygen concentration for this transition, a range consistent with previous empirical and recent theoretical work. However, the recently developed STOX sensor has revealed large regions with much lower oxygen concentrations, at or below its 1–10 nM detection limit. Here, we develop a simplified metabolic model of an aerobic microbe to provide a theoretical interpretation of this observed depletion. We frame the threshold as O_2^*, the subsistence oxygen concentration of an aerobic microbial metabolism, at which anaerobic metabolisms can coexist with or outcompete aerobic growth. The framework predicts that this minimum oxygen concentration varies with environmental and physiological factors, and is in the nanomolar range for most marine environments, consistent with observed concentrations. Using observed grazing rates to calibrate the model, we predict a minimum oxygen concentration of order 0.1–10 nM in the core of a coastal anoxic zone. We also present an argument for why anammox may be energetically favorable at a higher oxygen concentration than denitrification, as some observations suggest. The model generates hypotheses which could be tested in the field, and provides a simple, mechanistic, and dynamic parameterization of oxygen depletion for biogeochemical models, without prescription of a fixed critical oxygen concentration.

2.2 Introduction

Anaerobic processes in marine oxygen minimum zones (OMZs) are one of the major loss pathways for fixed nitrogen in the ocean (Ward 2013). With predicted marine deoxygenation and the open question of whether or not OMZs may expand due to global warming (IPCC 2014), establishing theory for the controls on aerobic vs. anaerobic processes is timely. Qualitatively, the mechanisms that form OMZs and lead to fixed nitrogen loss are well understood: in productive areas of the ocean, enhanced aerobic respiration in poorly ventilated subsurface waters depletes oxygen (Devol 2008). When oxygen is sufficiently low, anaerobic metabolisms become energetically competitive pathways, resulting in the accumulation of metabolic products such as nitrogen gas (N_2) and nitrous oxide (N_2O) (Devol 2008; Ulloa et al. 2012; Wright et al. 2012). In OMZs, two pathways- heterotrophic denitrification and chemoautotrophic anaerobic ammonium oxidation (anammox)- account for the majority of fixed nitrogen loss (Ward 2013).

Studies of microbial processes in aquatic oxygen minimum zones have revealed complex biogeochemical habitats (Lam and Kuypers 2011; Wright et al. 2012). Microbial community composition exhibits structure along the oxygen gradient between end-member fully oxic and fully sulfidic environments (Gonsalves et al. 2011; Ulloa et al. 2012; Jayakumar et al. 2013; Hawley et al. 2014). In the oxycline, as oxygen sharply depletes by up to five orders of magnitude (Fig. 2.1), microbial communities have been observed to be more diverse than in the anoxic cores (Jayakumar et al. 2009; Zaikova et al. 2010; Bryant et al. 2012), though not always (Stevens and Ulloa 2008). Organic matter supply to the subsurface that varies in time and space creates a dynamic oxycline (Ward 2008), which may support this diversity, with competitive exclusion operating progressively with depth as environmental conditions stabilize (Hutchinson 1961).

Devol (1978) noted that predicting the oxygen concentration of the switch between aerobic and anaerobic respiration is crucial for accurate OMZ modeling. He conducted an exhaustion curve experiment with bacterial isolates from anoxic marine areas to determine average growth-limiting oxygen concentrations of about 1–4 μM, at the limits of then-current sensors. Many biogeochemical models prescribe a critical oxygen concentration in this range or higher, setting the transition to nitrate reduction and denitrification (e.g. Najjar et al. 2007; Anderson et al. 2007; Deutsch et al. 2011; Bianchi et al. 2012; Suntharalingam et al. 2012; Gnanadesikan et al. 2012; Gutknecht et al. 2013). Brewer et al. (2014) proposed a theoretical basis for a critical oxygen concentration of this magnitude by considering the energy available from external oxygen and nitrate. Their analysis shows a higher energetic yield from the use of nitrate as an electron acceptor once oxygen drops to about 10 μM, with nitrate concentration at 40 μM. They interpret this as an upper-bound oxygen concentration for the onset of anaerobic nitrate reduction, pertinent when respiration is limited by the supply of an electron acceptor.

The recent development of the STOX (Switchable Trace amount OXygen) sensor has lowered the detection limit for dissolved oxygen measurements in the ocean from about 1 μM to 1–10 nM, and its deployment has revealed that large volumes of OMZ water have

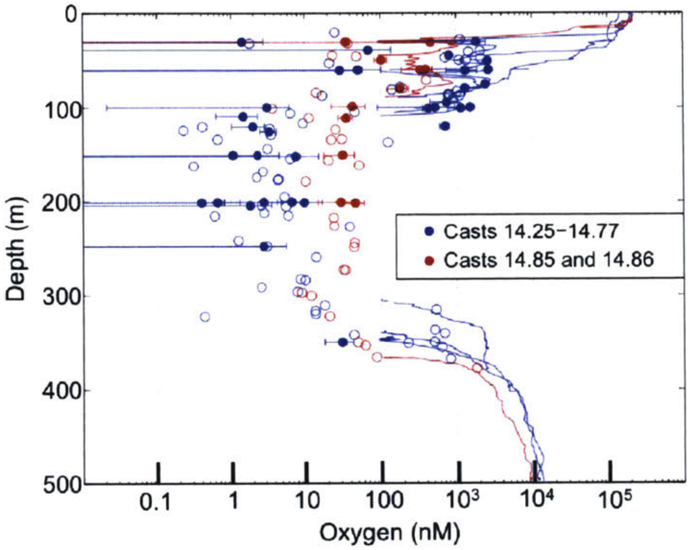

Figure 2.1: Oxygen measured by Thamdrup et al. (2012) with the STOX (Switchable Trace amount OXygen) sensor (circles) and a STOX-calibrated conventional oxygen sensor (lines) in the Eastern South Pacific along the west coast of South America. As in Thamdrup et al. (2012), locations with multiple measurements (solid circles) include error bars (standard deviations), and locations with one measurement (open circles) have a detection limit of 10 nM. Error bars that intersect with the y-axis signify error to or below zero. Oxygen was consistently below 10 nM at the core of the anoxic zone at five sites, with nine total casts (blue), and varied from 10–50 nM at one site, with two casts (red).

oxygen concentrations at or below these limits (Fig. 2.1; Revsbech et al. 2009; Jensen et al. 2011; Kalvelage et al. 2011; Thamdrup et al. 2012; Tiano et al. 2014). Though recent studies show the bulk of anaerobic activity occurring at the STOX detection limit, they also reveal denitrification and anammox at much higher concentrations (up to 10s of µM) both sporadically (Dalsgaard et al. 2012; De Brabandere et al. 2014) and consistently (Kalvelage et al. 2011). It is not clear whether these latter observations can be explained by favorable anaerobic metabolisms at these concentrations, by micro-anoxic zones within particles (Karl et al. 1984; Woebken et al. 2007; Klawonn et al. 2015; Kalvelage et al. 2015), experimental effects (De Brabandere et al. 2012), or dispersal processes.

The STOX-enabled observations imply feasible aerobic growth at nanomolar levels of oxygen. Stolper et al. (2010) demonstrated aerobic growth of *E. coli* down to 3 nM oxygen in the laboratory, with data fit to a Monod model of oxygen-dependent growth with a half-saturation (K_m) value of 120±20 nM. Complementary studies of OMZ microbes have used the STOX sensor and careful development of tanoxic conditions to provide evidence of a nanomolar threshold between aerobic and anaerobic metabolism. Dalsgaard et al. (2014) demonstrated that oxygen suppresses denitrification rates, with 50% inhibition at about 200 and 300 nM for N_2 and N_2O production, respectively. Complimentarily, Tiano et al. (2014) found that aerobic respiration continues until oxygen is depleted to nanomolar levels, with apparent K_m values of 10–200 nM. Gong et al. (2016) also measured varying K_m values of 30–60 nM for marine bacteria, some of which decreased to below 10 nM with changes in cell physiology. Dalsgaard et al. (2014) observed a 50% inhibition of anammox at much higher concentrations- almost 900nM oxygen. Other observations also suggest that anammox tolerates higher oxygen concentrations than heterotrophic denitrification (Jensen et al. 2008; Kalvelage et al. 2011; Dalsgaard et al. 2012).

The physiological basis for these very low limiting oxygen concentrations is linked to underlying enzymatic affinities (Gong et al. 2016). Using spectrophotometric methods to indirectly measure oxygen, high-affinity terminal oxidases for oxygen have been identified with half-saturation K_m values of 3–8 nM, which have been found to yield less energy per oxygen molecule than the low-affinity oxidases with K_m around 200 nM (Bott and Niebisch 2003; Morris and Schmidt 2013). Most anaerobes are thought to be facultatively so, switching between oxygen and other terminal electron acceptors such as nitrate or nitrite (Zumft 1997), and may or may not encode the high-affinity terminal oxidases (Morris and Schmidt 2013). Those that do not may switch their cellular machinery away from aerobic growth at a higher oxygen concentrations. Yet oxygen depletion to nanomolar detectability limits is widespread in marine oxygen minimum zones (e.g. Revsbech et al. 2009; Jensen et al. 2011; Kalvelage et al. 2011; Thamdrup et al. 2012; Tiano et al. 2014), and metagenomic analysis shows that the high-affinity oxidase is widespread in nature (Morris and Schmidt 2013), with both metagenomic and metatranscriptomic analysis showing its significance in the ETSP (Kalvelage et al. 2013, 2015). Hence the use of oxygen even at these very low levels must be a viable strategy in many environments, including OMZs.

Why is the minimum of dissolved oxygen in the ocean at or below nanomolar concentrations? In this study, we present a theory for a dynamic lower oxygen limit for aerobic microbial growth. Assuming that aerobic prokaryotes control the minimum oxygen concentrations in the dark pelagic water column, we model a generic aerobic prokaryotic cell, and relate the uptake of oxygen to its physiological demand. The framework is also sufficiently general to reflect chemoautotrophic, heterotrophic, and facultatively anaerobic metabolisms. We employ resource competition theory to frame the critical oxygen concentration as the minimum necessary to sustain an aerobic microbial population in a given environment, and suggest that the transition to energetically favorable anaerobic growth begins at this subsistence concentration, O_2^*. It follows that the ambient oxygen concentration is then maintained at O_2^* as anaerobic activity becomes significant, if no other sinks for oxygen are present. O_2^* is not a fixed concentration, but varies as a function of predatory and other loss rates, cell size, temperature, and the yield of biomass synthesis with respect to oxygen. The quantitative model shows that a wide range of conditions correspond to a nanomolar minimum oxygen concentration, with tenths to hundreds of nanomolar also plausible.

2.3 Derivation of O_2^*

We first consider how the supply of oxygen limits the growth of the generic aerobic functional type. We can calculate an oxygen-limited growth rate μ_{O_2} (t^{-1}) by relating the uptake rate of oxygen into a cell, ρ_{O_2} (mol O_2 cell^{-1} t^{-1}), to the yield of biomass with respect to oxygen, y_{O_2} (mol C synthesized mol O_2^{-1}), and an estimate of the carbon quota of the cell, Q (mol C cell^{-1}), as:

$$\mu_{O_2} = \rho_{O_2} y_{O_2} Q^{-1} \tag{2.1}$$

The oxygen yield y_{O_2} represents the moles of biomass synthesized per mole of oxygen respired for an aerobic heterotroph or chemoautotroph. Fig. 2.4(a) shows estimates of $y_{O_2}^{-1}$ as the oxygen demand (mol O_2 mol C synthesized^{-1}), calculated as the ratio of bacterial respiration to bacterial production from the global database of community and bacterial respiration (http://web.pml.ac.uk/amt/data/respiration.xls; version: Jan 22, 2015; Robinson and Williams 2005), which assumes a respiratory quotient of one (1 mol O_2 consumed = 1 mol CO_2 produced). The median oxygen demand is 5.4 mol O_2 mol $^{-1}$ C (mean 11 ± 16 mol O_2 mol C^{-1}). The oxygen yield and organic matter yield (often referred to as the growth efficiency) of a heterotroph can also be related theoretically, based on mass and electron balance. We describe this prognostic approach in Appendix 2.A.1.

Michaelis-Menten kinetics are used to describe the uptake of substrates, with the form dictated by a combination of factors, including diffusion through a molecular boundary layer, the density of porters, and/or the characteristics of the internal enzymes which utilize the substrate (Armstrong 2008; Fiksen et al. 2013). In Appendix 2.A.2, we show that at low oxygen concentrations and with high-affinity capabilities, the Michaelis-Menten model reduces to a linear, diffusive parameterization of transport across the molecular boundary layer (Gerard 1931; Gong et al. 2016), as:

$$\rho_{O_2} = 4\pi r D O_2 \tag{2.2}$$

where r is the cell radius, D is the temperature-dependent diffusion coefficient for oxygen in seawater, and O_2 is the external concentration of oxygen. We consider this diffusive limit an appropriate description of a mixed microbial community, independent of K_m values. (Fig. 2.5; see Appendix 2.A.2 for discussion).

Resource competition theory then provides an ecological context. In a steady-state environment, a population has grown sufficiently to reduce a limiting resource, R, to its subsistence concentration, R^* (Tilman 1982). We evaluate the subsistence concentration of oxygen of the aerobic microbial functional type as the balance of oxygen-limited growth and loss rates. The rate of change of the biomass, B, neglecting physical transport and mixing terms, varies as a function of its growth μ and losses L, as:

$$\frac{dB}{dt} = \mu B - LB \tag{2.3}$$

where L represents all forms of loss and mortality, including maintenance metabolism (Pirt 1965), grazing, viral lysis and programmed cell death.

We make a steady-state assumption ($\frac{dB}{dt} = 0$), which is approximately true for conditions in which $\mu B \approx LB$, and $\frac{dB}{dt} \ll \mu B$. Then combining equations 2.1, 2.2, and 2.3, and including a more explicit description of the cell carbon quota ($Q = q\frac{4}{3}\pi r^3$, where q is a given volumetric carbon content of the cell; 18.3 fmol C μm^{-3} from Bratbak and Dundas 1984) gives an expression for the subsistence oxygen concentration O_2^*:

$$O_2^* = \frac{Lqr^2}{3y_{O_2}D} \tag{2.4}$$

which is also the steady-state environmental concentration, given no other sinks of oxygen. This expression is general, and relevant for an oxygen-limited microbial community with high-affinity capabilities (Appendix 2.A.2). O_2^* is thus the concentration governing the viability of the aerobic metabolism at the population level.

Following resource ratio theory of Tilman (1982), once oxygen is depleted to O_2^*, coexistence of aerobic and anaerobic growth is feasible. We would not expect to observe energetically favorable anaerobic activity at oxygen concentrations higher than O_2^*, but aerobic and anaerobic metabolism can co-exist to varying degrees when oxygen is at this concentration. For a facultative anaerobic population, we can consider this variation as the fraction of the population's respiration as a whole that utilizes oxygen vs. alternative electron acceptors.

2.4 Estimating O_2^*

Parameter space for O_2^* across marine environments

The subsistence concentration O_2^* for an aerobic microbe is not a constant; it is a function of the parameters in Eqn. 2.4: losses L, cell size (here assuming a spherical cell with radius r), the oxygen yield y_{O_2}, and temperature (via the diffusion coefficient D for oxygen

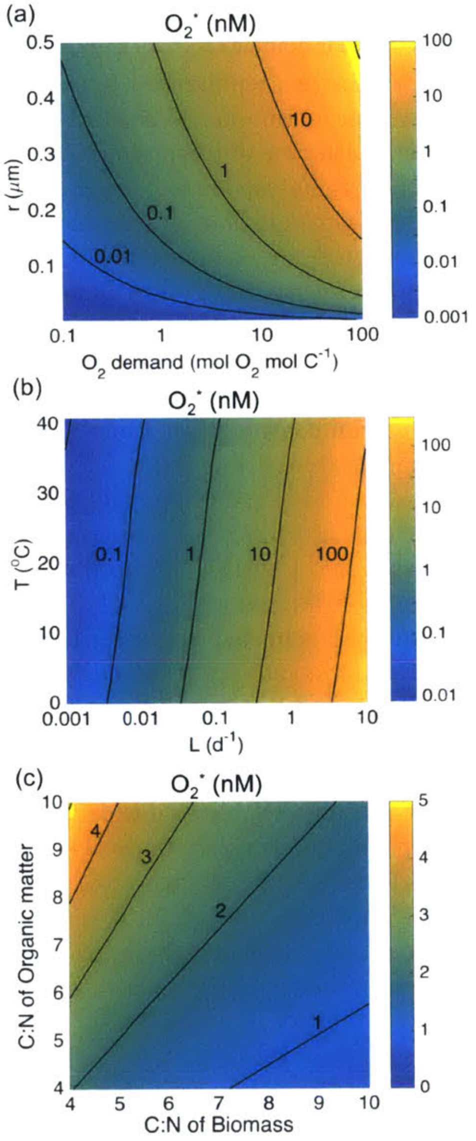

Figure 2.2: O_2^* as a function of (a) cell radius r and oxygen demand ($y_{O_2}^{-1}$), (b) losses L and temperature T (via D, the diffusion coefficient for oxygen in seawater), and (c) the C:N stoichiometry of organic matter substrate and biomass composition. Unless varying, parameters are set as best estimates for marine oxygen minimum zones: $L = 0.1\ d^{-1}$, $T = 12°C$, $r = 0.25$ μm, and $y_{O_2}^{-1} = 7$ mol O_2 mol $^{-1}$ C.

in solution). What is the plausible range of O_2^* in marine environments? Syntheses of observations that characterize most marine environments inform values for these parameters, and we illustrate the resulting range of reasonable O_2^* values in Fig. 2.2.

O_2^* increases linearly with oxygen demand $y_{O_2}^{-1}$. In Fig. 2.2(a), we illustrate O_2^* for $y_{O_2}^{-1}$ for 0–100 mol O_2 mol $^{-1}$ C synthesized, representing a range in growth efficiency of 1–0.01, respectively, assuming average marine stoichiometries (Appendix 2.A.1). Mean bacterial growth efficiencies from the database of Robinson (2008) for open ocean and coastal regions (0.14 and 0.19, respectively) correspond to oxygen demands of 5–14 mol O_2 mol $^{-1}$ C synthesized (Appendix 2.A.1), though none of the data come from oxygen minimum zones. We note that O_2^* has an asymptotic relationship with growth efficiency (Eqn. 2.8), once oxygen demand converges to zero as cell growth approaches perfectly efficient synthesis from organic substrate.

In Fig. 2.2(a), we also illustrate O_2^* over the range in the size of marine heterotrophic bacteria: 0.15–0.5 µm in radius (Sherr and Sherr 2000). O_2^* increases quadratically with cell radius for a constant cellular carbon density q (18.3 fmol C μm^{-3}; Bratbak and Dundas 1984). Seawater temperature ranges from below 0°C in the deep ocean to over 30°C at the surface; we illustrate O_2^* for 0–40°C, which coincides with about a threefold variation in D of $1.1–3.6 \times 10^{-5}$ cm^2 s^{-1} (for a salinity of 35; www.unisense.com/files/PDF/Diverse/Seawater & Gases table.pdf, accessed Jan. 7, 2016). O_2^* thus decreases slightly as temperature increases (Fig. 2.2b).

A relevant range for losses can be estimated from mean bacterial growth rates, since for a stable population at steady state, loss rates must balance growth rates. Bacterial growth rates at the surface vary substantially, but on average range from about 0.1 to 1 day^{-1} (Ducklow 2000), with 0.1 day^{-1} as a calculated average (Kirchman 2016). Subsurface pelagic bacterial growth rates are also on average 0.1 day^{-1} (Aristegui et al. 2009). Since observations in OMZs are lacking, we illustrate O_2^* across a wider range of loss rates, from 10^{-3} to 10 day^{-1}, which represents population doubling times of two years to two hours, respectively (Fig. 2.2b). O_2^* increases linearly with loss rates.

Across the parameter space illustrated in Fig. 2.2, O_2^* varies from less than 0.1 to a few hundred nanomolar. Large values coincide with high oxygen demands, large cell sizes, and high loss rates. We next explore a more targeted parameter space.

Using observations to predict O_2^* in an OMZ

For predictions of O_2^*, total rates of losses– to grazing, viruses, maintenance, and cell death– are key (Fig. 2.2), yet poorly constrained for heterotrophic microbes in subsurface marine environments. Here, we use a dataset that specifically provides these loss rates for aerobic microbes to more carefully predict the minimum oxygen concentration in the core of an anoxic zone.

We calculate O_2^* from Eqn. 2.4 for a site in the coastal upwelling region off of northern Chile using the observations of Cuevas and Morales (2006) of temperature and the specific grazing rates on bacteria by heterotrophic nanoflagellates (Fig. 2.3a,b). The diffusion coefficient for oxygen D was calculated as a function of temperature using a linear fit to published values for 2–25°C seawater (www.unisense.com/files/PDF/Diverse/Seawater & Gases table.pdf, accessed Jan. 7, 2016; $R^2 = 0.998$). To increase the uncertainty of our estimate, we calculate O_2^* with and without the contribution of an additional 0.1 day^{-1} loss rate, representing other mortality or maintenance. This gives two estimates of loss rates that differ by a factor of two (Fig. 2.3b). Cuevas and Morales (2006) infer that grazing rates fully compensate for bacterial production rates in the anoxic core below 40m, which suggests that additional mortality is in fact negligible.

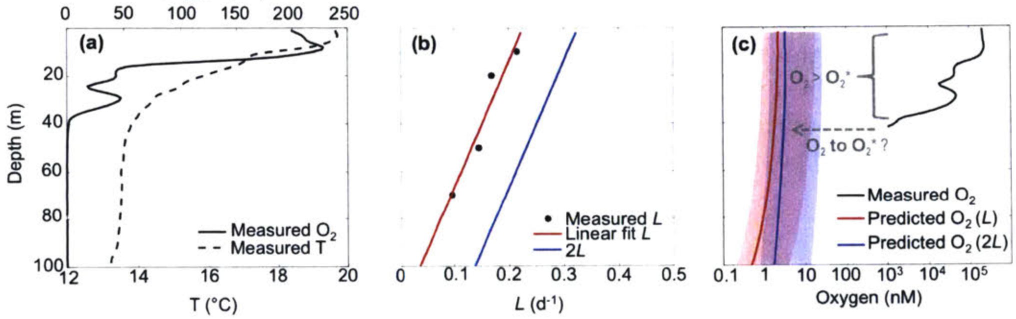

Figure 2.3: Predicted O_2^* from measured vertical distributions of (a) temperature, oxygen, and (b) the specific grazing rate on bacteria by heterotrophic nanoflagellates at a coastal upwelling site off Iquique, Chile (20.06°S, 70.19°W) (Cuevas and Morales 2006). O_2^* is calculated with and without an additional loss rate of 0.1 day^{-1}. For both estimates, (c) calculations reflect the average coastal growth efficiency of 0.19 (lines) with uncertainty due to its standard deviation of 0.16 (shaded regions). Measured oxygen concentrations (a and c) are omitted below the detection limit of 1 μM.

We then calculate O_2^* for $r = 0.25$ μm (which gives 14 fg C cell^{-1} with the cellular carbon density (q) of Bratbak and Dundas (1984), close to the midpoint for the estimated 10–20 fg C cell^{-1} from Ducklow 2000) and using the coastal marine average growth efficiency and its standard deviation of 0.19±0.16 (Robinson 2008) to estimate the oxygen demand (Appendix 2.A.1). The model uncertainty (shaded areas) corresponds to the resulting range in oxygen demand of 3–35 mol O_2 mol C^{-1}. Because growth using the high-affinity oxidases required to utilize oxygen at low levels is presumably less efficient than that represented by the average, we may expect better predictive power of the higher end of this range (and higher resulting O_2^*).

The model predicts O_2^* consistently below 25 nM, and decreasing slightly with depth (Fig. 2.3c); though temperature and grazing rate both decrease with depth, their opposing influence (as illustrated in Fig. 2.2b) leads to a smaller net impact on O_2^*. In the "anoxic" core, below 40m, the model predicts a mean O_2^* concentration of 0.5–3 nM, just at and below the STOX sensor detectability. The range in oxygen demand results in the model uncertainty of 0.2–24 nM, with the high end representing the highest oxygen demand (corresponding to a growth efficiency of 0.03). This prediction could be partially tested, to the few nanomolar detection limit, by deployment of the STOX sensor at this location.

Beyond marine environments

Since low oxygen environments are not constrained to the marine realm, this model may have broader application. We compare marine estimates to the parameters documented by Stolper et al. (2010) for the growth of *E. coli* to 3 nM oxygen at 37°C, human body temperature. We find that the apparent half-saturation (K_m) values of bacteria in OMZs and *E. coli* in optimal laboratory conditions can be more than an order of magnitude different: <10 nM and 120 nM, respectively (Gong et al. 2016; Stolper et al. 2010). Yet in both environments, oxygen is depleted to a few nanomolar or less (Thamdrup et al. 2012; Stolper et al. 2010). In Appendix 2.A.2, we demonstrate how the diffusive supply of oxygen similarly limits prokaryotic growth in the deep ocean and in optimal laboratory conditions, despite the different K_m values, since apparent K_m values reflect maximum rates. This suggests that this framework is sufficiently flexible to represent the limiting oxygen concentration for a variety of microbial populations growing at a variety of rates across environments.

2.5 Discussion

Summary of results

We hypothesize that the limiting oxygen concentration for aerobic respiration in an aquatic environment is O_2^*, the subsistence oxygen concentration for an aerobic prokaryotic population, and that O_2^* represents the minimum oxygen concentration in that environment. This anticipates the observed nanomolar oxygen concentrations in the ocean's oxygen minimum zones (e.g. Revsbech et al. 2009; Jensen et al. 2011; Kalvelage et al. 2011; Thamdrup et al. 2012; Tiano et al. 2014). As the threshold for sustainable aerobic growth, O_2^* is also the concentration at which external oxygen is maintained as diverse suites of anaerobic metabolisms activate, excepting the presence of other sinks for oxygen. This minimum oxygen concentration varies as a function of environmental factors as well as cell physiology: O_2^* increases with losses to mortality and predation, decreases with temperature, and increases with oxygen demand and cell size (Fig. 2.2). Plausible estimates for these factors in marine environments suggest that O_2^* may vary substantially– up to tens or hundreds of nanomolar for rapid microbial population turnover rates or high oxygen demand– but is largely in the nanomolar range. Using grazing rates on bacteria measured by Cuevas and Morales (2006) in a coastal anoxic zone, we predicted an O_2^* concentration of order 0.1–10 nM.

Implications of a flexible, nanomolar O_2^* for diverse species and environments

O_2^* as the minimum oxygen concentration in "anoxic" marine zones. We hypothesize that O_2^* is likely to represent the minimum ambient oxygen concentration of essentially anoxic pelagic marine zones. When $O_2 = O_2^*$, aerobic respiration is at the edge of being a non-viable metabolism for the microbe in its environment. Once oxygen is depleted to O_2^*, either coexistence with or competitive exclusion by an anaerobic metabolism is possible (Tilman 1982). The theory anticipates both in an anoxic zone: that aerobic respiration will maintain the O_2^* concentration while anaerobic metabolisms also operate, and that diverse anaerobic metabolisms may operate exclusively at the core of the zone.

In anoxic zones, $O_2 = O_2^*$ only if no other process is capable of further depleting oxygen. Sulfide oxidation in sulfidic environments could potentially scavenge oxygen to lower levels (Preisler et al. 2007; Canfield et al. 2010), thus excluding aerobic respiration entirely. Also, we have so far considered the O_2^* of strictly aerobic growth. If aerobic respiration and denitrification occur simultaneously in cells (Chen and Strous 2013), lowering a population's demand for oxygen relative to biomass synthesis, the O_2^* of that aerobic-anaerobic hybrid activity would be lower. Thus a hybrid metabolism would potentially further deplete oxygen as long as it remains energetically favorable. In these ways, the O_2^* of strictly aerobic growth represents an upper bound on the lowest oxygen concentration in an oxygen minimum zone.

O_2^* varies across environments. The O_2^* framework reflects variation among steady-state environments, and provides an explanation for how the minimum oxygen concentration may differ among sampling sites and times, and between different organisms adapted to various conditions. We might anticipate that the limiting oxygen concentration decreases with depth if bacterial grazing by nanoheteroflagellates, for example, decreases with depth. On the other hand, such an effect on O_2^* may be dampened or cancelled out by a decrease in growth efficiency with depth, since it is plausible that bacteria may optimize carbon utilization rather than their growth efficiency in the 'oligotrophic' deep ocean (del Giorgio and Cole 1998).

At one site in the Eastern South Pacific OMZ, oxygen was consistently measured by the STOX sensor at 10–50 nM, in contrast to nine other casts at five sites, in which oxygen was below the detection limit (Fig. 2.1; Thamdrup et al. 2012). The authors point to a perturbation in the hydrography at this site as evidence of an injection of water from another source, probably by mixing. We may consider this higher oxygen concentration as indicative of aerobic activity. However, our analysis suggests that this 50 nM concentration may be the O_2^* concentration of the intruding water body, and thus it might also be undergoing anaerobic activity. Fig. 2.2 shows that 50 nM is a plausible O_2^* concentration, reflecting, for example, a microbial population subject to a low growth efficiency, and thus higher oxygen demand, due to a less nutritious food source or some other energetic limitation. Simultaneous sampling for the presence of anaerobic activity could test this hypothesis. This case exemplifies how the theory of a dynamic oxygen threshold can impact interpretation of observations: we do not expect one fixed limiting oxygen concentration for all environments.

An argument against a 10 μM threshold. Our results are quantitatively different from Brewer et al. (2014), who propose that nitrate should offer more free energy than oxygen once oxygen is depleted to about 10 μM, assuming nitrate concentrations of about 40 μM. They conclude that this could represent the conditions for the onset of nitrate reduction. On one hand, Brewer et al. consider a case for which O_2^* theory does not apply: when growth is not limited by the electron donor (such as organic matter), but rather by the electron acceptor. This initially poses the question of whether or not these two theories are complementary, i.e., that a 10 μM onset for nitrate reduction and a nanomolar lower limit for aerobic respiration together represent a window for the energetically favorable coexistence of both.

Further analysis suggests not, with two lines of reasoning. First, the framework of Rittman and McCarty (2001), which serves as a base for O_2^* theory (Appendix 2.A.1), poses that for this electron acceptor-limited case, the relevant comparative rates are the uptake rates of substrate into the cell relative to the yields of biomass for those substrates. These would be $\rho_{O_2} y_{O_2}$ for oxygen (as in Eqn. 2.1) and $\rho_{NO_3} y_{NO_3}$ for nitrate. Brewer et al. consider diffusive supply rates for both oxygen and nitrate. But the fact that oxygen is a small, uncharged molecule that can passively diffusive into cell, in comparison to nitrate, which requires enzyme-controlled, active transport suggests that these two uptake rates differ significantly and consistently. In this way, the framework of Brewer et al. is relevant from a geochemical, but not microbial, perspective. From the microbial perspective, we consider O_2^* and a similarly-calculated NO_3^* star to be the comparable limits, and expect O_2^* to be consistently lower than NO_3^* due to the diffusive-uptake advantage of oxygen.

Second, Brewer et al. consider the electron acceptor-limited case, and we can further demonstrate that oxygen and nitrate concentrations of order 10 μM should not limit most marine microbial growth, and thus that this case is rare. The model developed here quantitatively links external concentrations to growth. For oxygen to pose an energetic limitation to growth at 10 μM, growth rates would have to be at least about 50 d^{-1}, and over 100 d^{-1} for average efficiencies (Fig. 2.5). This could limit the >140 d^{-1} growth rate of the fastest-growing marine heterotrophic bacteria, *Vibrio natriegens* (Maida et al. 2013; Kirchman 2016). But for most populations, organic matter processing or other internal constraints results in much lower rates (about 1 d^{-1} maximum, 0.1 d^{-1} on average; Kirchman 2016). We conclude that a 10 μM oxygen threshold can only be reconciled for the very fastest heterotrophic bacteria.

Potential for a higher O_2^* for chemoautotrophic metabolisms. We might assume that the aerobic heterotrophic metabolism, due to a lower respiratory requirement per unit biomass, can draw down oxygen to a lower concentration than aerobic chemoautotrophs, such as nitrifiers, that undergo energy-intensive carbon fixation. This would imply that the switch from aerobic to anaerobic chemoautotrophy occurs at a higher oxygen concentration than the switch (within facultative cells) from aerobic to anaerobic heterotrophy. For example, we can consider the competition for ammonium between chemoautotrophic aerobic and anaerobic ammonia oxidation (i.e., the first step of nitrification and anammox), with the former using oxygen and the latter using nitrite as a terminal electron acceptor. All else being the same, the difference in O_2^* between nitrification and heterotrophy scales linearly with any difference in their oxygen demand (Eqn. 2.4): if the nitrifying population requires ten times more oxygen than the heterotrophic population to sustain the same rate of biomass turnover, its O_2^* will be ten times higher than that of heterotrophy. If this is 50 nM instead of 5 nM, for example, we might expect to see anammox occurring once oxygen is depleted to

50 nM, as it begins to favorably coexist with (and potentially eventually outcompete) nitrification at this higher O_2^*, even as oxygen continues to be depleted to 5 nM by heterotrophs. This is consistent with observations that anammox occurs at higher levels of oxygen than does heterotrophic denitrification (Jensen et al. 2008; Kalvelage et al. 2011; Dalsgaard et al. 2012, 2014).

However, Füssel et al. (2012) and Kalvelage et al. (2013) observe aerobic nitrification throughout oxygen minimum zones, suggesting that the O_2^* of nitrifiers may be comparable to that of heterotrophs. The smaller cell size of ammonia-oxidizing archaea (Martens-Habbena et al. 2009) or lower predation rates could allow for a comparable or even lower O_2^*. If this is the case, limitation by ammonium or nitrite, rather than oxygen, may govern chemoautotrophic dynamics.

Broad application. The theory here applies to oxygen minimum zones as well as to *E. coli* in the laboratory (Stolper et al. 2010): a simple, mechanistic model links oxygen-limited microbial growth to nanomolar oxygen concentrations (Appendix 2.A.2). While Stolper et al. (2010) similarly conclude that the limiting oxygen concentration should increase with cell size, as postulated by Fenchel and Finlay (1995), we suggest that other factors are also important. This consistency for two very different environments demonstrates a predictable limitation for aerobic microbial growth in diverse environments, and a broadly applicable model.

Limitations of O_2^* theory

The steady-state assumption vs. a dynamic oxycline. The results here define O_2^* for a steady state with respect to the growth of microbial populations. This approximation is valid for environments in which microbial metabolisms operate on much shorter timescales than physical changes in the environment, and thus control nutrient distributions. Departure from this steady state- such as from a pulse of quickly sinking organic matter- frees the threshold from the definition of O_2^*. In this way, O_2^* best describes the core of the anoxic zone, and not necessarily the diverse transition zone of a dynamic oxycline (Ward 2008; Bryant et al. 2012; Zaikova et al. 2010).

Additionally, when local dispersal rates exceed microbial growth and loss rates, anaerobic cells may be swept away from their ideal O_2^* conditions but still carry out denitrification or other anaerobic metabolisms while adjusting their cellular machinery to their new surroundings. Depending on these adjustment timescales, such dispersal may allow for the documentation of 'immigrant' anaerobic activity at higher concentrations (Clayton et al. 2013). Anoxic micro-environments inside particles (Karl et al. 1984; Woebken et al. 2007; Klawonn et al. 2015; Kalvelage et al. 2015) or methodological difficulties (De Brabandere et al. 2012) may also explain observations of anaerobic activity at tens of micromolar oxygen concentrations (e.g. Dalsgaard et al. 2012; De Brabandere et al. 2014; Kalvelage et al. 2011).

Other impacts on growth efficiency. If the efficiency of aerobic growth decreases as oxygen decreases, O_2^* will increase as oxygen decreases. Alternatively, if a facultative cell can acquire energy using oxygen and a form of nitrogen simultaneously, then O_2^* could decrease with decreasing oxygen, as nitrogen assumes a portion of the respiratory requirement. The model here is suitably general to incorporate either or both of these effects: as written, the model considers the oxygen yield (mole of biomass synthesis per moles of oxygen utilized) as an independent variable. One could instead consider it as a dependent variable ($y_{O_2} = \mathrm{f}[O_2]$), if this relationship is known.

However, if y_{O_2} decreases to the point that anaerobic metabolism becomes more efficient than aerobic, O_2^* theory no longer applies. For example, if the reduced efficiency of the high-affinity terminal oxidase system for oxygen utilization translates into a lower growth rate than that enabled by nitrate or nitrite utilization, the latter will be a more competitive strategy. Evaluating this difference in growth rate (i.e., how varying amounts of translocated protons of different oxidases relate to the competitive ability of aerobic and anaerobic cells at low oxygen concentration) would provide crucial insight, given that denitrification is much less efficient than its redox potential would suggest, for both bioenergetic as well as other kinetic reasons (Chen and Strous 2013). The fact that the STOX sensor has revealed large volumes of water at or below a few nanomolar concentrations suggests that utilization of oxygen to these low levels is a competitive strategy at those locations.

Utility of O_2^* theory for future observational and modeling work

The STOX sensor technology has already demonstrated nanomolar levels of oxygen in OMZs, and its attainable 1–2 nM detection limit could distinguish among oxygen concentrations within much of the predicted range for various environments. In this way, a sampling strategy could aim to analyze whether or not the minimum oxygen concentration actually does vary with the physiological and environmental parameters as predicted by the theory developed here. For example, concurrent measurements of temperature, bacterial production, bacterial respiration, and grazing rates on heterotrophic prokaryotes would enable a quantitative prediction of O_2^* (Eqn. 2.4) that the STOX sensor could then test. Conversely, the precision of STOX measurements could be used in combination with a subset of these measurements to infer one of the physiological or environmental parameters, such as total loss rates for anoxic bacterial populations.

We understand O_2^* as the concentration at which energetically favorable anaerobic activity begins. Including the aerobic microbial functional type in a biogeochemical model would allow for the depletion of oxygen to nanomolar concentrations without prescribing a critical oxygen concentration. Including nitrification, anammox, and intermediate steps of heterotrophic denitrification as additional functional types would further predict rates of fixed nitrogen loss and other nitrogen cycle dynamics. Our approach thus points to a means of dynamically modeling the feedbacks between diverse microbial metabolisms and nutrient distributions in anoxic zones in global biogeochemical models.

2.6 Conclusions

We develop a theory for the depletion of oxygen to nanomolar concentrations in marine oxygen minimum zones. We hypothesize that the minimum oxygen concentration in many aquatic environments is the subsistence concentration, O_2^*, of the bulk aerobic microbial population. For environments under steady microbial control, we expect anaerobic metabolisms to be energetically favorable while this minimum concentration is maintained. The resulting model predicts that this threshold concentration varies with loss rates, cell size, growth efficiency, and temperature, and that the parameters describing marine environments constrain it largely to the 0.1–10 nanomolar range. The theory presented supports the understanding that the smallest microbes tolerate the lowest oxygen concentrations, and thus inhabit low oxygen environments. The model also leads to a hypothesis for why anammox may be favorable at a higher oxygen concentration than denitrification, which is implied by some observations. Consistency with the growth of *E. coli* in optimal laboratory conditions suggests that the framework and its nanomolar predictions apply broadly, spanning diverse microbes and environments. The model thus predicts the essentially anoxic oxygen concentrations observed in OMZs, reconciling theory with observations, and provides testable hypotheses for future field work. In general, the description of the aerobic microbial metabolism exemplifies a simple, mechanistic parameterization of the interactions between microbial communities and nutrient distributions suitable for global marine biogeochemical modeling, absolving the need for a prescribed critical oxygen concentration.

2.A Appendix

2.A.1 The oxygen yield of an aerobic heterotroph

Here, we theoretically link the oxygen yield y_{O_2} of a heterotrophic microbe to the organic matter yield y_{OM}, often termed the bacterial growth efficiency (hereafter, referred to as 'growth efficiency'). This allows us to use observed growth efficiencies to estimate oxygen demand. To proceed, we define an aerobic heterotroph with the set of redox reactions that, to first order, underlies its metabolism, following the methodology of Rittman and McCarty (2001). The description consists of three half-reactions: organic matter decomposition, biomass synthesis, and the reduction of oxygen. Organic matter provides the elements and electrons for both the synthesis of biomass and energy production, and oxygen serves as the electron acceptor. We thus describe the metabolism as the combination of cell synthesis and energy production, partitioned by the fraction f of electrons going into the former vs. the latter. The aerobic heterotrophic metabolism is then represented by the sum of the three half-reactions, partitioned by f, and as a function of the stoichiometry for organic matter (OM) and biomass (B), as (neglecting water):

$$\frac{1}{d_{OM}}\mathrm{C}_{c_{OM}}\mathrm{H}_{h_{OM}}\mathrm{O}_{o_{OM}}\mathrm{N}_{n_{OM}} + \frac{1-f}{4}\mathrm{O}_2 \rightarrow \frac{f}{d_B}\mathrm{C}_{c_B}\mathrm{H}_{h_B}\mathrm{O}_{o_B}\mathrm{N}_{n_B} + \left(\frac{c_{OM}}{d_{OM}} - \frac{c_B f}{d_B}\right)\mathrm{CO}_2 + \left(\frac{n_{OM}}{d_{OM}} - \frac{n_B f}{d_B}\right)\mathrm{NH}_4^+ \quad (2.5)$$

where d is the number of electron equivalents for the generic organic composition $\mathrm{C}_c\mathrm{H}_h\mathrm{O}_o\mathrm{N}_n$ that correspond to the oxidation states of its inorganic constituents, here as $d = 4c + h - 2o - 3n$. The oxygen yield (mol C synthesized mol O_2^{-1}) is then defined in terms of f as:

$$y_{O_2} = \frac{4f}{d_B(1-f)} \quad (2.6)$$

The growth efficiency (mol B mol $^{-1}$ OM, or, mol C synthesized mol $^{-1}$ C consumed) then relates to f as:

$$y_{OM} = \frac{d_{OM}}{d_B}f \quad (2.7)$$

and so $y_{OM} = f$ when assuming the same stoichiometry for both the organic matter substrate and microbial biomass. With the above, we can then express the oxygen yield in terms of the growth efficiency as:

$$y_{O_2} = \frac{4y_{OM}}{d_{OM}(1 - y_{OM}\frac{d_B}{d_{OM}})} \quad (2.8)$$

which allows us to explore the relationship between the growth efficiency, organic matter stoichiometry, prokaryotic biomass stoichiometry, and the oxygen yield.

Fig. 2.4b (blue line) illustrates the inverse oxygen yield (the oxygen demand) as a function of growth efficiency when assuming the average stoichiometry of marine organic matter

($C_{106}H_{175}O_{42}N_{16}$ from Anderson 1995) for both the organic matter substrate and microbial biomass, for which the full metabolism is represented as:

$$\begin{aligned} C_{106}H_{175}O_{42}N_{16} &+ \frac{467(1-y_{OM})}{4}O_2 \\ &\rightarrow \quad y_{OM}C_{106}H_{175}O_{42}N_{16} + 106(1-y_{OM})CO_2 + 16(1-y_{OM})NH_4^+ \end{aligned} \tag{2.9}$$

In comparison, the data from the bacterial respiration database of Robinson and Williams (2005) fall exactly on a line because of the recursive relationship between growth efficiency and oxygen demand (Fig. 2.4b). This line is very close to the theoretically predicted line because of the underlying assumption that total carbon demand equates to the sum of the respiration and production (i.e., the respiratory quotient of one CO_2 produced per mole O_2 consumed; Robinson 2008). Also plotted Fig. 2.4b are the resulting curves for a high C:N of organic matter substrate ($c_{OM} = 160$; C:N = 10), and a low C:N of biomass ($c_B = 80$; C:N = 5). Both show a higher oxygen demand for a particular growth efficiency, since both mandate a decrease in the C:N from organic matter to biomass composition, and thus less efficient use of the substrate. As y_{OM} approaches zero, the oxygen demand for these varying stoichiometries approaches a positive constant, a model artifact reflecting the excess carbon in the organic matter source. The effect of this varying stoichiometry on O_2^* is illustrated in Fig. 2.2c.

This model of prokaryotic metabolism, while simplified, demonstrates the electron-balanced relationship between bulk organic matter usage and the oxygen yield (Fig. 2.4). As ballpark estimates, the average growth efficiency of the open and costal oceans of 0.14 ± 0.14 and 0.19 ± 0.16, respectively (Robinson 2008), corresponds to an average oxygen demand of about 7–14 mol O_2 mol^{-1} C synthesized, with the lower end corresponding to the curves exhibited by the data and by the assumed equal stoichiometries of organic matter and biomass, and the higher end to the varying stoichiometries. The lowest reported growth efficiency of 0.01 (del Giorgio and Cole 1998) corresponds to 100–200 mol O_2 mol^{-1} C synthesized. We illustrate the resulting sensitivity of O_2^* to a wide range in oxygen demand in Fig. 2.2a.

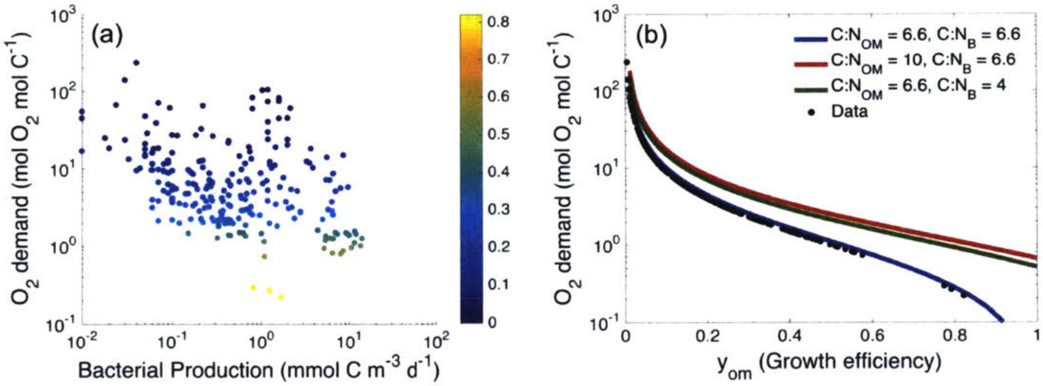

Figure 2.4: (a) The observed bulk oxygen demand ($y_{O_2}^{-1}$) against bacterial production, with color indicating the associated growth efficiency (BGE) from the bacterial respiration database of Robinson and Williams (2005). (b) The observed and theoretical oxygen demand against growth efficiency for a heterotrophic microbe, for varying stoichiometries of marine organic matter (C:N_{OM}) and microbial biomass (C:N_B). The recursive relationship between calculations of oxygen demand and growth efficiency result in the data lying exactly on a curve close to the blue curve.

2.A.2 Comparing Michaelis-Menton and diffusive models of oxygen uptake

The uptake of oxygen, ρ_{O_2}, or of any substrate S, can be understood either as a diffusive process or as a saturating Michaelis-Menton (MM) function ($\rho = \rho_{max}\frac{[S]}{K_S+[S]}$). Armstrong (2008) develops a model of substrate uptake that combines both, normalized to uptake per cell in Bonachela et al. (2011) as:

$$\rho_{O_2} = \rho_{max}\frac{O_2}{k_P + \rho_{max}/(4\pi rD) + O_2} \tag{2.10}$$

where ρ_{max} is a maximum uptake rate and k_P is the half-saturation constant representing the concentration near the cell surface, r is the cell radius, D is the temperature-dependent diffusion coefficient for oxygen in seawater, and O_2 is the external concentration of oxygen. We would expect to measure a bulk half-saturation constant $k_S = k_P + \rho_{max}/(4\pi rD)$ in experiments or samples (Fiksen et al. 2013). Here, we neglect reduced permeability of oxygen through the cell wall and membrane given estimates of their insignificant effects on the order of the diffusion coefficient (Stewart 1998; Kihara et al. 2014). Armstrong (2008) includes the non-spherical influence and advective influence around the cell with Phi and the Sherwood number as $D = \Phi ShD_0$, though estimates that for small cells, the Sherwood number (which is similar to the Peclet number) should be close to one. If most marine bacteria are close to spherical, Φ should also be close to one. Here, we leave as D for simplicity, noting the ability to include these effects.

We can anticipate a cell's switch to a high-affinity terminal oxidase system: all else the same, reducing k_P increases the affinity for oxygen. Yet, as k_P and O_2 become small, the middle term in the denominator dominates, and the expression reduces to a diffusion-limited uptake rate for a spherical cell (Gerard 1931):

$$\rho_{O_2diff} = 4\pi rDO_2 \tag{2.11}$$

Comparing the two models of oxygen-limited growth (Eqn. 2.1 with Eqn. 2.10 or 2.11) scales their convergence for real values, and justifies the reduction of the coupled model to the diffusive model (Fig. 2.5). We parameterize both models with the values approximating microbial growth in a marine oxygen minimum zone ($r = 0.25$ μm, $y_{O_2}^{-1} = 7$ mol O_2 mol $^{-1}$ C, $T = 12°C$; blue lines). The coupled model requires two additional inputs: a half-saturation constant k_P of 3 nM, the minimum for high-affinity oxidases (Morris and Schmidt 2013), and ρ_{max}, computed as $\mu_{max}y_{O_2}^{-1}Q$ with a maximum growth rate μ_{max} of 1.1 day^{-1}, the average growth rate for heterotrophic bacteria in seawater cultures, which is an order of magnitude larger than the estimated bulk average growth rate (Kirchman 2016). The two functional forms converge at low oxygen- approximately the computed value of the middle term in the denominator, 20 nM. This demonstrates how the diffusive supply of oxygen begins to limit growth at nanomolar concentrations. We can thus explain why 3-8 nM is the k_S range for the high-affinity oxidase of an aerobic microbe (Morris and Schmidt 2013); we might expect that prokaryotes have adapted their cellular machinery as such as a competitive strategy to reach the diffusive limit.

In comparison, Fig. 2.5 (black lines) also illustrates the parameters of Stolper et al. (2010) for the growth of *E. coli* to 3 nM oxygen: a yield of 0.51 mol C mol O_2^{-1}, and $T = 37°C$, human body temperature. We again plot both the coupled and diffusive models of oxygen-limited growth, with a 0.25 μm radius cell for the diffusion model, and with the Monod model as fit by Stolper et al. (2010): $k_S = 120$ nM and $\mu_{max} = 0.4$ h^{-1}. The convergence of the two models again illustrates how diffusive supply ultimately describes oxygen-limited growth. The measurements of Stolper et al. (2010) thus provide explicit demonstration that diffusive limitation serves as the maximum affinity.

The diffusive limitation is similar for both parameterizations, despite the fact that the reduction to the diffusion model is justified at an order-of-magnitude higher oxygen concentration for the faster growing *E. coli*. This difference is reflected in the order-of-magnitude different half-saturation values for marine bacteria (order 10 nM; Gong et al. 2016) and for Stolper et al.'s *E. coli* (120 nM). We suggest that apparent half-saturation values vary substantially for the same underlying diffusive limitation because they ultimately reflect internal growth constraints. Since k_S values are intrinsically linked to maximum rates, they alone are not useful indicator of a cell's competitive ability to use a substrate; rather, the affinity (ρ_{max}/k_S) is the indicative parameter by which one can compare different populations across environments (Fiksen et al. 2013). We understand the diffusive supply rate $4\pi rD$ as the "maximum uptake affinity" (Thingstad et al. 2005; Fiksen et al. 2013). We assume that given low oxygen supply, a portion of the aerobic population will optimize their affinity for oxygen. In short, O_2^* should represent the limiting oxygen concentration for diverse aerobic microbial communities in diverse environments.

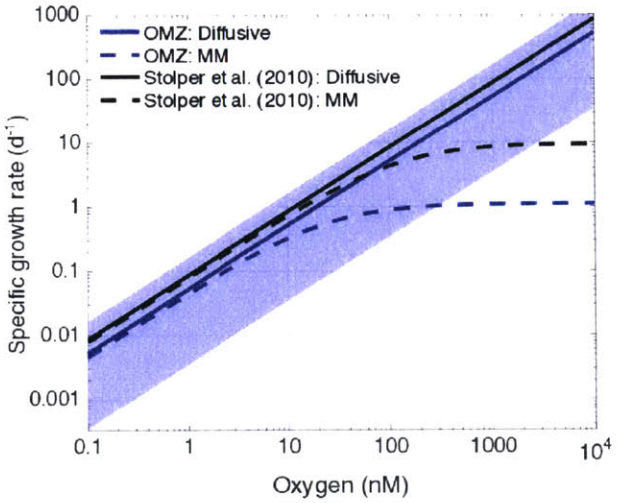

Figure 2.5: The two models of microbial growth rates as a function of external oxygen concentration: the coupled Michaelis-Menton model of Armstrong (2008) (Eqn. 2.10, solid lines) and its reduced diffusive version (Eqn. 2.2/2.11, dashed lines). Blue lines indicate the estimate for average marine microbial growth ($r = 0.25$ μm, $y_{O_2}^{-1} = 7$ mol O_2 mol $^{-1}$ C, $T = 12$°C, $\mu_{max} = 1.1$ day^{-1}, $k_P = 3$ nM), and black lines for the results of Stolper et al. (2010) ($r = 0.25$ μm, $y_{O_2} = 0.51$, $T = 37$°C, $\mu_{max} = 9.6$ day^{-1}, $k_S = 120$ nM). The shaded region indicates the uncertainty of the diffusive model due to a range in oxygen demand of 2–110 mol O_2 mol $^{-1}$ C.

Chapter 3

The transition to aerobic-anaerobic coexistence in marine oxygen minimum zones

The work in the main section of this chapter was completed in collaboration with Mick Follows and Amala Mahadevan. The work in Addendum 2 was done in collaboration with Jonathan Lauderdale, who guided the calculations of transport, and Reiner Schlitzer, who provided the gridded POC flux estimate.

3.1 Overview

The transition from aerobic to anaerobic metabolisms in the ocean is qualitatively well understood, but quantitative description is necessary for understanding how fixed nitrogen loss might change over time. Here, we describe this transition mechanistically as the outcome of the competition of aerobic and anaerobic microbial metabolisms. In a simple ecological model, greater efficiency of biomass production when oxygen is used as an electron acceptor rather than nitrate or nitrite allows for the competitive exclusion of anaerobic metabolisms in oxygenated environments. We use a resource ratio theory approach to define a threshold for the onset of anaerobic metabolism as a function of the relative supply of oxygen and an electron donor (here, organic matter), rather than as a specific oxygen concentration. At this threshold, coexistence of aerobic and anaerobic metabolisms is sustained at the limiting oxygen concentration. The ratio of aerobic to anaerobic biomass and activity declines with decreasing oxygen supply, which is consistent with observations of aerobic and anaerobic sulfur bacteria in a laboratory. The model suggests the likelihood of stably coexisting aerobic and anaerobic metabolisms at the periphery of oxygen minimum zones (OMZs) in anoxic conditions. Coexistence in the core of an anoxic zone may also be favorable, with a small, sustainable aerobic population consuming trace amounts of oxygen. We demonstrate these dynamics in a two-dimensional idealized OMZ model.

In Addendum 1, we demonstrate the analogous dynamics of coexistence of anammox and the two steps of aerobic nitrification in particular, without any forced oxygen inhibition. We then analyze the interactions of the six main metabolisms (half aerobic, half anaerobic, half heterotrophic, half chemoautotrophic) understood to control the N cycle in oxygen minimum zones. This demonstrates the transition of the three aerobic to the three anaerobic metabolisms as oxygen decreases, and the convergence of the rates of anammox and denitrification to the chemically-determined theoretical ratio, thus aligning geochemical and population ecology approaches to understanding OMZ dynamics. In Addendum 2, we calculate the transition in the real ocean to identify the anaerobic domain. We find that data is insufficient for it to be quantitatively meaningful.

3.2 Introduction

Oxygen minimum zones in the ocean result from a combination of physical and biological processes: high levels of aerobic respiration in areas with poor ventilation leads to oxygen depletion (Devol 2008; Paulmier and Ruiz-Pino 2009; Brandt et al. 2015). In Fig. 3.1a, the isopycnals along the 10°S transect in the Pacific ocean show an upward slope in the east, indicating the upwelling currents that supply nutrients to the surface and fuel primary productivity, and also show a lack of outcropping of denser waters. Respiration of the sinking organic matter to these areas depletes oxygen, with microorganisms able to access oxygen at its lowest concentrations. When sufficiently depleted, and while inorganic nitrogen remains abundant, diverse anaerobic microbial metabolisms utilize inorganic nitrogen species for energy, which can lead to the loss of fixed nitrogen from these zones (Ulloa et al. 2012; Wright et al. 2012; Ward 2013). Deoxygenation of the oceans due to global warming is expected (IPCC 2014), and understanding the controls on anaerobic vs aerobic processes is necessary to anticipate its consequences. What quantitatively defines the transition to anaerobic metabolism?

Observations of microbial activities suggest the coexistence of aerobic and anaerobic metabolisms in low oxygen environments. Aerobic nitrification has been shown to co-occur with anaerobic ammonium oxidation (anammox), nitrate reduction, and/or denitrification (Lipschultz et al. 1990; Lam et al. 2007; Füssel et al. 2012; Kalvelage et al. 2013; Peng et al. 2015). Many of these co-occurrences are measured where oxygen is in the nanomolar range or undetectable, though observations show anaerobic activity occurring at higher (1–10 micromolar) oxygen concentrations (Dalsgaard et al. 2012; De Brabandere et al. 2014; Kalvelage et al. 2011). Observed co-occurring aerobic and anaerobic metabolisms may reflect the physical mixing of cells away from the environments in which they can survive and sustain a population, or may indicate a steady co-existence of the two metabolisms. Are the co-occurrences sustainable co-existences, or a product of physical transport?

In a laboratory, van den Ende et al. (1996) observed the coexistence of aerobic and anaerobic sulfur bacteria when oxygen was limiting, with the ratio of the aerobic to anaerobic biomass decreasing with oxygen supply. How can we explain this co-existence? Resource competition theory articulates conditions for the sustained coexistence of two metabolisms (Tilman 1982; Ward 2013; Dutkiewicz et al. 2014); we here examine this theory as

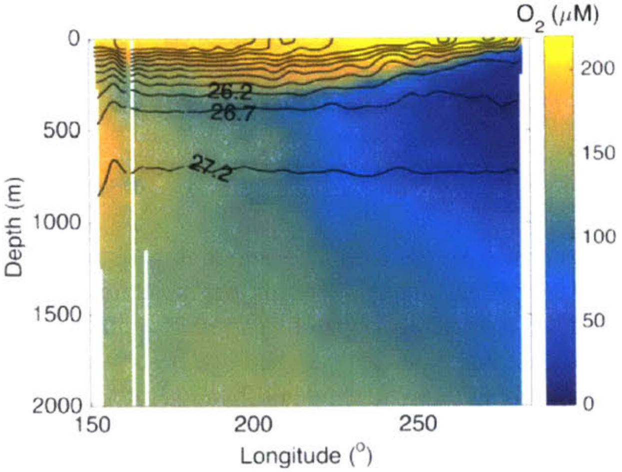

Figure 3.1: Oxygen concentration and potential density anomaly contours (kg m^{-3}) at 10°S in the Pacific ocean (Data: WOA 2013).

applied to aerobic and anaerobic microbial metabolisms in pelagic oxygen minimum zones.

Though diverse heterotrophic and chemoautotrophic N-cycling metabolisms populate oxygen minimum zones, with their interactions critically determining the fate of fixed nitrogen (Ward 2013; Penn et al. 2016), the chemical energy for all originates from exported organic matter. Therefore, the supply of two substrates – oxygen and organic matter – can be thought of as the dominant control on pelagic OMZ formation (Babbin et al. 2014). Examining the interactions of microbial heterotrophs is thus a relevant case study for understanding the transition of aerobic to anaerobic respiration.

Here, we define two microbial metabolisms – aerobic and anaerobic heterotrophy – as an exemplary pair competing for a shared substrate, organic matter. We analyze the interactions of the two metabolisms as two functional type populations, and also as occurring within one facultatively anaerobic population. We determine the conditions that allow for their coexistence, and develop a precise definition for the threshold for the transition to favorable anaerobic activity.

3.3 Simplified microbial metabolisms of O_2 depletion and fixed N loss

In general, we pose the aerobic-anaerobic transition as the change in the outcome of the competition between aerobic and anaerobic microbial metabolisms for a substrate. We here describe a heterotrophic pair: an aerobic heterotroph (B_O), reducing oxygen for energy, and an anaerobic heterotroph B_N, reducing dissolved inorganic nitrogen (*DIN*) to elemental nitrogen (written as N_2, though a small part of N loss can be as the potent greenhouse gas N_2O; Ward 2013). Both use organic matter (*OM*) as the source of electrons and chemical energy for (ultimately) biosynthesis. We describe each metabolism with its substrate demand and respiration products in terms of yields y (mol biomass B synthesized per mol substrate required), as:

$$\frac{1}{y_{OM_O}} OM + \frac{1}{y_{O_2}} \mathrm{O_2} \rightarrow B_O + \left(\frac{1}{y_{OM_O}} - 1 \right) DIN \tag{3.1}$$

$$\frac{1}{y_{OM_N}} OM + \frac{1}{y_{DIN}} DIN \rightarrow B_N + \left(\frac{1}{y_{OM_N}} - 1 \right) DIN + \frac{1}{2y_{DIN}} \mathrm{N_2} \tag{3.2}$$

where organic matter and biomass here are considered in units of nitrogen. Though these balanced metabolisms do not accurately represent the stoichiometry of N loss in anoxic environments, because the discretized steps of denitrification and anammox are also key (Koeve and Kähler 2010; Babbin et al. 2014; Penn et al. 2016), they are useful for illustrating the connections of microbial growth and denitrification rates in the model results.

We assume that anaerobic heterotrophy is less efficient than aerobic heterotrophy. We use the average coastal marine bacterial growth efficiency aerobic heterotrophy of 0.19 ± 0.16 mol C synthesized mol C $^{-1}$ consumed compiled by Robinson (2008) to inform the organic matter yields. We assign a slight difference in yields: $y_{OM_O} = 0.2$ mol B mol OM^{-1} for the aerobe and $y_{OM_O} = 0.19$ for the anaerobe; the relative difference in yield does not qualitatively affect the model solutions. The only assumption integral to model results is that $y_{OM_O} > y_{OM_N}$. We later discuss the implications for the results if $y_{OM_O} < y_{OM_N}$ at low oxygen.

3.4 The virtual chemostat model

To examine the dynamics of aerobic and anaerobic metabolisms in an environment, we first analyze the metabolic functional types as a continuous culture in a virtual chemostat. Oxygen, organic matter, and DIN of specified concentrations (O_{2in}, OM_{in}, DIN_{in}) flow into the volume at a given rate (the dilution rate κ, here as 0.1 d^{-1}), with an equal rate of outflow. We assume abundant DIN availability ($DIN_{in} = 30\ \mu$M, a typical nitrate concentration surrounding pelagic oxygen minimum zones). Biomass and nutrients (in units of μM N except for $\mathrm{O_2}$) are modeled with the expressions for their rates of change with time, defined by incoming nutrient supply, nutrient uptake, growth rate, and excretion of waste respiration products, and chemostat outflow as:

$$\frac{dB_O}{dt} = B_O(\mu_O - \kappa) \tag{3.3}$$

$$\frac{dB_N}{dt} = B_N(\mu_N - \kappa) \tag{3.4}$$

$$\frac{dOM}{dt} = \kappa(OM_{in} - OM) - \frac{1}{y_{OM_O}}\mu_O B_O - \frac{1}{y_{OM_N}}\mu_N B_N \tag{3.5}$$

$$\frac{d\mathrm{O}_2}{dt} = \kappa(O_{2in} - O_2) - \frac{1}{y_{O_2}}\mu_O B_O \tag{3.6}$$

$$\frac{dDIN}{dt} = \kappa(DIN_{in} - DIN) + \left(\frac{1}{y_{OM_O}} - 1 \right) \mu_O B_O + \left(\left(\frac{1}{y_{OM_N}} - 1 \right) - \frac{1}{y_{DIN}} \right) \mu_N B_N \tag{3.7}$$

where $\mu = \kappa$ for equilibrated model solutions. Growth of the aerobe is limited by either organic matter or oxygen. Growth of the anaerobe is effectively limited only by organic matter because of abundant DIN_{in}. We assume a growth rate μ as the product of the uptake rate and yield, and the limiting growth rate as the minimum product for the aerobe. We describe the uptake of organic matter with a saturating Michaelis-Menten form, and the uptake of oxygen with a diffusive limitation (Zakem and Follows 2016). This gives the growth rates of B_O and B_N as μ_O and μ_N, respectively, as:

$$\mu_O = min\left[y_{OM_O} V_{max}\left(\frac{OM}{OM+K_{OM}}\right), y_{O_2}\left(\frac{3D}{qr_{cell}^2}\right)O_2\right] \tag{3.8}$$

$$\mu_N = y_{OM_N} V_{max}\left(\frac{OM}{OM+K_{OM}}\right) \tag{3.9}$$

with maximum specific uptake rate V_{max} ((mol OM / mol biomass) d^{-1}) and half-saturation constant K_{OM} (μM N), the temperature-dependent diffusion coefficient for oxygen in solution D, cell radius r_{cell}, and volumetric carbon content of a cell q (18.3 fmol C μm^{-3} from Bratbak and Dundas 1984). The parameters to describe the uptake of organic matter are not well-known, but presuming that both types have the same limitation by organic matter (i.e., the same parameters) allows us to proceed with the dynamics despite the uncertainty. Here, we use parameters that result in an organic matter-limited growth rate that is consistent with the observed bulk rates in the ocean of about 0.1 d^{-1} (Kirchman 2016). (See Table 3.1 for parameter values.)

The rate of denitrification is here estimated for illustration as linearly related to anaerobic biomass, as $\frac{1}{y_{DIN}}\mu_N B_N$ (nM N d^{-1}) assuming the demand for DIN as an electron acceptor $\frac{1}{y_{DIN}}$ by considering the underlying redox reactions for NO_3^- reduction to N_2 and Redfieldian stoichiometry (Anderson 1995), denitrification remineralization ratio $r_{denitr}^{N:C}$ of 104:106 of Gruber and Sarmiento (1997) (See Appendix 3.A.2 for detail on denitrification stoichiometry).

Most anaerobic denitrifiers are thought to be facultatively aerobic, switching between oxygen and other terminal electron acceptors such as nitrate or nitrite (Zumft 1997). With a parallel model, we compare the results with one bulk facultatively aerobic microbial population that grows at whichever metabolism allows a higher growth rate at each time step (it grows aerobically if $\mu_O \geq \mu_N$). We integrate the solutions numerically in time with an explicit Euler forward scheme until an equilibrium solution is reached, independent of initial conditions. We then calculate steady state solutions to find the sensitivity to the incoming concentrations of oxygen and organic matter.

Resource subsistence concentrations

We anticipate that the aerobe will competitively exclude the anaerobe in oxygenated environments by comparing their subsistence concentrations of organic matter. At the subsistence concentration, the growth of a population is limited by that resource in a steady-state environment (Tilman 1982). If more than one population requires that resource, in the case

Table 3.1: Chemostat model parameters.

Parameter	Symbol	Value	Units
Aerobic organic matter yield	y_{OM_O}	0.2	mol B_O / mol OM
Anaerobic organic matter yield	y_{OM_N}	0.19	mol B_N / mol OM
Aerobic oxygen yield	y_{O_2}	$\frac{4y_{OM_O}}{d_{OM}(1-y_{OM_O}\frac{d_B}{d_{OM}})}$	mol B_O / mol O_2
Anaerobic oxygen yield	y_{DIN}	$\frac{5y_{OM_N}}{d_{OM}(1-y_{OM_N}\frac{d_B}{d_{OM}})}$	mol B_N / mol DIN
Dilution rate	κ	0.1	d^{-1}
Maximum specific uptake rate of OM	V_{max}	1	(mol OM / mol B) d^{-1}
OM half-saturation	K_{OM}	0.1	μM OM
Diffusion coefficient for oxygen in solution	D	2.5×10^{-5}	$cm^2\ s^{-1}$
Cellular carbon quota	q	18.3	fmol C μm^{-3}
Cell radius	r_{cell}	0.25	μm
Ratio of oxygen to organic matter demand of B_O	r	y_{OM_O}/y_{O_2}	mol O_2 / mol OM

that all are limited by that resource, the population with the lowest subsistence concentration can exclude the others. For the chemostat model, these subsistence concentrations can be calculated from Eqns. 3.8 and 3.9 assuming a steady state ($\mu = \kappa$). The subsistence concentrations of organic matter for the aerobic and anaerobic types are:

$$OM_O^* = \frac{K_{OM}\kappa}{y_{OM_O}V_{max} - \kappa} \tag{3.10}$$

$$OM_N^* = \frac{K_{OM}\kappa}{y_{OM_N}V_{max} - \kappa} \tag{3.11}$$

where $y_{OM}V_{max}$ represents the maximum growth rate of the organic matter-limited population. These concentrations differ only by the yield. since $y_{OM_O} > y_{OM_N}$, $OM_O^* < OM_N^*$, and the aerobic type can competitively exclude the anaerobic type when both are limited by organic matter.

The aerobic type can also become oxygen-limited at its subsistence concentration of oxygen, O_2^*:

$$O_2^* = \frac{\kappa q r_{cell}^2}{3y_{O_2}D} \tag{3.12}$$

With the assumed diffusive limitation to growth, O_2^* is consistently in the nanomolar range (Zakem and Follows 2016). Realistically, the anaerobic type could also become limited by its electron acceptor (which is often nitrate or nitrite in OMZs), though we do not consider this case in this study.

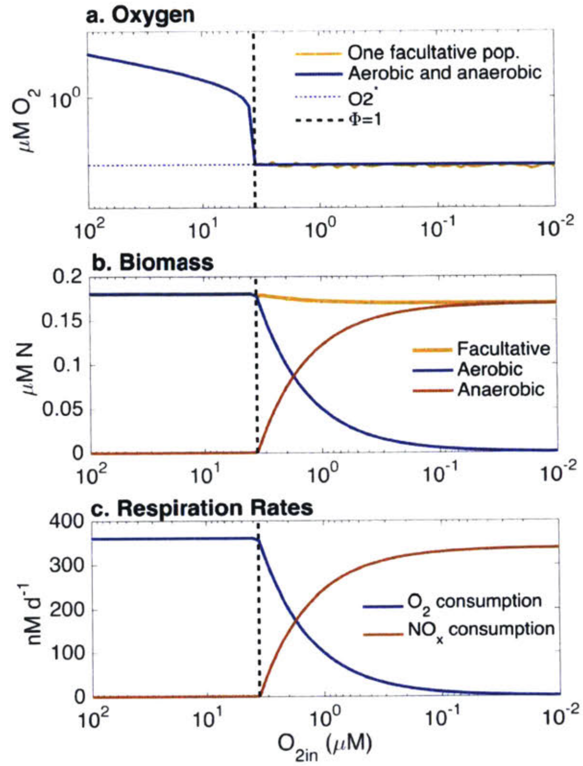

Figure 3.2: Solutions of the virtual chemostat for varying oxygen supply for two versions of the model: discrete aerobic and anaerobic populations, and one facultatively anaerobic population. Facultative biomass equals the sum of the two discrete populations. Respiration rates were identical for both versions. The dashed black lines indicate $\phi = 1$.

Chemostat simulations

Fig. 3.2 shows the steady-state solutions of the chemostat model as a function of the incoming oxygen concentration O_{2in}. At high oxygen, the anaerobic type is competitively excluded. This exlusion occurs dynamically, without a prescribed oxygen inhibition or threshold as is common in other types of models. Organic matter is depleted to OM_O^*, the subsistence concentration of the aerobic population, which is lower than the concentration necessary to support the anaerobic population. Even though the growth rate of the anaerobic type is only slightly lower than that of the aerobic type, multiple cycles of growth result in this competitive exclusion. This result reflects our assumption that oxygen is the more efficient oxidant, and simply anticipates the reason that, along with oxygenic primary production, aerobic metabolism is the dominant metabolism from a global perspective.

As oxygen supply becomes low, a threshold is crossed, and anaerobic metabolisms become sustainable. Past this threshold, aerobic metabolism is limited by oxygen, and is only able to oxidize a proportional amount of organic matter, and so cannot deplete organic matter to OM_O^*. Thus, the anaerobic metabolism can access the remaining organic matter and sustain its population; organic matter in this case is depleted to the slightly higher OM_N^*. Throughout this domain of coexistence, oxygen is maintained at the subsistence concentration of the aerobe, O_2^*. Incorporating both metabolisms into one facultative population gives identical results: solutions show identical total biomass and respiration rates, with oxygen concentration slightly wavering due to the discrete aerobic and anaerobic metabolisms.

The ratio of the aerobic to anaerobic biomass and respiration decreases as oxygen supply decreases, which matches the observations of aerobic and anaerobic sulfur bacteria of van den Ende et al. (1996). Total biomass remains relatively constant in the chemostat model; the steady state total biomass concentration can be calculated from Eqn. 3.5 as $B_{Tot} = (OM_{in} - OM^*)y_{OM}$. Since $y_{OM_N} < y_{OM_O}$, when biomass is predominantly anaerobic, B_{Tot} is slightly lower. The slope of the decrease in aerobic biomass – and thus of the increase in anaerobic biomass – is linearly related to the decrease in oxygen supply, since from Eqn. 3.6, $B_O = (O_{2in} - O_2^*)y_{O_2}$ at steady state. This linearity reflects the constant yields and the constant input of organic matter; in reality, varying yields and availability of organic matter would complicate predictions of biomass.

These results thus suggest that the observed co-occurring aerobic and anaerobic activity in oxygen minimum zones could indicate a steady coexistence, and not just reflect physical transport. The model hypothesizes that this coexistence could be a consistent feature of the periphery of anoxic zones, with oxygen concentration maintained at its lowest levels (O_2^*) throughout the domain. The fact that a small aerobic population remains sustainable in the model at very low oxygen supply also suggests the potential for very low (perhaps undetectable) aerobic activity within the core anoxic zone, if trace amounts of oxygen are produced there. Such trace aerobic activity may be more likely to be carried out by a facultatively anaerobic population; facultative capability as modeled expands the niche of the population, and so is perhaps the most fit for surviving in environments with fluctuating oxygen supply.

3.5 Condition for stable coexistence

What is the threshold that marks the transition to the accumulation of anaerobic biomass in Fig. 3.2? Following Tilman (1982), Ward (2013), and Dutkiewicz et al. (2014), we formalize the relative supply rates of organic matter and oxygen that determine whether aerobic heterotrophy competitively excludes anaerobic heterotrophy, or whether the two coexist. From Eqns. 3.5 and 3.6, we derive the expression for the conditions required to allow both aerobic and anaerobic biomass to exist. We call the quantity dictating this threshold ϕ (see Appendix 3.A.1 for derivation). For the chemostat, ϕ is:

$$\phi = \frac{\kappa(O_{2in} - O_2^*)}{\kappa(OM_{in} - OM_N^*)} r^{-1} \tag{3.13}$$

where r is the ratio of oxygen to organic matter demand of the aerobic heterotrophic metabolism: $r = y_{OM_O}/y_{O_2}$ (mol O_2 utilized per mol OM utilized). If $\phi > 1$, more oxygen is supplied than is required to consume all of the organic matter supplied. If $\phi = 1$, oxygen and organic matter are supplied in almost exact proportion to the aerobic heterotroph's needs: just a trace amount of organic matter remains (the difference between OM_N^* and OM_O^*), which a trace anaerobic population can access. If $\phi \ll 1$, significantly more organic matter is supplied than can be processed by the aerobe, and so a significant anaerobic heterotrophic population is sustained. Thus, $\phi = 1$ is the threshold at which anaerobic metabolism can coexist with aerobic.

A generalized expression for ϕ, relevant for marine environments, considers the fluxes of oxygen and organic matter to and from a given location. It again incorporates the limiting oxygen concentration O_2^* in the form of the outgoing flux of oxygen $F_{O_2^* out}$. Because O_2^* is in the nanomolar range, a good approximation of ϕ results from neglecting this outgoing flux. In contrast, the subsistence concentration of organic matter in natural environments is unclear; particulate and dissolved organic matter exist at relatively high concentrations in the water column, and additional sources and sinks of OM, such as the literal sinking of POM, make such a subsistence concentration meaningless for understanding this threshold. An alternative relationship results by considering the divergence of OM at any location, and whether or not sufficient oxygen is supplied to that location to allow for solely aerobic respiration. This generalized ϕ is then:

$$\phi = \frac{F_{O_2 in} - F_{O_2^* out}}{F_{OM in} - F_{OM out}} r^{-1} \approx \frac{F_{O_2 in}}{\nabla \cdot OM} r^{-1} \tag{3.14}$$

where the latter represents the approximation when O_2^* is at nanomolar concentrations. In the model results presented here, neglecting $F_{O_2^* out}$ results in an indistinguishable value of ϕ. In natural environments, the components of r, y_{O_2} and y_{OM_O}, should vary significantly. However, if we assume that as organic matter yield decreases, oxygen demand increases, then r is relatively stable across a wide range in these yields. When considering aerobic respiration of organic carbon, r^{-1} is similar to the often-discussed "respiratory quotient," which varies with specific substrates over a range of about 0.7 to 1.3 mol CO_2 produced per mol O_2 consumed, and a value of the respiratory quotient of one is often assumed (Robinson 2008).

In Fig. 3.3, we plot the threshold $\phi = 1$ with solutions for varying organic matter and oxygen supply, following Tilman's graphical approach to resource competition (Tilman 1980). Both aerobic and anaerobic biomass (and respiration) increase with increasing organic matter input. As this input increases, the threshold oxygen supply also increases. Thus, the model suggests that knowing the oxygen concentration and/or supply in the ocean alone is insufficient for predicting the existence of anaerobic metabolisms; it is the relative availability that matters.

The horizontal and vertical lines in the plot indicate OM^* and O_2^* concentrations, respectively. The theoretical approach suggests that the supply of oxygen or organic matter below these subsistence concentrations inhibits a sustainable population. In previous work, we argue that O_2^* can be considered the limiting concentration for mixed microbial communities (Zakem and Follows 2016). An analogous limiting concentration of organic matter, OM^*, may not be quantifiable in natural environments. A relevant limitation by organic matter includes both the physical and biological sinks of organic matter at a particular location.

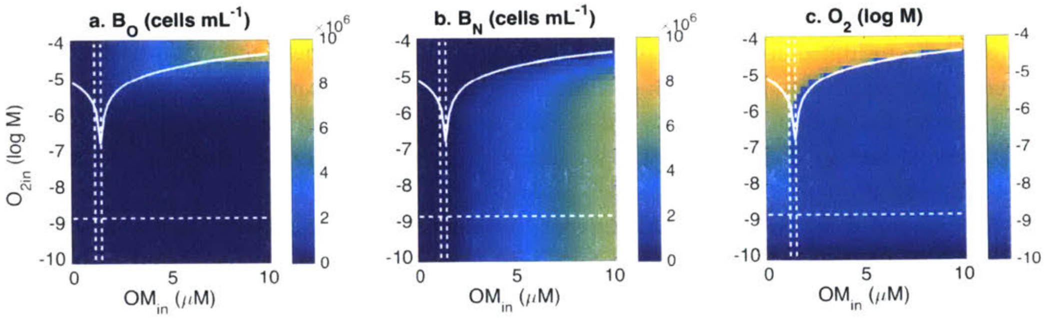

Figure 3.3: Solutions for the virtual chemostat model for varying organic matter and oxygen supply. The solid white line ($\phi = 1$) indicates the onset of the sustainable coexistence. The dashed white lines indicate substistence concentrations of oxygen (for the aerobic population) and organic matter (for both populations; the lower concentration corresponds to the aerobic population).

3.6 Idealized OMZ model

The chemostat set-up dictates that population growth rates equal its dilution rate. What is the outcome of the interactions of aerobic and anaerobic populations in the water column, where microbial growth rates are independent from ocean circulation, and sinking POM decouples oxygen supply from organic matter supply?

To investigate the model in a more realistic environment, we subject the aerobic and anerobic heterotrophic functional types in an idealized model of an oxygen minimum zone. A two-dimensional overturning circulation aims to crudely simulate the S. Pacific OMZ as shown in Fig. 3.1. A closed flow field with a width of 10,000 km and a height of 2000 m is forced with wind stress mimicking the climatological mean over the Pacific Basin at 10°S. The resulting flow field simulates intense eastern coastal upwelling, with dispersed downwelling in the west (Fig. 3.4). A mixed layer is simulated with a vertical mixing coefficient that attenuates with depth. See Appendix 3.A.2 for more detail on the model, all equations, and parameter values.

Oxygen equilibrates across the air–sea interface at a monthly timescale, estimated from an air-sea gas transfer coefficient of K_g (3×10^{-5} m s^{-1}; Williams and Follows 2011) and an equilibration depth of 100 m, and with a constant saturation concentration of 212 μM (the saturation concentration for 25°C and a salinity of 35). Sinking organic matter results from light- and nutrient-limited oxygenic export production, bypassing resolution of a phytoplankton population for simplification. One grazing population represents small zooplankton bacteriovores and can consume both aerobic and anaerobic functional types. A parameterization of zooplankton oxygen consumption allows for implicit zooplankton migration in and out of oxygen minimum zones (Escribano et al. 2009; Wishner et al. 2013; Bianchi et al. 2014), and allows for grazing within the anoxic core: oxygen demand by the zooplankton at a given location is spread vertically above and below that location, weighted by the oxygen concentration at that location, with zero weight if O_2 is below a critical oxygen concentration for zooplankton (here, 8 μM).

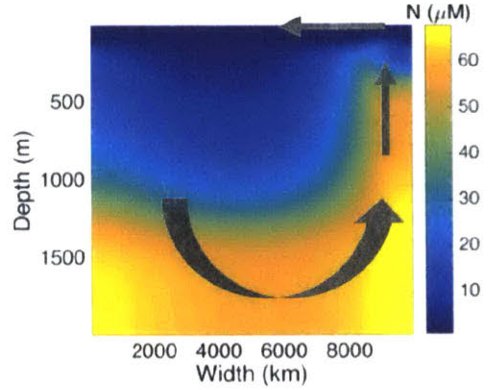

Figure 3.4: Schematic of the 2D idealized basin-wide OMZ model showing the resulting steady-state DIN concentration, indicating the intensified upwelling in the east (right) of the domain.

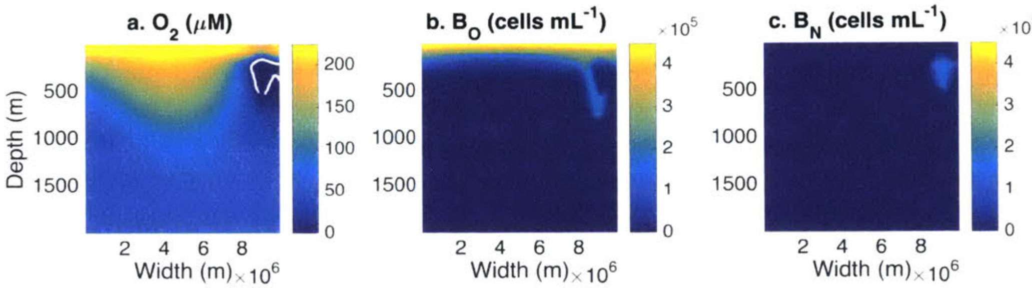

Figure 3.5: Idealized OMZ 2D model solutions of oxygen, aerobic heterotrophic abundance (B_O), and anaerobic heterotrophic abundance (B_N). The white contour ($\phi = 1$) in (a) indicates the domain of sustainable coexistence of favorable anaerobic activity.

Simulations

The 2D steady-state solutions of oxygen and microbial abundance (assuming a conversion of 0.2 fmol N cell^{-1}) are illustrated in Fig. 3.5 (see Appendix 3.A.2 for *OM*, *DIN*, and zooplankton solutions). Where upwelling supplies nutrients to the surface, export production is enhanced, providing more sinking organic matter input to the unventilated zone below. This mimicks the oxygen climatology of the 10°S transect in Fig. 3.1. There, the aerobic metabolism depletes oxygen to O_2^* (Fig. 3.6), and simulates the sharp oxycline characteristic of pelagic anoxic zones (Ulloa et al. 2012).

This depletion creates the habitat for the anaerobic population and denitrification. The N loss gives the characteristic profile of nitrate in OMZs, evidence of the depletion of nitrate within the anoxic zone (Fig. 3.6). Some organic matter sinks below this anoxic zone, and due to sufficient oxygen supply there, fuels a deep aerobic population for an additional few hundred meters.

The computed value of ϕ (Eqn. 3.15) is plotted in Fig. 3.7a. The $\phi = 1$ line is predicts

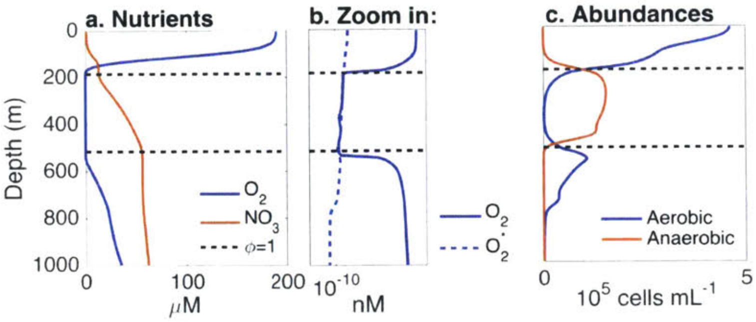

Figure 3.6: Profiles through the anoxic zone of the idealized OMZ model. The dashed black lines indicate $\phi = 1$.

the boundaries of the emergent region of anaerobic metabolism in Fig. 3.5c and Fig. 3.7c,d. Since we assign the O_2 and organic matter demands (i.e., r), $\phi \leq 1$ predicts the anaerobic domain with good skill. The $\phi = 1$ threshold represents the onset of the coexistence of the anaerobic metabolism, and so it precisely isolates the sustainable anaerobic domain, but not exclusive anaerobic activity. 77% of the organic matter consumed within the $\phi \leq 1$ area is respired anaerobically, with most of the aerobic activity at the periphery of the zone. Additionally, physical transport results in some anaerobic cells being mixed into the oxygenated waters above the anoxic zone; thus, low rates of denitrification occur at relatively high oxygen concentrations (tens of micromolar) in the oxycline because of this transient population.

3.7 Discussion

We used resource ratio competition theory to suggest that aerobic and anaerobic metabolisms can co-exist when oxygen supply is low in marine environments. Throughout the domain of coexistence, aerobic metabolisms should maintain the ambient oxygen at their subsistence concentration, O_2^*. We developed an expression which which to predict sustainable anaerobic activity, ϕ (Eqn. 3.15), where $\phi = 1$ represents the onset of the theoretical coexistence.

These results anticipate the observations of van den Ende et al. (1996) for aerobic and anaerobic chemoautotrophic sulfur bacteria competing for sulfide. In their experiment, the ratio of aerobic to anaerobic biomass also decreases with decreasing oxygen supply, with simultaneous measurements of activity directly indicating their coexistence. As implied by the model here, oxygen was below detectability during the period of coexistence. The model here thus provides the theory for these laboratory observations, and hypothesizes a similar result for aerobic and anaerobic metabolisms in pelagic OMZs.

The model suggests the likelihood of simultaneous aerobic and anaerobic activity at varying ratios in OMZs, as has been observed (Lipschultz et al. 1990; Lam et al. 2007; Füssel et al. 2012; Kalvelage et al. 2013; Peng et al. 2015), with ambient oxygen at its lowest

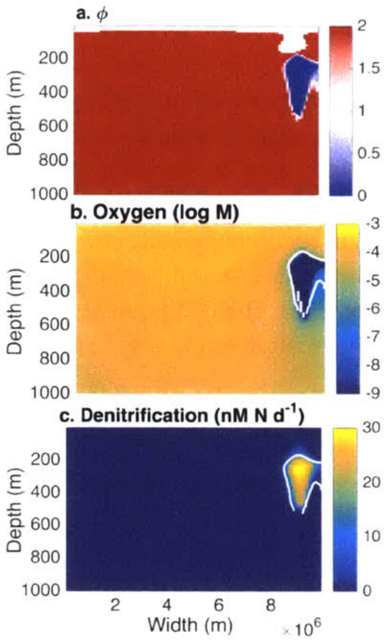

Figure 3.7: Idealized OMZ 2D model solutions of ϕ, oxygen, and denitrification, with the $\phi = 1$ line overlaid in white in (b) and (c).

levels. The model also suggests a potential for undetectable rates of aerobic metabolism occurring deeper in the anoxic zone, depleting any trace oxygen supply.

The model hypothesizes almost exclusively aerobic activity in anoxic conditions at the very periphery of an anoxic zone. Just at the onset of coexistence (ϕ at and just less than 1), in theory, aerobic metabolisms remain dominant, with trace anaerobic activity able to utilize trace amounts of surplus substrate. Observations and theory have indicated that aerobic microbial growth is sustained at nanomolar concentrations of oxygen or lower (Thamdrup et al. 2012; Tiano et al. 2014; Zakem and Follows 2016; Bristow et al. 2016a). Results here provide an additional ecological explanation for significant levels of aerobic metabolism (heterotrophic or chemoautotrophic) at these lowest levels of oxygen in the ocean.

The speculation that aerobic metabolism remains sustainable in anoxic zones depends upon the assumption that it remains a more efficient competitor for a substrate. However, if oxygen poses an additional thermodynamic limitation on the efficiency of the metabolism (so that for heterotrophs, $y_{OM_O} < y_{OM_N}$, and so $OM_O^* > OM_N^*$ at low oxygen), then aerobic metabolism would end more abruptly when this transition occurs. However, in reality, denitrifying heterotrophs are usually facultatively anaerobic (Zumft 1997). Even if strict aerobic heterotrophic populations are competitively excluded at low oxygen concentrations, facultative metabolisms may be able to exploit their expanded niche and occasionally respire aerobically.

In the expression for ϕ, we approximate that the outgoing flux of oxygen, $F_{O_2^*out}$, is negligible. This is a legitimate approximation when O_2^* is at nanomolar concentrations, but what if the relevant minimum oxygen concentration is much higher, at 10s of micromolar, as has been suggested by observations and modeling for the onset of nitrate reduction (Kalvelage et al. 2011; Penn et al. 2016)? If this is the case, and, following Penn et al. (2016), call this concentration O_2^{crit}, then the numerator in ϕ is $F_{O_2 in} - F_{O_2^{crit} out}$, and so the value of ϕ is lower. This enlarges the projected domain of anaerobic activity.

The threshold $\phi = 1$ is relevant for a steady-state environment. This steady state assumption is valid when the rates of growth and mortality of the population are well-balanced, and so the biomass of the population is not changing quickly. However, bloom-like conditions, such as a pulse of sinking organic matter, could also explain the co-occurrences of aerobic and anaerobic activity.

Here, we present the aerobic-anaerobic transition using a pair of metabolisms. In reality, a diverse suite of heterotrophic and chemoautotrophic aerobic and anaerobic metabolisms control organic matter cycling and N loss in pelagic OMZs. Examining the interactions among these diverse metabolisms is beyond the scope of this work, though it is a logical next step for progressing our understanding of anaerobic activity and N loss in the ocean.

3.8 Conclusions

We use ecological theory to develop a precise description of the transition from aerobic to anaerobic metabolisms in the ocean. Theory suggests that it is not the concentration of oxygen that determines this transition, but the relative availability of oxygen and organic matter. We define the threshold for the transition from exclusively aerobic metabolism to the coexistence of aerobic and anaerobic metabolisms.

An idealized model of OMZ circulation simulates this domain of aerobic-anaerobic coexistence as a consequence of the interactions between aerobic and anaerobic populations. The model serves as a means by which to understand oxygen depletion and nitrogen loss dynamically, without oxygen inhibition of anaerobic metabolisms imposed. Results provide an ecological explanation for the observations of co-occurring aerobic and anaerobic activity in OMZs, including the observations of significant aerobic activity at the lowest oxygen concentrations.

3.9 Addendum 1: The ecology of nitrogen loss in marine oxygen minimum zones

3.9.1 Overview

Here, we extend the analysis of aerobic and anaerobic interactions to a wider range of metabolisms. We first compare the six metabolisms currently understood to dominate nitrogen cycling in pelagic oxygen minimum zones (OMZs). We examine their interactions, again in a virtual chemostat. We first demonstrate that both steps of aerobic nitrification can coexist with anaerobic ammonium oxidation (anammox), which may explain the observations of nitrite oxidation in anoxic zones. We then analyze the steady-state distributions of all six metabolisms as a function of organic matter and oxygen supply. In general, the distributions of metabolisms match observed environments: all aerobic metabolisms dominate at high oxygen, and all anaerobic metabolisms dominate at low oxygen. The ratio of anammox to denitrification at low oxygen supply matches the theoretical ratio estimated from geochemistry, which shows that describing the system with ecological interactions is consistent with that geochemistry. Results provide an organized framework for interpreting the ecology of the diverse N-cycling metabolisms in OMZs.

We then make two additional points, which call for further investigation. First, a steady-state solution during the transition from aerobic to anaerobic metabolisms (at intermediate oxygen supply) has similar characteristics to the recently observed system in the Bay of Bengal by Bristow et al. (2016b): anammox dominates nitrogen loss, and oxygen remains at a concentration higher than the lowest observed. The model system matches some, but not all, of the observed dynamics, and we discuss the relevance for understanding the observed system as on the verge of transitioning to a more anaerobic system as a consequence of the projected marine deoxygenation. Second, due to this discrepancy, we compare the model results when aerobic heterotrophy is assumed to end at a critical oxygen concentration, following the conclusions of previous work that facultative anaerobes may not use oxygen at all once oxygen becomes low. If this is the case, then aerobic nitrifiers, rather than aerobic heterotrophs, become the viable aerobic metabolism at the lowest oxygen concentrations. We discuss the knowns and unknowns of the resulting models.

3.9.2 Questions

Diverse heterotrophic and chemoautotrophic metabolisms characterize the microbial community in and around oxygen minimum zones. When oxygen is abundant, as in most of the ocean, microbial metabolisms other than photoautotrophy can be divided into three types: heterotrophic oxidation of organic matter, for which ammonium is one of the waste products, ammonium oxidation to nitrite, and nitrite oxidation to nitrate. When oxygen is sufficiently depleted, anaerobic metabolisms become favorable, as described in the main text. In pelagic OMZs, nitrogen-cycling anaerobic metabolisms are most significant, since nitrate (the most favorable electron acceptor after oxygen) remains abundant. Anaerobic ammonia oxidation (anammox) and denitrification are known to dominate the losses of fixed nitrogen (Ward 2013). Sulfur-cycling metabolisms are understood to be less significant than in coastal waters, although cryptic sulfur cycling may occur in the open ocean (Canfield et al. 2010). The subsets of the heterotrophic denitrification reaction ($NO_3^- \rightarrow NO_2^- \rightarrow N_2O \rightarrow N_2$) are understood to be carried out by different organisms (Devol 2008). Considering just two discrete reactions – nitrate reduction to nitrite, and denitrification of nitrite to N_2 – is a justifiable simplification of the system for two reasons: N_2O excretion is much smaller than N_2 formation, and nitrite accumulates to order 10 μM in anoxic zones potentially because of a decoupling of these two steps (Babbin et al. 2017). Dissimilatory nitrate reduction to ammonium (DNRA) is generally understood to be less relevant in pelagic OMZs (Babbin, personal communication). Anaerobic nitrite oxidation may be a newly appreciated significant metabolism (Babbin et al. 2017).

A minimum of six metabolisms can therefore describe the current understanding of N cycling in and around anoxic zones (Devol 2008; Ward 2013): aerobic oxidation of organic matter, dissimilatory nitrate reduction, denitrification, aerobic ammonia oxidation, aerobic nitrite oxidation, and anammox. Observations consistently show co-occurrences of many of these metabolisms, at varying levels of oxygen concentrations (Devol 2008; Füssel et al. 2012; Kalvelage et al. 2013; Babbin et al. 2017). Which subsets of the metabolisms can steadily coexist, and why?

Chemoautotrophic anammox accounts for a significant portion of fixed nitrogen loss in OMZs (Ward 2013). The ratio of anammox to heterotrophic denitrification varies among studies (Bulow et al. 2010; Dalsgaard et al. 2012; De Brabandere et al. 2014). A theoretically calculated fraction of anammox to total N loss of about 30% has been shown to be consistent with observations when integrated over time (Koeve and Kähler 2010; Ward 2013; Babbin et al. 2014). Does a model of the ecological interactions of populations carrying out these metabolisms show this same fraction? I.e., do denitrifying and anammox functional types converge to a steady state at which the fraction of N loss from each type matches the theoretical ratio?

Also, what determines the variance from this theoretical fraction? Can the model explain environments that differ from this pattern? For example, recently, Bristow et al. (2016b) measured only anammox contributing to nitrogen loss (little or no denitrification was measured) in the Bay of Bengal. One theory for the varying significance of anammox versus denitrification is that anammox operates more consistently at lower rates and denitrification more sporadically at higher rates, perhaps responding to time-varying supplies of organic matter (Ward 2013; Kalvelage et al. 2013). Another is that anammox dominates at the periphery of oxygen minimum zones, which has been clearly observed in other environments (Babbin et al. 2017), and is consistent with laboratory experiments that show that anammox tolerates higher oxygen concentrations than heterotrophic denitrification (Jensen et al. 2008; Kalvelage et al. 2011; Dalsgaard et al. 2014). Are the areas of enhanced anammox in peripheral transition zones due to transience, or can anammox be sustained without denitrification in a steady-state environment?

Furthermore, the observations of Bristow et al. (2016b) from the Bay of Bengal show oxygen concentrations seemingly maintained at intermediate concentrations: a few hundred nanomolar on average. This, combined with the above hypothesis that anammox tolerates higher oxygen concentrations than denitrification, led the authors to speculate that the Bay of Bengal represents an environment at a 'tipping point.' They speculate that if oxygen was removed from the system, denitrification would then become favorable, resulting in higher total losses of fixed nitrogen from the environment. Can a microbial ecosystem model explain this 'tipping point' state?

3.9.3 Approach: Six interacting metabolisms in OMZs

Here, we develop a microbial ecosystem model relevant for pelagic oxygen minimum zones, and thus relevant for answering the above questions. We resolve six metabolic functional types fundamental to N cycling in OMZs. Rather than using only observed parameters from cultured species, we describe the types more fundamentally as being driven by their underlying chemistry. This allows for a predictive model that complements, rather than solely extends, observed metabolisms and nutrient distributions. The ability of each functional type population to sustain itself is the currency of the model, determining the presence of that population, with the respiration rates of each population giving the rates of activity that can be compared to observed rates. The ecological model links metabolisms to the interactions – both competitive and syntrophic – that regulate the sustainability of each functional type. This modeling framework allows us to formally examine these ecological interactions.

3.9.4 Metabolic functional types

We resolve the six microbial metabolic functional types that are understood to be most significant to N cycling in and around oxygen minimum zones (Ward 2008): aerobic heterotrophy (B_{HetO}), nitrate-reducing heterotrophy (B_{HetNO_3}), denitrifying heterotrophy (B_{HetNO_2}), aerobic ammonia oxidation (B_{AOO}), aerobic nitrite oxidation (B_{NOO}), and anaerobic ammonia oxidation (anammox) (B_{anx}). We here do not consider dissimilatory nitrate reduction to ammonium (DNRA) or anaerobic nitrite oxidation, but we provide the tools with which the ecology of these (and other) metabolisms could also be examined. We define these metabolic types as follows with nitrogen as the currency, with the amount of each required substrate and respiration product expressed in terms of yields. The values for each yield are listed in Table 3.3).

$$
\begin{gathered}
\frac{1}{y_{OM_O}} OM + \frac{1}{y_{\mathrm{O}_{2-O}}} \mathrm{O}_2 \rightarrow B_{HetO} + \left(\frac{1}{y_{OM_O}} - 1\right)(\mathrm{NH}_4^+) \\
\frac{1}{y_{OM_N}} OM + \frac{1}{y_{\mathrm{NO}_{3-het}}} \mathrm{NO}_3^- \rightarrow B_{HetNO_3} + \left(\frac{1}{y_{OM_N}} - 1\right)(\mathrm{NH}_4^+) + \frac{1}{y_{\mathrm{NO}_{3-het}}} \mathrm{NO}_2^- \\
\frac{1}{y_{OM_N}} OM + \frac{1}{y_{\mathrm{NO}_{2-het}}} \mathrm{NO}_2^- \rightarrow B_{HetNO_2} + \left(\frac{1}{y_{OM_N}} - 1\right)(\mathrm{NH}_4^+) + \frac{1}{2y_{\mathrm{NO}_{2-het}}} \mathrm{N}_2 \\
\frac{1}{y_{\mathrm{NH}_{4-AOO}}} \mathrm{NH}_4^+ + \frac{1}{y_{O_{2-AOO}}} \mathrm{O}_2 \rightarrow B_{AOO} + \left(\frac{1}{y_{\mathrm{NH}_{4-AOO}}} - 1\right)\mathrm{NO}_2^- \\
\frac{1}{y_{\mathrm{NO}_{2-NOO}}} \mathrm{NO}_2^- + \mathrm{NH}_4^+ + \frac{1}{y_{O_{2-NOO}}} \mathrm{O}_2 \rightarrow B_{NOO} + \frac{1}{y_{\mathrm{NO}_{2-NOO}}} \mathrm{NO}_3^- \\
\frac{1}{y_{\mathrm{NH}_{4-anx}}} \mathrm{NH}_4^+ + \frac{1}{y_{NO_{2-anx}}} \mathrm{NO}_2^- \rightarrow B_{anx} + \frac{1}{2}\left(\frac{1}{y_{\mathrm{NH}_{4-anx}}} + \frac{1}{y_{\mathrm{NO}_{2-anx}}} - 1\right)\mathrm{N}_2
\end{gathered}
$$

For simplicity of the expressions, we neglect water and charge balance (from bicarbonate), and consider ammonium and ammonia interchangeably.

We then estimate the values for all of the yields using the redox reactions underlying each of these metabolisms, using an approach similar to that used for bioreactors in wastewater treatment plants (Rittman and McCarty 2001). We determine the fraction of electron flow that partitions biomass synthesis and respiration using a combination of theory and observed yields from the growth of real organisms (see Appendix 3.A.3 for detail). Fig. 3.8 illustrates the resulting stoichiometries assumed for the remainder of this study (yields are also listed in Table 3.3). Large uncertainties accompany each of these values, due to variation in the costs of biomass synthesis, the assumed electron fraction of each metabolism, the efficiency of the transfer of energy from one chemical form to another, and versatilities of real metabolisms. Thus, these yields should be understood as ballpark values for the metabolisms. We consider where departures from these ballpark values will impact the outcome of the interactions throughout this study.

We make two main assumptions when assigning the electron fractions. First, we assume that anaerobic heterotrophy is less efficient than aerobic heterotrophy; this assumption and the yields themselves are the same as in the main text. Second, we assume that the electron fraction is the same for all of the chemoautotrophs, which is a plausible assumption knowing nothing else about the metabolisms. Observations show that this fraction is lower for marine nitrifiers than wastewater nitrifiers (about 0.03; see Chapter 3 for detail), and only wastewater anammox stoichiometry has been documented to our knowledge (Strous et al. 1998). In light of these observations, we opt to use the same efficiency of 0.03 for anammox as well as both steps of aerobic nitrification. We test that the solutions do not depend qualitatively on this assumption: assuming the stoichiometry of Strous et al. (1998) does not impact the fitness of the anammox relative to each of the nitrifiers.

In Table 3.2, we list the R^* concentrations for each substrate for each metabolism using the yields and the parameters for uptake listed in Table 3.3, and assuming a constant loss

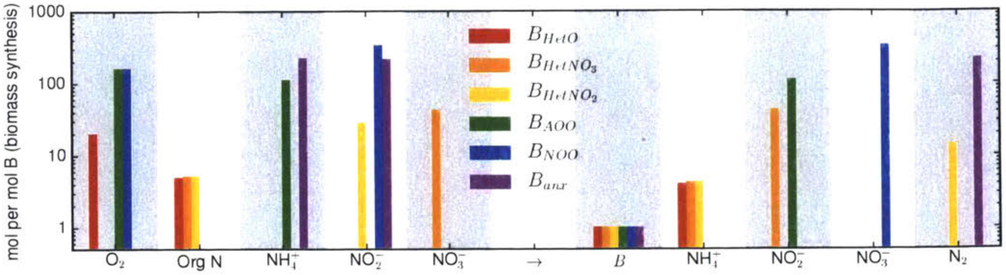

Figure 3.8: Ballpark values for the stoichiometries of the six metabolic functional types as a function of their underlying redox chemistry and estimation of the efficiency of each reaction. The three heterotrophs have roughly the same efficiency, with the aerobic heterotroph slightly more efficient. The three chemoautotrophs all have the same efficiency, and so differences between them reflect only the redox reactions. Biomass B is in units of nitrogen.

rate of 0.1 d^{-1} (the dilution rate for the chemostat model). As in the main text, we assume a Michaelis-Menton form for the uptake of organic matter and DIN and a diffusive limitation for the uptake of oxygen. To simplify the interpretation of the model, we assume the same uptake parameters for organic matter for all heterotrophs, and the same uptake parameters for all species of dissolved inorganic nitrogen for all metabolisms that use DIN.

The interaction matrix

Table 3.2 represents the matrix of all possible competitive and syntrophic interactions in the model. All metabolisms that have the potential to be limited by any one substrate (all red squares in any column) have the potential to compete with one another for that substrate, and the estimated values of R^* provide a first-order estimate of the relative competitive ability of each. For example, three metabolic types – heterotrophic denitrifiers, nitrite-oxidizers, and anammox – require nitrite. The values that we assign for the yields and uptake parameters result in an ordering of the subsistence concentration for nitrite, from low to high (i.e., of the affinity for nitrite), as first denitrifiers, and then anammox, and then nitrite-oxidizers. Table 3.2 also indicates the substrates that are produced by each metabolism with a filled-in blue square: thus, for any column, a metabolism that requires that substrate has a possibility for a cross-feeding dependency on any metabolism that provides that substrate. Using nitrite again as an example, nitrite-oxidizers have the potential to co-exist with ammonium-oxidizers in oxygenated environments (as in Chapter 3), as well as with nitrate reducers in OMZs. This complex network prevents any simple prediction of the outcome of the system, and thus a model allowing for all of these interactions in an environment becomes a useful tool.

We next turn to a simple virtual chemostat model to examine the solutions of this complex network as a function of the supply rates of substrate. We again solve for equilibrium functional type biomasses and nutrient concentrations (See Appendix 3.A.3 for Equations).

Table 3.2: The interaction matrix of the six metabolisms. Red squares indicate substrate requirements, with the R^* concentration computed for the virtual chemostat model overlaid. Blue squares indicate waste metabolic products. For each column, all organisms requiring that substrate (all red squares in the column) can potentially compete with one another. Each pair of red and blue within a column has the potential for a syntrophic, cross-feeding interaction.

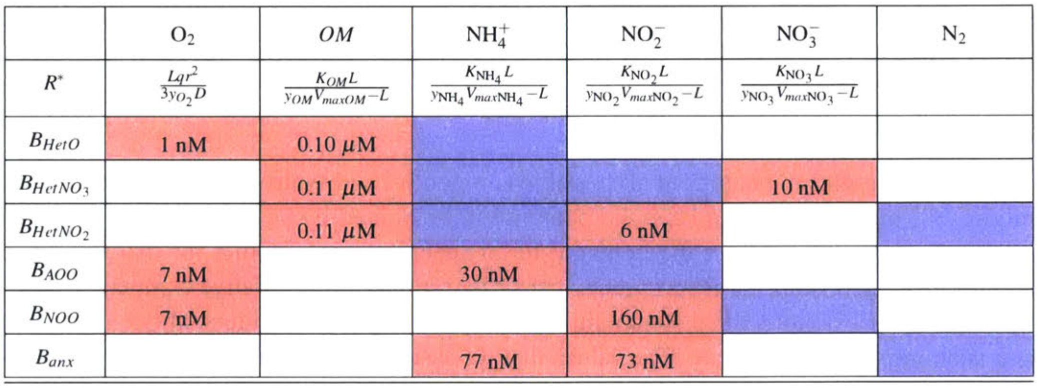

	O_2	OM	NH_4^+	NO_2^-	NO_3^-	N_2
R^*	$\frac{Lqr^2}{3y_{O_2}D}$	$\frac{K_{OM}L}{y_{OM}V_{maxOM}-L}$	$\frac{K_{\mathrm{NH_4}}L}{y_{\mathrm{NH_4}}V_{max\mathrm{NH_4}}-L}$	$\frac{K_{\mathrm{NO_2}}L}{y_{\mathrm{NO_2}}V_{max\mathrm{NO_2}}-L}$	$\frac{K_{\mathrm{NO_3}}L}{y_{\mathrm{NO_3}}V_{max\mathrm{NO_3}}-L}$	
B_{HetO}	1 nM	0.10 μM	🟦			
B_{HetNO_3}		0.11 μM	🟦	🟦	10 nM	
B_{HetNO_2}		0.11 μM	🟦	6 nM		🟦
B_{AOO}	7 nM		30 nM	🟦		
B_{NOO}	7 nM			160 nM	🟦	
B_{anx}			77 nM	73 nM		🟦

Table 3.3: Ballpark values for yields, presented as the inverse of the yields, y^{-1}, and uptake parameters for estimations of R^* in Table 3.2. Organic matter OM and biomass B are in units of nitrogen. (See Table 3.1 for oxygen uptake parameters and Appendix 3.A.3 for derivation of yields.)

Parameter	Symbol	Type	Value	Units
Yields				
Oxygen demand	$y^{-1}_{\mathrm{O}_{2-O}}$	B_{HetO}	26	mol O_2 / mol B
	$y^{-1}_{\mathrm{O}_{2-AOO}}$	B_{AOO}	162	
	$y^{-1}_{\mathrm{O}_{2-NOO}}$	B_{NOO}	162	
Organic matter demand	$y^{-1}_{OM_O}$	B_{HetO}	5.0	mol OM / mol B
	$y^{-1}_{OM_N}$	B_{HetNO_3}	5.3	
	$y^{-1}_{OM_N}$	B_{HetNO_2}	5.3	
Ammonium demand	$y^{-1}_{\mathrm{NH}_{4-AOO}}$	B_{AOO}	112	mol NH_4^+ / mol B
	$y^{-1}_{\mathrm{NH}_{4-anx}}$	B_{anx}	112–223	
Nitrite demand	$y^{-1}_{\mathrm{NO}_{2-het}}$	B_{HetNO_2}	37	mol NO_2^- / mol B
	$y^{-1}_{\mathrm{NO}_{2-NOO}}$	B_{NOO}	334	
	$y^{-1}_{\mathrm{NO}_{2-anx}}$	B_{anx}	136–216	
Nitrate demand	$y^{-1}_{\mathrm{NO}_{3-het}}$	B_{HetNO_3}	55	mol NO_3^- / mol B
Uptake				
Max specific uptake of OM	V_{maxOM}		1	(mol OM / mol B) d^{-1}
OM half-saturation	K_{OM}		0.1	μM OM
Max specific uptake of DIN	$V_{max\mathrm{NH}_4}, V_{max\mathrm{NO}_2}, V_{max\mathrm{NO}_3}$		60	(mol DIN / mol B) d^{-1}
DIN half-saturation	$K_{\mathrm{NH}_4}, K_{\mathrm{NO}_2}, K_{\mathrm{NO}_3}$		0.13	μM N
Loss rate	L (= Dilution rate κ)		0.1	d^{-1}

3.9.5 Stable coexistence of nitrification and anammox

Analogous to the heterotrophic metabolisms in the main text, we analyze just the aerobic and anaerobic chemoautotrophic metabolisms competing for and cross-feeding with the three inorganic nitrogen species. We solve the system for three functional types – aerobic ammonia-oxidizers, aerobic nitrite-oxidizers, and anammox (B_{AOO}, B_{NOO}, and B_{anx}) – and for three incoming nutrients: oxygen, nitrite, and ammonium.

Fig. 3.9 illustrates the resulting steady-state solutions for varying incoming concentrations of oxygen and ammonium. Incoming nitrite concentration is fixed at 5 μM, simulating the core of an anoxic zone where nitrite is presumably supplied by heterotrophs. The system is dependent on nitrite, and thus Fig. 3.9 is an incomplete description of the solutions. However, the concepts for understanding the full set of solutions, which are function of nitrite supply as well as of oxygen and ammonium supply, are evident.

As with the anaerobic heterotroph, anammox is competitively excluded when oxygen is abundant, without any prescribed oxygen inhibition. Coexistence of the aerobic nitrifiers and anammox is again established once a threshold of relative supply rates is crossed. Where coexistence occurs, oxygen is held at the O_2^* of the aerobic nitrifiers. Ammonium is held at the NH_4^* of anammox, indicating that anammox is limited by ammonium. Nitrite is abundant throughout the anaerobic domain, indicating that nitrite is not limiting in this illustrated subset of the solution space. The resulting steady state concentration of nitrite decreases as ammonium supply increases since the metabolisms are able to utilize a larger share of the nitrite when more ammonium is supplied.

This result demonstrates a three-way, unintuitive dependency: in a pair-wise competition, anammox could competitively exclude nitrite-oxidation even when oxygen supply is high because of its lower subsistence concentration for nitrate (Table 3.2). Thus, it is the aerobic ammonia oxidizing population that competitively excludes anammox when oxygen supply is large. Once oxygen is low enough for the anammox population to sustain itself, it cannot metabolize all of the nitrite available because of its requirement for ammonia. Thus, nitrite oxidation is able to steadily coexist with anammox and the ammonia oxidizers.

Because of the large differences in yields, (1/112 and 1/222 for NH_4^* for AOO and anammox, respectively, and 1/333 and 1/212 for NO_2^- for NOO and anammox, respectively), which translate into the large differences in R^* (Table 3.2), we expect that these relative competitive abilities to be robust for variations in these yields and uptake parameters. If instead anammox follows the stoichiometry of Strous et al. (1998) in marine environments, which would mean that it is significantly more efficient at acquiring electrons than aerobic nitrification, then it would be a very close competitor for ammonia against the aerobic ammonia-oxidizers. As long as aerobic ammonia oxidizing population has a lower R^* than anammox for for ammonium, this does not change the results quantitatively. The extremely low affinity of ammonia-oxidizers measured by Martens-Habbena et al. (2009) also contributes to their fitness, and represents a further reason to suspect that ammonia oxidizers will outcompete anammox for for ammonium.

In summary, these results thus anticipate that aerobic nitrification may continue at significant rates once oxygen is depleted to limiting concentrations. Coexistence with anam-

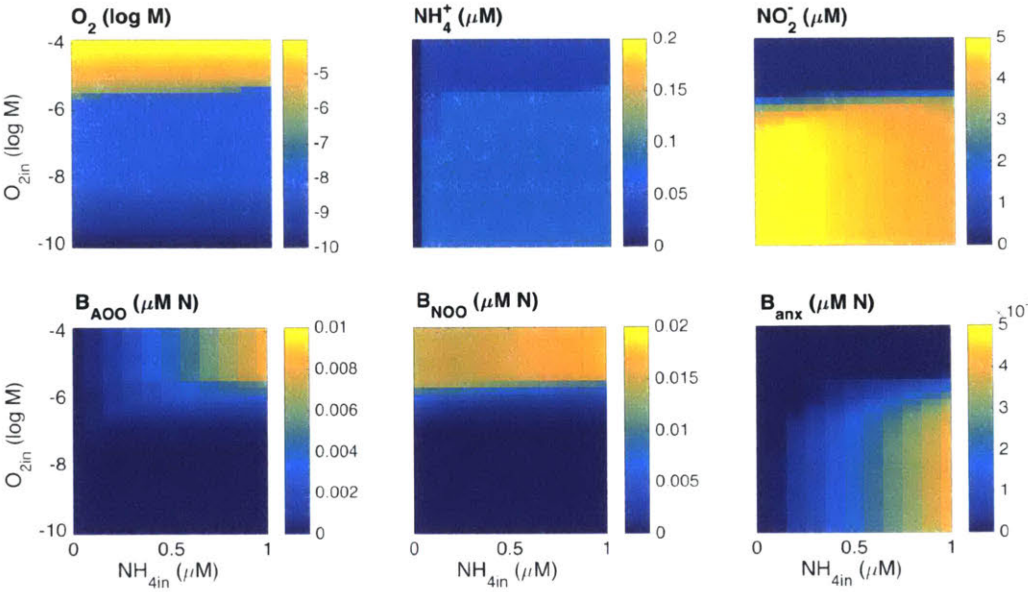

Figure 3.9: Solutions for the three chemoautotrophic metabolisms in the virtual chemostat model for varying organic matter and ammonium supply. Incoming nitrite concentration is fixed at 5 μM, and so nitrite only limits the growth of the aerobic nitrite oxidizers when oxygen is abundant. Aerobic nitrifiers and anaerobic anammox coexist when oxygen supply is low.

mox is sustainable: anammox is able to access the DIN that the aerobic nitrifiers cannot access due to their oxygen limitation. This potentially explains the observations of nitrite oxidation in anoxic zones and the co-occurrences of nitrite oxidation and anammox (Füssel et al. 2012; Kalvelage et al. 2013; Bristow et al. 2016b; Babbin et al. 2017).

3.9.6 Syntrophic coexistence of six metabolisms

Fig. 3.10 shows the steady state model results of the interaction of all six metabolic types in the chemostat as a function of varying oxygen concentration. Incoming organic matter concentration is fixed at 1 μM; organic matter supply controls the magnitudes of biomasses and rates, but not the relative distributions of the metabolisms. As in the main text, incoming nitrate concentration is fixed at 30 μM to avoid nitrate limitation.

Syntrophic interactions explain the coexistence of the aerobic metabolisms at high oxygen supply, and of the anaerobic metabolisms at low oxygen. At high oxygen supply, the three anaerobic types are competitively excluded, and both NH_4^+ and NO_2^- are maintained at the subsistence concentrations of the aerobic AOO and NOO populations, respectively. This anticipates the microbial community structure in oxygenated environments below the euphotic zone examined in Chapter 4.

At low oxygen supply, oxygen is depleted to O_2^*, and the three anaerobic metabolisms become sustainable. Because the parameters chosen have resulted in a lower subsistence

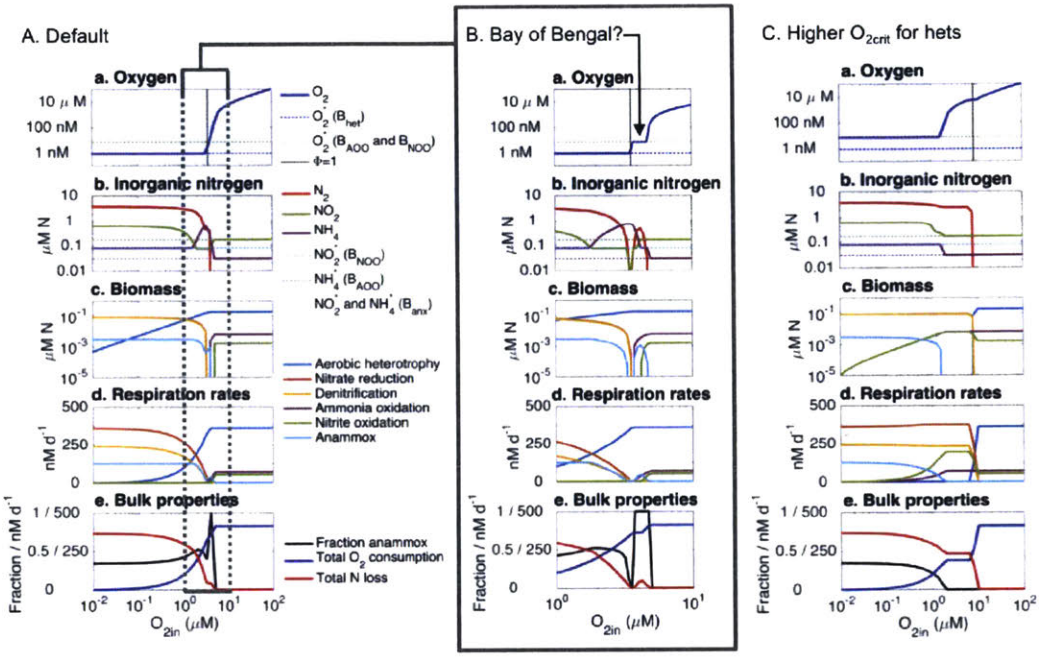

Figure 3.10: Solutions for all six metabolisms in the virtual chemostat model for varying oxygen supply. Incoming organic matter supply is fixed at 1 μM. Two models are shown: (a) First, the model when assuming that the emergent nanomolar oxygen limitation O_2^* limits the growth of all aerobic metabolisms, resulting in the aerobic heterotrophs outcompeting the aerobic nitrifiers at low oxygen. Plot (b) provides a higher resolved version of the solutions at intermediate oxygen supply, which shares many characteristics with recent observations from the Bay of Bengal (Bristow et al. 2016b). (c) Second, the model when assuming a higher (here, 5 μM) oxygen concentration excludes aerobic heterotrophy.

oxygen concentration for the aerobic heterotroph (1 nM) than for the aerobic nitrifiers (7 nM), oxygen is maintained at the O_2^* of the aerobic heterotroph. Thus, in this model, the aerobic nitrifiers are competitively excluded by the aerobic heterotroph once oxygen limits its growth. Aerobic heterotrophy coexists with the anaerobic metabolisms, continues to utilize trace amounts of oxygen, as in the main text. NH_4^* is maintained at the subsistence concentration of the anammox population. NO_2^- accumulates due an imbalance in NO_2^- supply and demand, which reflects that NH_4^* is the limiting species for the community at low oxygen supply. N_2 accumulates because of both anammox and denitrification.

3.9.7 Simulation of observed patterns of N loss

At low oxygen supply, nitrate reduction and denitrification metabolisms co-exist with anammox. Their relative contributions to fixed nitrogen loss match the theoretical calculations and observations of Babbin et al. (2014). To explain, the rates of the three metabolisms converge to a constant ratio as oxygen supply decreases: the fraction of anammox contribution to total fixed N loss is 35% in the illustrated model (Fig. 3.10e). This ratio reflects the assumed stoichiometry of the biomasses, and is consistent with theoretically and empirically observed ratio of about 30% (Koeve and Kähler 2010; Babbin et al. 2014; Ward 2013; Dalsgaard et al. 2014).

As anticipated by theory (Koeve and Kähler 2010; Babbin et al. 2014), the modeled fraction is sensitive to the stoichiometry of the organic components, independent of the growth rates of the populations. If the model is run with microbial C:N biomass stoichiometry of 6.6, instead of 5, assuming the average stoichiometry of marine organic matter (Anderson 1995) instead of bacterial biomass (Zimmerman et al. 2014), then the fraction is 29%, which is almost exactly the theoretical value. The fraction remains the same for constant stoichiometries even if the assumed yields for anammox are doubled, or if the heterotrophs grow at a faster rate than anammox (accomplished by forcing a higher rate of loss on the heterotrophs; results not shown). The model thus points out that the stoichiometry of bacterial biomass and remineralization itself may affect the theoretical fraction, in addition to the stoichiometry of sinking organic matter as predicted by Babbin et al. (2014). However, the model here assumes the same efficiency for carbon and nitrogen utilization (Goldman et al. 1987), so more research would be needed to qualify and quantify this sensitivity.

3.9.8 Simulation of recent observations from the Bay of Bengal

Though the model and theory predict the above pattern of N loss where oxygen supply is lowest, the model results differ when oxygen is supplied at intermediate levels. Over a small range of intermediate oxygen supply, only anammox, and not heterotrophic denitrification, contributes to N loss (Fig. 3.10b). This steady state regime has much in common with the recent observations of the Bay of Bengal by Bristow et al. (2016b), which the authors conclude may be a 'tipping point' environment, at the brink of much more fixed N loss should conditions change. In the sites measured in the Bay of Bengal, anammox was nitrite-limited, nitrite oxidation was significant, little or no denitrification was measured, nitrate reduction was significant, and oxygen was maintained at a higher concentration: 10–200 nM.

Like these observations, oxygen is also maintained at a higher concentration in the model at this intermediate state. The model shows this as the slightly higher O_2^* of the aerobic nitrifiers (Fig. 3.10b), and so in the model, the ambient oxygen concentration is controlled by the nitrifiers, rather than the heterotrophs. In this model, this concentration is 7 nM instead of the 0.9 nM O_2^* of the aerobic heterotrophs, which is significantly lower than the observed concentrations of about 100 nM Bristow et al. (2016b). The discrepancy in magnitude could be explained by a model underestimate of the subsistence oxygen concentration of the nitrifiers (due to an overestimate of their efficiency, for example), or due to a continual supply of oxygen as an alternative control on the ambient concentration in the real environment, and thus, demonstrating an effect of physical transport that the simplified chemostat model does not resolve. This latter effect would be analogous to the effect of transport on setting the magnitude of the primary nitrite maximum (see Chapter 4).

Another discrepancy between model and observations is that the model does not predict nitrate reduction at this intermediate state. Observations have suggested that nitrate reduction to nitrite occurs at ambient oxygen concentrations much higher than O_2^*, perhaps due to anoxic activity within particles, or perhaps due to a different energetic threshold for that transition (Kalvelage et al. 2013; Brewer et al. 2014; Penn et al. 2016). Both of these explanations may explain the lack of nitrate reduction in the model. However, attempting to remedy this difference by using a higher limiting oxygen concentration for nitrate reduction changes the model solutions drastically. When including this higher limiting oxygen concentration, the model no longer predicts favorable anammox and no heterotrophic denitrification. We discuss this experiment and its results further below.

The model results suggest an interpretation of the Bay of Bengal environment. The model hypothesizes that at the location observed by Bristow et al. (2016b), oxygen was just low enough to limit the growth of the nitrifiers, allowing for sustainable anammox to coexist, but not yet low enough to limit the aerobic heterotroph, and so denitrification does not yet sustainably coexist. The lack of anaerobic heterotrophy results in a state where the ratio of nitrate reduction to nitrite oxidation is not yet high enough to allow for an accumulation of nitrite. Anammox is thus nitrite-limited, which is evident by the maintenance of nitrite at its subsistence concentration during this period.

These model results depend on the assumption that aerobic heterotrophy more efficiently utilizes oxygen than aerobic chemoautotrophy. This assumption allows for the resulting higher oxygen concentration, the occurrence of anammox without denitrification, and the nitrite-limitation of anammox. We next forego this assumption and modify the model to include nitrate reduction at a higher ambient oxygen concentration.

3.9.9 Effects of a higher oxygen limitation for nitrate reduction

The observations of (Kalvelage et al. 2013) show the anaerobic reduction of nitrate at much higher oxygen concentrations than direct limitation of oxygen supply to a microbial cell predicts (Zakem and Follows 2016). Anaerobic activity within particles or an unexplained energetic constraint on aerobic metabolism at low oxygen may explain this distinction.

Here, we consider this in the model by forcing a higher critical oxygen concentration for aerobic heterotrophy, and analyze the resulting ecosystem. Following the approach of Penn et al. (2016), we allow nitrate reduction to set in at a prescribed O_{2crit} (here, as 5 μM).

Fig. 3.10c shows the results. Aerobic heterotrophy ends abruptly at O_{2crit} as in Penn et al. (2016). In contrast with Fig. 3.10a, aerobic nitrifiers are the popluations that utilize the trace amounts of available oxygen, and oxygen concentrations are maintained at their subsistence concentration (here, of 7 nM). Because nitrifiers are sustainable at lower oxygen concentrations, anammox does not become a sustainable metabolism until much lower concentrations. This is in contrast to observations of anammox as active at higher oxygen concentrations and at the periphery of oxygen minimum zones (Dalsgaard et al. 2014; Babbin et al. 2017). This does, however, allow for the coexistence of nitrification and denitrification, as has also been observed (Füssel et al. 2012; Peng et al. 2015). Thus, both Fig. 3.10a and Fig. 3.10c are able to represent some but not all of the characteristics of OMZ biogeochemistry.

3.9.10 Discussion

We organized the six dominant N-cycling metabolisms that occur in pelagic marine oxygen minimum zones as metabolic functional type populations, and by doing so, have been able to link these metabolisms to the ecological interactions that regulate the favorability of each.

First, the model establishes the conditions for the coexistence of aerobic nitrification and anammox in anoxic zones. As in the main text, intermediate levels of oxygen supply allow for this coexistence. Unlike the pair of heterotrophs in the main text, this three-way coexistence was not intuitive, since aerobic nitrite oxidation seems to be less efficient at utilizing nitrite than anammox. These results may explain observed nitrite oxidation in anoxic zones (Füssel et al. 2012; Kalvelage et al. 2013; Bristow et al. 2016b; Babbin et al. 2017).

Second, the model with all six metabolisms establishes the general pattern of syntrophic aerobic metabolisms giving way to anaerobic metabolisms as oxygen supply decreases. The model simulates the convergence to the theoretical fraction of anammox to total nitrogen loss at low oxygen supply. This corroborates the general assumption of the model that the network of microbial interactions ultimately reflects the chemistry of the system: the biogeography of N-cycling metabolisms is crudely predicted by redox chemistry.

Third, at intermediate oxygen supply, the model anticipates many of the observations from the Bay of Bengal, which Bristow et al. (2016b) concluded also demonstrated an environment with an intermediate oxygen supply. The model does not completely replicate all of the observations, however. The modeled nitrite-limitation of anammox is consistent with the observations, and the interpretation of the authors. Unlike the model, however, observations show active nitrate reduction. This presents a puzzle for the theoretical model: in the model, nitrate reduction without denitrification results in an accumulation of nitrite, and so would not result in nitrite-limitation for anammox.

One explanation could be that the measured nitrate reduction actually occurs inside particles, with the resulting nitrite somehow not accessible to the anammox population. Unfortunately, the nitrite concentrations were not reported for the Bay of Bengal site. This potential for an onset of nitrate reduction at a higher ambient oxygen concentration is consistent with observations (Kalvelage et al. 2013), and thus this led to the comparison of a model with a different treatment of the way oxygen limits heterotrophic growth.

Both model versions (Fig. 3.10a,c) capture some of the elements of the observed biogeochemistry. Fig. 3.10a predicts that anammox should become sustainable in the environment at a higher oxygen supply than heterotrophic denitrification, which matches observations of oxygen inhibition in anammox in the laboratory as well as observations showing a higher fraction of anammox to total N loss at the periphery of an anoxic zone, where oxygen supply is presumeably higher (Dalsgaard et al. 2014; Babbin et al. 2017). Fig. 3.10c, on the other hand, predicts the continuation of nitrite oxidation at very low levels of oxygen, which simulates the measurements in the core of an anoxic zone by Füssel et al. (2012).

Previous modeling also anticipates a higher fraction of anammox at the periphery of the anoxic zone, but for different reasons. Penn et al. (2016) simulate anammox dominating N loss at the periphery because hetetrotrophic denitrification is excluded at the low levels of oxygen in the periphery by aerobic nitrite oxidation. In their model, chemoautotrophic aerobic nitrifiers win the competition for nitrite against heterotrophic denitrifiers. This is due to a prescribed lower half-saturation constant for nitrite uptake and lower rate of mortality: using their parameters (their Table S1), R^* for NO_2^- for the nitrite-oxidizing bacteria and the heterotrophic denitrifiers is 0.02 and 0.25 μM, respectively, in that model. I.e., the subsistence concentration of the heterotrophic denitrifiers is over an order of magnitude higher than that of the chemoautotrophic nitrifiers. Our parameterization has assumed the opposite: that the heterotrophs are better competitors for nitrite.

Whether or not in the real ocean heterotrophic denitrifiers or chemoautotrophic nitrifiers are better competitors for nitrite, and whether this varies across environments, thus remains an open question. Here, we provide the tools with which to identify this competitive ability: R^* incorporates the half-saturation constant as well as the mortality rates to comprehensively predict this ability. This particular comparison – the R^* for nitrite for denitrifiers and nitrifiers – should serve as a sharp focus for more research on the ecological dynamics of N loss, since the outcome critically determines the fate of fixed nitrogen.

Is Fig. 3.10a or Fig. 3.10c a more realistic simulation? In order to answer this question, more observations may be required. It remains to be seen whether the abrupt end to aerobic heterotrophy, as in Fig. 3.10c, occurs in the ocean. Facultative anaerobes may choose to respire only with nitrate or nitrite as an electron acceptor once oxygen reaches a low, but not absolutely limiting, concentration. Or, facultative anaerobes could continue to utilize low levels of oxygen when available, as in the models in the main text. Testing for the activity of aerobic heterotrophy in anoxic marine zones could determine which scenario is realistic.

Similarly, it remains unknown whether anaerobic nitrite oxidation may explain the documented nitrite oxidation in anoxic zones. Though the models here demonstrate the plausibility of aerobic ammonium and nitrite oxidation occurring at low (nanomolar) levels of oxygen, it is unclear whether these chemoautotrophic nitrifiers may be competitively excluded by aerobic heterotrophs, in the case that aerobic heterotrophy does proceed at the lowest oxygen concentrations. If that competitive exclusion occurs, as anticipated by the default model result here (Fig. 3.10a), then the anaerobic nitrite oxidation as proposed by Babbin et al. (2017) seems a plausible explanation for the observations of Füssel et al. (2012).

One explanation is that real OMZs consist of a combination of both model results, reflecting a heterogeneous environment. Dynamics within particles may decouple the ecology from that of the ambient environment, resulting in greater diversity of metabolism than simulated in the models here.

In sum, the theoretical model here is able to provide insight into many, but not all, of the observed patterns of nitrogen loss in marine anoxic zones. Future research on the ecology surrounding sinking particles could provide further insight. Unaccounted for versatility of metabolisms, such as mixotrophy, as well as novel metabolisms, such as anaerobic nitrite oxidation, may also prove to play central roles in the nitrogen cycling in oxygen minimum zones.

3.10 Addendum 2: Calculation of ϕ for the ocean

3.10.1 Overview

In the main text, we developed an expression which which to predict the domain of sustainable anaerobic activity, ϕ, where $\phi = 1$ represents the onset of the coexistence of aerobic and anaerobic metabolisms. Here, we extend this analysis to the real ocean. We use data-based estimates of oxygen, transport, and the particulate carbon flux to calculate ϕ in three dimensions in the ocean below the euphotic zone. This calculation has the potential to estimate an upper bound on the volume of ocean where anaerobic metabolism should be steadily favorable. However, uncertainties in the datasets prohibit a meaningful quantification of this volume and of the implied maximum global rate of N loss. Nevertheless, we here demonstrate the calculation as an example of how to carry out such a quantification with more accurate and precise data.

3.10.2 Approach: Calculating ϕ in the ocean

We hypothesize that the volume encircled by $\phi = 1$ represents an upper bound on the domain of steady anaerobic activity in the ocean. We use the expression for ϕ from Eqn. 14 in the main text, taking the approximation that O_2^* is at nanomolar concentrations, as:

$$\phi = \frac{F_{O_2 in}}{\nabla \cdot OM} r^{-1} \tag{3.15}$$

where r is the ratio of oxygen to organic matter demand of the aerobic heterotrophic metabolism: $r = y_{OM_O}/y_{O_2}$ (mol O_2 utilized per mol OM utilized). Uncertainties in ϕ result from measurement error and sampling bias of the datasets, the assumption of r, and the assumption that O_2^* is negligible.

We calculate the gross fluxes of oxygen in the ocean with estimates of oxygen and ocean circulation, and relate them to the gridded inverse model of the POC flux as estimated by Schlitzer (2002). We use the WOA 2013 climatology of dissolved oxygen concentration, incorporating the correction scheme of Bianchi et al. (2012) for the systematic overestimate of O_2. This does not account for sampling bias and interpolation that also contributes to a systematic overestimate of O_2 in the oxygen minimum zones in particular. For ocean circulation, we use the OCCA state estimate from Forget (2010), which gives a dynamically plausible inverse estimate of advective and diffusive flows using comprehensive observations. The inverse of the ratio r is similar to the respiratory quotient, which is estimated to be about 0.9 mol CO_2 produced per mol O_2 consumed for algal material (Robinson 2008), though can vary from 0.7 to 1.3 for specific substrates. This range is consistent with the modeled stoichiometries here (see Appendix Fig. 3.14). We consider an average r of 1/0.9 = 1.1 with 10% uncertainty for the ocean on average. We incorporate the 35% uncertainty of the POC flux estimate (Schlitzer 2002), which contributes the most uncertainty to the calculation.

Fig. 3.11 shows the components of ϕ' at 270m: the incoming transport (d^{-1}) calculated as the gross fluxes from the OCCA estimate (Forget 2010), the oxygen concentration, the resulting incoming flux of oxygen ($F_{O_2 in}$), and the divergence of the POC flux ($\nabla \cdot POC$). This transport rate (Fig. 3.11a) can be thought of as the 'dilution rate,' representing the rate of supply of oxygen and other dissolved nutrients. The parameterization schemes for along-isopycnal eddy transport and mixing are accounted for in this estimate. If microbial rates are significantly faster than this rate, microbial metabolisms should fully control the resulting nutrient concentrations. The 0.01 d^{-1} contour is overlaid on the plot in white. Oxygen minimum zones are all within this contour, quantifying the lack of ventilation there. We can infer that microbial rates are likely to dominate the fluxes of nutrients in these zones.

The incoming oxygen flux $F_{O_2 in}$ was computed as the sum of all incoming fluxes of oxygen at the faces of each grid box (i.e., the transport routines were altered to isolate just these 'positive,' incoming fluxes.) The divergence of the organic matter flux is estimated just as the vertical divergence of the POC flux; horizontal transport of dissolved organic matter is neglected. Fig. 3.11c-d show that incoming oxygen is low in oxygen minimum zones, and the divergence of the POC flux (i.e., the inferred consumption of POC at that location) is large in the equatorial Pacific. Both of these effects should contribute to resulting low values of ϕ at this location.

3.10.3 Results and discussion

Fig. 3.12a shows the resulting values of ϕ at the 300m depth. In Fig. 3.12b, the contour $\phi = 1$ is plotted on top of the oxygen climatology. Three contours are plotted, corresponding to the average values of the POC divergence, as well as its ±35% uncertainty. The $\phi \leq 1$ area encircles the oxygen minimum zones.

The $\phi = 1$ contour predicts the onset of aerobic and anaerobic coexistence, and not exclusively anaerobic activity. If all of the organic matter consumed in the volume with $\phi \leq 1$ were oxidized anaerobically, assuming the bulk estimate denitrification remineralization ratio $r^{N:C}_{denitr}$ of 104:106 of Gruber and Sarmiento (1997), a calculated average of 58 Tg N yr^{-1} would be lost from the ocean globally. A 10% uncertainty in r contributes about a 25% uncertainty, giving a range of 41–71 Tg N yr^{-1}, and the 35% uncertainty in the POC flux gives a range of 16–108 Tg N yr^{-1}. This represents an upper bound on the estimation of the N loss, since the condition that $\phi \leq 1$ is a necessary but not sufficient condition for denitrification. In the idealized OMZ model in the main text, 77% of the organic matter oxidation within this volume was respired anaerobically; this may roughly estimate the expected fraction for the real ocean.

Though the range is large, this estimate is low compared to other estimates of global denitrification, which range from 65–150 Tg N yr^{-1} (compiled by Bianchi et al. (2012), their Table 1). The underestimate here reflects the fact that the oxygen climatology is most certainly an overestimate in low oxygen regions. However, the range is within the order of magnitude expected in the ocean. This indicates that the oxygen and POC flux estimates are in rough balance. This is unsurprising since the POC flux is an inverse estimate, with oxygen concentrations as one of the inputs for that estimate (Schlitzer 2002).

Knowing that this rough balance holds can be useful, then, in comparing other estimates of the POC flux. When using the POC flux estimate derived from thorium measurements by

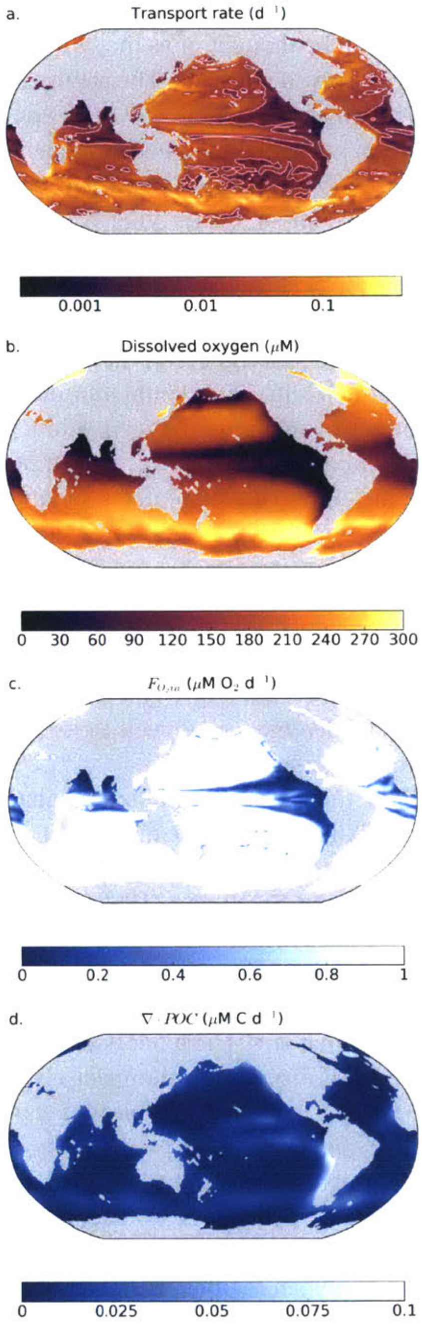

Figure 3.11: The components of ϕ at 270m depth: (a) The gross transport rate from the OCCA state estimate (Forget 2010), which can be thought of as the 'dilution rate' at each location. The 0.01 d^{-1} contour is overlaid, which isolates the oxygen minimum zones; (b) the oxygen concentration from WOA 2013, incorporating a correction for its systematic overestimate (Bianchi et al. 2012); (c) the resulting incoming flux of oxygen computed; (d) the divergence of the POC flux from the inverse estimate of Schlitzer (2002).

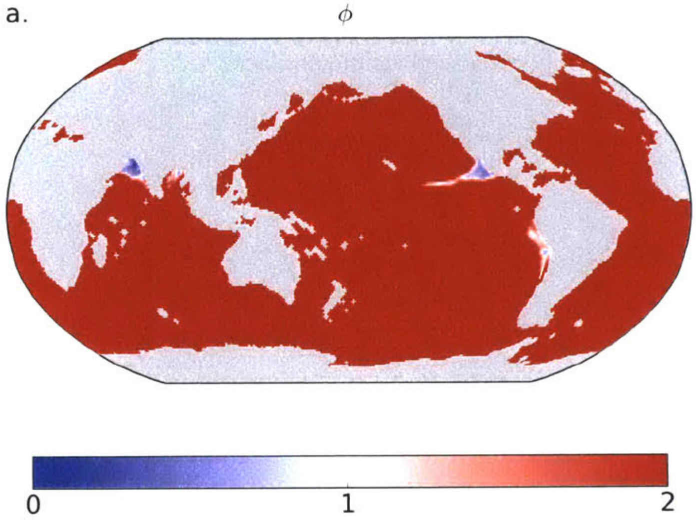

b. Dissolved oxygen (μM) with $\phi = 1$ contour

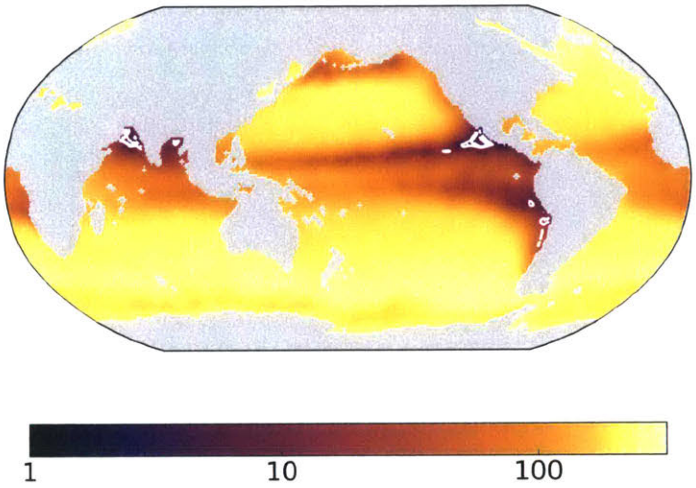

Figure 3.12: (a) Resulting estimate of ϕ at 270m depth, for $r = 1.1$. $\phi = 1$ indicates the computed threshold for the onset of anaerobic activity. (b) Contours of $\phi = 1$ for the average calculation as well as with the 35% uncertainty in the POC flux.

Henson et al. (2011), the calculation of ϕ suggests that zero denitrification occurs (results not shown), independent of the assumption of the b coefficient (Martin et al. 1987). Thus, ϕ can be used as a crude inverse estimate for the POC flux required – in the oxygen minimum zones, at least – to give a plausible amount of global denitrification. We infer that the POC flux in the eastern equatorial Pacific and Indian oceans as estimated by Henson et al. (2011) is too low, since it does not give these plausible numbers.

3.A Appendix

3.A.1 Derivation of ϕ

From Eqn. 3.6, the steady state concentration of just aerobic biomass is:

$$B_O = \frac{\kappa}{\mu_O}(\mathrm{O}_{2in} - \mathrm{O}_2^*)y_{\mathrm{O}_2} \tag{3.16}$$

Thus, for aerobic biomass to exist, $\mathrm{O}_{2in} > \mathrm{O}_2^*$.

From Eqn. 3.5 at steady state, the biomasses of both the aerobic and anaerobic populations are related as:

$$0 = \kappa(OM_{in} - OM) - \frac{1}{y_{OM_O}}\mu_O B_O - \frac{1}{y_{OM_N}}\mu_N B_N \tag{3.17}$$

where the organic matter subsistence concentration for anaerobic biomass OM_N^* is relevant, since we are working towards an expression for the coexistence of both populations, and this is the larger subsistence concentration (if $OM_{in} < OM_N^*$ and $OM_{in} \geq OM_O^*$), aerobic but not anaerobic biomass can accumulate.) Since $\mu = \kappa$ at steady state in the chemostat, further simplification can be made, but we retain these values in order to more easily extend the expression to environments.

Plugging in the expression for aerobic biomass from Eqn. 3.16, and rearranging to solve for anaerobic biomass:

$$B_N = y_{OM_N}\kappa(OM_{in} - OM_N^*) - \frac{y_{OM_N}}{y_{OM_O}}\kappa(\mathrm{O}_{2in} - \mathrm{O}_2^*)y_{\mathrm{O}_2} \tag{3.18}$$

Thus, for anaerobic biomass to exist,

$$0 < \kappa(OM_{in} - OM_N^*) - \frac{y_{\mathrm{O}_2}}{y_{OM_O}}\kappa(\mathrm{O}_{2in} - \mathrm{O}_2^*) \tag{3.19}$$

$$\frac{y_{\mathrm{O}_2}}{y_{OM_O}}\kappa(\mathrm{O}_{2in} - \mathrm{O}_2^*) < \kappa(OM_{in} - OM_N^*) \tag{3.20}$$

$$\frac{y_{\mathrm{O}_2}}{y_{OM_O}}\frac{\kappa(\mathrm{O}_{2in} - \mathrm{O}_2^*)}{\kappa(OM_{in} - OM_N^*)} < 1 \tag{3.21}$$

In the main text, we label the LHS expression as ϕ, and thus the threshold $\phi = 1$ is relevant for identifying the domain of coexistant aerobic and anaerobic biomass. We also use r to represent the ratio of oxygen to organic matter demand: $r = \frac{y_{OM_O}}{y_{\mathrm{O}_2}}$ (mol O_2 utilized per mol OM utilized), and so:

$$\phi = \frac{\kappa(\mathrm{O}_{2in} - \mathrm{O}_2^*)}{\kappa(OM_{in} - OM_N^*)}r^{-1} \tag{3.22}$$

3.A.2 2D model

Flow field for 2D model

Governing Equations A two-dimensional, basin-wide closed flow field is developed with conservation of momentum (with no gradients in y) and a wind stress forcing. The governing momentum equations are:

$$\frac{\partial u}{\partial t} = -u\frac{\partial u}{\partial x} - w\frac{\partial u}{\partial z} - \frac{1}{\rho_0}\frac{\partial p}{\partial x} + fv + \nabla \cdot \kappa \nabla u \tag{3.23}$$

$$\frac{\partial v}{\partial t} = -u\frac{\partial v}{\partial x} - w\frac{\partial v}{\partial z} - fu + \nabla \cdot \kappa \nabla v \tag{3.24}$$

With horizontal u computed, a non-divergent 2D circulation field can then be computed by imposing continuity as:

$$\frac{\partial u}{\partial x} + \frac{\partial w}{\partial z} = 0 \tag{3.25}$$

and integrating downwards (or upwards) to solve for the vertical velocity field w, with $w = 0$ as the top (or bottom) boundary condition.

The Pressure Field The wind-driven Ekman transport stirs up an overturning circulation through resolution of the pressure field, or, more specifically, the horizontal pressure gradient. The hydrostatic pressure field can be divided into the baroclinic pressure, calculated from density anomalies, and the surface pressure component, which are the deviations in sea surface height, r:

$$\frac{\partial p}{\partial x} = \frac{\partial}{\partial x}\int_{z}^{0} \rho' g dz + \frac{\partial p_{surf}}{\partial x} \tag{3.26}$$

Advecting the potential temperature and the salinity as tracers allows for the calculation of density anomalies at each time step. However, in this model, temperature and salinity are not resolved dynamically, and density anomalies are set to zero throughout the domain.

The rigid lid approximation is used to constrain this unknown; the total flux in and out of each water column must sum to zero, as:

$$\sum_{j=1}^{nj} (u_{j,i+1} - u_{j,i}) dz_j = 0 \tag{3.27}$$

Subbing Eqn. 3.26 (deconstruction of the pressure gradient) into Eqn. 3.23 (momentum in the x-direction) and then inserting this into the above rigid lid constraint allows for solving the horizontal surface pressure derivative. A boundary condition needed for this; $\frac{\partial p}{\partial x} = 0$ was imposed on the left (or right) boundary, and the pressure gradient was solved for at the face of each column by integrating from left to right (or right to left), which resulted in an analogous boundary pressure gradient of zero at the far boundary. The u velocity was then calculated with the newly updated pressure gradient at each time step, and checked for consistency with Eqn. 3.27.

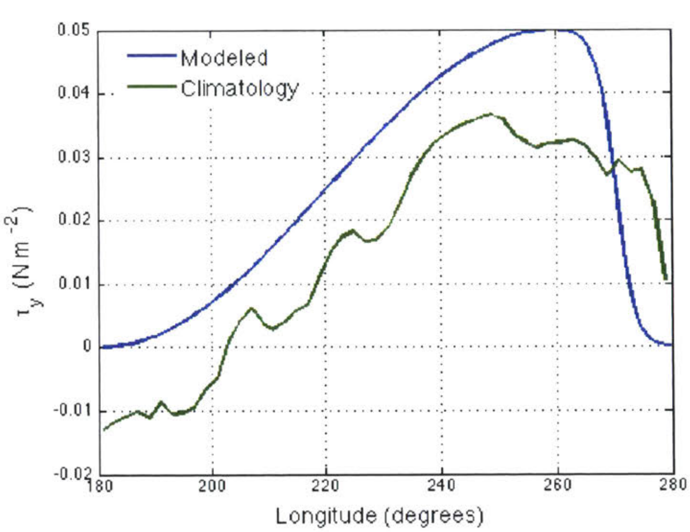

Figure 3.13: The modeled wind stress used as the forcing for the circulation, against climatological mean. Annual mean wind stress (y component) from the Hellerman and Rosenstein Global Wind Stress Climatology (Hellerman and Rosenstein 1983) from 180°E to 80°W, and from 0°S to 10°S, was averaged meridionally.

Wind Stress Forcing The overturning circulation was ultimately driven by an imposed wind stress forcing, only in the y-direction. The y-component of the wind stress was modeled not very elegantly as:

$$\tau_y(x) = 0.0125(\sin(\frac{\pi x}{0.8L} - \frac{\pi}{2}) + 1)(-\tanh(\frac{\pi x}{0.1L} - 9\pi) + 1) \tag{3.28}$$

where L is the length of the domain (10,000 km). Fig. 3.13 compares this modeled wind stress to the climatological mean from Hellerman and Rosenstein (1983) over the Pacific Basin, at 10°S latitude. The wind stress was imposed into the momentum equations as the top boundary condition for the diffusive flux of momentum in the y-direction as:

$$\frac{\tau_y(x)}{\rho_0} = \kappa\frac{\partial v}{\partial z} \tag{3.29}$$

Mixing A mixed layer was imposed by varying the vertical diffusion with depth. The vertical diffusion coefficient κ_Z was decreased exponentially from a maximum of 10^{-2} m^2 s^{-1}at the surface to a minimum with a length scale of z_{mld}. Additionally, since the boundary conditions of the sinking velocity for the detritus are prescribed as zero at both the top and the bottom edges (z=0 and $z = H$) of the domain, D often accumulates at the bottom of the domain. To smooth over numerical error, vertical mixing was allowed to increase there to 10^{-2} m^2 s^{-1}, simulating a bottom boundary mixed layer. Calculation of κ_Z (m^2 s^{-1})

thus results from summing the exponentially decaying terms at both the top (simulating the surface mixed layer) and the bottom (simulating the bottom boundary layer) of the domain with a minimum diffusion coefficient of 10^{-5} m^2 s^{-1}:

$$\kappa_Z = 10^{-2} e^{-\frac{z}{z_{mld}}} + 10^{-5} + 10^{-2} e^{-\frac{z-H}{100}} \tag{3.30}$$

where H is the height of the domain (2000 m). κ_Z is calculated at cell faces, and so the maximum values of 10^{-2} m^2 s^{-1} are never quite reached at either boundary.

The horizontal diffusion was prescribed as a constant 10^3 m^2 s^{-1}, a value thought to represent mixing by submesoscale eddies.

Numerical solution The momentum equations were solved to calculate the flow field, with a resolution of 10 m in the vertical and 100 km in the horizontal. The choice to resolve the time step explicitly led to the need to resolve gravity waves, and so a 10^{-3} day time step was necessary. Equations were integrated forward in time using the 4th order Runge-Kutta method. Advection was carried out using the QUICK advection scheme, consisting of a linear interpolation between points weighted by an upstream 2nd order curvature, resulting in 3rd order accuracy. Fluxes were calculated at the faces of each grid cell, and concentrations at the centers. The resulting u and w fields used for the biogeochemistry model were saved after 100 years of spin up.

Biogeochemistry detail for 2D model

The idealized ecological model of an oxygen minimum zone has six state variables: the aerobic (B_O) and anaerobic (B_N) types, sinking particulate organic matter (OM), small zooplankton grazers (Z), dissolved inorganic nitrogen (DIN), and oxygen (O_2). With nitrogen as the currency, the sum of all except oxygen is conserved over time.

Bypassing phytoplankton resolution, we parameterize a light- and DIN-limited export production as the source of OM as $\lambda e^{-z/z_L} N$. The parameter λ represents a maximum rate of export production (d^{-1}), which decays as z_L over depth z. OM is then a function of this export production, uptake by the microbial functional types, and mortality of all populations, and sinking at rate w_s.

The two metabolic functional types take up organic matter, oxygen, and DIN, and excrete DIN as in the virtual chemostat. The DIN taken up for respiration of the denitrifying functional type is balanced by immediately redistributing it evenly over the domain, which simulates a distant source of nitrogen fixation. The rate of change of the two types is a function of their growth rate μ (as in the main text), a linear mortality rate m_B, and linear grazing by zooplankton with a maximum grazing rate g.

The zooplankton population grows as the product of g, total microbial biomass ($B_O + B_N$), and growth efficiency γ (Armstrong 1994). A quadratic mortality rate m_Z implicitly represents their predation by higher trophic levels. Growth efficiency of zooplankton is assigned as 0.3, which is a consistent efficiency across size-classes as compiled by Taniguchi et al. (2014), and excretes DIN as a respiration product in accordance.

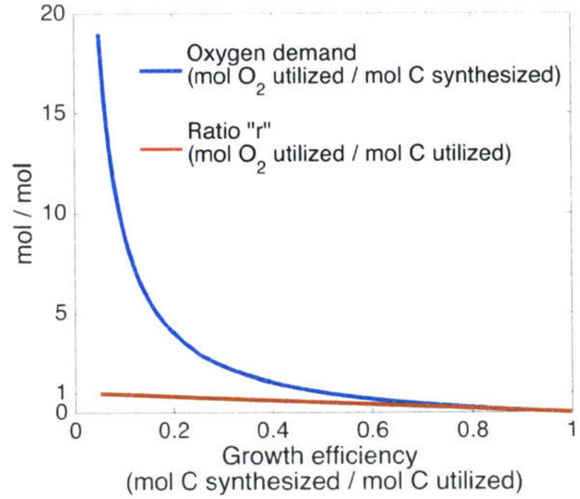

Figure 3.14: The ratio r used for the calculation of ϕ as a function of organic matter growth efficiency ($y_{OM_O}^{-1}$), compared to the oxygen demand $y_{O_2}^{-1}$. The ratio of the two, r, stays relatively similar (just below 1) for large variation in organic matter and oxygen demand, when assuming consistent substrate composition.

Zooplankton oxygen consumption is parameterized to allow for implicit zooplankton migration in and out of oxygen minimum zones: the oxygen demand by the zooplankton at a given location is spread vertically above and below that location, weighted by the oxygen concentration at that location. If the oxygen concentration is less than 8 μM at any spot along the spread, oxygen is not consumed there, but instead the weights are increased for the other boxes. This allows for zooplankton activity within the OMZ, mimicking their ability to breathe above or below the anoxic area, but swim into the area for grazing, as evidenced by Escribano et al. (2009). In the equations below, this is termed $f(O_2, Z)$.

All microbial and zooplankton growth, respiration, and mortality rates are temperature dependent, assuming a Q_{10} value of 2 (rate doublings per 10°C increase); values listed correspond to a reference temperature of 24°C. The model assumes a constant temperature profile, an average of the 10°S Pacific Ocean transect from the WOA 2013 climatology. This temperature dependency increases microbial rates by a factor of three from the deep to the surface.

Oxygen is sourced from export production with the same ratio r as in the expression for ϕ in the main text (Fig. 3.14). This assures that the formation and consumption of oxygen balance over time. Oxygen fluxes across the air-sea interface at a rate of about a month, estimated from an air-sea gas transfer coefficient of K_g ($3 * 10^{-5}$ m s^{-1}; Williams and Follows 2011) and an equilibration depth of 100 m, and with a constant saturation concentration of 212 μM (the saturation concentration for 25°C and a salinity of 35).

As in the flow field spin-up, the mixed layer was imposed by an exponential decay of a vertical mixing coefficient κ_z from 10^{-2} m^2 s^{-1} at the surface to an interior diapycnal mixing estimate of 10^{-5} m^2 s^{-1} with length scale z_{mld}. Horizontal diffusion was prescribed with a constant diffusion coefficient κ_x of 10^3 m^2 s^{-1}, simulating along-isopycnal stirring by submesoscale eddies (although in this model, isopycnal surfaces are not resolved as anything other than horizontal).

The biogeochemical model is then integrated forward in time using the 4th order Runge-Kutta method with a 0.1 d^{-1} time step. Advection, using the above resulting flow field, is carried out with the QUICK advection scheme, consisting of a linear interpolation between points weighted by an upstream 2nd order curvature, resulting in 3rd order accuracy. Fluxes are calculated at the faces of each grid cell, and concentrations at the centers. DIN, B_O, B_N, and Z are advected by the computed flow field. OM is advected the sum of the computed flow field and a constant sinking velocity w_s. Oxygen is resolved with a no-flux boundary over the domain everywhere except for the surface, where the air-sea flux is represented as an open boundary with a fixed equilibrium concentration as described above.

Denitrification stoichiometry estimate

The DIN demand of the denitrifying heterotroph can be estimated from the chemical reactions that, to first order, underlies its metabolism, following the methodology of Rittman and McCarty (2001). The description consists of three half-reactions: biomass synthesis, oxidation of an electron donor (organic matter), and reduction of an electron acceptor (here as NO_3 reduced completely to N_2, as a simplification of denitrification for the purposes of this study). The metabolism represents the combination of cell synthesis and energy production, partitioned by the fraction f of electrons fueling cell synthesis vs. respiration for energy.

These three reactions and their electron-partitioning coefficients are listed here for organic matter (OM) composition $C_{c_{OM}}H_{h_{OM}}O_{o_{OM}}N_{n_{OM}}$ and for biomass (B) composition $C_{c_B}H_{h_B}O_{o_B}N_{n_B}$ as (neglecting water for simplification):

$$(1)\left[\frac{1}{d_{OM}}C_{c_{OM}}H_{h_{OM}}O_{o_{OM}}N_{n_{OM}} \rightarrow \frac{n_{OM}}{d_{OM}}(NH_4^+ + HCO_3^-) + \frac{c_{OM}-n_{OM}}{d_{OM}}CO_2 + H^+ + e^-\right]$$

$$(1-f)\left[\frac{1}{5}NO_3^- + \frac{4}{3}H^+ + e^- \rightarrow \frac{1}{10}N_2\right]$$

$$(f)\left[\frac{n_B}{d_B}NH_4^+ + \frac{c_B-n_B}{d}CO_2 + \frac{n_B}{d_B}HCO_3^- + H^+ + e^- \rightarrow \frac{1}{d_B}C_{c_B}H_{h_B}O_{o_B}N_{n_B}\right]$$

When summed, the full metabolism forming denitrifying biomass B_N is:

$$\begin{aligned}&\frac{1}{d_{OM}}OM + \frac{1-f}{5}NO_3^- \\ &\quad\rightarrow \quad \frac{f}{d_B}B_N + \left(\frac{c_{OM}}{d_{OM}} - \frac{c_B f}{d_B}\right)CO_2 + \left(\frac{n_{OM}}{d_{OM}} - \frac{n_B f}{d_B}\right)NH_4^+ + \frac{1-f}{10}N_2 \qquad (3.31)\end{aligned}$$

From these equations, the yield of DIN $y_{DIN} = \frac{5y_{OM_N}}{d_{OM}(1-y_{OM_N}\frac{d_B}{d_{OM}})}$. When assuming the average stoichiometry of marine organic matter ($C_{106}H_{175}O_{42}N_{16}$; Anderson 1995) for both the organic matter substrate and microbial biomass, $y_{OM_N} = f$, and the full metabolism is represented as:

$$\begin{aligned} &OM + \frac{467(1-y_{OM_N})}{5}\mathrm{NO_3^-} \\ &\quad \rightarrow y_{OM_N}B_N + 106(1-y_{OM_N})\mathrm{CO_2} + 16(1-y_{OM_N})\mathrm{NH_4^+} + \frac{467(1-y_{OM_N})}{10}\mathrm{N_2} \end{aligned} \tag{3.32}$$

The DIN demand for nitrification $\frac{1}{y_{DIN}}$ is equivalent to $\frac{467(1-y_{OM_N})}{5y_{OM_N}}$, which is about 400 mol DIN per mol synthesized C, or about 25 mol DIN per mol synthesized N. This value is a bit lower when assuming bacterial stoichiometry (with C:N = 5); a value of 17 that reflects this is used in the illustrated models. The equivalent comparison with the Gruber and Sarmiento (1997) estimate for $r^{N:C}_{denitr}$ of 104:106 is $\frac{467(1-y_{OM_N})}{5\cdot 106}$, which here is about 0.7, in the range of other theoretically calculated values listed in (Gruber and Sarmiento 1997).

Equations for 2D model

Equations for the six state variables are:

$$\frac{DB_O}{Dt} = B_O(\mu_O - m_B - gZ) + \kappa\nabla^2 B_O$$

$$\frac{DB_N}{Dt} = B_N(\mu_N - m_B - gZ) + \kappa\nabla^2 B_N$$

$$\frac{DZ}{Dt} = \gamma g(B_O + B_N)Z - m_Z Z^2 + \kappa\nabla^2 Z$$

$$\begin{aligned} \frac{D(DIN)}{Dt} &= -\lambda DIN + \left(\frac{1}{y_{OM_O}} - 1\right)\mu_O B_O + (1-\gamma)g(B_O+B_N)Z \\ &\quad + \left(\left(\frac{1}{y_{OM_N}} - 1\right) - \frac{1}{y_{DIN}}\right)\mu_N B_N + \frac{\iint(\frac{1}{y_{DIN}}\mu_N B_N)dydz}{\iint dydz} + \kappa\nabla^2(DIN) \end{aligned}$$

$$\begin{aligned} \frac{D(OM)}{Dt} &= \lambda DIN - \frac{1}{y_{OM_O}}\mu_O B_O - \frac{1}{y_{OM_N}}\mu_N B_N + m_B(B_O + B_N) + m_Z Z^2 \\ &\quad - w_s\frac{\partial}{\partial z}(OM) + \kappa\nabla^2(OM) \end{aligned}$$

$$\frac{D(O_2)}{Dt} = r\lambda DIN - \frac{1}{y_{O_2}}\mu_O B_O - f(O_2, Z) + \frac{K_g}{h}(O_{2sat} - O_2) + \kappa\nabla^2 O_2$$

Table 3.4 lists the notations of all variables and parameters, their units, and default model values.

Table 3.4: The additional parameter values used in the 2D model. See the main text and Table 3.1 in main text for the growth rate equations and other metabolic parameters for the two microbial functional types. M, L, and T represent mass, length, and time.

Symbol	Description	Dimensions	Value
g	Maximum grazing rate	$L^3M^{-1}T^{-1}$	2 μM^{-1}d^{-1}
γ	Growth efficiency of zooplankton		0.3
κ_x	Horizontal Diffusion Coefficient	L^2T^{-1}	10^3 m^2 s^{-1}
κ_z	Vertical Diffusion Coefficient	L^2T^{-1}	f(z)
$\frac{K_g}{h}$	Air-sea flux transfer rate	T^{-1}	0.8 mo^{-1}
K_{DIN}	DIN half-saturation for B_N	ML^{-3}	0.1 μM
λ	Maximum export production rate	T^{-1}	0.1 d^{-1}
O_2sat	Saturated dissolved oxygen concentration	ML^{-3}	212 μM
m_B	Bacteria mortality rate	T^{-1}	0.01 d^{-1}
m_Z	Zooplankton mortality rate (quadratic)	$L^3M^{-1}T^{-1}$	1 μM^{-1} d^{-1}
Q_{10}	Temperature coefficient		2
V_{maxDIN}	Max specific uptake rate of DIN	T^{-1}	20 d^{-1}
w_s	Sinking velocity of detritus	ML^{-1}	3 m s^{-1}
z_{euph}	Length scale for light-limited export production	M	30 m
z_{mld}	Length scale for mixed layer depth/vertical diffusion	M	20 m

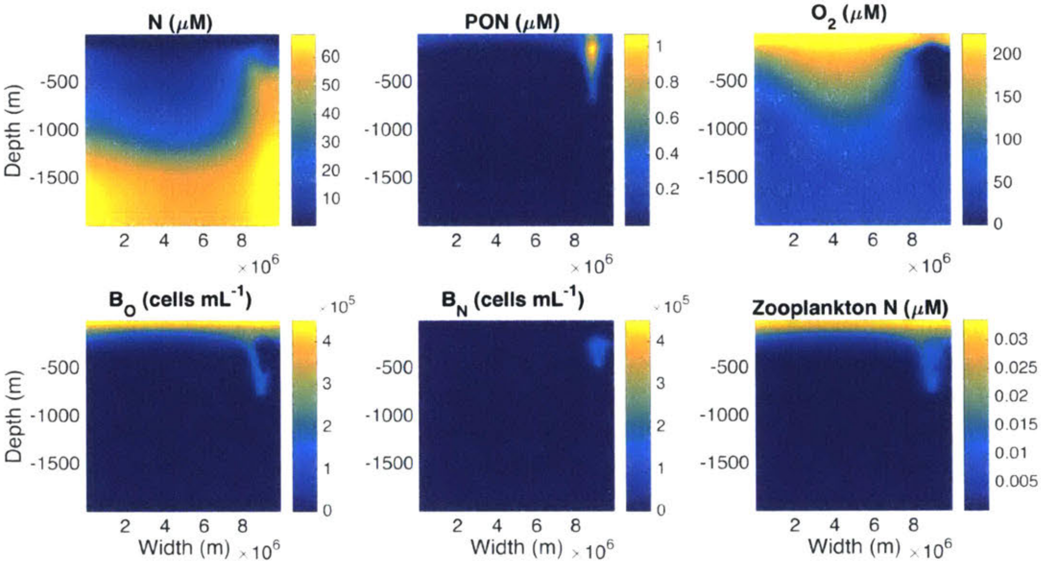

Figure 3.15: Full solutions for the six state variables in the 2D model.

Full solutions for 2D model

Fig. 3.15 illustrates the solutions for all six variables over the whole domain of the 2D model.

3.A.3 The six metabolic functional types

The six theoretical metabolisms considered here are: aerobic hetetrotrophy, nitrate-reducing heterotrophy, nitrite-reducing/denitrifying heterotrophy, ammonia oxidation, nitrite oxidation, and anaerobic ammonia oxidation (anammox).

We define the metabolic functional types with the set of redox reactions that, to first order, underlies each metabolism, following the methodology of Rittman and McCarty (2001). The description consists of three half-reactions: biomass synthesis, oxidation of an electron donor, and reduction of an electron acceptor. Each metabolism represents the combination of cell synthesis and energy production, partitioned by the fraction f of electrons fueling cell synthesis vs. respiration for energy.

Here, we list these reactions for each of the six metabolisms considered in this study and explain the estimate of their efficiency as a function of f. For the three heterotrophic metabolisms, we list the three reactions and their electron-partitioning coefficients for organic matter (OM) stoichiometry $C_{c_{OM}}H_{h_{OM}}O_{o_{OM}}N_{n_{OM}}$ and for biomass (B) stoichiometry $C_{c_B}H_{h_B}O_{o_B}N_{n_B}$. In the organic matter and synthesis half-reactions, we here neglect to type out the term for water (ex: $\frac{2c_{OM}-o_{OM}+n_{OM}}{d_{OM}}H_2O$) for conciseness, though this term is required for chemical balance.

For the values in the chemostat model, the average stoichiometry of marine organic matter ($C_{106}H_{175}O_{42}N_{16}$; Anderson (1995) is assumed for organic matter; the model normalizes this organic matter by nitrogen content. The average stoichiometry of bacterial biomass assumed by Rittman and McCarty (2001) ($C_{106}H_{175}O_{42}N_{16}$). This difference suggests a decoupling of the C and N cycling below. However, different efficiencies for C and N use have been reported for bacterial metabolisms as well (Goldman et al. 1987), and so insights into how bacterial metabolisms control C:N ratios in the environment are left for future research.

1. Aerobic heterotrophy: For the aerobic heterotroph, organic matter (OM) provides the elements and electrons for both the synthesis of biomass (B) and energy production, and oxygen serves as the electron acceptor, as:

$$(1)\left[\frac{1}{d_{OM}}C_{c_{OM}}H_{h_{OM}}O_{o_{OM}}N_{n_{OM}} \rightarrow \frac{n_{OM}}{d_{OM}}(NH_4^+ + HCO_3^-) + \frac{c_{OM}-n_{OM}}{d_{OM}}CO_2 + H^+ + e^-\right]$$

$$(1-f)\left[\frac{1}{4}O_2 + H^+ + e^- \rightarrow \frac{1}{2}H_2O\right]$$

$$(f)\left[\frac{n_B}{d_B}NH_4^+ + \frac{c_B-n_B}{d}CO_2 + \frac{n_B}{d_B}HCO_3^- + H^+ + e^- \rightarrow \frac{1}{d_B}C_{c_B}H_{h_B}O_{o_B}N_{n_B}\right]$$

where d_{OM} and d_B are the number of electron equivalents for the organic matter and biomass compositions, respectively, that correspond to the oxidation states of their inorganic constituents. We estimate d for $C_cH_hO_oN_n$ as $d = 4c + h - 2o - 3n$ when considering conversion of organic N to the reduced oxidation state of ammonium/a (-3); $d = 20$ for bacterial biomass. Summing gives the full metabolism forming aerobic heterotrophic biomass B_{HetO}

as:

$$\frac{1}{d_{OM}}OM+\frac{1-f}{4}\mathrm{O_2} \\ \rightarrow \quad \frac{f}{d_B}B_{HetO}+\left(\frac{c_{OM}}{d_{OM}}-\frac{c_Bf}{d_B}\right)\mathrm{CO_2}+\left(\frac{n_{OM}}{d_{OM}}-\frac{n_Bf}{d_B}\right)\mathrm{NH_4^+} \tag{3.33}$$

The commonly discussed bacterial growth efficiency, or yield y (mol B mol $^{-1}$ OM, or, mol C synthesized mol $^{-1}$ C consumed) relates to f as:

$$y_{OM}=\frac{d_{OM}}{d_B}f \tag{3.34}$$

and so $y_{OM}=f$ when assuming the same stoichiometry for both the organic matter substrate and microbial biomass. For the chemostat model, we assign y_{OM} as 0.2, the average bacterial growth efficiency for coastal marine environments (Robinson 2008).

2. Nitrate-reducing heterotrophy: For the nitrate reducer, organic matter (*OM*) provides the elements and electrons for both the synthesis of biomass (*B*) and energy production, and nitrate serves as the electron acceptor, which is reduced to nitrite:

$$(1)\left[\frac{1}{d_{OM}}\mathrm{C}_{c_{OM}}\mathrm{H}_{h_{OM}}\mathrm{O}_{o_{OM}}\mathrm{N}_{n_{OM}}\rightarrow\frac{n_{OM}}{d_{OM}}(\mathrm{NH_4^+}+\mathrm{HCO_3^-})+\frac{c_{OM}-n_{OM}}{d_{OM}}\mathrm{CO_2}+\mathrm{H^+}+e^-\right]$$

$$(1-f)\left[\frac{1}{2}\mathrm{NO_3^-}+\mathrm{H^+}+e^-\rightarrow\frac{1}{2}\mathrm{NO_2^-}\right]$$

$$(f)\left[\frac{n_B}{d_B}\mathrm{NH_4^+}+\frac{c_B-n_B}{d}\mathrm{CO_2}+\frac{n_B}{d_B}\mathrm{HCO_3^-}+\mathrm{H^+}+e^-\rightarrow\frac{1}{d_B}\mathrm{C}_{c_B}\mathrm{H}_{h_B}\mathrm{O}_{o_B}\mathrm{N}_{n_B}\right]$$

When summed, the full metabolism forming nitrate-reducing biomass B_{HetNO_3} is:

$$\frac{1}{d_{OM}}OM+\frac{1-f}{2}\mathrm{NO_3^-} \\ \rightarrow \quad \frac{f}{d_B}B_{HetNO_3}+\left(\frac{c_{OM}}{d_{OM}}-\frac{c_Bf}{d_B}\right)\mathrm{CO_2}+\left(\frac{n_{OM}}{d_{OM}}-\frac{n_Bf}{d_B}\right)\mathrm{NH_4^+}+\frac{1-f}{2}\mathrm{NO_2^-} \tag{3.35}$$

For the nitrate reducer in chemostat model, we assign y_{OM} as 0.19, an arbitrarily slightly lower value than that of the aerobic heterotroph. This is close to the theoretical difference in yields, though observations often show much higher reductions in yields for the use of nitrate as an electron acceptor than thermodynamics predicts (Roden and Jin 2011; Chen and Strous 2013).

3. Denitrifying heterotrophy: For the denitrifier, organic matter (*OM*) provides the elements and electrons for both the synthesis of biomass (*B*) and energy production, and nitrite serves as the electron acceptor, which we consider here as all being reduced completely to N_2 (ignoring the formation of N_2O for the purposes of this study).

$$\begin{aligned}
&(1)\left[\frac{1}{d_{OM}}\mathrm{C}_{c_{OM}}\mathrm{H}_{h_{OM}}\mathrm{O}_{o_{OM}}\mathrm{N}_{n_{OM}} \rightarrow \frac{n_{OM}}{d_{OM}}(\mathrm{NH}_4^+ + \mathrm{HCO}_3^-) + \frac{c_{OM}-n_{OM}}{d_{OM}}\mathrm{CO}_2 + \mathrm{H}^+ + e^-\right]\\
&(1-f)\left[\frac{1}{3}\mathrm{NO}_2^- + \frac{4}{3}\mathrm{H}^+ + e^- \rightarrow \frac{1}{6}\mathrm{N}_2 + \frac{2}{3}\mathrm{H}_2\mathrm{O}\right]\\
&(f)\left[\frac{n_B}{d_B}\mathrm{NH}_4^+ + \frac{c_B-n_B}{d}\mathrm{CO}_2 + \frac{n_B}{d_B}\mathrm{HCO}_3^- + \mathrm{H}^+ + e^- \rightarrow \frac{1}{d_B}\mathrm{C}_{c_B}\mathrm{H}_{h_B}\mathrm{O}_{o_B}\mathrm{N}_{n_B}\right]
\end{aligned}$$

When summed, the full metabolism forming denitrifying biomass B_{HetNO_2} is:

$$\begin{aligned}
&\frac{1}{d_{OM}}OM + \frac{1-f}{3}\mathrm{NO}_2^-\\
\rightarrow\quad &\frac{f}{d_B}B_{HetNO_2} + \left(\frac{c_{OM}}{d_{OM}} - \frac{c_B f}{d_B}\right)\mathrm{CO}_2 + \left(\frac{n_{OM}}{d_{OM}} - \frac{n_B f}{d_B}\right)\mathrm{NH}_4^+ + \frac{1-f}{6}\mathrm{N}_2 \qquad (3.36)
\end{aligned}$$

For the denitrifier in chemostat model, we assign y_{OM} as 0.19, the same value as the nitrate reducer. Thus, the only difference between these two modeled metabolisms results from the half-reactions of the nitrate and nitrite reduction.

For each of the three chemoautotrophic metabolisms, we list the three reactions and their electron-partitioning coefficients for biomass $C_cH_hO_oN_n$:

4. Ammonia oxidation: For the ammonia oxidizer (here considering NH_4^+ and NH_3 interchangeably), we here assume ammonium oxidation provides electrons for energy that fuels cell synthesis, with oxygen serving as the terminal electron acceptor:

$$\begin{aligned}
&(1)\left[\frac{1}{6}\mathrm{NH}_4^+ + \frac{1}{3}\mathrm{H}_2\mathrm{O} \rightarrow \frac{1}{6}\mathrm{NO}_2^- + \frac{4}{3}\mathrm{H}^+ + e^-\right]\\
&(1-f)\left[\frac{1}{4}\mathrm{O}_2 + \mathrm{H}^+ + e^- \rightarrow \frac{1}{2}\mathrm{H}_2\mathrm{O}\right]\\
&(f)\left[\frac{n}{d}\mathrm{NH}_4^+ + \frac{c-n}{d}\mathrm{CO}_2 + \frac{n}{d}\mathrm{HCO}_3^- + \mathrm{H}^+ + e^- \rightarrow \frac{1}{d}\mathrm{C}_c\mathrm{H}_h\mathrm{O}_o\mathrm{N}_n + \frac{2c-o+n}{d}\mathrm{H}_2\mathrm{O}\right]
\end{aligned}$$

This gives the full metabolism forming ammonia-oxidizing biomass B_{AOO} when summed (ignoring water and lumping bicarbonate into the CO_2 pool for simplification) as:

$$\left(\frac{1}{6} + \frac{f}{d}\right)\mathrm{NH}_4^+ + \frac{cf}{d}\mathrm{CO}_2 + \frac{1-f}{4}\mathrm{O}_2 \rightarrow \frac{f}{d}B_{AOO} + \frac{1}{6}\mathrm{NO}_2^- \qquad (3.37)$$

For the ammonia oxidizer in the chemostat model, we assign $f = 0.03$, the same value as used in Chapter 4. The derivation of this value as a ballpark estimate is extensively discussed in the Appendix to Chapter 4; its precise value is highly uncertain, but relatively large variations in this value do not affect model results qualitatively. Qualitatively, the solutions only depend on this f being lower than that of heterotrophy; this is reasonable given the basic assumption that heterotrophic metabolisms are overall more efficient (and faster) than chemoautotrophic lifestyles.

5. Nitrite oxidation: We assume that the nitrite oxidizer uses nitrite as its electron donor for energy, and reduced nitrogen (i.e., the same oxidation state as ammonium) as the source of elemental nitrogen (Santoro 2016), which could be due to mixotrophic growth or ammonium uptake capability. This has a negligible effect on the stoichiometry (since $f/d \ll 1/2$ below), but increases our burden of proof to distinguish the two metabolisms energetically:

$$
\begin{aligned}
(1)\ & \left[\frac{1}{2}\mathrm{NO_2^-} + \frac{1}{2}\mathrm{H_2O} \rightarrow \frac{1}{2}\mathrm{NO_3^-} + \mathrm{H^+} + e^-\right] \\
(1-f)\ & \left[\frac{1}{4}\mathrm{O_2} + \mathrm{H^+} + e^- \rightarrow \frac{1}{2}\mathrm{H_2O}\right] \\
(f)\ & \left[\frac{n}{d}\mathrm{NH_4^+} + \frac{c-n}{d}\mathrm{CO_2} + \frac{n}{d}\mathrm{HCO_3^-} + \mathrm{H^+} + e^- \rightarrow \frac{1}{d}\mathrm{C}_c\mathrm{H}_h\mathrm{O}_o\mathrm{N}_n + \frac{2c-o+n}{d}\mathrm{H_2O}\right]
\end{aligned}
$$

which gives the full metabolism forming nitrite-oxidizing biomass B_{NOO} when summed (again written without water, and with CO_2 as the carbon source) as:

$$
\frac{1}{2}\mathrm{NO_2^-} + \frac{f}{d}\mathrm{NH_4^+} + \frac{cf}{d}\mathrm{CO_2} + \frac{1-f}{4}\mathrm{O_2} \rightarrow \frac{f}{d}B_{NOO} + \frac{1}{2}\mathrm{NO_3^-} \tag{3.38}
$$

For the nitrite oxidizer in the chemostat model, we assign $f = 0.03$, the same value as the ammonia oxidizer. In the Appendix to Chapter 4, we discuss theoretical reasons for and observational evidence of the relatively equal efficiency of ammonia oxidation and nitrite oxidation. This same efficiency of electron flow results in significantly higher (a factor of three larger) nitrite demand compared to ammonium demand for the two metabolisms, respectively.

6. Anammox: For anammox, we here assume, to first order, that ammonium oxidation provides electrons for energy that fuels cell synthesis (here considering NH_4^+ and NH_3 interchangeably), and nitrite serves as the electron acceptor. Together, elemental N_2 is formed:

$$
\begin{aligned}
(1)\ & \left[\frac{1}{3}\mathrm{NH_4^+} \rightarrow \frac{1}{6}\mathrm{N_2} + \frac{4}{3}\mathrm{H^+} + e^-\right] \\
(1-f)\ & \left[\frac{1}{3}\mathrm{NO_2^-} + \frac{4}{3}\mathrm{H^+} + e^- \rightarrow \frac{1}{6}\mathrm{N_2} + \frac{2}{3}\mathrm{H_2O}\right] \\
(f)\ & \left[\frac{n}{d}\mathrm{NH_4^+} + \frac{c-n}{d}\mathrm{CO_2} + \frac{n}{d}\mathrm{HCO_3^-} + \mathrm{H^+} + e^- \rightarrow \frac{1}{d}\mathrm{C}_c\mathrm{H}_h\mathrm{O}_o\mathrm{N}_n + \frac{2c-o+n}{d}\mathrm{H_2O}\right]
\end{aligned}
$$

The anammox metabolism is more complicated than this (Kartal et al. 2008), but this description at least results in values that are consistent with the stoichiometry observed by (Strous et al. 1998). This description here gives the full metabolism forming anammox biomass B_{anmx} when summed as:

$$
\left(\frac{1}{3} + \frac{f}{d}\right)\mathrm{NH_4^+} + \frac{1-f}{3}\mathrm{NO_2^-} + \frac{cf}{d}\mathrm{CO_2} \rightarrow \frac{f}{d}B_{anmx} + \frac{2-f}{6}\mathrm{N_2} \tag{3.39}
$$

For anammox in the chemostat model, we assign $f = 0.03$ for the solutions that are illustrated, the same value as the aerobic nitrifiers. We also compare theoretical stoichiometry with the values that result from the experiments of Strous et al. (1998) (their direct results, which are the unbalanced stoichiometries in their Table 1). Strous et al. (1998) report average ammonium and nitrite demands (here neglecting their reported uncertainty range of approximately 10%) of about 112 and 136 mol per mol biomass, respectively. These values are approximately the same as if $f = 0.05$ (theoretical ammonium and nitrite demand for $f = 0.05$ predicts about 130 mol /mol for each substrate). Interestingly and significantly, the model results do not change qualitatively as long as the ammonium demand by anammox is less than that of the aerobic ammonia oxidizer. Whether assuming $f = 0.03$ or $f = 0.05$, anammox demands significantly less nitrite than nitrite-oxidizers, as modeled here theoretically.

Chemostat equations for the six types

The biomass of the six functional types and nutrients (in units of μM N except for O_2) are modeled with the expressions for their rates of change with time, defined by incoming nutrient supply, nutrient uptake, growth rate, and excretion of waste respiration products, and the chemostat dilution rate κ as:

$$
\begin{aligned}
\frac{dB_{HetO}}{dt} &= B_{HetO}(\mu_{HetO} - \kappa)\\
\frac{dB_{HetNO_3}}{dt} &= B_{HetNO_3}(\mu_{HetNO_3} - \kappa)\\
\frac{dB_{HetNO_2}}{dt} &= B_{HetNO_2}(\mu_{HetNO_2} - \kappa)\\
\frac{dB_{AOO}}{dt} &= B_{AOO}(\mu_{AOO} - \kappa)\\
\frac{dB_{NOO}}{dt} &= B_{NOO}(\mu_{NOO} - \kappa)\\
\frac{dB_{anx}}{dt} &= B_{anx}(\mu_{anx} - \kappa)\\
\frac{dOM}{dt} &= \kappa(OM_{in} - OM) - \frac{1}{y_{OM_O}}\mu_{HetO}B_{HetO} - \frac{1}{y_{OM_N}}(\mu_{HetNO_3}B_{HetNO_3} + \mu_{HetNO_2}B_{HetNO_2})\\
\frac{d[\mathrm{NH}_4^+]}{dt} &= (\frac{1}{y_{OM_O}} - 1)\mu_{HetO}B_{HetO} + (\frac{1}{y_{OM_N}} - 1)(\mu_{HetNO_3}B_{HetNO_3} + \mu_{HetNO_2}B_{HetNO_2})\\
&\quad - \frac{1}{\mathrm{NH}_{4-AOO}}\mu_{AOO}B_{AOO} - \mu_{NOO}B_{NOO} - \frac{1}{y_{\mathrm{NH}_{4-anx}}}\mu_{anx}B_{anx} - \kappa[\mathrm{NH}_4^+]\\
\frac{d[\mathrm{NO}_2^-]}{dt} &= \frac{1}{y_{\mathrm{NO}_{3-het}}}\mu_{HetNO_3}B_{HetNO_3} - \frac{1}{y_{\mathrm{NO}_{2-het}}}\mu_{HetNO_2}B_{HetNO_2}\\
&\quad + (\frac{1}{y_{\mathrm{NH}_{4-AOO}}} - 1)\mu_{AOO}B_{AOO} - \frac{1}{y_{\mathrm{NO}_{2-NOO}}}\mu_{NOO}B_{NOO} - \frac{1}{y_{\mathrm{NO}_{2-anx}}}\mu_{anx}B_{anx} - \kappa[\mathrm{NO}_2^-]\\
\frac{d[\mathrm{NO}_3^-]}{dt} &= \frac{1}{y_{\mathrm{NO}_2}}\mu_{NOO}B_{NOO} - \frac{1}{y_{\mathrm{NO}_{3-het}}}\mu_{HetNO_3}B_{HetNO_3} - \kappa[\mathrm{NO}_3^-]\\
\frac{d[\mathrm{O}_2]}{dt} &= \kappa([\mathrm{O}_{2\mathrm{in}}] - [\mathrm{O}_2]) - \frac{1}{y_{O_{2-O}}}\mu_{HetO}B_{HetO} - \frac{1}{y_{O_{2-AOO}}}\mu_{AOO}B_{AOO} - \frac{1}{y_{O_{2-NOO}}}\mu_{NOO}B_{NOO}
\end{aligned}
$$

where $\mu = \kappa$ for equilibrated model solutions. As in the main text of the chapter, we assume a growth rate μ as the product of the uptake rate and yield, and the limiting growth rate as the minimum of this product for multiple required substrates.

Chapter 4

How nitrification can form the primary nitrite maximum

The work in this chapter was completed in collaboration with Mick Follows, Stephanie Dutkiewicz, Alia Al-Haj, Wally Fulweiler, Sarah Foster, Matt Church, Matt Mills, and Gert van Dijken.

4.1 Overview

The primary nitrite maximum (PNM), an accumulation of 10–1000 nM nitrite at the base of the euphotic zone, is a ubiquitous but poorly understood oceanographic feature. Peak nitrification often correlates with the PNM, but causation requires explaining why the two steps of nitrification – ammonia oxidation and nitrite oxidation – are decoupled, and why nitrification peaks at depth. Previous work has suggested that light inhibition restricts nitrification to dark waters, but observations show that this is not universally true. Here, we suggest mechanisms for the formation of the PNM using a microbial ecosystem model with explicit nitrifying metabolic functional type populations: ammonia oxidizers and nitrite oxidizers. First, the decoupling of the two nitrification steps and the accumulation of nitrite are quantitatively explained by two mechanisms: redox reaction-based descriptions of the two nitrifying metabolisms as well as differences in uptake kinetics based on cell size. Second, competition with phytoplankton for ammonium and nitrite excludes the nitrifiers from the surface in much of the model. The PNM emerges at the base of the euphotic zone as a consequence of ecological interactions, with no photoinhibition imposed. In a global simulation, this dynamic parameterization of nitrification also exhibits significant euphotic zone nitrification at high latitudes, which is consistent with observations. The model thus proposes favorable nitrification near the surface when phytoplankton growth is limited by light or perhaps iron, such as in high nutrient low chlorophyll regions, and otherwise where nitrogen supply is abundant, such as in bloom environments. Results provide a global framework for understanding the controls on nitrification in the ocean.

4.2 Introduction

Nitrogen locally limits primary productivity over about half of the surface ocean (Moore et al. 2013). Though dissolved inorganic nitrogen (DIN) in the form of ammonium (NH_4^+) or urea is a common nitrogen substrate for phytoplankton, most DIN exists as nitrate (NO_3^-) below the euphotic zone in the deep ocean. Nitrification – the microbially-mediated oxidation of NH_4^+ (technically as NH_3) to NO_3^-, with nitrite (NO_2^-) as the intermediary ($NH_4^+ \rightarrow NO_2^- \rightarrow NO_3^-$) – connects these pools (Ward 2008). Nitrification thus relates to NO_3^- supply, and has implications for estimates of new versus regenerated primary production. New production, traditionally considered that fueled by NO_3^-, is thought to balance export production over large time and space scales, but cycling in the euphotic zone complicates this definition (Dugdale and Goering 1967; Yool et al. 2007).

The primary nitrite maximum (PNM) is an accumulation of NO_2^- at the base of the euphotic zone in stratified water columns (Fig. 4.1), with concentrations ranging from 10–1000 nmol L^{-1}. The PNM is often just below the deep chlorophyll maximum (DCM), is occasionally accompanied by an ammonium maximum (cite Brzezinski LandO 1988), and varies with the degree of water column stratification (Zafiriou et al. 1992; Dore and Karl 1996b; Lomas and Lipschultz 2006; Ward 2008; Mackey et al. 2011; Santoro et al. 2013). Its location typically tracks the depth of the mixed layer: the PNM is shallower near equatorial upwelling, deeper in the center of subtropical gyres, and less evident at high latitudes where seasonality causes variance in mixed layer depth and production. The PNM is ubiquitous in the ocean (Fig. 4.1), in contrast to the secondary nitrite maximum that forms in low oxygen environments from anaerobic activity.

Despite its widespread occurrence, the formation of the PNM is still not well understood, which highlights a gap in our understanding of the marine nitrogen cycle. Two hypotheses, not mutually exclusive, have been put forward to explain its formation: 1. the two steps of nitrification – ammonia oxidation ($NH_4^+ \rightarrow NO_2^-$) and nitrite oxidation ($NO_2^- \rightarrow NO_3^-$) – are decoupled due to the activities of discrete populations of chemoautolithotrophs, and 2. nitrite is excreted due to incomplete assimilatory reduction of nitrate by phytoplankton (Lomas and Lipschultz 2006).

However, isotopic evidence increasingly points to nitrification as the dominant control (Santoro et al. 2013; Buchwald and Casciotti 2013). In a typical near-surface vertical profile, nitrification rates and nitrifier biomasses are usually observed to peak at the base of the euphotic zone, at or just below the PNM (Ward 1987; Ward et al. 1989; Dore and Karl 1996a; Santoro et al. 2010; Newell et al. 2011; Santoro et al. 2013; Buchwald and Casciotti 2013). On a recent research cruise in the oligotrophic N. Pacific, we again observed these typical patterns in the near-surface water column. We measured ammonia oxidation rates measured using stable isotope addition (^{15}N), amoA gene abundances, NO_2^-, NO_3^-, PAR, and chlorophyll *a* at four locations (Fig. 4.2; see Appendix 4.A.1 for locations and methods). Peak NO_2^- concentration in each water column was consistently just below the deep chlorophyll maximum, reaching 40-130 nmol L^{-1}. Ammonia oxidation rates peaked near the PNM at three out of four stations, reaching about 2 to 6 nmol L^{-1} d^{-1}. In general, rates

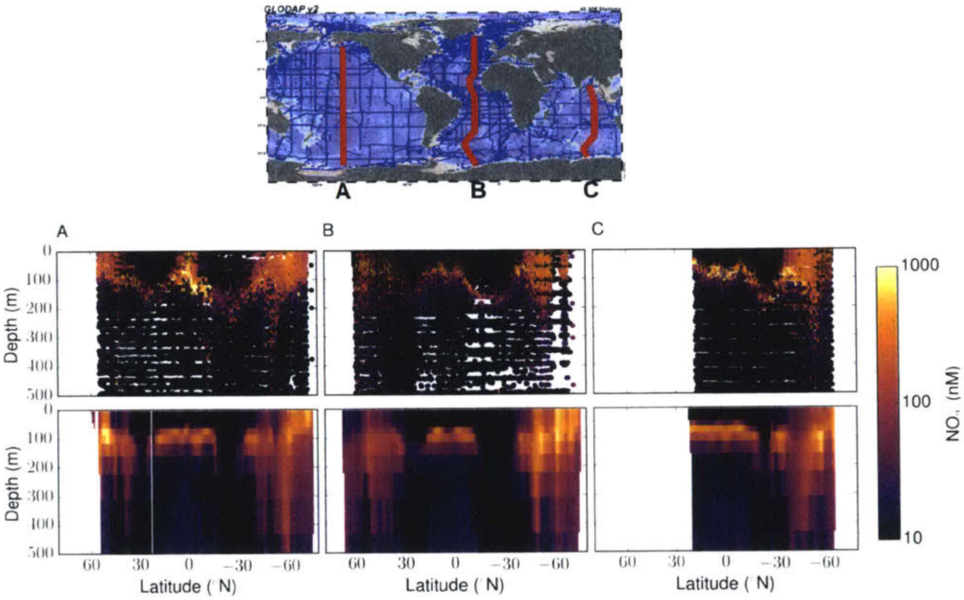

Figure 4.1: Nitrite (NO_2^-) concentrations along three transects from GLODAPv2 (top panel), illustrating the primary nitrite maximum at the base of the euphotic zone, and along similar transects in the 3D simulation (bottom panel). GLODAPv2 data: Key et al. (2015); Olsen et al. (2016)

and abundances correlated with NO_2^- concentrations, and so were consistent with previous observations (Newell et al. 2011; Santoro et al. 2013).

If nitrification is indeed the dominant control on PNM formation, two explanations are required: 1. the mechanism by which nitrification often peaks at depth, and 2. the mechanism for the decoupling of the two steps of nitrification that allows for the accumulation of nitrite. Light inhibition has been hypothesized as an explanation for both, with differential inhibition affecting the oxidation of NH_4^+ to NO_2^- and NO_2^- to NO_3^- (Lomas and Lipschultz 2006; Merbt et al. 2012). However, studies of this photoinhibition are inconclusive (Lomas and Lipschultz 2006), and observations of nitrification in the euphotic zone suggest that this cannot be a universal mechanism (Ward 1987; Dore and Karl 1996a; Ward 2005; Clark et al. 2008; Cavagna et al. 2015; Fripiat et al. 2015). Smith et al. (2014) propose that phytoplankton may outcompete slow-growing chemolithotrophic nitrifiers in most surface conditions, favoring nitrification once light is depleted. Indeed, Preheim et al. (2016) model metabolic processes in a lake as a function of chemical gradients and show ammonia oxidation peaking at depth. Thus light may indirectly govern the typical vertical profile, and limitations to phytoplankton growth other than light may allow for surface nitrification.

The decoupling of the two steps of nitrification is plausible because it is understood that they are carried out by distinct groups of chemolithoautotrophs in the water column (Costa et al. 2006; Ward 2008). Both ammonia-oxidizing archaea (AOA) and bacteria (AOB) are responsible for the oxidation of NH_4^+ to NO_2^-. However, AOA are currently understood to be

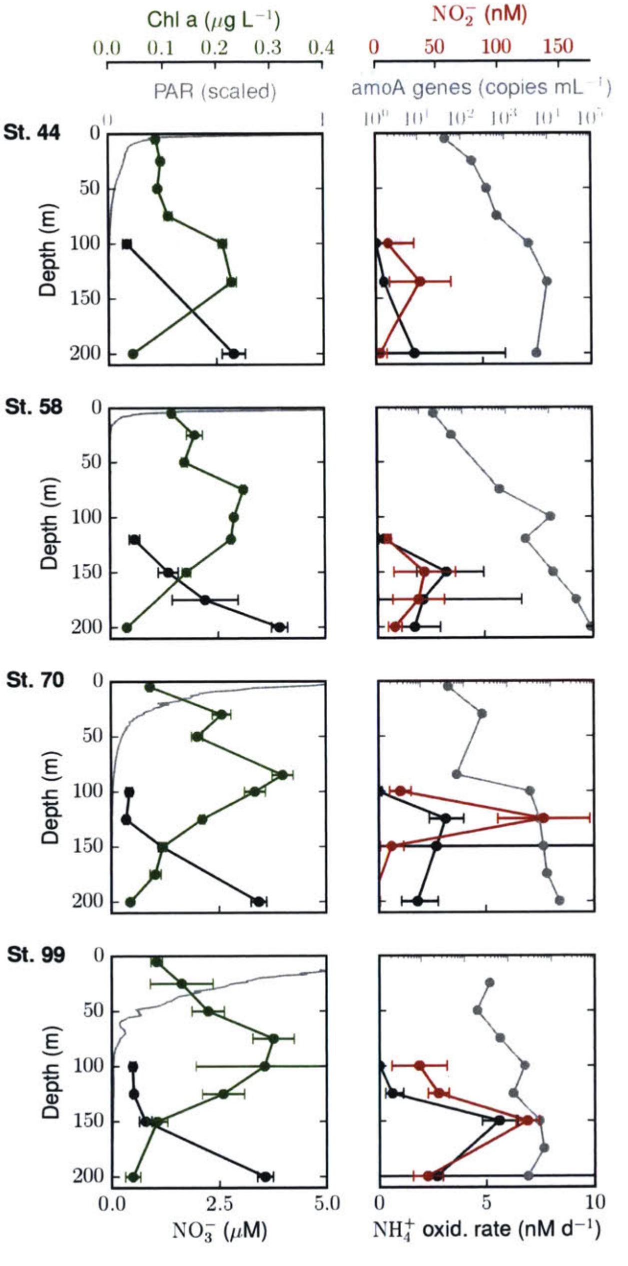

Figure 4.2: Data from four stations in the oligotrophic North Pacific from cruise NH1417: Chl *a* and nitrate concentrations, photosynthetically active radiation (PAR), *amoA* gene abundances, and ammonia oxidation rates.

more biogeochemically significant in the open ocean than AOB (Stahl and de la Torre 2012). Their extremely high affinity for ammonium makes them better adapted to oligotrophic environments than the larger AOB (Martens-Habbena et al. 2009). In contrast, the oxidation of NO_2^- to NO_3^- is understood to be dominated by nitrite-oxidizing bacteria (NOB) (Daims et al. 2016), although knowledge of nitrifying organisms is limited and rapidly expanding (Spieck et al. 2014; Daims et al. 2016; Santoro 2016). Both AOA and NOB have been demonstrated to have versatile metabolisms including mixotrophy (Ward 2008; Qin et al. 2014; Daims et al. 2016). Daims et al. (2015) and van Kessel et al. (2015) have demonstrated both steps of nitrification in one organism common in biofilms, however, it is still thought that two distinct groups characterize well-mixed environments such as the ocean (Costa et al. 2006).

Here, we aim to understand how nitrification may consistently form the PNM. Why does nitrification often peak at the base of the euphotic zone, and occasionally occur within the sunlit layer? Why does nitrite, but not ammonium, consistently accumulate, and how does the decoupling of the NH_4^+ and NO_2^- oxidation relate to nitrifier abundances and nitrification rates? Here, we develop a model microbial ecosystem to quantitatively examine the ecology of nitrification in the water column. We represent the microbial community responsible for the two steps of nitrification explicitly with two metabolic functional types: ammonia-oxidizing and nitrite-oxidizing organisms (AOO and NOO, respectively). The AOO and NOO types are distinguished in two ways: a theoretically-based difference in their biomass yields with respect to DIN uptake reflecting the underlying redox reactions of the metabolisms, and a difference in affinities for NH_4^+ and NO_2^- assumed from an observed difference in cell size. We do not impose light inhibition or any other direct constraint on nitrification, and instead explore the resulting nutrient, biomass, and nitrification rate distributions that emerge as a function of the microbial metabolisms and their ecological interactions in the upper ocean.

4.3 Ecosystem model

We include an explicit representation of nitrification in the development of a simplified marine ecosystem model, with nitrogen as the currency (Fig. 4.3a). In addition to the two nitrifying metabolic functional types (as described above), the model includes a heterotrophic prokaryotic functional type that consumes sinking particulate organic matter. Its assigned growth efficiency (the open ocean average $y = 0.14$; citetRobinson2008) partitions this consumption into biomass synthesis (as y) and its remineralization into ammonium (as $y - 1$). A single phytoplankton functional type assimilates ammonium, nitrite, and nitrate into biomass with light- and nutrient-limited growth. Two zooplankton grazers, one consuming phytoplankton and another consuming heterotrophic bacteria and nitrifiers, also produce ammonium via respiration. (See Appendix 4.A.3 for all equations and parameters.)

All functional types are modeled as populations with biomass B (μmol L^{-1} N), growing

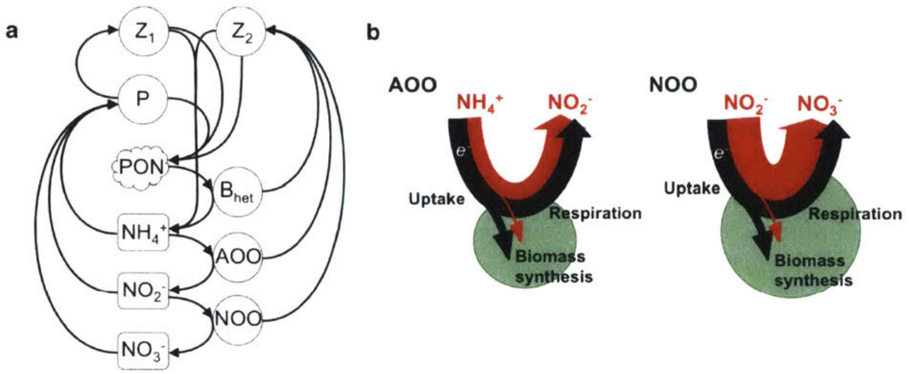

Figure 4.3: Schematics of the marine ecosystem model with explicit nitrification. (a) The microbial food web: three species of inorganic nitrogen, particulate organic nitrogen (PON), phytoplankton (P), zooplankton grazing on phytoplankton (Z_1) and bacterial types (Z_2), heterotrophic bacteria (B_{het}), ammonia-oxidizing organisms (AOO), and nitrite-oxidizing organisms (NOO). (b) The AOO and NOO metabolic functional types, illustrating their two distinctions: the higher yield of NH_4^+ vs. NO_2^- for the same production of energy, and cell size.

at rate μ (d^{-1}) with total losses L (d^{-1}) to mortality and grazing as:

$$\frac{\partial B}{\partial t} = \mu B - LB - \nabla \cdot (\vec{u}B) + \nabla \cdot (\vec{K}\nabla B) \tag{4.1}$$

where the last two terms represent advection and diffusion, respectively.

Nitrifier functional types

To parameterize nitrifier growth rates, we use a combination of observations, underlying energetic constraints, and cell size-based constraints. The growth rate μ of each nitrifier functional type is formulated as the product of its yield and the specific uptake rate (with Michaelis-Menten form) of DIN as:

$$\mu_{AOO} = y_{\mathrm{NH_4}} V_{max_{\mathrm{NH_4}}} \frac{[\mathrm{NH_4^+}]}{[\mathrm{NH_4^+}] + K_{\mathrm{NH_4}}} \tag{4.2}$$

$$\mu_{NOO} = y_{\mathrm{NO_2}} V_{max_{\mathrm{NO_2}}} \frac{[\mathrm{NO_2^-}]}{[\mathrm{NO_2^-}] + K_{\mathrm{NO_2}}} \tag{4.3}$$

Growth rate thus depends on three parameters: in general form, the yield y (mol biomass N / mol DIN), the maximum specific uptake rate V_{max} ((mol DIN / mol biomass N) d^{-1}), and the half-saturation concentration K_N. We here consider only oxygenated marine environments; we anticipate that oxygen becomes limiting to nitrifier growth at nanomolar concentrations (Bristow et al. 2016a; Zakem and Follows 2016). We next assign values for these parameters, which results in two distinctions between the two metabolisms.

First, theoretical yields are estimated using observations from previous studies as a guide. The electron-balanced equations for the two nitrifying metabolisms follow from the set of redox reactions that underlies each, as in Rittman and McCarty (2001) (Appendix 4.A.2). Ammonium serves as the electron donor for the AOO, and nitrite for the NOO, with oxygen as the terminal electron acceptor for both. The electron donor half-reactions reveal that three times more nitrite than ammonium is required to yield the same amount of electrons.

We assume both metabolisms use reduced nitrogen (i.e., the same oxidation state as ammonium or organic nitrogen) as the elemental nitrogen source. This leads to the requirement of one mole of NH_4^+ per mole biomass for the NOO below, which could result from either supplemental ammonium or organic uptake capabilities (Santoro 2016; Daims et al. 2016). This is the most realistic description of the nitrite-oxidizing population, and does not cause an ammonium dependence of the NOO population in any model solutions. This also increases the burden of proof to distinguish the two metabolisms, since no additional energy for the reduction of nitrite to the oxidation state of ammonium/organic is assumed. The electron donor half-reaction is the only difference impacting the resulting yields (see Appendix 4.A.1 for detail).

Stoichiometries of the nitrifying metabolisms are defined as a function of the fraction of electrons partitioned into biomass synthesis versus respiration. A smaller fraction equates to a lower efficiency, and thus a lower yield. Theory suggests that this fraction is very similar for the two nitrifying types (Rittman and McCarty 2001). Next, rather than estimate the magnitude of this fraction by estimating the free energies of reactions, which involves an assumption of the cumulative costs of biomass synthesis, published laboratory observations of AOO and NOO growth were used to infer it. Growth yield estimates from these data were used to compute an average yield for the AOO and the NOO groups, and then the electron fraction for each was inferred (Appendix 4.A.2). Though the list of observations that go into these averages is short, it provides two insights that allow for theoretical descriptions. First, the theoretical approach is validated because the inferred fraction is similar for the AOO and the NOO. Second, a ballpark value is provided for the fraction, which is 70% lower than predicted by the free energies and analysis of bioreactors by Rittman and McCarty (2001). This difference is not surprising, because marine organisms likely have higher affinity transport systems for the uptake of nutrients that are at concentrations orders of magnitudes lower than found in wastewater and thus require more energy.

Using the inferred average efficiency from observations, the resulting metabolisms forming ammonia-oxidizing biomass B_{AOO} and nitrite-oxidizing biomass B_{NOO} are:

$$(112 \pm 22)NH_4^+ + (5 \pm 1)CO_2 + (162 \pm 32)O_2 \rightarrow B_{AOO} + (111 \pm 22)NO_2^-$$

$$(334 \pm 67)NO_2^- + NH_4^+ + (5 \pm 1)CO_2 + (162 \pm 32)O_2 \rightarrow B_{NOO} + (334 \pm 67)NO_3^-$$

where the uncertainty results from incorporating the observed 1 mol/mol standard deviation of the C:N composition of heterotrophic marine bacteria (Zimmerman et al. 2014). This suggests that the second step of nitrification has a significantly lower yield than the first: average yields are $y_{NH_4} = 1/112$ and $y_{NO_2} = 1/334$ moles biomass N synthesized per mole DIN utilized. This distinction between the two metabolisms directly and solely reflects the electron donor half-reactions. The theoretical nitrite oxidizer requires three times as much nitrite to produce a unit of biomass, relative to the amount of ammonium the ammonia oxidizer requires to produce a unit of biomass. This differential in yield is consistent across variations in the electron fraction and the energetics of biomass synthesis (see Appendix 4.A.2). In real organisms, we expect wide variation of these stoichiometries due to variation in efficiency, biomass composition, energies of synthesis, and some versatility of metabolism, but hypothesize that the broad pattern, the significantly higher demand for nitrite than ammonium for the same amount of growth, remains.

Second, we hypothesize a difference in affinity for DIN between smaller ammonia-oxidizing archaea and larger nitrite-oxidizing bacteria. We assume $K_{NH_4} = 130$ nM from the laboratory data of Martens-Habbena et al. (2009), and constrain a plausible range for $V_{max_{NH_4}}$ with conversion from the maximum cellular nitrification rate measured by Martens-Habbena et al. (2009) and *in situ* observations (Appendix 4.A.2). The uncertainty of these parameters limits the quantitative predictive capability of the model; a larger V_{max} increases the competitive ability of the nitrifiers against phytoplankton (Appendix 4.A.4). In the illustrated models, we assume a constant $V_{max_{NH_4}} = 120$ mol NH_4^+ / mol biomass N d^{-1} at 20°C, which was tuned to simulate the distribution of the global water column maximum nitrite concentrations from GLODAPv2 (Fig. 4.6c).

We use allometry to assign the relative uptake parameters for the NOO. We assume a 10-fold larger cell volume for NOO, based on the minimum 10-fold difference in protein content between AOO and AOB measured by Martens-Habbena et al. (2009). Allometric theory predicts that the specific uptake rate should decrease with an increase in cell size due to a reduced surface to volume ratio, scaling as r^{-1}, and that K_N should increase, scaling as r. Together, this suggests a 4.6-fold lower specific affinity (V_{max}/K_N) of the NOO (Appendix 4.A.2).

The two distinctions between the resulting AOO and NOO types (summarized visually in Fig. 4.3b) both serve as mechanisms for the decoupling of the two steps of nitrification, and both suggest that AOO are better competitors for NH_4^+ than NOO are for NO_2^-. We do not consider mixotrophic growth and other metabolic versatility since a comprehensive understanding of these processes is lacking, though such capabilities could decouple the two steps further.

Nitrification in the model is a function of nitrifier growth and respiration. The yields partition the uptake of NH_4^+ and NO_2^- is into biomass synthesis versus respiration and excretion back into the water column in its more oxidized form. For example, nitrite accumulates and depletes due to nitrifier respiration and phytoplankton assimilation as:

$$\frac{D[NO_2^-]}{Dt} = (\frac{1}{y_{NH_4}} - 1)\mu_{AOO}B_{AOO} - \frac{1}{y_{NO_2}}\mu_{NOO}B_{NOO} - V_{NO_2}P \tag{4.4}$$

where the substantial derivative notation D/Dt includes physical transport. The other nitrogen pools are similarly accumulated and depleted (Appendix 4.A.3). Since yields are $\ll 1$, the rates of uptake of NH_4^+ or NO_2^- by nitrifiers are approximately the ambient nitrification rates.

Model of physical environment

We develop an idealized 2000m water column model environment, where light, mixing, and sinking organic matter decouple surface and deep microbial activity (see Appendix 4.A.3 for detail). Enhanced vertical mixing at the surface simulates the mixed layer, which decays to a minimum with a prescribed length scale. Light energy attenuates with depth due to water and biomass shading. One pool of organic matter is resolved with a constant sinking rate.

To explore the model in a variety of more realistic physical marine environments, we include the microbial functional types in a global biogeochemical model that uses the ECCO-GODAE state estimation of ocean circulation (Wunsch and Heimbach 2007). The model couples the nitrogen cycle to cycles of carbon, phoshorus, iron, and silica. Building upon previous work, we include six phytoplankton functional types and five zooplankton types (Follows et al. 2007; Dutkiewicz et al. 2015). Again, the non-photoautotrophic populations are grazed on by a single zooplankton population. Additional anaerobic metabolic types become favorable metabolisms in the model once oxygen is sufficiently depleted, assuming a diffusive limitation to aerobic growth (Zakem and Follows 2016) (more detail in Appendix 4.A.3). This results in nitrite accumulation in anaerobic zones to micromolar concentrations; examining this secondary maximum is beyond the scope of this study, but we do consider below whether this nitrite reaches aerobic waters due to mixing or other transport.

Subsistence concentrations

R^* is the minimum concentration of a resource required to sustain a particular population in its environment, according to resource ratio theory (RRT) (Tilman 1982). R^* translates the metabolic and kinetic characteristics of the functional types into ambient nutrient concentrations. For the nitrifiers, R^* is a function of the yield and uptake parameters. R^* concentrations also indicate competitive ability: if two populations compete for the same resource, the population with the lower R^* can competitively exclude the other. Application of RRT to nitrification is not new: Bellucci et al. (2015) use it for insight into the coexistence of multiple species of ammonia oxidizing bacteria in bioreactors.

To analyze the model results, we calculate these subsistence concentrations of ammonia and nitrite for the ammonia-oxidizing, nitrite-oxidizing, and phytoplankton functional types. In a steady-state environment, the growth of population described by Eqn. 4.1 will approximate loss rates as $\mu B = LB$. The subsistence concentrations for the two nitrifying populations result from defining μ with Eqns. 4.2 and 4.3, and solving for the steady-state NH_4^+ and NO_2^- concentrations as:

$$R^*_{\mathrm{NH_4}AOO} = \frac{K_{\mathrm{NH_4}} L}{y_{\mathrm{NH_4}} V_{max_{\mathrm{NH_4}}} - L} \tag{4.5}$$

$$R^*_{\mathrm{NO_2}NOO} = \frac{K_{\mathrm{NO_2}} L}{y_{\mathrm{NO_2}} V_{max_{\mathrm{NO_2}}} - L} \tag{4.6}$$

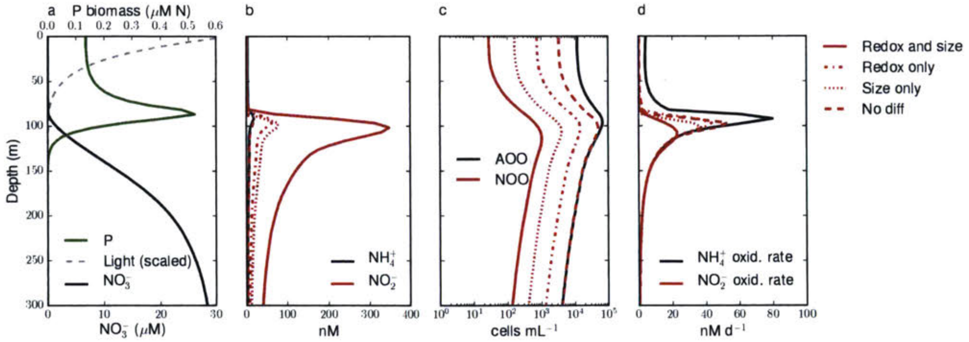

Figure 4.4: Water column model solution: (a) phytoplankton, light (scaled), and nitrate concentration. (b) ammonia and nitrite concentrations, (c) nitrifier abundances, and (d) nitrification rates. Also shown are the results when the model does not include one or both of the two factors that distinguishing the two nitrifier metabolisms: the redox-based difference in N demand and the size-based difference in uptake kinetics.

The R^* concentrations of the phytoplankton type are:

$$R^*_{\mathrm{NH_4}P} = \frac{K_{\mathrm{NH_4}P}L}{\mu_{max} - L} \tag{4.7}$$

$$R^*_{\mathrm{NO_2}P} = \frac{K_{\mathrm{NO_2}P}L}{\mu_{max} - L} \tag{4.8}$$

where maximum growth rate μ_{max} and half-saturation constants (K) for phytoplankton are those used for picoplankton by (Follows et al. 2007), based on literature data (listed in Appendix 4.A.3). We expect that the loss rates L for phytoplankton should be about an order of magnitude larger than those of the nitrifiers, given that phytoplankton grow at about an order of magnitude faster than bacteria in the ocean (Kirchman 2016).

4.4 Water column process model results

A PNM emerges in the steady-state water column model solution as a function of the interactions between the metabolic functional types and the environment (Fig. 4.4). Phytoplankton biomass reaches a peak concentration at the base of the euphotic zone. NO_2^-, nitrifier abundances, and nitrification rates peak below this DCM with no light-inhibition imposed. Model results are similar when resolving a daily light cycle (Appendix 4.A.4): surface nitrification does not occur during nightly inhibition of phytoplankton activity because of the longer (weekly) timescales of nitrifier growth.

Two factors distinguish the two steps of nitrification in the model – the redox chemistry-based metabolisms, and the size-based uptake kinetics – and as a consequence of both, NO_2^- accumulates at depth (Fig. 4.4b). In the illustrated version of the model, NO_2^- concentrations peak at 60-80 nmol L^{-1} due to each of these two factors alone, and 350 nmol L^{-1}

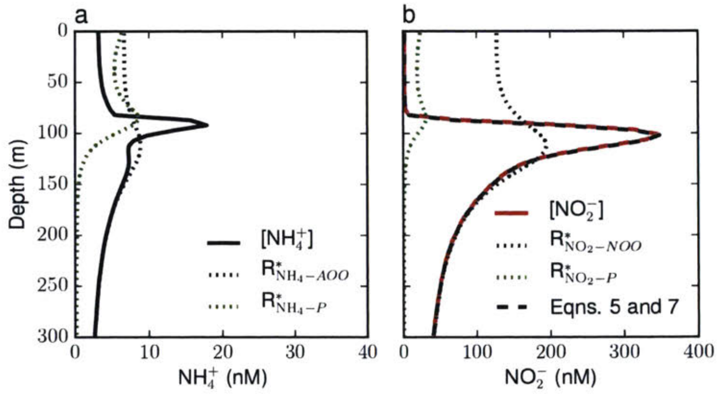

Figure 4.5: Water column model NH_4^+ and NO_2^- concentrations compared to computed steady state balances: R^* concentrations for nitrifiers and phytoplankton, and $NO2_{SS}$ (Eqn. 4.11) derived from the steady-state balance for nitrate.

together, over 10x higher than NH_4^+ concentrations. Without any distinction between the AOO and NOO, nutrient concentrations and nitrifier abundances are essentially identical at and below the PNM for each of the two steps. In contrast, the rates of both ammonia and nitrite oxidation are identical below the PNM regardless of the differences.

Redox chemistry and uptake kinetics cause nitrite accumulation at depth

R^* analysis identifies why nitrite accumulates to a higher concentration than ammonium in the model. The two distinctions between the two nitrifying functional types – yield and affinity differences – result in a higher $R^*_{NO_2}$ of the nitrite oxidizers than the $R^*_{NH_4}$ of the ammonia oxidizers (Fig. 4.5). Thus, the NOO are unable to deplete nitrite to as low of a concentration as the AOO are able to deplete ammonium. When these metabolic constraints are the same, nitrite and ammonium concentrations are identical (Fig. 4.4b).

Nitrifier abundances also reflect the two metabolisms (Fig. 4.4c). The NOO sustains 4.5 times less biomass than the AOO due to the lower yield for nitrite oxidation. The assumption of the 10-fold difference in cell volume results in an additional 10-fold lower cell count for the NOO, although the difference in affinity negligibly effects total biomass. The NOO access the same total amount of DIN at depth, just more slowly. Together, the model shows 50x higher cell count for AOO than NOO. Observations of AOO and NOO cell abundances suggest NOO is consistently 4–5-fold lower less abundant than AOO (Mincer et al. 2007; Santoro et al. 2010), which we discuss further below.

In contrast, nitrification rates are indistinguishable below the PNM (Fig. 4.4d). The decoupling of the two steps of nitrification due to the differences in the functional types emerges in the nutrient distributions and organism abundances, but not in the deep bulk nitrification rates. This result is consistent with the lack of a pattern of differences in observed rates (Ward 2008). It reflects that the flux of sinking organic matter ultimately limits all steps in the sequence of remineralization metabolisms below the euphotic zone.

Ecological dynamics set the location of the PNM

Phytoplankton subsistence concentrations of DIN are almost always lower than those of the nitrifiers. This articulates the mechanism for the exclusion of nitrification at the surface: phytoplankton will outcompete nitrifiers when both populations are limited by NH_4^+ or NO_2^-. At depth, phytoplankton are light-limited, and nitrifiers can access the DIN and sustain their populations.

Below about 125m, both NH_4^+ and NO_2^- almost exactly match the R^*s of the nitrifiers: this indicates that these concentrations are under strict nitrifier control. From the surface to about 80m, NH_4^+ and NO_2^- are below the respective phytoplankton R^*s: though DIN limits phytoplankton growth, mixing of cells up from the DCM allows for further depletion. In between (about 80–125m), NH_4^+ and NO_2^- are greater than all R^* concentrations, signifying that transport exerts significant control on DIN concentrations there.

The model suggests that phytoplankton and nitrifiers are close competitors for DIN. $R^*_{NH_4}$ concentrations for phytoplankton and ammonia-oxidizers reach similar values throughout the euphotic zone in Fig. 4.5, but the choice of grazing parameterization affects the degree of this similarity; increasing the grazing pressure on the nitrifiers further lowers their R^*s (Appendix 4.A.4). This uncertainty limits the quantitative predictive capability of the model; we cannot conclude the precise depth above which nitrification is excluded from the surface.

Though nitrification rates peak at depth, ammonia oxidation also occurs in the surface at low rates (Fig. 4.4d). Physical transport sweeps cells away from areas of sustainable growth, and supplies these cells at rates faster than their mortality rates. This allows for a small population of "unsustainable" AOO in the surface. This exemplifies how dispersal can increase biodiversity by preventing complete competitive exclusion (Clayton et al. 2013). This dispersal in the model is a function of the vertical mixing scheme, and so emphasizes the role that mixing plays in allowing varying degrees of favorable surface nitrification.

Why don't NOO also populate the surface? We find that differences in the supply of ammonium and nitrite also decouple the two steps of nitrification near the surface. Transient AOO are able to utilize a share of the supply of ammonia from zooplankton and heterotrophic bacteria populations (Appendix 4.A.4). These fluxes of NH_4^+ are larger than that of NO_2^- in the model euphotic zone. This explains why the modeled ammonia oxidation rate is higher than the nitrite oxidation rate at shallower depths, even for the case where there is no other distinction between the two metabolisms.

4.5 What controls the magnitude of the PNM?

Though R^* concentrations explain why NO_2^-, and not NH_4^+, consistently accumulates, NO_2^- concentrations are much higher than R^*. This indicates that transport processes are non-negligible in setting the magnitude of the PNM. How can we understand this peak concentration?

First, we consider the influence of physical transport on R^* by including the advective and diffusive fluxes in the equation for NOO biomass (Appendix 4.A.3; Eqn. S6). We again solve for $\mathrm{NO_2^-}$ at steady state, which we term $\bar{R}^*$, as:

$$\bar{R}^*{}_{\mathrm{NO_2}NOO} = \frac{K_{\mathrm{NO_2}}(L - \frac{1}{B_{NOO}} J_{B_{NOO}})}{y_{\mathrm{NO_2}} V_{max_{\mathrm{NO_2}}} - (L - \frac{1}{B_{NOO}} J_{B_{NOO}})} \tag{4.9}$$

where $J_{B_{NOO}}$ represents both advection and diffusion of biomass ($J_{B_{NOO}} = -\nabla \cdot (\vec{u} B_{NOO}) + \nabla \cdot (\vec{K} \nabla B_{NOO})$. This expression does not neglect any terms in the model, and so exactly predicts the resulting nitrite concentration. Conceptually, it signifies that the steep gradient in NOO at depth fuels a diffusive flux of cells away from the PNM, increasing the subsistence concentration from R^* to $\bar{R}^*$. At the PNM, the NOO cannot sustain a population large enough to draw down $\mathrm{NO_2^-}$ to the original R^*.

We examine an alternative balance for the concentration of $\mathrm{NO_2^-}$, derived from the fluxes of $\mathrm{NO_3^-}$, that includes the effects of transport and phytoplankton as well as nitrifiers and so predicts the $\mathrm{NO_2^-}$ concentration throughout the water column. For a steady-state environment, defined as such when the change in total $\mathrm{NO_3^-}$ concentration is small relative to its fluxes, three $\mathrm{NO_3^-}$ fluxes should be in balance: production by NOO, assimilation by phytoplankton ($V_{NO_3}P$), and physical transport (Appendix 4.A.3; Eqn. S3). Substituting in the expression for the $\mathrm{NO_2^-}$-dependent growth rate (Eqn. 4.3) gives:

$$0 = V_{max_{NO_2}} \frac{\mathrm{NO_2^-}}{\mathrm{NO_2^-} + K_{NO_2}} B_{NOO} - V_{NO_3}P + J_{\mathrm{NO_3}} \tag{4.10}$$

where $J_{\mathrm{NO_3}}$ represents both advection and diffusion of nitrate ($J_{\mathrm{NO_3}} = -\nabla \cdot (\vec{u}\mathrm{NO_3^-}) + \nabla \cdot (\vec{K}\nabla \mathrm{NO_3^-})$). Rearranging gives:

$$\mathrm{NO2}_{SS} = \frac{K_{NO_2}(V_{NO_3}P - J_{\mathrm{NO_3}})}{V_{max_{NO_2}} B_{NOO} - (V_{NO_3}P - J_{\mathrm{NO_3}})} \tag{4.11}$$

This steady-state $\mathrm{NO_2^-}$ concentration varies with three factors: the 'potential' for nitrite oxidation as set by NOO biomass and its affinity, the assimilation of $\mathrm{NO_3^-}$ by phytoplankton, and the physical supply or removal of $\mathrm{NO_3^-}$ due to advection and diffusion.

Like $\bar{R}^*$, the balance still reflects the metabolic constraints of the nitrite-oxidizing functional type. $\mathrm{NO2}_{SS}$ is negatively correlated with the NOO affinity: lower $V_{max_{NO_2}}$ and higher K_{NO_2} give a higher $\mathrm{NO2}_{SS}$. Unlike $\bar{R}^*$, the yield is reflected implicitly: a lower yield results in less NOO biomass and a higher $\mathrm{NO_2^-}$ concentration.

The balance reveals how phytoplankton activity and ocean circulation are crucial to setting the PNM. Phytoplankton assimilation and transport of $\mathrm{NO_3^-}$ appear in Eqn. 4.11 as two fluxes that are summed. This may be a relatively small sum: if phytoplankton assimilate nearly all of the physically supplied $\mathrm{NO_3^-}$, $\mathrm{NO_2^-}$ will approximate zero concentration. This characterizes the surface ocean.

If phytoplankton cannot assimilate NO_3^- because they are light-limited, NO_3^- may be transported away from that location ($J_{NO_3} < 0$), which contributes to a high NO_2^- concentration in Eqn. 4.11. This occurs in the water column model at the PNM. At the onset of the nitricline, just below the zone where phytoplankton consume nitrate, the accumulation of nitrate from nitrite oxidation maintains a steep gradient, which fuels a constant upward diffusive flux of NO_3^-. This upward flux of NO_3^- correlates with the accumulation of NO_2^- beyond R^*.

Alternatively, if phytoplankton assimilate more NO_3^- than is provided by physical supply, that signifies that the source of that NO_3^- is localized nitrite-oxidation, rather than an influx from another location. This effect alone would contribute to a higher NO_2^- concentration according to Eqn. 4.11, although if this is the case, the biomass of nitrite oxidizers may also be relatively high, which would contribute to a lower NO_2^- concentration.

At some distance below the PNM, in the thermocline, the physical supply of NO_3^- becomes less significant, and control of the NO_2^- concentration transitions to the nitrite-oxidizers: NO_2^- is predicted by the original R^*. Does this transition have any significance in understanding the double-peaked character of the PNM in some locations? This sets up a plausible framework for interpreting the upper and lower primary nitrite maximums described by Dore and Karl (1996b) at Station ALOHA. The water column model does show a change in concavity where the nitrite-oxidizer control sets in; including different classes and speeds of sinking organic matter or more mechanistic thermocline dynamics in a similar model may provide further insight.

Interestingly, phytoplankton excretion of NO_2^- would not enter into Eqn. 4.11 directly. Rather, we might expect that the impact of excessive NO_3^- reduction by phytoplankton would emerge implicitly as a lower phytoplankton biomass. Thus the balance holds for all sources of NO_2^-, including both ammonia oxidation and nitrate reduction.

4.6 Global simulations

Like the water column model, the global simulation results in peak NO_2^-, nitrifier abundance, and nitrification rates at depth (Appendix 4.A.5). It also captures the observed deviation from this pattern at high latitudes: the annually averaged simulation of the PNM is consistent with the three transects from the GLODAPv2 database (Fig. 4.1; Key et al. 2015; Olsen et al. 2016). Like the observations, the modeled PNM roughly tracks the depth of the mixed layer zone, and transitions poleward of about $\pm 45^o$ latitude into the broader accumulation of NO_2^- throughout the top few hundred meters.

The maximum water column NO_2^- concentrations and nitrification rates match broad global patterns (Fig. 4.6a-b; Fig. 4.7a): water column NO_2^- generally correlates with primary production (Appendix 4.A.5), reaching higher concentrations in upwelling zones and at high latitudes. This is consistent with the observations of Santoro et al. (2013) over the gradient in productivity across the California Current, and reflects that deep nitrification rates ultimately depend on surface production above as the source for reduced nitrogen substrate. The range in the maximum water column nitrification rate (annually averaged) is consistent with the order 10–100 nmol L^{-1} d^{-1} range of many marine nitrification rate measurements listed by Ward (2008).

The dataset shows a large area of much higher nitrite concentrations in the equatorial Pacific than the model predicts in oxygenated waters. In Fig. 4.6, we illustrate only the points where oxygen concentration is > 10 μM. In the model, anaerobic activity results in high nitrite (> 1 μM) – the secondary nitrite maximum – where oxygen is sufficiently low (in the nanomolar range), even though anaerobic activity within particles, not represented in this model, can occur when ambient oxygen is at tens of μM (Kalvelage et al. 2011; Penn et al. 2016). However, in the dataset, such high nitrite concentrations also occur well above 50 μM; Fig. 4.6a appears the same when plotted with this threshold. This observed nitrite accumulation could suggest that nitrate-reduction occurs inside particles at much higher oxygen concentrations than previously thought. On the other hand, this could suggest an unaccounted-for difference in aerobic nitrifier activity, or another microbial process, in the equatorial Pacific.

The global simulation predicts significant nitrite oxidation to nitrate in the mixed layer at high latitudes, up to about 20 nM d^{-1} as an annual average at the surface (Fig. 4.7b; Appendix 4.A.5). Surface ammonia oxidation rates are much higher than nitrite oxidation rates in the model; in Appendix 4.A.5, we use the net biological production rate (Clayton et al. 2013) to show that almost all of this annually averaged surface ammonia oxidation is transient, as in the 1D water column model, and its presence is dependent on the grazing parameterization as well as growth parameter values (Appendix 4.A.4). The model results of Preheim et al. (2016) also show significant ammonia oxidation rates at the surface of a lake, which is in contrast with observations there.

The predictions of high latitude nitrification are consistent with the observations of Cavagna et al. (2015) in the mixed layer in the Southern Ocean, though those rates, measured during a bloom, reach 1 μM d^{-1}. Model rates are higher and surface coverage is broader in the early winter in both hemispheres (Appendix 4.A.5), though the S. Ocean shows significant surface nitrification throughout the model year. With seasonal resolution, surface nitrite-oxidation is a sustainable metabolism in many locations, rather than solely an effect of physical transport (Appendix 4.A.5).

The global model results lead to the general hypothesis that nitrification can be favorable at the surface when phytoplankton growth is limited by light, iron, or anything other than nitrogen. The seasonal pattern in the results suggests that the competition between phytoplankton and nitrifiers is relevant over seasonal cycles as well as over depth, as phytoplankton growth becomes more light-limited in the winter. Results show that surface nitrification is higher in high-nutrient, low-chlorophyll (HNLC) regions, where competition with phytoplankton is reduced due to iron limitation, and thus DIN accumulates in the surface and is available to nitrifiers.

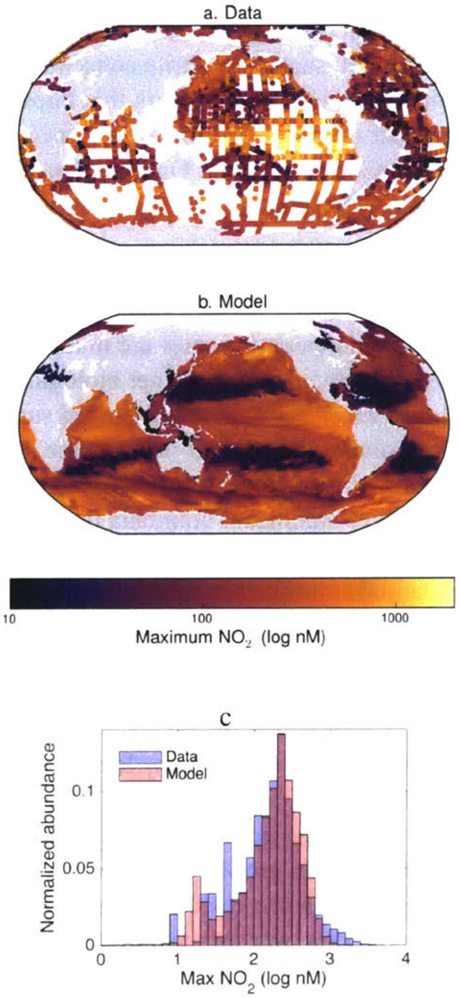

Figure 4.6: The maximum concentration of NO_2^- in the water column, (a) from the GLODAPv2 database for all observations, and (b) from the annually averaged 3D simulation, and (c) distributions of both. GLODAPv2 data: Key et al. (2015); Olsen et al. (2016)

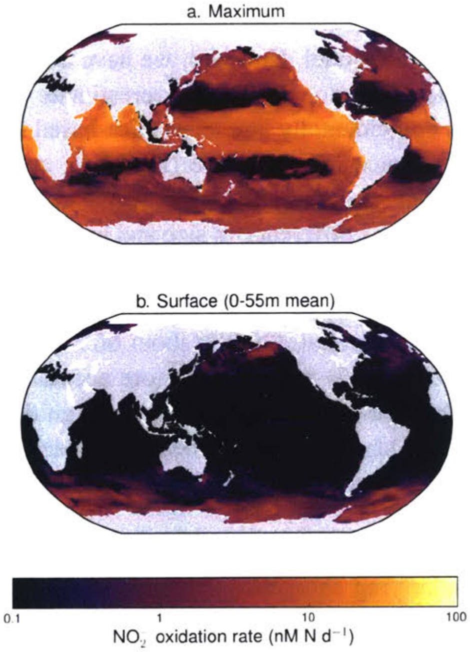

Figure 4.7: Annually averaged (a) maximum and (b) surface (0-55m mean) nitrite oxidation rate in the water column in the 3D simulation.

4.7 Comparison with observed abundances

Observed differences in AOO and NOO abundances serve as evidence, in addition to nitrite accumulation, of the distinctions between the nitrifying types. Across the California Current, Santoro et al. (2010) find a four-fold difference in the abundances of ammonia-oxidizing Marine Group 1 (MG1) (*Thaumarchaea*) and nitrite-oxidizing *Nitrospina*. They also find that abundances of *amoA* gene copies are 1–5 times higher than MG1, suggesting the potential for up to 20-fold difference in cell count in some locations. In Monterey Bay, Mincer et al. (2007) find a 1–5-fold lower abundance of *Nitrospina*-like bacteria compared to *amoA* gene and MG1 (thaumarchaeal) abundances: at each of four profiles, the difference reached at least a factor of three, but no more than six. Mincer et al. (2007) also show a 1–4-fold difference at Station ALOHA.

These observed differences between the two nitrifier types are much less than the resulting 50-fold difference in the model. However, we have no means to speculate whether the model overestimates the difference due to an overestimate of the distinctions in yield, cell size, or both. Perhaps coincidentally, the energetics-based distinction alone shows an approximately 4.5-fold difference in abundance (Fig. 4.4), approximating observed differences. Can energetics alone cause the decoupling? We considered this scenario in the global simulation by removing the difference in size and lowering the maximum uptake rate $V_{max_{NH_4}}$ to again simulate the observed concentrations: the resulting tuned rate of 50 (rather than 120) mol NH_4^+ / mol biomass N d^{-1} at 20°C is closer to the estimated maximum rate as measured by Martens-Habbena et al. (2009) (about 60 mol NH_4^+ / mol biomass N d^{-1}, assuming $Q_{10} = 2$; Appendix 4.A.2) and so may more accurately represent AOO affinity. Thus, it is plausible that the size-based difference is not significant in the real ocean, and that a small, high-affinity NOO type has not yet been discovered, especially since it is only within the last decade that the ubiquity of the high-affinity AOA has been appreciated (Stahl and de la Torre 2012).

On the other hand, kinetics alone may explain the decoupling. This could be the case if the difference in the underlying energetics is compensated for by the known metabolic versatility of nitrite-oxidizing organisms (Daims et al. 2016). For example, an ability to use other inorganic or organic molecules as additional sources of energy may supplement the energy acquired from nitrite oxidation, and negate the theoretical difference in yield.

4.8 A framework for marine nitrification ecology

Where does nitrification occur?

Our approach provides a framework with which to understand why nitrification rates often peak at depth, and are often, but not always, restricted from the surface. We summarize the three main factors found to control the locations of nitrification:

1. Competitive exclusion by phytoplankton. As hypothesized by Smith et al. (2014), when phytoplankton and bacteria both compete for ammonia and/or nitrite, nitrifiers lose the competition because their subsistence concentrations of DIN are higher than those of phytoplankton. This result should apply to the nitrogen-limited surface ocean, including much of the oligotrophic subtropical gyres. However, due to their high affinity, the competition between AOA and phytoplankton for NH_4^+ is close, which hypothesizes that AOA may outcompete phytoplankton in some environments even when phytoplankton are DIN limited.

2. Favorable nitrification when other factors limit primary production. When phytoplankton growth is limited by something other than DIN, nitrifiers can sustain growth. This characterizes the base of the euphotic zone and below, where phytoplankton are light-limited and DIN is typically not limiting. This may also apply to surface environments where phytoplankton are iron-limited, such as in high-nutrient, low-chlorophyll regions, and to high-latitude surface environments during winter when phytoplankton are light-limited.

3. Transient and dynamic environments sustain coexisting nitrifiers and phytoplankton. Sufficient continual supply of ammonium or nitrite, or supply of nitrifying biomass from favorable locations, prevents competitive exclusion by phytoplankton and allows nitrifiers to sustain a population. This may characterize the surface of the ocean where sufficient mixing from depth supplies nitrifying cells faster than they can die off. This also may characterize coastal areas with high nutrient injection from river runoff, the depth of the deep chlorophyll maximum, or where heterotrophic respiration supplies a sufficiently large flux of ammonium to support both populations.

In sum, we hypothesize that ecological dynamics are the predominant control on nitrification, with light as an indirect control. This is not irreconcilable with laboratory data suggesting direct light inhibition (cite again), since subsets of nitrifiers may have adapted to long-term exclusion from the surface. We find that the base of the euphotic zone is an optimal location for nitrification in stratified water columns: nitrifying chemoautotrophy is outcompeted photoautotrophy above and limited by the availability of reduced DIN, ultimately sourced from the remineralization of organic matter by heterotrophs, below.

Why does nitrite accumulate?

We identify two underlying causes for the decoupling of the two steps of nitrification, which both allow for nitrite accumulation:

1. The underlying redox chemistry of nitrifier metabolisms. Energetics suggest that nitrite oxidizers require significantly more nitrite to produce biomass relative to the amount of ammonium required by ammonia oxidizers. The minimum subsistence concentrations of ammonia and nitrite for the two groups diagnoses the mechanism of accumulation: nitrite oxidizers cannot deplete nitrite to as low of a concentration.

2. Size-based differences in affinity. Allometric theory for nutrient uptake suggests that the larger nitrite-oxidizing bacteria have a lower affinity than the smaller ammonia-oxidizing archaea. This also translates into a difference in the subsistence concentrations.

Physical transport in the environment can also play a significant role in setting the peak nitrite concentration. The simple balance that we developed for nitrite (Eqn. 4.11) incorporates this impact. However, transport influences both ammonium and nitrite concentrations: that the primary nitrite maximum is a consistent feature, while an ammonium maximum is a transient feature, suggests that transport alone cannot explain the accumulation.

4.9 Uncertainties

Results here provide the mechanisms and conditions for favorable nitrification, but do not aim to predict magnitudes or precise locations due to the uncertainty of the parameters describing the nitrifying functional types. Growth efficiencies were estimated from marine batch cultures grown in initially nutrient-rich conditions. How different are the efficiencies of cells growing in low-nutrient conditions, such as at the base of the euphotic zone? Also, estimates of in situ cell-specific nitrification rates provided necessary constraints, but what controls the variance in *in situ* maximum rates as measured by Santoro et al. (2013)? More observations of simultaneous in situ AOO, NOO, and phytoplankton activity, abundances, and physiologies could bring new patterns to light.

Additionally, how well do the theoretical AOO and NOO metabolic types represent real nitrifying populations? We make the assumption that two distinct groups of organisms are responsible for ammonia and nitrite oxidation, despite the recent discovery of both steps occurring in one organism (Daims et al. 2015; van Kessel et al. 2015). Costa et al. (2006) predicted this 'commamox' before it was observed in biofilms using the theory that the length of a metabolic pathway is optimized for ATP generation. In biofilms, growth efficiency may be optimized at the expense of growth rate, favoring a longer pathway (i.e., comammox). In contrast, growth rate may be optimized at the expense of efficiency in well-mixed systems, favoring shorter pathways (Costa et al. 2006), which supports our traditional understanding of discrete populations of nitrifers in the ocean and other aquatic environments.

However, we know that organisms can develop enzymatic machinery to overcome physiological or energetic constraints. For example, the results of Martens-Habbena et al. (2009) suggest that AOA and AOB have potentially diverged to fill different niches, with AOB having much lower affinity in comparison to AOA than just allometry would predict. We also know that real NOO, and potentially AOO as well, have diverse and versatile metabolisms, which would easily decouple their growth efficiency from that predicted by the underlying chemistry of nitrogen oxidation. Yet nitrite does accumulate, and isotopic evidence points to nitrification as its source. We therefore hypothesize two underlying mechanisms (redox chemistry and/or affinity differences) as the simplest explanations for the formation of the PNM. Future biochemical and physiological studies may further connect the dots between these mechanisms and real organisms.

4.10 Conclusions

By representing nitrification explicitly in an ecosystem, we can explain the formation of the primary nitrite maximum (PNM) by nitrifying microorganisms. Nitrifier activity is restricted to depth because of competition with phytoplankton, while nitrite accumulates to higher concentrations than ammonium because of energetic and kinetic distinctions between the two metabolisms.

The model provides a framework for understanding nitrification in marine ecosystems, and serves as a dynamic, mechanistic parameterization of nitrifying metabolisms suitable for regional and global biogeochemical studies. For example, examining the controls on aerobic nitrification within an aerobic-anaerobic microbial ecosystem may provide insight into the fate of fixed nitrogen. Also, the model articulates the dynamic base of the euphotic zone, characterized by many maximas of nutrient fluxes, and so can aid in sharpening descriptions of export production. These results further progress our understanding of the ecology of nitrification and its biogeochemical impacts.

4.A Appendix

4.A.1 Measurement locations and methods

Measurements were made in the subtropical N. Pacific on Cruise NH1417 in August and September 2014. Stations thought to be at productive locations were chosen for nitrification rate measurements using satellite data to increase changes of detectable concentrations and rates. Measurements were taken at stations 44, 58, 70, and 99; Fig. 4.8 maps their locations.

Nitrification rates, nitrite, and nitrate concentrations were measured by Emily Zakem, with support from the lab of Robinson (Wally) Fulweiler at Boston University. Two treatments were completed at each stations: 1. addition of $^{15}NH_4^+$ as a tracer to measure the rate of ammonia oxidation, and 2. addition of $^{15}NO_2^-$ to measure the rate of nitrite oxidation, but only the former was successful. Triplicate samples of each treatment were spiked to a final concentration of 100 nM, incubated for 24 hours, filtered through 0.2 μm pore-sized nylon filters, and frozen. For ammonia oxidation rate samples, thawed aliquots were treated with sodium azide to convert all of the NO_2^- to N_2O gas. (For nitrite oxidation rate samples, in situ NO_2^-- was removed with sulfamic acid. NO_3^- in the sample was then reduced to NO_2^-- using cadmium, and then samples were treated with azide to convert the resulting NO_2^- to N_2O gas.) The ^{14}N:^{15}N ratio of the N_2O gas was analyzed on an isotope ratio mass spectrometer at the University of California Davis Stable Isotope Facility. Unlabeled carrier nitrite (to 1 μM) was added to reach instrument detection limits, which introduced most of the uncertainty to the calculations as indicated by the error bars in Fig. 4.2. NO_2^-, and NO_3^- concentrations were measured using standard colorimetric techniques.

Chlorophyll *a* was measured by the Arrigo lab at Stanford Univeristy. Samples were extracted in 90% acetone for 24 hours and measured fluorometrically using the Welschmeyer protocol (1992).

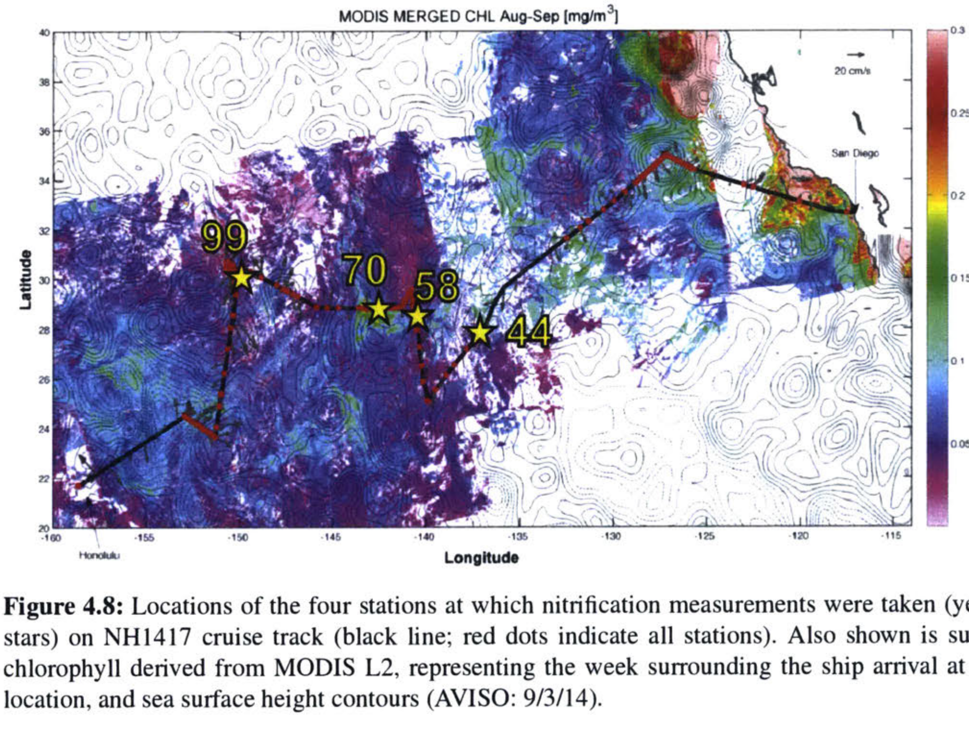

Figure 4.8: Locations of the four stations at which nitrification measurements were taken (yellow stars) on NH1417 cruise track (black line; red dots indicate all stations). Also shown is surface chlorophyll derived from MODIS L2, representing the week surrounding the ship arrival at each location, and sea surface height contours (AVISO: 9/3/14).

4.A.2 Nitrifying functional type detail

Stoichiometries

Following the methodology of Rittman and McCarty (2001), three half-reactions together combine to form the catabolic and anabolic full reactions for each nitrifier metabolism: 1. the oxidation of ammonia or nitrite, 2. the reduction of oxygen, and 3. biomass synthesis. The parameter f represents the partitioning of these reactions into biomass synthesis and respiration, and specifically represents the fraction of electrons from the electron donor that are channelled into biomass synthesis.

For the ammonia oxidizer (here considering NH_4^+ and NH_3 interchangeably), these three reactions, for generic biomass $C_cH_hO_oN_n$, and their electron-partitioning coefficients, are:

$$\begin{aligned}
(1) &\quad \left[\frac{1}{6}NH_4^+ + \frac{1}{3}H_2O \rightarrow \frac{1}{6}NO_2^- + \frac{4}{3}H^+ + e^-\right] \\
(1-f) &\quad \left[\frac{1}{4}O_2 + H^+ + e^- \rightarrow \frac{1}{2}H_2O\right] \\
(f) &\quad \left[\frac{n}{d}NH_4^+ + \frac{c-n}{d}CO_2 + \frac{n}{d}HCO_3^- + H^+ + e^- \rightarrow \frac{1}{d}C_cH_hO_oN_n + \frac{2c-o+n}{d}H_2O\right]
\end{aligned}$$

where d normalizes the biomass synthesis reaction to one electron, representing the number of electron equivalents that correspond to the oxidation states of the inorganic constituents of that synthesis (Rittman and McCarty 2001). This gives the full metabolism for ammonia-oxidizing biomass B_{AOO} when summed (ignoring water and lumping bicarbonate into the CO_2 pool for simplification in the main text), with the fraction f representing this partitioning, as:

$$\left(\frac{1}{6}+\frac{f}{d}\right)NH_4^+ + \frac{cf}{d}CO_2 + \frac{1-f}{4}O_2 \rightarrow \frac{f}{d}B_{AOO} + \frac{1}{6}NO_2^- \tag{4.12}$$

Our assumption that the nitrite oxidizer also uses reduced nitrogen (i.e., the same oxidation state as ammonium) is realistic (Santoro 2016; Daims et al. 2016), and also increases our burden of proof to distinguish the two metabolisms energetically; the only difference between the stoichiometry of the two steps is the electron donor reaction. For the nitrite oxidizer, the three reactions are:

$$\begin{aligned}
(1) &\quad \left[\frac{1}{2}NO_2^- + \frac{1}{2}H_2O \rightarrow \frac{1}{2}NO_3^- + H^+ + e^-\right] \\
(1-f) &\quad \left[\frac{1}{4}O_2 + H^+ + e^- \rightarrow \frac{1}{2}H_2O\right] \\
(f) &\quad \left[\frac{n}{d}NH_4^+ + \frac{c-n}{d}CO_2 + \frac{n}{d}HCO_3^- + H^+ + e^- \rightarrow \frac{1}{d}C_cH_hO_oN_n + \frac{2c-o+n}{d}H_2O\right]
\end{aligned}$$

which when summed (again written without water, and with CO_2 as the carbon source) gives the full metabolism nitrite-oxidizing biomass B_{NOO} as:

$$\frac{1}{2}\mathrm{NO}_2^- + \frac{f}{d}\mathrm{NH}_4^+ + \frac{cf}{d}\mathrm{CO}_2 + \frac{1-f}{4}\mathrm{O}_2 \rightarrow \frac{f}{d}B_{NOO} + \frac{1}{2}\mathrm{NO}_3^- \tag{4.13}$$

Comparing Eqns. 4.12 and 4.13 suggests that the second step of nitrification is much less efficient than the first. For any value of f, the theoretical nitrite oxidizer requires three times as much nitrite to produce a unit of biomass, relative to the amount of ammonium the ammonia oxidizer requires to produce a unit of biomass. The resulting nitrifier efficiencies, or yields y defined as moles biomass N synthesized per mole DIN utilized, are:

$$y_{NH_4} = \frac{1}{1+\frac{d}{6f}} \tag{4.14}$$

$$y_{NO_2} = \frac{2f}{d} \tag{4.15}$$

which are the parameters that we include in the ecosystem model. Since we assume in Eqn. 4.13 that the nitrite oxidizer also uses reduced nitrogen (Santoro 2016), we use the same estimate for d for both functional types: $d = 4c + h - 2o - 3n$. If we instead considered nitrite to serve as both the electron donor and the substrate for assimilation, as do Rittman and McCarty (2001), energetics would be accounted for by adjusting d from 20 to 26 (representing the change in oxidation state of the substrate for synthesis), and would further decrease the nitrite-oxidizer yield.

Estimating f from data

Theory suggests that f should be similar for the two types (Rittman and McCarty 2001). (Rittman and McCarty 2001) assume an even larger difference in f by assuming nitrite as the source for biomass nitrogen, and use free energies of reactions to estimate f as 0.14 and 0.10 for ammonia oxidizers and nitrite oxidizers, respectively. Their analysis of nitrifiers in bioreactors shows a consensus of this theory and observations (their Tables 9.1 and 9.2).

With the assumption that ammonium or organic nitrogen serves as the source for biomass nitrogen, the values of f for the AOO and NOO are much more similar; the difference in the free energy of ammonium oxidation to nitrite versus nitrite oxidation to nitrate does not impact the free energy estimate as much as the additional energy required to reduce nitrite to the oxidation state of ammonium/organic matter for synthesis (which is reflected in the above assumption of d).

We estimate the magnitude of f from observations of marine nitrifying microorganisms instead of using the free energies of reactions to estimate it theoretically. We find that our list of observations, albeit short, supports the theory that f should be similar for the two types, but suggests much lower magnitudes. In Table 1, we list the studies, the implied yields as estimated from observations of cell growth on ammonium or nitrite, and the resulting inferred value of f for each from Eqns. 4.14 and 4.15. We assume $d = 20$, representing the generic microbial biomass composition of $C_5H_7O_2N$ used by Rittman and McCarty (2001).

For most of the observations, calculating the dimensionless yield from observed cell growth requires an estimate of the cell quota of nitrogen. We use the 10 fg protein cell^{-1} content of AOA measured by Martens-Habbena et al. (2009), and assume a 10-fold larger quota for the NOO, as we do for the uptake kinetics, based on the measured minimum 10-fold difference in protein content between AOO and AOB Martens-Habbena et al. (2009). Assuming the mean composition of phytoplankton protein compiled by Anderson (1995) of $C_{3.83}H_{6.05}O_{1.25}N$, nitrogen is about 16% of protein by weight. This calculation estimates a nitrogen quota of about 0.1 and 1 fmol N cell $^{-1}$ for the AOO and NOO groups, respectively. We can also independently estimate the 10-fold larger nitrogen quota of the NOO by considering the sphereoidical volume inferred from the average size of the new marine strain of *Nitrospina* of 0.3–0.4 μm × 1–3 μm observed by Spieck et al. (2014): converting from the average bacterial carbon quota of 0.22 g C cm^{-3} of Bratbak and Dundas (1984) with a C:N of 5 also suggests a quota of order 1 fmol N cell $^{-1}$.

Even though the calculations have a large uncertainty, they justify the use of the theory that f should be similar for the AOO and NOO metabolic types, and provide a ballpark estimate of f. For the AOO and the NOO groups, the average yields are 1/135 and 1/322 moles biomass N synthesized per mole DIN utilized, respectively. The f values corresponding to these yields are 0.025 and 0.031, respectively.

For the stoichiometries presented in the main text, we assume $f = 0.03$ and $d = 20 \pm 4$. The C:N uncertainty of 1 mol/mol, the standard deviation of the C:N composition of heterotrophic marine bacteria compiled by Zimmerman et al. (2014), gives the uncertainty in d (and neglecting the changes in H and O stoichiometry for the largest impact on the resulting stoichiometric uncertainty).

Notes on the estimated yields

AOA observations: From Martens-Habbena et al. (2009), we estimated ΔDIN as the initial and end NH_4^+ concentrations and cell yield from their Fig. 1 for *Nitrosopumilus maritimus* strain SCMI. From Qin et al. (2014), used the upper limit of the reported ranges in cell yield per mole of ammonia oxidized (pg. 12507) for growth in organic carbon supplemented media for each of three strains of *Nitrosopumilus maritimus*. From Santoro and Casciotti (2011), we estimated the initial and end NH_4^+ concentrations and cell yield from their Fig. 3 for AOA strain CN75.

NOB observations: From Spieck et al. (2014), we used the reported cell yields (pg. 172) for chemolithoautotrophic growth of the new bacterium, named *Nitrospina watsonii*, and for mixotrophic growth of *Nitrospina gracilis*. From Watson and Waterbury (1971), the ratio of NO_2^- oxidized to CO_2 fixed was calculated for the results of each of the two reaction mixtures listed in their Table 2 for *Nitrospina gracilis* and *Nitrococcus mobilis*, the average taken for the reaction mixtures, and a C:N of 5 assumed for the conversion to the growth yield.

Yields for variation in parameters f and d

Figure 4.9 illustrates the DIN demand, the inverse of the yield y, as a function of f and d for the AOO and the NOO metabolic types, following Eqns. 4.12 and 4.13. The ranges of values are arbitrary but aim to represent a realistic range in parameter space. Values correspond to the range in values of f implied by the observations, and the range in d for the C:N variation of one as above. The midpoint of both ranges is that used in the illustrated model solutions ($f = 0.03, d = 20$).

This plot supports our claim that there should be a broad pattern of significantly higher demand for nitrite than ammonium for the same rate of growth of the AOO and NOO metabolic types. The yield is lowest (DIN demand highest) for low f and high d. The highest NH_4^+ demand for the AOO – about 200 moles NH_4^+ per mole biomass synthesized – is smaller than the lowest NO_2^- demand that corresponds to high values of f and low d.

Uptake kinetics

Estimating $V_{max_{NH_4}}$ Martens-Habbena et al. (2009) report $K_{NH_4} = 130$ nM and a maximum cellular rate of 0.53 fmol cell^{-1} h^{-1} (13 fmol cell^{-1} d^{-1}) at 30°C for ammonia-oxidizing archaea. Using the above assumption of a cell nitrogen quota of 0.1 fmol cell^{-1} suggests a maximum specific rate of 130 mol NH_4^+ cycled per mole biomass N per day at 30°C, or 65 at 20°C assuming a Q10 temperature-dependency of two. In comparison, *in situ* cellular rates range from 0.2 to 15 fmol cell^{-1} d^{-1} at water column temperatures, all below 20°C (Wuchter et al. 2006; Santoro et al. 2010; Santoro and Casciotti 2011). Assuming the same cell quota, this suggests that actual, not maximum, specific rates from 2 to 150 mol NH_4^+ cycled per mole biomass N per day are plausible at lower temperatures. Acknowledging its uncertainty, we assume $V_{max_{NH_4}} = 100$ mol NH_4^+ per mol biomass N per day at 20° in the model.

Allometric theory and affinity Allometric theory predicts that though the cellular uptake rate should increase with cell size, the specific uptake rate should decrease due to a decrease in the surface to volume ratio: the cellular rate scales with surface area as cell radius r^2, volume increases as r^3, and so the specific rate scales as r^{-1}. Theory also predicts that the half-saturation constant increases with cell size: the diffusion-limited cellular uptake rate, which explains the steep slope of the Michaelis-Menton form, increases as r (and so the cellular affinity increases as r). The cellular affinity equates to the quotient of the cellular uptake rate and K_N, which suggests that K_N scales as $r^2/r = r$. Together, allometry thus suggests that the specific affinity decreases with cell size as r^{-2}, which is supported by more detailed analysis of nutrient update models (Fiksen et al. 2013).

With the 10-fold difference in volume, we assume a cell radius of NOO larger than that of AOO by $10^{1/3} = 2.2$, and so for the NOO estimate a specific uptake rate of about half and a half-saturation constant of about double that of the AOO. This gives a 4.6-fold lower specific affinity (V_{max}/K_N) of the NOO.

Table 4.1: Estimated NH_4^+ and NO_2^- biomass yields from cultures, with electron fraction f calculated from Eqns. 4.14 and 4.15.

	Organism	Δ[DIN] (μM)	Cell yield $\left(\frac{10^6\text{cells}}{\text{mL}}\right)$	Cell yield $\left(\frac{10^6\text{cells}}{\mu\text{M DIN}}\right)$	Quota $\left(\frac{\text{fmol N}}{\text{cell}}\right)$	NO_2^-: CO_2	C:N	y^{-1} $\left(\frac{\text{mol DIN}}{\text{mol N}}\right)$	f
AOO:									
Martens-Habbena et al. (2009)	SCM1	850	44	52	0.1			190	
Qin et al. (2014)	SCM1			112.6	0.1			88.9	
Qin et al. (2014)	HCA1			80.8	0.1			124	
Qin et al. (2014)	PS0			70.4	0.1			142	
Santoro and Casciotti (2011)	CN75	40	3.2	80	0.1			130	
Average								**130**	**0.025**
NOO:									
Spieck et al. (2014)	*N. watsonii*			6.6	1			150	
Spieck et al. (2014)	*N. gracilis*			7.2	1			139	
Watson and Waterbury (1971)	*N. gracilis*					160	5	780	
Watson and Waterbury (1971)	*N. mobilis*					44	5	220	
Average								**320**	**0.031**

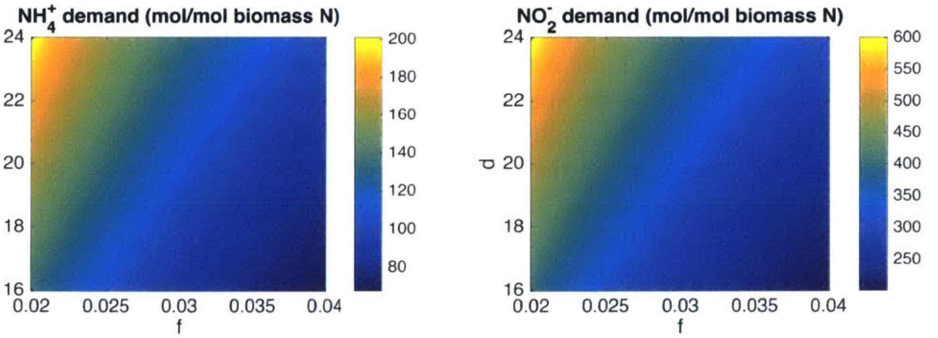

Figure 4.9: Prediction of NH_4^+ and NO_2^- demands (y^{-1}) for the AOO and NOO types, respectively, as a function of parameters f and d.

4.A.3 Ecosystem model detail

Equations

Ten state variables were conserved as concentrations of nitrogen over the domain: seven functional type populations (ammonia-oxidizers B_{AOO}, nitrite-oxidizers B_{NOO}, phytoplankton P, heterotrophic bacteria B_{het}, and zooplankton grazers Z_1 and Z_2), three inorganic nutrients (NH_4^+, NO_2^-, and NO3), and organic detritus D. Growth rates, efficiencies, and grazing rates are described below. Table 1 lists all parameters, their dimensions, and the default values used in the model.

$$(S1)\qquad \frac{D[NH_4^+]}{Dt} = -\frac{1}{y_{NH_4}}\mu_{AOO}B_{AOO} - \mu_{NOO}B_{NOO} - V_{NH_4}P + (\frac{1}{y_D} - 1)\mu_{het}B_{het} + (1-\gamma)[g_1Z_1 + g_2Z_2]$$

$$(S2)\qquad \frac{D[NO_2^-]}{Dt} = (\frac{1}{y_{NH4}} - 1)\mu_{AOO}B_{AOO} - \frac{1}{y_{NO2}}\mu_{NOO}B_{NOO} - V_{NO2}P$$

$$(S3)\qquad \frac{D[NO_3^-]}{Dt} = \frac{1}{y_{NO2}}\mu_{NOO}B_{NOO} - V_{NO3}P$$

$$(S4)\qquad \frac{DD}{Dt} = -\frac{1}{y_D}\mu_{het}B_{het} + m_B[B_{AOO} + B_{NOO} + B_{het}] + m_Z[Z_1^2 + Z_2^2] + m_PP - \frac{\partial(w_sD)}{\partial z}$$

$$(S5)\qquad \frac{DB_{AOO}}{Dt} = B_{AOO}(\mu_{AOO} - m_B - \frac{g_2Z_2}{B_{het} + B_{AOO} + B_{NOO}})$$

$$(S6)\qquad \frac{DB_{NOO}}{Dt} = B_{NOO}(\mu_{NOO} - m_B - \frac{g_2Z_2}{B_{het} + B_{AOO} + B_{NOO}})$$

$$(S7)\qquad \frac{DB_{het}}{Dt} = B_{het}(\mu_{het} - m_B - \frac{g_2Z_2}{B_{het} + B_{AOO} + B_{NOO}})$$

$$(S8)\qquad \frac{DP}{Dt} = P(\mu_P - m_P - g_1Z_1)$$

$$(S9,10)\qquad \frac{DZ_{1,2}}{Dt} = \gamma g_{1,2}Z_{1,2} - m_ZZ_{1,2}^2$$

where the substantial derivative D/Dt includes the diffusive flux as function of the diffusive coefficient K as $\nabla \cdot (\vec{K}\nabla C)$ for tracer C, and advective fluxes as functions of velocity $\vec{u}$ as $\nabla \cdot (\vec{u}C)$.

Phytoplankton growth

Phytoplankton grow as a function of DIN and light concentrations, following the approach of Follows et al. (2007), as:

$$\mu_P = \mu_{max} \min \left[\frac{I}{I + k_I}, \left(\frac{\mathrm{NH_4^+}}{\mathrm{NH_4^+} + K_{\mathrm{NH_4}P}} + \frac{\mathrm{NO_2^-}}{\mathrm{NO_2^-} + K_{\mathrm{NO_2}P}} + \frac{\mathrm{NO_3^-}}{\mathrm{NO_3^-} + K_{\mathrm{NO_3}P}} \right) \right] \tag{4.16}$$

The inhibition of nitrite and nitrate assimilation in the presence of ammonium had a negligible effect in the water column model solutions, and so was not included (though is included in the 3D model). The half-saturation constants for DIN uptake for phytoplankton are the lower limit to the range of those used by Follows et al. (2007), and so representative of the smallest phytoplankton; the water column model aims to represent the characteristics of the small picoplankton typical in oligotrophic environments. The specific rates of uptake V (d^{-1}) of each DIN species are:

$$V_{\mathrm{NH_4}} = \mu_P \left(\frac{\frac{\mathrm{NH_4^+}}{\mathrm{NH_4^+} + K_{\mathrm{NH_4}P}}}{\frac{\mathrm{NH_4^+}}{\mathrm{NH_4^+} + K_{\mathrm{NH_4}P}} + \frac{\mathrm{NO_2^-}}{\mathrm{NO_2^-} + K_{\mathrm{NO_2}P}} + \frac{\mathrm{NO_3^-}}{\mathrm{NO_3^-} + K_{\mathrm{NO_3}P}}} \right)$$

$$V_{\mathrm{NO_2}} = \mu_P \left(\frac{\frac{\mathrm{NO_2^-}}{\mathrm{NO_2^-} + K_{\mathrm{NO_2}P}}}{\frac{\mathrm{NH_4^+}}{\mathrm{NH_4^+} + K_{\mathrm{NH_4}P}} + \frac{\mathrm{NO_2^-}}{\mathrm{NO_2^-} + K_{\mathrm{NO_2}P}} + \frac{\mathrm{NO_3^-}}{\mathrm{NO_3^-} + K_{\mathrm{NO_3}P}}} \right)$$

$$V_{\mathrm{NO_3}} = \mu_P \left(\frac{\frac{\mathrm{NO_3^-}}{\mathrm{NO_3^-} + K_{\mathrm{NO_3}P}}}{\frac{\mathrm{NH_4^+}}{\mathrm{NH_4^+} + K_{\mathrm{NH_4}P}} + \frac{\mathrm{NO_2^-}}{\mathrm{NO_2^-} + K_{\mathrm{NO_2}P}} + \frac{\mathrm{NO_3^-}}{\mathrm{NO_3^-} + K_{\mathrm{NO_3}P}}} \right)$$

Heterotrophic growth

The bacterial heterotrophic functional type grows as a function of organic matter (detritus D) as:

$$\mu_{het} = y_D V_{maxD} \frac{D}{D + K_D} \tag{4.17}$$

where the growth efficiency y_D is assumed as the average bacterial growth efficiency of 0.14 for the open ocean as compiled by Robinson (2008), and the maximum uptake rate V_{maxD} is assigned as 0.7 d^{-1} to constrain the heterotrophic bacterial growth rate to about 0.1 d^{-1}, matching the average bulk bacterial growth rate estimated by Kirchman (2016).

Grazing

The rate of grazing g (d^{-1}) for each of the two zooplankton types is calculated as a function of its total prey biomass as:

$$g_1 = g_{max} \frac{P}{P + K_g}$$

$$g_2 = g_{max} \frac{B_{het} + B_{AOO} + B_{NOO}}{B_{het} + B_{AOO} + B_{NOO} + K_g}$$

where maximum grazing rate g_{max} and half-saturation k_g are estimated from the ranges of values compiled by Taniguchi et al. (2014) for small organisms.

1D model detail

In the water column model, the mixed layer was imposed by varying the vertical diffusion coefficient K_Z with depth, from a maximum of 10^{-2} $\mathrm{m}^2\ \mathrm{s}^{-1}$ at the surface to a minimum with a length scale of z_{mld}. The fixed (no flux) boundary conditions result in some accumulation of D at the bottom of the domain, conceptually representing a sediment layer. To smooth over numerical error, vertical mixing was allowed to increase there, simulating a bottom boundary mixed layer. K_Z ($\mathrm{m}^2\ \mathrm{s}^{-1}$) is thus calculated at cell faces as:

$$K_Z = 10^{-2} e^{-\frac{z}{z_{mld}}} + 10^{-5} + 10^{-2} e^{-\frac{z-H}{100}} \tag{4.18}$$

where H is the height of the domain (2000m).

Light energy I decreases with depth according to the attenuation coefficients for water k_w and for biomass k_{bio}, following the approach of Dutkiewicz et al. (2001) as:

$$I(z) = I_{in} e^{(-z(k_w + \sum_{n=1}^{z} (Bio(z) k_{Bio})))} \tag{4.19}$$

where Bio is the sum of the concentrations of microbial biomass and organic matter. I_{in} is the incoming irradiance, which is $0.5 I_{max}$, or for resolution of the daily cycle, $I_{in}(t) = 0.5 I_{max}(\cos(2\pi t) + 1)$.

A temperature curve was fit to the mean observations from the four stations sampled on cruise NH1417, with linear and exponential curves as:

$$T(z) = \max((25 - z)/18, (12e^{z/150} + 12e^{z/500} + 2)) \tag{4.20}$$

with which the temperature-dependence of all microbial growth, grazing, and mortality rates was represented with a Q10 of two. The temperature-dependencies have a small but non-negligible effect, slowing microbial rates with depth and so altering the solutions quantitatively but not qualitatively.

The illustrated domain was 2000 m in height, with 5m resolution. Equations were integrated forward in time using the 4th order Runge–Kutta method. Advection was carried out using the QUICK advection scheme, consisting of a linear interpolation between points weighted by an upstream 2nd order curvature, resulting in 3rd order accuracy. Fluxes were calculated at the faces of each grid cell, and concentrations at the centers.

3D model detail

Nine microbial metabolic functional types are included in the global ecosystem model, and are responsible for all organic matter remineralization, nitrification, and denitrification. Particulate and dissolved organic matter (POM and DOM) are consumed and subsequently remineralized by two aerobic heterotrophic bacterial functional types, two nitrate-reducing ($NO_3^- \rightarrow NO_2^-$) heterotrophic types, and two denitrifying ($NO_2^- \rightarrow N_2$) heterotrophic types. A 'sloppy feeding'-like parameterization provides a source of DOM as a function of the uptake of POM: according to parameter α, POM is taken up by the particle-associated bacterial types in excess to what is incorporated into biomass or remineralized via respiration (a factor of α more than is required), and the remainder ($\alpha - 1$) is converted into DOM. This parameterization crudely mimicks the hydrolysis of high-molecular-weight organic molecules by extracellular enzymes excreted by heterotrophic bacteria. The particulate-associated types sink at the same rate as the particulate organic matter.

The depletion of oxygen and switch from aerobic to anaerobic respiration occurs dynamically in the model, following the parameterization of Zakem and Follows (2016), with organic matter growth efficiency (y_{OM}; Eqn. 4.22 below) of 0.14 moles biomass N per mole uptake PON or DON for the aerobic types (Robinson 2008). The organic matter yield for the anaerobic types is assigned at 0.13; the lower yield results in the competitive exclusion of the anaerobic heterotrophs in oxygenated environments, as in Chapter 3.

C:N:P:Fe stoichiometries of bacterial types and demands are constant, as the stoichiometries of average marine organic matter (Anderson 1995). The two nitrifier types are identical to those in the water column model. The anammox type ($NH_4^+ + NO_2^- \rightarrow N_2$) is excluded from oxygenated environments by the aerobic ammonia-oxidizer because of its higher demand for ammonium; its stoichiometry is similarly calculated from the underlying redox chemistry, with ammonium as the electron donor and nitrite as the electron acceptor, and results in very similar stoichiometry to that reported by (Strous et al. 1998) for anammox bacteria.

The stoichiometries, developed analogously to the nitrifiers, for these additional metabolic functional types are as follows:

Aerobic heterotrophy Organic matter (OM) provides the elements and electrons for both the synthesis of biomass (B) and energy production, and oxygen serves as the electron acceptor.

$$\begin{aligned} &\frac{1}{d_{OM}} C_{c_{OM}} H_{h_{OM}} O_{o_{OM}} N_{n_{OM}} + \frac{1-f}{4} O_2 \\ &\rightarrow \quad \frac{f}{d_B} C_{c_B} H_{h_B} O_{o_B} N_{n_B} + \left(\frac{c_{OM}}{d_{OM}} - \frac{c_B f}{d_B} \right) CO_2 + \left(\frac{n_{OM}}{d_{OM}} - \frac{n_B f}{d_B} \right) NH_4^+ \end{aligned} \quad (4.21)$$

where d is the number of electron equivalents for generic organic matter stoichiometry $C_cH_hO_oN_n$ that correspond to the oxidation states of its inorganic constituents (below as $d = 4c + h - 2o - 3n$).

The growth efficiency (mol B mol $^{-1}$ OM, or, mol C synthesized mol $^{-1}$ C consumed) relates to f as:

$$y_{OM} = \frac{d_{OM}}{d_B} f \tag{4.22}$$

and so $y_{OM} = f$ when assuming the same stoichiometry for both the organic matter substrate and microbial biomass. When assuming the average stoichiometry of marine organic matter ($C_{106}H_{175}O_{42}N_{16}$; Anderson 1995) for both the organic matter substrate and microbial biomass, the full metabolism is represented as:

$$\begin{aligned} &C_{106}H_{175}O_{42}N_{16} + \frac{467(1-y_{OM})}{4} O_2 \\ &\quad \rightarrow \quad y_{OM}C_{106}H_{175}O_{42}N_{16} + 106(1-y_{OM})CO_2 + 16(1-y_{OM})NH_4^+ \end{aligned} \tag{4.23}$$

Nitrate-reducing heterotrophy For the nitrate reducer, organic matter (OM) provides the elements and electrons for both the synthesis of biomass (B) and energy production, and nitrate serves as the electron acceptor, which is reduced to nitrite. The full metabolism forming nitrate-reducing biomass B_{HetNO_3} is:

$$\begin{aligned} &\frac{1}{d_{OM}} OM + \frac{1-f}{2} NO_3^- \\ &\quad \rightarrow \quad \frac{f}{d_B} B_{HetNO_3} + \left(\frac{c_{OM}}{d_{OM}} - \frac{c_B f}{d_B}\right) CO_2 + \left(\frac{n_{OM}}{d_{OM}} - \frac{n_B f}{d_B}\right) NH_4^+ + \frac{1-f}{2} NO_2^- \end{aligned} \tag{4.24}$$

For marine stoichiometry, the full metabolism is:

$$\begin{aligned} &C_{106}H_{175}O_{42}N_{16} + \frac{467(1-y_{OM})}{2} NO_3^- \\ &\rightarrow \quad y_{OM}C_{106}H_{175}O_{42}N_{16} + 106(1-y_{OM})CO_2 + 16(1-y_{OM})NH_4^+ + \frac{467(1-y_{OM})}{2} NO_2^- \end{aligned} \tag{4.25}$$

Denitrifying heterotrophy For the denitrifier, organic matter (OM) provides the elements and electrons for both the synthesis of biomass (B) and energy production, and nitrite serves as the electron acceptor, which we consider here as all being reduced completely to N_2 (here neglecting the formation of N_2O). The full metabolism forming denitrifying biomass B_{HetNO_2} is:

$$\begin{aligned} &\frac{1}{d_{OM}} OM + \frac{1-f}{3} NO_2^- \\ &\quad \rightarrow \quad \frac{f}{d_B} B_{HetNO_2} + \left(\frac{c_{OM}}{d_{OM}} - \frac{c_B f}{d_B}\right) CO_2 + \left(\frac{n_{OM}}{d_{OM}} - \frac{n_B f}{d_B}\right) NH_4^+ + \frac{1-f}{6} N_2 \end{aligned} \tag{4.26}$$

For marine stoichiometry, the full metabolism is:

$$
\begin{aligned}
&C_{106}H_{175}O_{42}N_{16} + \frac{467(1-y_{OM})}{3}NO_2^- \\
\rightarrow\quad & y_{OM}C_{106}H_{175}O_{42}N_{16} + 106(1-y_{OM})CO_2 + 16(1-y_{OM})NH_4^+ + \frac{467(1-y_{OM})}{6}N_2
\end{aligned}
\tag{4.27}
$$

The difference in stoichiometry for the DIN demand and excretion between the nitrate-reducer and denitrifier results in the accumulation of nitrite in the water column where both steps of anaerobic heterotrophy occur.

Anammox For chemoautotrophic anaerobic ammonium oxidation, ammonium oxidation to elemental N provides electrons for energy that fuels cell synthesis (here considering NH_4^+ and NH_3 interchangeably), and nitrite serves as the electron acceptor. Together, elemental N_2 is formed. The three half-reactions are:

$$
\begin{aligned}
&(1) && \left[\frac{1}{3}NH_4^+ \rightarrow \frac{1}{6}N_2 + \frac{4}{3}H^+ + e^-\right] \\
&(1-f) && \left[\frac{1}{3}NO_2^- + \frac{4}{3}H^+ + e^- \rightarrow \frac{1}{6}N_2 + \frac{2}{3}H_2O\right] \\
&(f) && \left[\frac{n}{d}NH_4^+ + \frac{c-n}{d}CO_2 + \frac{n}{d}HCO_3^- + H^+ + e^- \rightarrow \frac{1}{d}C_cH_hO_oN_n + \frac{2c-o+n}{d}H_2O\right]
\end{aligned}
$$

which gives the full metabolism forming anammox biomass B_{anx} when summed as:

$$
\left(\frac{1}{3}+\frac{f}{d}\right)NH_4^+ + \frac{1-f}{3}NO_2^- + \frac{cf}{d}CO_2 \rightarrow \frac{f}{d}B_{anx} + \frac{2-f}{6}N_2 \tag{4.28}
$$

A value of f of 0.05, higher than that of the nitrifiers, best matches the measured stoichiometry of Strous et al. (1998), though this reflects optimal laboratory conditions. Rather, we also assume $f = 0.03$ for anammox in the global model; using the same value of f as for the nitrifiers allows for an equal, theoretical consideration of the three chemoautotrophic metabolisms. And importantly, this choice does not affect the resulting ecological competitive outcomes of the metabolisms, since the aerobic ammonia-oxidizers outcompete anammox bacteria, excluding anammox from the oxygenated ocean, with either stoichiometry. With $f = 0.03$, the anammox metabolism, normalized to one mole of N in order to compare with the nitrifier metabolisms, is:

$$
223NH_4^+ + 216NO_2^- + 5CO_2 \rightarrow B_{anx} + 219N_2 \tag{4.29}
$$

Other than the above microbial types and consequent remineralization schemes, the global biogeochemical ecosystem model is similar to the model of Dutkiewicz et al. (2015), though with six phytoplankton populations with parameters that represent the traits of the following six functional types: diatoms, picoplankton, diazotrophs, coccolithophores, and other large and other small phytoplankton. Four zooplankton types graze on the phytoplankton: one each on the picoplankton, other small, and coccolithophore types, and the fourth on the diatom, other large, and diazotroph type. A fifth zooplankton type grazes on the heterotrophic, nitrifier, and denitrifying microbial types. The model resolves the cycles of carbon, phosphorus, nitrogen, silica, iron, and oxygen. We refer to Dutkiewicz et al. (2015) for further detail. The 3D ocean circulation state estimate (the ECCO-GODAE state estimate) is from the configuration of the MITgcm as constrained by observations (Marshall et al. 1997; Wunsch and Heimbach 2007), and has a horizontal resolution of $1^\circ \times 1^\circ$ and 23 levels of vertical resolution, from 10m at the surface to 500m at depth.

Table 4.2: Model parameters

Parameter	Symbol	Value	Units
Nitrifier electron partition fraction	f	0.03	
Denominator for nitrifier biomass synthesis	d	20	
Maximum specific NH_4^+ uptake rate, AOO	$V_{max_{NH_4}}$	100	d^{-1}
Maximum specific NO_2^- uptake rate, NOO	$V_{max_{NO_2}}$	$100 \times 10^{-1/3}$	d^{-1}
NH_4^+ half-saturation, AOO	K_{NH_4}	0.13	μM
NO_2^- half-saturation, NOO	K_{NO_2}	$0.13 \times 10^{1/3}$	μM
Maximum growth rate, P	μ_{max}	2	d^{-1}
NH_4^+ half-saturation, P	K_{NH_4P}	0.043	μM
NO_2^- half-saturation, P	K_{NO_2P}	0.16	μM
NO_3^- half-saturation, P	K_{NO_3P}	0.24	μM
Maximum detritus normalized uptake rate	V_{maxD}	0.7	d^{-1}
Detritus half-saturation	K_D	0.1	μM N
Microbial mortality rate	m_B	0.01	d^{-1}
Phytoplankton mortality rate	m_P	0.01	d^{-1}
Zooplankton mortality rate (quadratic)	m_Z	.3	μM N^{-1} d^{-1}
Maximum grazing rate	g_{max}	10	d^{-1}
Grazing half-saturation	K_g	10	μM N
Grazing efficiency	γ	0.3	
Maximum light flux	I_{max}	1400	W m^{-2}
Light half-saturation	k_I	10	W m^{-2}
PAR attenuation in water	k_w	0.04	m^{-1}
PAR attenuation due to biomass	k_{bio}	0.005	μM N^{-1} m^{-1}
Mixed-layer attenuation depth	mlz	20	m
Minimum vertical mixing coefficient	K_{min}	10^{-5}	m^2 s^{-1}
Maximum vertical mixing coefficient	K_{max}	10^{-2}	m^2 s^{-1}
Detrital sinking rate	w	5	m d^{-1}

4.A.4 Expanded water column model results

Daily cycle

If phytoplankton are light-limited at night, does nitrification occur in the surface? Fig. 4.10 shows the water column model results over time, with resolution of a daily light cycle. Primary production varies with time of day. At the base of the euphotic zone, both ammonia-oxidation and nitrite-oxidation occur continuously in the model; the time-scales of sinking and remineralization of organic matter are sufficiently long as to allow for continual remineralization at depth. Ammonia-oxidation occurs at higher rates and shallower in the model due to the larger supply of ammonia than nitrite in the euphotic zone, and its intensity does exhibit a daily cycle: ammonium concentration and ammonia-oxidation rates are slightly enhanced at night, as phytoplankton cease DIN uptake. Though the model resolves the daily cycle very simplistically, it suggests that nitrification does not occur at significantly higher rates at night in the surface; the weekly population turnover rates of the nitrifying types inhibit them from growing a significant population during the model period of light-limited phytoplankton growth.

Grazing parameterizations

The microbial ecosystem model is sensitive to the parameterization of top-down control: the resulting microbial population sizes differ depending on whether the zooplankton grazing populations are 'generalists' or are 'host-specific.' Fig. 4.11 illustrates the model solutions for three different parameterizations: with one generalist zooplankton grazer, with two zooplankton grazers – one consuming just phytoplankton and the other consuming the bacterial heterotroph and the nitrifiers, and with three zooplankton grazers – one each consuming phytoplankton, the bacterial heterotroph, and the nitrifiers.

With one generalist grazer (Fig. 4.11a), the larger zooplankton population, sustained by the phytoplankton, subjects the bacterial and nitrifier types to a stronger grazing pressure, and so these types are completely excluded from the euphotic zone because the rate of grazing on their population exceeds their maximum growth rates. Data shows that this solution is unrealistic; heterotrophic bacteria do inhabit the surface. The order of magnitude difference in phytoplankton and heterotrophic bacterial growth, as documented by Kirchman (2016), suggests that the two populations – in order to sustain a steady population – must be analogously subjected to an order of magnitude difference in loss rates due to grazing, mortality, or viruses.

With two grazers (Fig. 4.11b), the bacterial and nitrifier types are sheltered from the large phytoplankton-feeding zooplankton population, and can inhabit the surface. The heterotrophic bacterial population size is significantly larger than the nitrifier population size, as observed, and this results in a stronger grazing pressure on the nitrifiers than the model with three grazers (Fig. 4.11c). When the nitrifiers are sheltered from the heterotrophic bacterial-feeding zooplankton population, they are subjected to much lower loss rates, and so can sustain a significant population at the surface. Whether the two grazer or the three grazer model is more realistic remains unclear: are nitrifying archaea and bacteria subject to being grazed upon by the same small ciliates or heterotrophic nanoflagellates?

We suspect that the real world exhibits a sense of all three parameterizations, and without the observations available to sufficiently parameterize grazing more realistically, we note the impact that top-down control has on this ecosystem model: the profiles in general remain very similar, but as grazing pressure on the nitrifiers decreases (from 1Z to 3Z), the nitrifier fitness increases, and they are able to sustain their populations at increasingly shallower depths.

Sensitivity to uncertainties in physiology

Though the overall pattern of the nitrite accumulation at depth is robust, the model solutions are sensitive to the parameters describing nitrifier physiology. Fig. 4.12 illustrates the resulting peaks in nitrification profiles for the variation of two parameters: f and ρ_{max}. Decreasing the efficiency of the nitrifying metabolisms by decreasing f leads to a significantly higher PNM and lower nitrifier biomasses.

Fluxes

Fig. 4.12 illustrates the steady-state fluxes of DIN in Eqns. $S1 - S3$, including the vertical flux, for the water column model results. The concentrations of NH_4^+, NO_2^-, and NO_3^- are overlaid on the plots in gray.

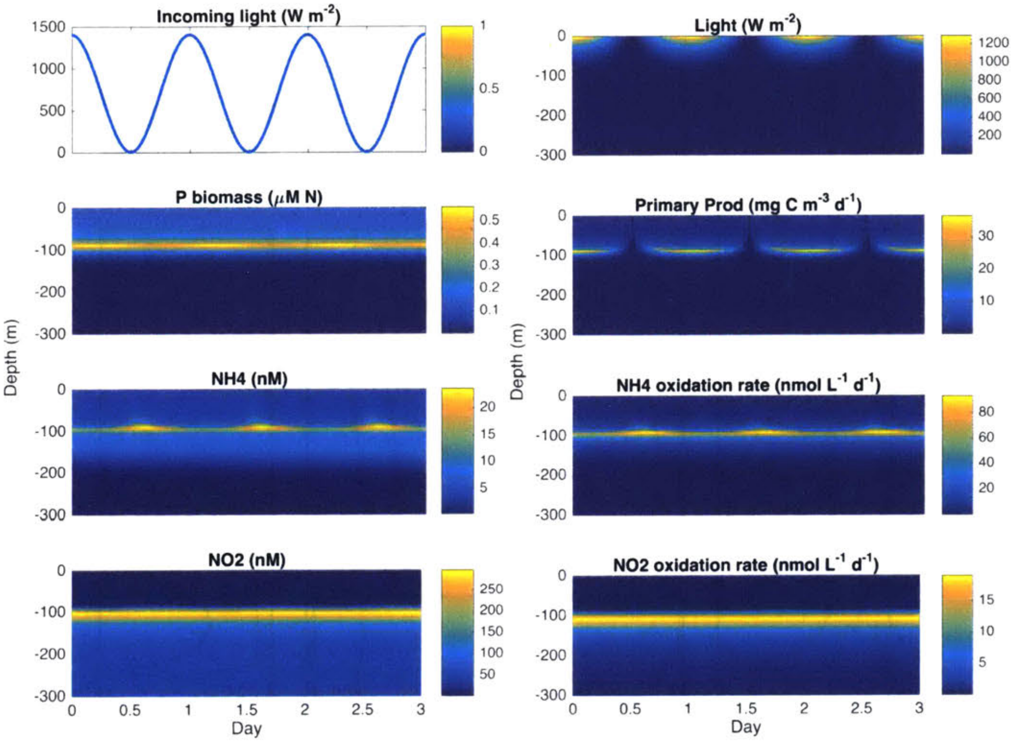

Figure 4.10: Model solutions as a function of a daily light cycle. Because of the slow nitrifier growth rates, with population turnover times of over a week, the nitrifying populations cannot populate the surface during the night, when phytoplankton uptake of DIN ceases in the model.

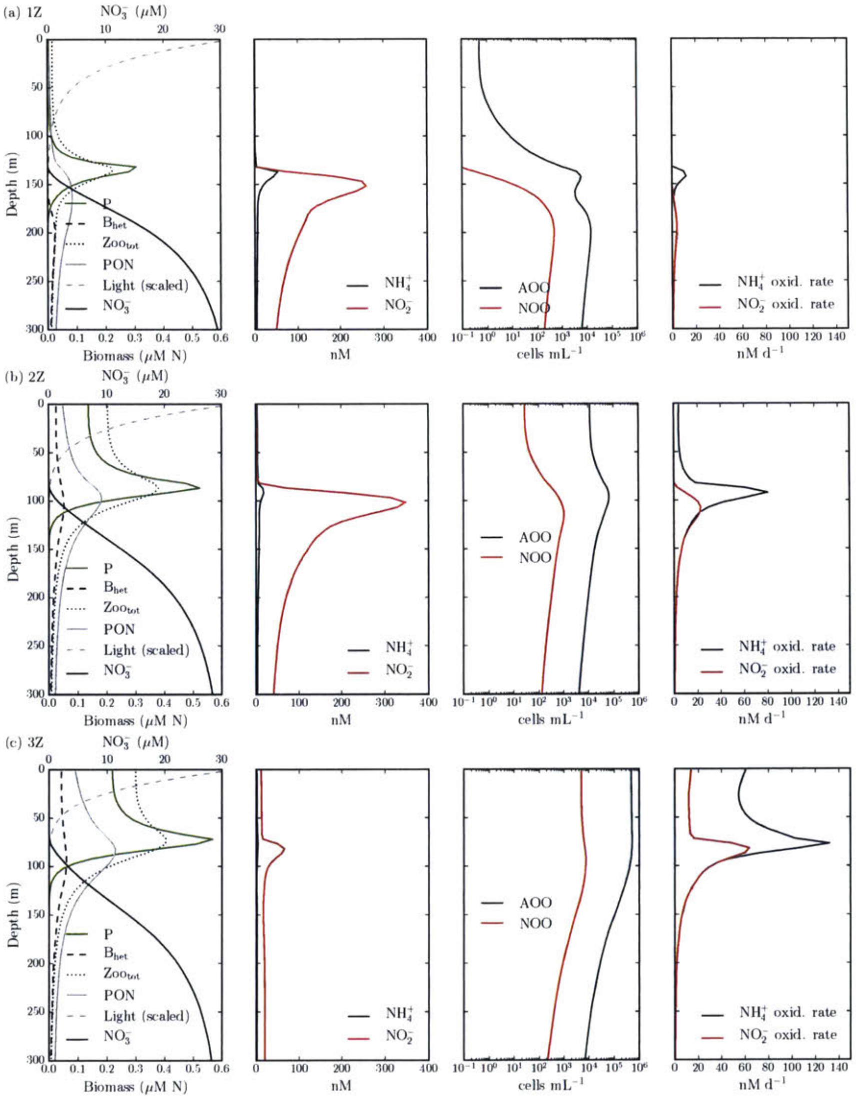

Figure 4.11: Solutions to 1D model for (a) one grazer, (b) two grazers (one for phytoplankton, and one for heterotrophic bacteria and nitrifiers), and (c) three grazers (one for phytoplankton, one for heterotrophic bacteria, and one for both nitrifiers).

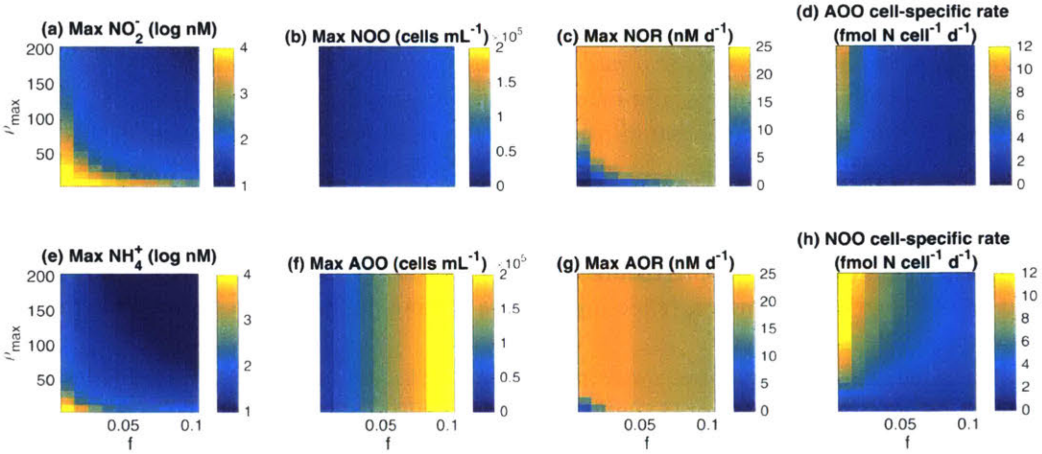

Figure 4.12: Water column maximum values in the 1D model for variations in electron partitioning parameter f and maximum inorganic nitrogen uptake rate ρ_{max}.

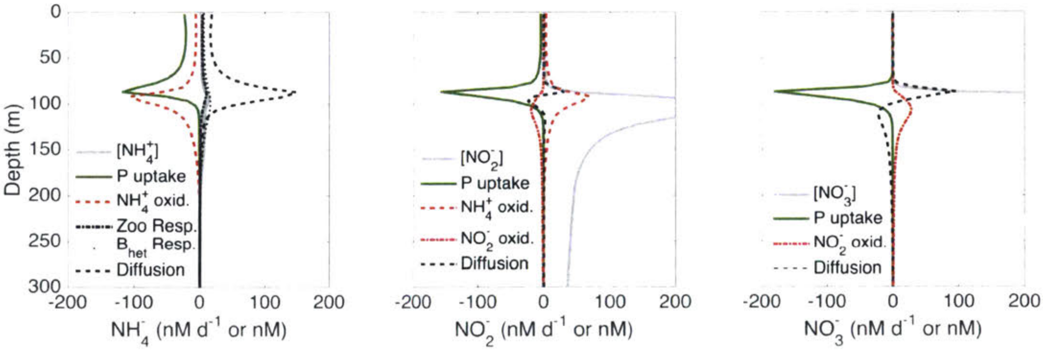

Figure 4.13: Steady state fluxes (nM d^{-1}) of NH$_4^+$, NO$_2^-$, and NO$_3^-$ for the 1D model. Concentrations (nM) are also shown in light gray.

4.A.5 Expanded global simulations

Fig. 4.14 shows the resulting maximum water column and surface mean ammonia oxidation and nitrite oxidation rates (AOR and NOR) in the global simulation. We also analyze the net biological production rate μ_{NET} of the populations (Clayton et al. 2013): if $\mu_{NET} > 0$, a population produces biomass at a rate greater than or equal to its losses at that location, and so is "locally sustainable." The blue contours identify the locations where $\mu_{NET} = 0$, partitioning the areas of favorable nitrification vs nitrification that is there due to physical transport. This shows that almost all of the surface AOR and NOR is due to transport.

Though the spatial patterns are similar, maximum AOR is higher than maximum NOR as in the water column model: larger fluxes of ammonium in the euphotic zone sustain a larger population of ammonia-oxidizers. At or just below the depth of the PNM, AOR and NOR become very similar, reflecting that the sinking flux of particulate organic matter ultimately controls both rates.

Fig. 4.15 illustrates the monthly average (from one model year) primary production and surface nitrite oxidation rate in December and May. Nitrification rates are higher and more widespread in the early winter in both hemispheres. Analysis of μ_{NET} (again with the blue contour) shows that surface nitrification is sustainable throughout the year in the S. Ocean, though more so in May than in December. Much of the surface nitrification in the N. Pacific and N. Atlantic is locally sustainable in December, but none is in May.

Fig. 4.16 illustrates the annually averaged integrated primary production in the global simulation.

Fig. 4.17 shows the resulting mean profiles of nitrite, ammonium, nitrifier biomass, and nitrification rates as a function of depth in the annually averaged global simulation. This demonstrates the consistency between the water column model and the global simulation; nitrite, nitrification rates, and nitrifier populations on average peak at depth, near the base of the euphotic zone.

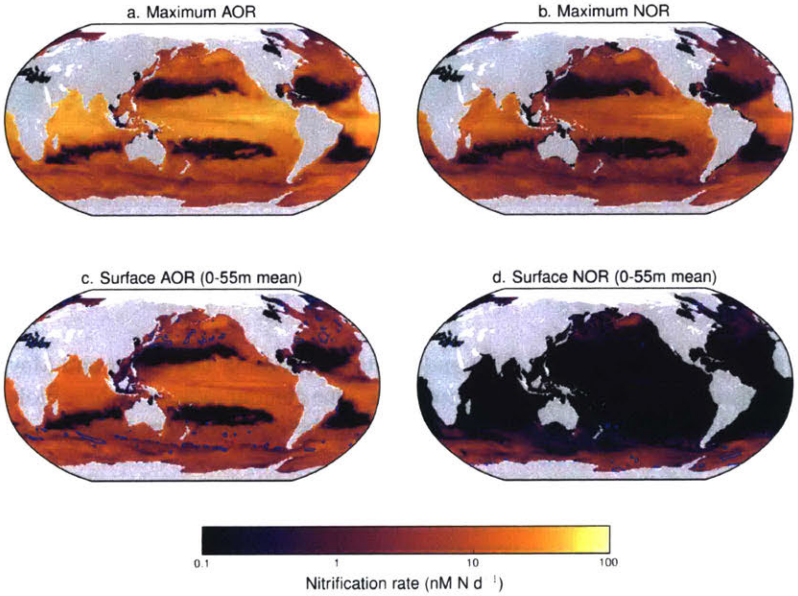

a. Maximum AOR

b. Maximum NOR

c. Surface AOR (0-55m mean)

d. Surface NOR (0-55m mean)

Figure 4.14: Annually averaged nitrification rates: (a) maximum water column and (b) surface mean ammonia oxidation rates, and (c) maximum water column and (b) surface mean nitrite oxidation rates. The blue contour indicates where biological growth rates of the AOO and NOO exactly balance loss rates for the AOR and NOR surface means, respectively, encircling the small areas in which the two metabolisms are 'locally sustainable.'

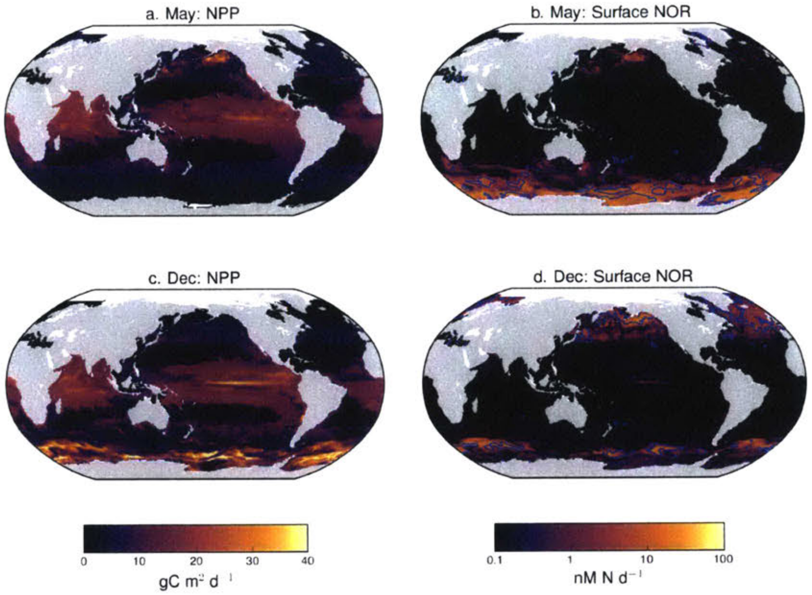

Figure 4.15: Surface primary production and nitrite oxidation in December and May, the months where their negative correlation is most obvious. The blue contour indicates where biological growth rates of the NOO exactly balance loss rates, encircling the regions where nitrite oxidation is a sustainable metabolism.

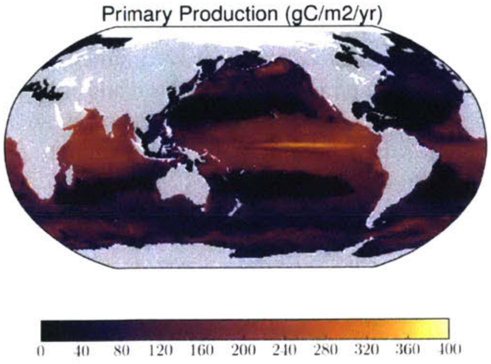

Figure 4.16: Annually averaged primary productivity in the 3D simulation.

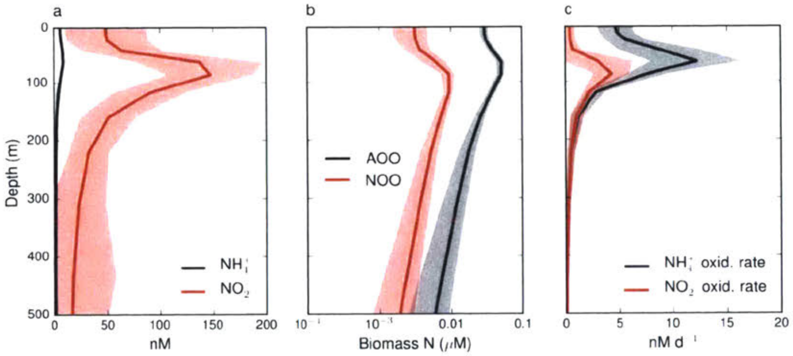

Figure 4.17: Mean (line) and standard deviation (shaded region) of (a) nutrients, (b) nitrifier biomass, and (c) nitrification rates in the 3D simulation.

Chapter 5

Conclusions and outlook

This thesis has provided insight into a few features of marine biogeochemistry by connecting microbial metabolisms explicitly with nutrient distributions and circulation. Metabolic functional types, linked to underlying chemical potential and physiological limitations of cell size, have enabled this connection. Here, the main conclusions found in each chapter and their broad implications are summarized. Specific extensions of the work are outlined with new questions and hypotheses. Finally, some general comments are made on potential ways to progress in representing microbial activity at larger scales.

5.1 Main conclusions

In Chapter 2, a simple model of how oxygen limits the growth rate of a microbial cell was developed. Incorporating an ecological perspective allowed for the estimation of the limiting oxygen concentration for growth. These limiting oxygen concentrations match observed minimum concentrations in the ocean when considering a wide range of plausible parameters, and thus Chapter 2 serves as an explanation for why these observed concentrations are as low as they are.

Chapter 3 extends the scope of Chapter 2 by considering the full set of conditions that limit the growth of an aerobic population. It describes the transition for aerobic to anaerobic metabolisms as governed by not just oxygen supply, but also the supply of an electron donor, the other half of the redox reaction. For heterotrophs in general, organic matter serves as this electron donor. Using established ecological theory for the coexistence of two populations competing for a resource, Chapter 3 then theoretically defines the transition from exclusively aerobic activity to steady coexisting aerobic and anaerobic activity. The predicted dynamics match observations of coexisting aerobic and anaerobic sulfur bacteria in a laboratory, and so provide a substantiated interpretation of observations of co-occurring aerobic and anaerobic activity at low oxygen concentrations in pelagic oxygen minimum zones. Results then serve to organize predictions about anaerobic activity and its associated losses of fixed nitrogen in these anoxic zones: with steady coexistence, less anaerobic activity is expected than would be if exclusively anaerobic metabolisms were sustainable in these environments.

A further utility of Chapters 2 and 3 is that the dynamics of limiting oxygen developed are general, and so are appropriate limits for diverse populations of microbes. This is because the expression for oxygen limitation is a flexible function of parameters like cell size and specific oxygen efficiency, and in this way, was able to predict the observed minimum oxygen concentrations for both small, slow-growing bacteria in the cold, pelagic ocean as well as larger *E. coli* growing ten times faster in a laboratory at 37°C (Stolper et al. 2010). In both cases, nanomolar oxygen concentrations limited the growth, which suggests that both the expression for the oxygen limitation (as a function of the parameters) and its return value (nanomolar oxygen concentrations) may be broadly applicable.

Chapter 4 explains how chemoautotrophic nitrifying microorganisms may form the primary nitrite maximum. Mechanisms are proposed for the location of the nitrite accumulation – the competition with phytoplankton for ammonium and nitrite – as well as the accumulation itself – the differences in the physiology and efficiencies of the two guilds of nitrifiers responsible for the two steps of nitrification. Light inhibition has been traditionally proposed as an explanation for both of these mechanisms, but since nitrification has been measured in sunlit waters, another explanation was required. The model here realizes a previous hypothesis that competition with phytoplankton may control the geography of nitrification.

Results are not incompatible with observations of light inhibition: certain species of nitrifying microorganisms in stratified environments may have evolved or adapted to lose photoprotective cellular machinery as a consequence of long-term exclusion from the surface. In this sense, direct observations of light inhibition of nitrifiers may signify how real microorganisms have evolved to reflect their original underlying energetic constraints, as anticipated by the functional type approach.

The dynamical model of nitrification in Chapter 4 led to a hypothesis that nitrification may be favorable in sunlit waters where phytoplankton (but not nitrifiers) are limited by something other than nitrogen, or in surface waters where phytoplankton are limited by light. One caveat to this hypothesis is the possibility that a higher grazing pressure near the surface also contributes to nitrifier exclusion. These results provide testable hypotheses for future work, which are discussed below.

5.2 Future work: Specific

Beyond Chapter 3: Aerobic-anaerobic interactions in OMZs

Addendum 1 of Chapter 3 considers the full suite of the microbial metabolisms currently understood to control nitrogen loss in oxygen minimum zone. The interactions of six metabolic functional types – including heterotrophic, chemoautotrophic, aerobic, and anaerobic metabolisms – are examined as a function of the supply of oxygen and organic matter, since organic matter is the ultimate source of all chemical energy in the pelagic ecosystem. Analysis shows that the distributions of metabolisms are largely consistent with observed patterns: for one, all aerobic metabolisms coexist due to cross-feeding, and give way to anaerobic metabolisms as oxygen supply decreases. For another, the ratio of denitrification to anammox activity converges to that calculated theoretically for marine organic matter, reconciling models of microbial growth, respiration, and cross-feeding with this geochemically-inferred theoretical ratio. However, outstanding questions complicate the interpretation of these results.

Does the stable coexistence explain the 'tipping point' of the Bay of Bengal?

The model results in Addendum 1 shows a stable state at an intermediate supply of oxygen that explains much of, but not all of, recent observations in the Bay of Bengal (Bristow et al. 2016b). Results seem to provide insight into the dynamics that create the observed environment. In the model, the nitrifiers become oxygen limited at a higher concentration than the aerobic heterotrophs because they have a higher oxygen demand, and so anammox, competing with the nitrifiers for inorganic nitrogen, becomes favorable at this higher limiting oxygen concentration. This matches the observations showing co-occuring nitrite-oxidation and anammox, no heterotrophic denitrification, and with anammox nitrite-limited.

In both model and observations, oxygen concentrations are maintained at levels that are higher than a potential minimum: observations show oxygen at seemingly fixed levels higher than those observed in other anoxic marine zones (10-200 nM). In the model, a lower supply of oxygen to the model results in a lower concentration of oxygen and higher rates of denitrification. In this way, the model agrees with Bristow et al.'s conclusion that the observations indicate a tipping point state: a decrease in the supply of oxygen, such as that projected by global warming, could change the Bay of Bengal into an anoxic zone with higher rates of denitrification.

However, the observations differ from the model results in significant ways that reflect the limitations of the descriptions of the microbial metabolisms in the model, and so currently inhibit any robust conclusions. For one, the subsistence oxygen concentration estimated for the nitrifiers is 7 nM, about an order of magnitude lower than the observed concentrations. For another, the observations show significant rates of nitrate reduction. The model considers a scenario in which nitrate reduction is favorable at higher oxygen concentrations to address this discrepancy, but it cannot simulate nitrate reduction without accumulation of nitrite, and so does not anticipate nitrite-limited anammox.

In the current model, insufficiently described dynamics of anaerobic heterotrophy may cause this mismatch between model and observations. At least two questions arise for further research: when does dissimilatory nitrate reduction become a favorable metabolism? And why does nitrite accumulate? Another reason for a discrepancy could be that nitrate reduction occurs on or within particles, and thus is decoupled from the dynamics of the chemoautotrophic metabolisms active in the ambient environment, with both observations and the model unable to distinguish the two. Either way, future research into both metabolisms and descriptions of the physical environment in OMZs could provide further insight.

Beyond Chapter 4: Geography of nitrification and new production

Chapter 4 establishes a broad framework for the biogeography of nitrification in the ocean. Observations of nitrification peaking at the base of the euphotic zone or below are numerous. However, observations are sparse in the deep mixed layers at high latitudes, which is where the model predicts significant amounts of favorable nitrification. Thus, proposed work to extend progress made in Chapter 4 includes measurements of *in situ* microbial activity at these locations in particular.

A testable hypothesis inferred from Chapter 4 is whether surface nitrification occurs in high-nutrient, low-chlorophyll (HNLC) regions, and particularly in the wintertime at high latitude regions when light further limits photoautotrophy. HNLC regions are named as such because of the accumulation of nitrate at the surface, and are often explained by a lack of iron availability (Martin and Fitzwater 1988; Gruber and Galloway 2008). Surplus nitrate concentrations indicate that excess ammonium and nitrite may also be accessible to nitrifiers.

Measurements of nitrification rates in HNLC environments could test this hypothesis. It would be most useful to measure both ammonia- and nitrite-oxidation rates simultaneously. Often, only ammonia oxidation is measured, for a few reasons: 1. it is understood as the rate-limiting step for nitrification (Ward 2008), 2. we know more about the ammonia-oxidizing organisms than the nitrite-oxidizing organisms (Daims et al. 2016), and 3. it is difficult to measure nitrite oxidation (Ward 2008). However, the calculated resource subsistence concentrations in Chapter 4 suggest that ammonia oxidizers may be closer competitors for DIN against phytoplankton than nitrite oxidizers. For this reason, as well as because of the larger fluxes of ammonia than nitrite in the euphotic zone, model predicts more locations and higher rates with stable ammonia-oxidation than nitrite-oxidation. Thus, ammonia-oxidation may not be a sufficient indicator of full nitrification.

Observations could provide needed information about the limiting factors to nitrifier growth other than DIN. In Chapter 4, the potential for iron limitation of nitrifiers was not considered. It has been shown that bacterial growth is limited by iron in the Southern Ocean (Church et al. 2000). Are the high-affinity ammonia oxidizers also iron limited, and thus, also unable to process available surface nutrients? Also, how much grazing pressure do nitrifiers experience in the euphotic zone vs. at depth? Enhanced losses to grazers at the surface increases the likelihood of their competitive exclusion there; Appendix 4.A.4 emphasizes the uncertainty of the modeled rates.

The size of prey is a strong predictor of grazing behavior (Taniguchi et al. 2014). Does there then exist a relatively higher grazing pressure on nitrifiers in these HNLC regions, where large phytoplankton compose a larger fraction of total phytoplankton, than in oligotrophic subtropical gyres, where picoplankton dominate (Barton et al. 2010; Ward et al. 2014)? If so, then this would serve as an additional mechanism for the exclusion of nitrifiers in the surface in oligotrophic environments, and for their favorability in HNLC zones. The exceptionally small size of ammonia-oxidizing archaea may further shelter them from such an effect (Martens-Habbena et al. 2009), which may even potentially serve to further decouple ammonia oxidizers from nitrite oxidizers. It would be useful to investigate the grazing dynamics in these environments with experiments.

Is there a more mechanistic definition of new production (and export production)?

The model here articulates how the nitrification peak at the base of the euphotic zone is linked to the overlying surface production. Sinking organic matter fuels the remineralization and nitrification that happens most intensely just as phytoplankton become light-limited, at or just below the PNM. All else the same, if surface production as higher, nitrification rates are higher.

Much of the newly formed nitrate then may be mixed back into the euphotic zone to fuel further production, as happens in the model. Should this newly-formed-nitrate-fueled production be considered as new production? Some of the earliest work to consider the ecology of chemoautotrophic nitrification considered it this way (Ward 1987). Yool et al. (2007), motivated to reexamine the role of euphotic zone nitrification specifically, instead considered all nitrate formed in the thermocline as 'regenerated' nitrate.

Either perspective could be justified depending on a choice of timescale. The rate at which nitrate is supplied from the zone of peak nitrification may be considered significantly slower than the rate of supply of nitrate formed within the mixed layer, but significantly faster than the rate at which the amounts of nitrate formed in the mesopelagic is returned to the mixed layer in far-away locations of upwelling as a consequence of larger-scale ocean circulation. What is the most meaningful way to divide production into 'new' and 'regenerated'?

The concept of such a divide is useful because of the research focus on export production (Siegel et al. 2016), which must balance new production in the ocean as a whole (Eppley and Peterson 1979). A current operational definition of the export flux is that which exits the base of the euphotic zone (Buesseler and Boyd 2009; Siegel et al. 2014). However, the model here suggests that this definition may inappropriate in that much of this export is then actively remineralized just at this particular depth.

A modified conception of new and export production could embrace this interdependency of surface production and subsurface nitrification. Future work could use the dynamic model of nitrification to determine a strategic combination of a depth and a timescale with which to define export production. The slope of nitrite or nitrate accumulation, for example, may identify the strongest fluxes of nitrification, and enable the determination of a characteristic length-scale at which these fluxes taper off. This deeper depth would of course of course predict an export flux smaller than the one estimated at the base of the euphotic zone.

5.3 Future work: Broad

The conclusions here regarding microbially-mediated biogeochemical cycling result from considering discrete, interacting metabolisms. Metabolic functional types, modeled as populations, were the means of connecting these metabolisms to environmental conditions as an extension of traditional 'NPZ' ecosystem models (Franks 2002). In these models, a functional type population that could not sustain itself in an environment with its defined metabolism was excluded entirely from that environment.

However, real microbial communities exhibit characteristics that are not captured dynamically in this approach. These characteristics lead to at least two conceptual descriptions of microbial communities:

A continuum of specialists and generalists.

First, the length of the metabolic pathway that occurs within one organism is not always known or predictable. For example, the two steps of nitrification occur in two distinct guilds of microorganisms in most environments, but have been recently shown to occur within a single organism in biofilms (with the metabolism of the full pathway termed 'comammox') (Santoro 2016). For another, all combinations of the subsets of the multiple steps of dissimilatory denitrification from NO_3^- to N_2 may occur in different organisms (Ward 2008).

Can these length of pathways be anticipated? As discussed in Chapter 3, theory predicts comammox in biofilms, but not mixed systems, as a function of these environmental conditions (Costa et al. 2006). The length of denitrification pathways may similarly be related to ambient conditions (Lilja and Johnson 2016). A consensus is that the lengths of pathways are not fixed in space or in time. Thus, the nitrification model here, with distinct ammonia- and nitrite-oxidizing populations, would not be appropriate for studying nitrification in biofilms. A more broadly applicable approach would be to incorporate such theory of pathway length into modeled environments. For example, an algorithm could dynamically estimate the favorable lengths of pathways as a function of that environment.

Beyond pathway length, uncertainty lies in the versatility of metabolism occurring within a species or functional guild. Nitrite oxidizers, ammonia oxidizers, and cyanobacteria, all traditionally considered as autotrophic, have been shown to utilize organic matter and other various substrates (Zubkov et al. 2003; Ward 2008; Qin et al. 2014; Daims et al. 2016). The role of mixotrophy – the combination of photoautotrophy and the ingestion of prey – is becoming increasingly appreciated, with significant consequences for ecosystem function (Stoecker et al. 2009; Ward and Follows 2016). Can the degree versatility of the metabolism carried out by a particular species be predicted?

In one sense, such versatility may be inferred from observing coexistences: syntrophic interactions among groups of organisms gives rise to their coexistences in the water column. For example, the nitrification model shows how cross-feeding results in a consistent coexistence of heterotrophic bacteria, nitrite oxidizers, and ammonia oxidizers at depth. A perhaps overly bold speculation arising from this coexistence is that an overlapping of those coexisting metabolisms may occur over time via lateral gene transfer. Whether or not such a speculation can be substantiated, there could be some utility in considering these coexisting populations as one, and thus blanketing all of the metabolisms being carried out into one bulk population. This may be one way to account for known versatility and mixotrophy in ecosystem models. We next explore this idea in more depth.

A continuum of individual and community.

Cross-feeding interactions constitute chains of dependencies. In the models here, it is assumed that nitrite oxidizers can utilize any available nitrite irrespective of its source – whether from ammonia oxidation or from dissimilatory nitrate reduction. But observations show interactions between organisms with dependencies on specific substrates and organisms (Biller et al. 2016). Definitions of such symbioses are unclear, but may be distinguished from cross-feeding by considering them as 'active' vs. 'passive' interactions (Kazamia et al. 2016).

How can we quantitatively account for the impacts of numerous and complex interactions in ecosystems? Evidence suggests that modeling populations that mimick individual cells carrying out one specific metabolism with a few required substrates is insufficient to capture mutualisms as well as passive dependencies for specific metabolites. If these complex exchanges are more of the rule than the exception, and are thus integral to ecosystem function, how can ecosystem models accurately consider such semi-autonomous populations? One way forward is to increase the level of detail of the models to incorporate many more metabolites and species, but in addition to being computationally expensive, this could also lead to model solutions that are too complex to interpret and understand. Another way forward could lie in considering the microbial consortia itself as the minimum unit of functioning microbial biomass (Strom 2008; Tikhonov 2015b,a; Rillig et al. 2015).

A consortia approach to describing microbial ecosystems aims to move beyond population models with fixed metabolisms to something that represents known metabolic versatility and interdependencies. Another benefit to such an approach may be to gain insight into aggregate effects of microbial biomass on nutrient distributions, which may be particularly useful for understanding the heterogeneity and complexity of organic matter dynamics. It also may pave the way to move beyond a sharp distinction between organic and inorganic nutrients – a holistic perspective could consider the mix of necessary metabolites that fuels the consortia.

But how would such a representation best work? What level of detail would need to be included? One could consider a mixed biomass as a unit for population modeling, with the function of that biomass predicted theoretically from the ambient chemical potential. This is similar to the metabolic functional type approach, except without dividing up the functional types into discrete populations. But in this case, how would the resolution of intermediates be represented? If both steps of nitrification were a part of such a consortia, for example, how could the release of nitrite be predicted? Could the redox-reaction-based different energetic efficiencies of each step be reflected within a large unit of biomass that then predicts a leak of nitrite as an excreted waste product? These questions are left for future research.

5.4 Concluding notes

The approach here has served to open up the 'black box' of the microbial control of marine biogeochemical cycling. Knowledge has been gained about the aerobic-anaerobic interactions in oxygen minimum zones that lead to the losses of fixed nitrogen there, and the potential controls on the locations of nitrification in marine environments have been described. The approach here additionally serves as a means of representing microbial growth and respiration explicitly and consistently in large-scale ocean circulation models. Describing microbial populations as grounded by their underlying energetic constraints provides a dynamical way to connect these metabolisms with global distributions of oxygen, nitrogen, and carbon dioxide. This ultimately enables the incorporation of the feedbacks of microbial activity to changes in global biogeochemistry and the climate system.

Appendix A

A simple correction scheme for the inherent error in multi-dimensional cell quota models

The work in this chapter was completed in collaboration with Mick Follows, David Talmy, and Glenn Flierl.

A.1 Overview

Cell quota models calculate the growth rate of the population from a single, average value of the quota of the modeling point or grid box. In multiple dimensions, this calculation by a single quota value meant to represent the average of a heterogeneous population results in an inherent averaging error, which overestimates the growth rate of the population. Here, we propose a simple, diagnostic calculation as a correction for this error in multi-dimensional cell quota numerical models: an 'explicit' scheme, since no prior measure of the heterogeneity of the population is required. We also demonstrate a method to correct for the error when the standard deviation of the represented heterogeneous population is known: an 'implicit' calculation, since the calculation requires knowing the variance of the quota. To quantify the effectiveness of both correctional methods, we compare equivalent (for point balances) individual-based and population level quota models, subjected to a continual inflow of cells with differing quotas. For scenarios with non-negligible error (greater than 1% error) of the population model with respect to the IBM, both methods reduce this error significantly: by an average of 62% (σ=34%) for the explicit numerical scheme, and by 81% (σ=9.6%) for the implicit calculation. The explicit method serves as a simple conditional addition to existing quota models: a few lines of code with small computational cost.

A.2 Introduction

Cutting edge marine global biogeochemical modeling considers the internal nutrient storage of phytoplankton cells (Blackford et al. 2004; Le Quere et al. 2005; Ward et al. 2012). Modeling nutrient storage decouples nutrient uptake from assimilation into biomass, a more accurate representation of cell dynamics (Caperon and Meyer 1972; Droop 1973), as first developed into a model by Burmaster (1979) with subsequent variations (Sharples and Tett 1994; Verdy et al. 2009; Flynn 2008).

As these models are adopted, questions emerge about their application beyond controlled laboratory environments. Hellweger and Kianirad (2007a) point out the error inherent in applying the nonlinear Droop model to a heterogeneous population. The average of the growth rates of the individuals in a heterogeneous population is always less than the growth rate calculated from the average quota of that population. Hellweger and Kianirad (2007a) demonstrate how analogous individual and population models show identical results for a homogenous population, but for a heterogeneous population, the population model overestimates population size and underestimates the internal quota because of this inherent error.

How does this inherent error affect global marine microbial quota modeling? First, 'explicit' error can result in multi-dimensional quota models, deriving from the convergence of different populations from contiguous grid boxes. Thus, heterogeneity results in the downstream grid box, which must represent this convergent population. Figure A.1 depicts an area of the ocean where such a convergence is likely to occur, at the intersections of the swift, nutrient-rich Kuroshio current with the surrounding slower, more oligotrophic ocean areas. As an example, an eddy filament in this environment could advect a few 'fat' cells from the current ($Q = 10Q_{min}$, giving growth rate $\mu = 0.9$ day^{-1} from Eqn. A.1 below for $\mu_{max} = 1$) into the oligotrophic area containing five times more 'skinny' cells ($Q = Q_{min}$, giving $\mu = 0$ day^{-1}). The average of the individual growth rates for this heterogeneous population is 0.15 day^{-1}, while the growth rate calculated from the average quota ($Q = 2.5Q_{min}$) is 0.6 day^{-1}, four times higher.

A second, 'implicit' characterization of this error derives from the choice to use a population-density model in the first place: the decision to represent phytoplankton community as a single point in a grid box, rather than resolving each individual. Population-density models ignore the heterogeneity contributed by the individuals at a single place and time. Bucci et al. (2011) modeled a heterogeneous population of river phytoplankton, and found that internal quotas were distributed from 1 to 6 times the minimum phosphorus quota. Calculating the average population level growth rate gave a rate 47% higher than that of the average of the individual rates. They concluded that the microscale patchiness of the environment largely contributed to the heterogeneity. At the microscale, changes in the external nutrient concentration can occur by excretion by zooplankton and other organisms, and cells encountering such a patch can increase their internal nutrient storage.

Such implicit heterogeneity may or may not be represented by data sampling, and can be considered itself as an additional source of uncertainty in marine ocean models. Param-

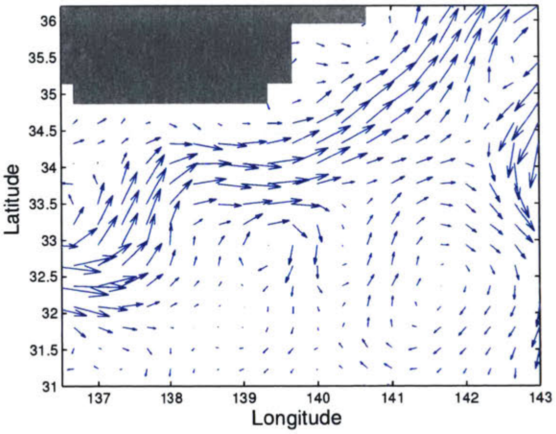

Figure A.1: Surface velocity in the northwest Pacific Ocean, depicting areas of intersection of the swift, productive Kuroshio Current with nearby slower, oligotrophic waters, where convergence of phytoplankton populations with different internal nutrient quotas may occur. (Data: Geostrophic velocity, AVISO, Oct. 2, 2013.)

eters used for population models were measured at the population level, and thus perhaps sidestep the error in the models themselves since the parameters already incorporate a population average bias. However, Bucci et al. point out that the parameters are measured from culturing experiments of largely more homogenous populations, and so, neglect to incorporate error from heterogeneity. To correct for his bias, they suggest that models could use a lower maximum growth rate parameter, where the factor of decrease reflects the prediction of the error.

Here, we examine both considerations of error. To abate the explicit error, we develop a numerical scheme to estimate the error in multi-dimensional quota models. The scheme is a diagnostic calculation using the fluxes and quotas of the incoming populations for converging populations on a gridded domain. Second, we examine a theoretical estimation of the implicit error using prior knowledge of a heterogeneous population: the calculation requires knowing the (statistical/normal) variance of the population. Both strategies involve estimating a factor by which to reduce the modeled growth rate, and so follow the suggestion of Bucci et al. (2011).

Though individual-based models (IBMs) by definition avoid this inherent error, they remain very expensive for application to large-scale phytoplankton population studies. Armed with a way by which to predict and prevent this error, we compare analogous IBM and population models of phytoplankton physiology. We aim to demonstrate the utility of the numerical scheme to correct for explicit error in areas of convergence, and thus the utility of population quota modeling at regional and global scales.

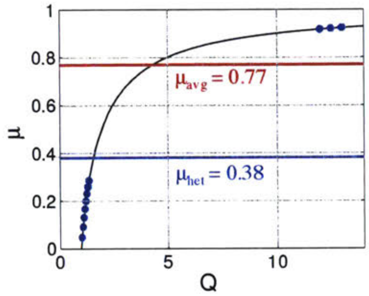

Figure A.2: Growth rate μ against nutrient quota Q (for μ_{max} = 1 and Q_{min} = 1), and discrete individual quota values (blue dots), illustrating the error in calculating μ from the average quota of the individuals (red line) rather than as an average of the values of μ calculated from each of the individual quotas (blue line). The averaged quota calculation overestimates the growth rate by 102%.

A.3 Inherent error in multi-dimensional cell quota models

Cell quota models calculate the growth rate μ (time^{-1}) from a maximum growth rate $\mu_{\max}$ modified by the cell's internal nutrient storage quota as:

$$\mu = \mu_{\max} \frac{Q - Q_{min}}{Q} \tag{A.1}$$

where the total quota Q (internal nutrient concentration, μmol cell^{-1}), consists of the sum of a minimum amount, Q_{min}, and a variable amount of 'luxury' storage. Overestimation of the growth rate is implicit to using averaged quota values for a heterogeneous population due to Jensen's inequality (Hellweger and Kianirad 2007a). Figure A.2 illustrates this error, showing the average of the growth rates of individuals (blue dots) compared to the growth rate calculated from the average quota of the individuals; the latter rate is 102% higher than the former, more accurate representation of the population.

Two factors contribute to large error. First, error is maximized when individuals vary along the steepest slope of the growth rate-quota curve, thus constituting a population that optimizes change in growth rate by a change in quota. Second, error is maximized when the distribution of the population's internal quotas is skewed towards smaller quotas, when individuals with bigger quotas represent a smaller fraction of the total population. In short, a few fat cells mixed into many skinny cells causes enormous error.

For example, if a population of cells with the highest phosphorus quota in the experiments of Burmaster (1979) ($Q = 18Q_{min}$) were mixed converged into a downstream model grid cell with a population at the subsistence quota ($Q = Q_{min}$) at a ratio of 1:10, the phosphorus-limited growth rate calculated by the population model would overestimate the average growth rate of the individuals by a factor of 7, almost an order of magnitude. But if the ratio were 10:1, the growth rate of the population model would be only 10% higher than the average of the individual rates.

When and where would we predict significant error in global marine quota models? Since error is correlated with the degree of difference of the mixing quotas, we would expect error with sharp gradients in productivity, and thus luxury nutrient storage, and with sustained mixing or transport across this gradient. Most of the open ocean, and perhaps the entire domains of coarse resolution models may not exhibit such error-prone areas. Eddy-resolving biogeochemical models, however, may contain such large gradients across eddy fronts or from filaments. Since many of the scientific questions asked of these models involve the difference in biological productivity with and without eddy resolution (Mahadevan 2014), this question of numerical error becomes particularly relevant.

A.4 Theory: correction methods

To investigate and address this numerical error, we examine a simple 1D model environment of sustained convergence of a sharp gradient in cell quotas. The middle box B of a three box model is subjected to the immigration of cells from the outer two boxes A and C: the blending of two populations (Fig. A.3). The parameter f $(0 \leq f \leq 1)$. controls the portion of the outflow of box C that flows into B, thus allowing for experimentation with the effect of different proportions of 'fat' and 'skinny' cells and error. In this section, we present two methods by which to estimate the error due to heterogeneity of this downstream, middle box.

Explicit error correction: A diagnostic numerical scheme

In ocean population models, we cannot know the implicit distribution of quotas within each grid box, but, we can estimate the error from the convergence of different populations that causes the distribution. For box B in the 1D model, the population growth rate is calculated as:

$$\mu_B = \mu_{\max}\frac{Q_B - Q_{min}}{Q_B} \tag{A.2}$$

The fluxes of incoming cells from boxes A and B cause heterogeneity. The error from this heterogeneity can be predicted by first calculating the growth rate from the average quota of the incoming populations and comparing that to the average growth rate calculated from each of the distinct incoming populations from boxes A and B, weighting each by the size of the flux of incoming cells. The growth rate of the average incoming population, $\mu_{in,avg}$, is:

$$\mu_{in,avg} = \mu_{\max}\frac{Q_{in,avg} - Q_{min}}{Q_{in,avg}} \tag{A.3}$$

where

$$Q_{in,avg} = \frac{D_A X_A(Q_A) + fD_C X_C(Q_C)}{D_A X_A + fD_C X_C} \tag{A.4}$$

The more accurate growth rate of the incoming population that incorporates its heterogeneity, $\mu_{in,het}$, is calculated from each of the incoming quotas:

$$\mu_{in,het} = \mu_{\max}\left[\frac{D_A X_A}{D_A X_A + f D_C X_C}\left(\frac{Q_A - Q_{min}}{Q_A}\right) + \frac{f D_C X_C}{D_A X_A + f D_C X_C}\left(\frac{Q_C - Q_{min}}{Q_C}\right)\right] \quad (A.5)$$

The original growth rate calculation can then be modified to reflect ratio of these two:

$$\mu_B = \mu_{\max}\frac{Q_B - Q_{min}}{Q_B}\cdot\frac{\mu_{in,het}}{\mu_{in,avg}} \quad (A.6)$$

Since Jensen's inequality shows that $\mu_{in,het}$ will always be less than $\mu_{in,avg}$, this modification always decreases the resulting growth rate for box B, and so follows the advice of Bucci et al. (2011). The modification itself, the last term on the right hand side in Eqn. A.6, represents a prediction of the error. Thus, the modification prevents the error by lowering the calculated growth rate by a factor that approximates the error due to ignoring the heterogeneity from distinct incoming populations.

Implicit error correction: Incorporating known variance

We can estimate the error of the heterogeneous grid box if from its mean value $\bar{Q}$ and its variance σ. We can express the growth rate (Eqn. 2) as an integral of the quotas over the population p:

$$\mu = \mu_{max}\int dq\frac{Q - Q_{min}}{Q} \quad (A.7)$$

Using this expression, we can derive an approximation for this growth rate (derivation in Appendix A.A.1) as:

$$\mu \approx \mu_{max}\left[\frac{\bar{Q} - Q_{min}}{\bar{Q}} - \sigma^2\frac{Q_{min}}{\bar{Q}^3}\right] \quad (A.8)$$

Models can use this expression to more accurately approximate the growth rate, and prevent the error, but only if the mean and variance of the quota distribution is known, and so this method is less useful for numerical models. Rather, it provides a proof of concept that knowing the patchiness of an environment can give an improved population-level model.

A.5 Application: A three box cell quota model

We next evaluate the skill of each of the two methods in estimating and thus preventing error by comparing individual and population cell models of the three box convergence environment. As demonstrated by Hellweger and Kianirad (2007b) and Klausmeier et al. (2004), individual and population models can be developed for equivalence in one dimension. We build an idealized quota model of phytoplankton and one nutrient (Burmaster 1979; Caperon and Meyer 1972; Droop 1973), which are equivalent in one dimension (to 0.3% error due to nonlinear dynamics, see Appendix A.A.1 for model description.) We develop the parameters in 1D for a virtual model of a chemostat, following Burmaster (1979). To build to 1D, the chemostat model is modified to include three multiple connected 'flasks,' which become analogous to grid boxes of a numerical model (Figure A.3).

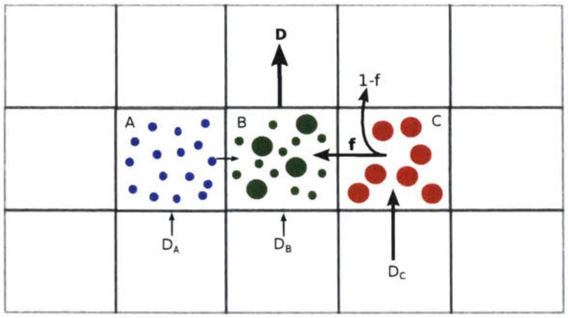

Figure A.3: The three box model environment. Cell quotas (sizes of dots) reflect the different dilution rates D of boxes A and C, and are blended into box B, forming the continuously heterogeneous population used to examine error. The population density version of the model compared to the individually based version of the model demonstrates significant error in resolving the quota of box B.

Methods

In a traditional chemostat, increasing the rate of the inflow of concentrated nutrient increases the quota of the resulting population. At steady state, the dilution rate D, the dividend of the flow rate and the volume of the flask (D = time^{-1}), is equal to the growth rate of the population of cells. In the three box model environment pictured in Fig. A.3, the outflow of two boxes (boxes A and C) becomes the inflow of a third, downstream box (box B). We vary two parameters: D_3, the dilution rate of one of the outer boxes, and f, the portion of the outflow of this box that is directed into the middle, downstream box. Increasing D_3 increases the quota of the cells in that box, and thus the cells immigrating to the downstream box. Increasing f increases the contribution from this outer box relative to the other outer box, affecting the distribution of quota values as well as the total flux of the heterogeneous box. We conducted this blending experiment for three values of f: 1, 1/2, and 1/4.

For each value of f, the dilution rate D_C was varied by increasing increments of 0.1 day^{-1} , until washout (less than 5,000 individuals in any box). Dilution rates D_A and D_B were constant at 0.1 day^{-1} for all runs. In this way, the populations of the two source boxes became increasingly different. For each increment, the model was run to equilibration with an explicit Euler forward scheme (explained in detail in Appendix A.A.1). All results are expressed against the outgoing dilution rate D of box B (where $D = D_A + D_B + D_C$).

For all simulations, error was calculated as the deviation of the population model from the IBM (see Appendix A.A.1 for detail). Following the numerical correction method, the quota and flux values from boxes A and C are used to calculate the modification to the growth rate for Box B at each timestep. This modification alone provides a prediction of the error, which can be compared to the population model simulations to determine how skillful such a prediction is compared to resulting model solution for the quota and population size of box B. The modification can then be applied to the diagnostic growth rate calculation at each time step, without using any previously determined information about heterogeneity.

	f=1	Original	Numerical		Implicit		f=0.5	Original	Numerical		Implicit		f=0.25	Original	Numerical		Implicit	
QC/QA	D	Error(%)	Error(%)	%Diff	Error(%)	%Diff	D	Error(%)	Error(%)	%Diff	Error(%)	%Diff	D	Error(%)	Error(%)	%Diff	Error(%)	%Diff
1.00	0.3	**0.472**	0.507	-7.5	0.802	-69.9	0.25	**0.127**	0.172	-35.4	0.440	-247.1	0.23	**0.206**	0.051	75.0	0.298	-44.9
2.13	0.4	**0.142**	0.791	-458.0	0.442	-211.8	0.30	**0.173**	1.132	-554.5	0.429	-148.2	0.25	**0.051**	1.004	-1867.6	0.326	-539.2
3.40	0.5	**-0.479**	1.141	-138.2	0.400	16.5	0.35	**-0.594**	1.981	-233.7	0.228	61.6	0.28	**-0.983**	2.217	-125.4	0.320	67.5
4.86	0.6	**-1.623**	0.945	41.8	0.025	98.5	0.40	**-2.169**	2.039	6.0	-0.034	98.4	0.30	**-2.634**	3.154	-19.8	-0.190	92.8
6.55	0.7	**-3.000**	0.284	90.5	-0.513	82.9	0.45	**-4.005**	1.536	61.7	-0.613	84.7	0.33	**-4.728**	3.318	29.8	-0.551	88.3
8.52	0.8	**-4.661**	-0.688	85.2	-1.065	77.1	0.50	**-6.349**	0.568	91.1	-1.388	78.1	0.35	**-7.475**	2.965	60.3	-1.510	79.8
10.86	0.9	**-6.188**	-1.666	73.1	-1.877	69.7	0.55	**-8.822**	-0.361	95.9	-2.246	74.5	0.38	**-10.466**	2.612	75.0	-2.486	76.2
13.66	1.0	**-8.000**	-2.584	67.7	-2.522	68.5	0.60	**-11.261**	-1.456	87.1	-3.037	73.0	0.40	**-13.705**	2.032	85.2	-3.253	76.3
Avg %Diff for Error > 1%				**71.7**		**79.3**				**68.3**		**81.8**				**46.1**		**82.7**

Table A.1: Values of the error illustrated in Fig. A.4 for varying D and f compared to the degree of heterogeneity of the incoming cells (QC/QA, the dividend of the quotas of Boxes A and C) and the percent difference in error by the two correction methods: the explicit, numerical scheme, and the implicit method using the priorly calculated variance in the IBM. For the average percent differences, only values for the original error greater than 1% are used (the blue values).

Following the implicit error estimation, we use the improved growth rate calculation (Eqn. A.8). Here, a time series of the mean $\bar{Q}_B(t)$ and variance $\sigma_B(t)$ of the quota distribution of box B are first determined from a completed run of the individual model. These statistics are then input as parameters into the expression of the growth rate for Box B in the population model for each of the same time steps t.

Results

Fig. A.4 shows the resulting error, predicted error, and reduced error from each of the correction methods for the quota and population size of box B. Table A.1) lists the values of the errors for the original and modified simulations against a measure of the distribution of the quota of the incoming population: Q_C/Q_A, which increases with D_C.. As parameters D_C and f vary, two trends result (Figure A.4). First, as the dilution rate of box C increases, the difference in the quotas of the two incoming populations increases, and thus the negative slope of the error against D. Second, as the fraction of flow f of box C into the downstream box increases, error decreases as the population consists of a higher proportion of 'fat' cells. Thus, our model is able to reproduce the error predicted from a heterogeneous population from these two effects.

The predicted error agrees with the resulting error in the quota (Figure A.4, upper left). The negative error signifies that the population model underestimates the quota, though it did not significantly overestimate the population density itself (lower left). That the growth rate error was reflected in the quota, rather than the population size, reflects the dynamics of the chemostat model, which requires the growth rate to equal the dilution rate at steady state; the error is thus 'forced' into the quota pool. (More subtly, the timescale of growth is slower than the timescale of nutrient uptake by a factor of two in this model, and so the internal quota adjusts more quickly than the population size.)

Figure A.4 also compares the results of correcting for heterogeneity using each of the two correction methods. Both methods significantly reduce the error of the quota to less than

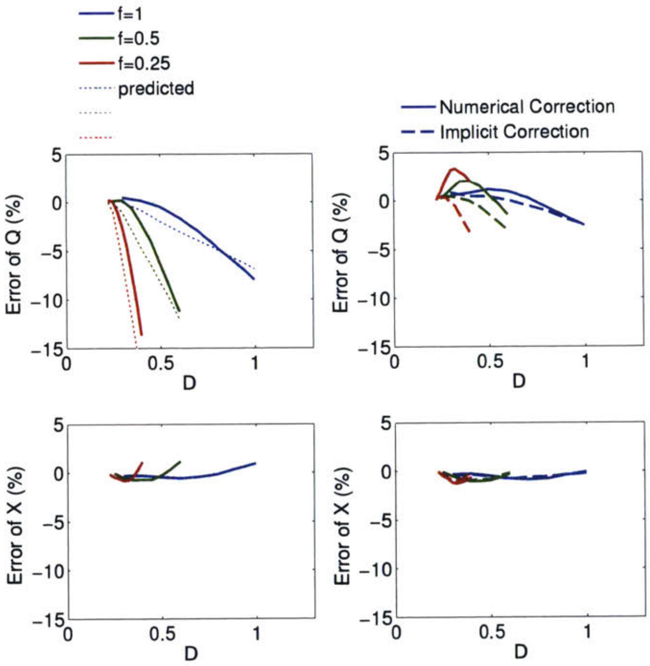

Figure A.4: Error of the population model's representation of the heterogeneous population with respect to the IBM, for varying dilution rate D and *f* = 1, 1/2, and 1/4. Upper left: The original error in the modeled quota (solid lines) and the predicted error (dashed lines). Lower left: The original error in the modeled population size. Right: The error in the modeled quota (upper right) and population size (lower right) using each of the two correction schemes.

3% for all values of f, and further reduce the small error of the population size. In general, the correction schemes are robust across the parameter space. Though both give a similar magnitude of error, the explicit correction method results in an overestimate of the quota, while the implicit correction method reduces the underestimate of the quota. This may reflect the fact that the numerical scheme estimates an upper bound to the error, and so an overcorrection results when whenever this method overestimates the error; overcorrections correlate with overestimated predictions.

Table A.1 also lists the percent decrease in error by each of the two correction methods. For large error ($\geq$1%), both methods reduce this error significantly: by an average of 62% (σ=34%) for the explicit numerical scheme, and by 81% (σ=9.6%) for the implicit calculation. However, when the error is small ($\leq$1%), overcorrection results in error of the same or larger magnitude. This can be understood by considering that the corrective methods themselves contain error, which is dwarfed when the original error is sufficiently large.

Appendix A.A.2 contains pseudocode for implementing the numerical scheme in two dimensions, including a conditional statement for implementation when error is greater than 1%.

A.6 Discussion

The inherent error in cell quota models due to Jensen's inequality results from the necessity of averaging diverse cell quotas in a population level Hellweger and Kianirad (2007a). This error causes a significant overestimation of the growth rate, which manifests in the model solutions as underestimated quotas or overestimated population densities. The error is theoretically predictable for any modeled population of cells for a known distribution of internal quotas in the population. When we do not know these values, such as in numerical models, we need an approach that can estimate the error in order to make the necessary correction that decreases the growth rate.

We demonstrate the utility of two methods by which to predict and prevent the error invoked by comparing a population-averaged quota model to an individual-based model. Both correction methods are robust enough to apply to any parameterization of a quota model; the error is similarly predicted and prevented for various parameterizations of the model here, such as varying cell size and varying uptake to growth rate ratios, with consistent results. The first, a numerical scheme, involves no prior knowledge of population heterogeneity. Rather, it prevents the 'explicit' heterogeneity caused by the confluence of populations in gridded models. It calculates the upper bound of the error as a function of the quotas of incoming populations, weighted by the incoming flux of each. The second method requires knowledge of the distribution of the quota among the population. It is a simple way to incorporate the effects of known patchiness.

Correction methods are estimations, rather than exact calculations of error, and so add an amount of error to the model themselves. When the predicted error was greater than 1% in the simulations here, the corrective methods reduced the total error significantly. When the inherent error is low, both corrective methods are a hindrance, rather than a help, to improving the accuracy of the population model. For more homogenous populations of perhaps the majority of the domain of global quota models. Therefore, we recommend applying the corrective methods conditionally, when the predicted error is greater than a few percentage points.

In what conditions, then, would these corrective methods be utilized? The first method can be easily incorporated into existing cell quota models, with a conditional implementation command when error is predicted to be large. The second, implicit method relies on such knowledge of the system, and so this method becomes less useful as a permanent feature of population models where such patchiness is determined to be significant, such as in small-scale, coastal areas. Individually-based models may be the preferred choice for studying these areas.

In ocean models, the prediction of error will be significant only in areas of sharp convergence, when adjacent grid cells contain very different internal quotas of the growth-limiting nutrient, and so only when a non-smooth/discontinuous-like quota distribution exists. For most areas of the ocean, quotas may not differ that drastically in adjacent grid cells, and so not exhibit the necessary sharp gradients that introduce error.

Additionally, sustained error requires that convergence is also sustained in time. For a pulse of convergence with large error, this error should be reduced on daily timescales as the cells adjust to their new environmental conditions. I.e., for an overestimated growth rate at an initial timestep, at the following timestep, the quota will complementarily be smaller, and the growth rate consequently smaller; both the quota and the growth rate continue to adjust away from the error until the population converges to homogeneity, in the absence of continued input of new heterogeneous cells. Thus, only continual convergence would result in a steadily large error.

The largest error should then occur for a sustained convergence of small amounts of cells with large quotas and large amounts of cells with minimal quotas. An example of this in the ocean is downstream of productivity hotspots, where a few cells still storing much nutrient continuously merge via an eddy-induced filament into an oligotrophic area consisting of a population surviving at a subsistence quota. This would have the effect in models of amplifying growth rates or storage quotas significantly in these areas.

It should be noted that other uncertainties and error of ocean biogeochemical modeling may dwarf this inherent error in most cases. Steinberg et al. (2011) showed that the difference between four methods used to estimate numbers of total and live cells is of order 10% and can be as great as a factor of two. In other words, if we could model each cell individually, our model would likely contain at least 10–100% error. More generally, much uncertainty exists among many characteristics of biogeochemical marine modeling: estimates of net primary productivity differ significantly among different models (Saba et al. 2010).

The examples of very significant error presented here (error of 500%) arise from determination of the growth rate by the phosphorus quotas ranging by an order of magnitude, as in (Burmaster 1979). But in much of the ocean, the limiting growth rate is nitrogen, which typically ranges in cell quotas by only about a factor of two (Dortch et al. 1984). And so, quota models running with nitrogen as a currency should give lower error. However, the potential for large error remains, since even a factor of two difference in quota can lead to significant error when small numbers of larger cells and large numbers of smaller cells converge.

A.7 Conclusions

An averaging error is inherent in multi-dimensional cell quota modeling when representing a converging, heterogeneous population as a single point. This error results most drastically from flows between sharp differences in cell population sizes and quotas. In most of the domain of ocean models, we would not expect much sharp gradients. However, these fronts emerge in models that resolve eddies and filaments. The averaging error would result in an artificially high prediction of growth rate in these areas of convergence. Here, we present a computationally inexpensive way to correct for this error diagnostically in quota models in these areas. A few lines of code within any advection scheme can quickly contribute the factor by which to modify the growth rate of a grid cell in accordance with the heterogeneity of the incoming population. This method is a feasible, simple way by which to avoid the artificial numerical effect of the convergence of a heterogeneous population. With this corrective method, we propose the utility of the population level quota models at regional and global scales.

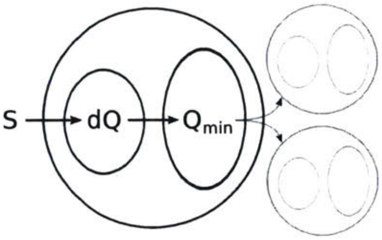

Figure A.5: Schematic of the cell quota model, illustrating the flow of nutrient from external concentration S to the varying internal storage quota δQ and the fixed minimum quota Q_{min}.

A.A Appendix

A.A.1 Equivalent Population and Individual-based Quota Models

The quota model

We build an idealized quota model of phytoplankton and one nutrient (Burmaster 1979; Caperon and Meyer 1972; Droop 1973). The total quota Q (internal nutrient concentration, μmol cell^{-1}), consists of the sum of a minimum amount, Q_{min}, and a variable amount of 'luxury' storage, δQ (Figure A.5).

The rate of external nutrient uptake ρ (μmol cell^{-1} day^{-1}) is calculated with a Michaelis–Menton limitation by the external nitrogen concentration S (μmol m^{-3}):

$$\rho = \rho_{max} \frac{S}{K_\rho + S} \tag{A.9}$$

where ρ_{max} is a maximum uptake rate and K_ρ the half-saturation constant.

The size of the quota then controls growth rate μ as:

$$\mu = \mu_\infty \frac{Q - Q_{min}}{Q} \tag{A.10}$$

where μ_∞ is a maximum theoretical growth rate.

The population model conserves biomass, the product of the quota and the population density X (cells m^{-3}), by conserving the biomass of each of the two quota components, $X\delta Q$ and XQ_{min} (μmol m^{-3}). Three differential equations describe the chemostat system, which has no analytic solution:

$$\frac{\partial S}{\partial t} = D(S_0 - S) - \rho X \tag{A.11}$$

$$\frac{\partial (X\delta Q)}{\partial t} = \rho X - \mu(XQ_{min}) - D(X\delta Q) \tag{A.12}$$

$$\frac{\partial (XQ_{min})}{\partial t} = \mu(XQ_{min}) - D(XQ_{min}) \tag{A.13}$$

where D is the dilution rate (day^{-1}) and S_0 is the nitrogen concentration of the external inflow (μmol m^{-3}) into each box. For constant Q_{min}, this system of equations is exactly that of Burmaster (1979). With constant Q_{min}, the rate of change of the population density X is derived from Eqn. A.13 as:

$$\frac{\partial X}{\partial t} = \mu X - DX \tag{A.14}$$

Combining Eqns. A.12 and A.14 gives a differential equation for the storage quota δQ. For constant Q_{min}, the rates of change of the two components of the cell quota for the population model are thus:

$$\frac{\partial(\delta Q)}{\partial t} = \rho - \mu Q \tag{A.15}$$

$$\frac{\partial(Q_{min})}{\partial t} = 0 \tag{A.16}$$

The individual-based model

The IBM resolves each individual as an analog of the population model, referring to the minimum and storage components of the quota as q_{min} and δq, respectively. In the IBM, q_{min} fluctuates within fixed bounds, representing growth and division of cells, and so is fixed over a time average. The rates of change of the two components of the quota of the ith cell, analogous to Equations 8 and 9, are calculated as:

$$\frac{\partial(\delta q(i))}{\partial t} = \rho(i) - \mu(i) q_{min}(i) \tag{A.17}$$

$$\frac{\partial(q_{min}(i))}{\partial t} = \mu(i) q_{min}(i) \tag{A.18}$$

A cell divides once its protein content reaches a given limit q_{minL}, with each resulting cell containing half of the former values of q_{min} and δq (Figure A.5). The number of cells to be transported in and out of a box is calculated as the product of the dilution rate, the timestep, and the number of individuals. This number of individuals are randomly selected from the population and then transported, transferring their corresponding q_{min} and δq values. Uptake and growth rates are calculated for each individual cell (Eqns. 1 and 2). The rate of change of the external nutrients S is calculated in the same way as Eqn. A.11 by summing up the individual uptake rates. The mean value of each quota sand the number of individuals are recorded at each time step.

IBM and population model equivalence

Hellweger and Kianirad (2007b) provide an in-depth analysis of the equivalence of population and IBM models for a point balance. Output of the model in this study visually demonstrates this equivalence (Figure A.6, $D = 0.5$ day^{-1}). The two models show closely matched external nutrient concentration, internal quotas, and the total number of individuals in the flask for the transient as well as steady states. The synchronous cell life cycles

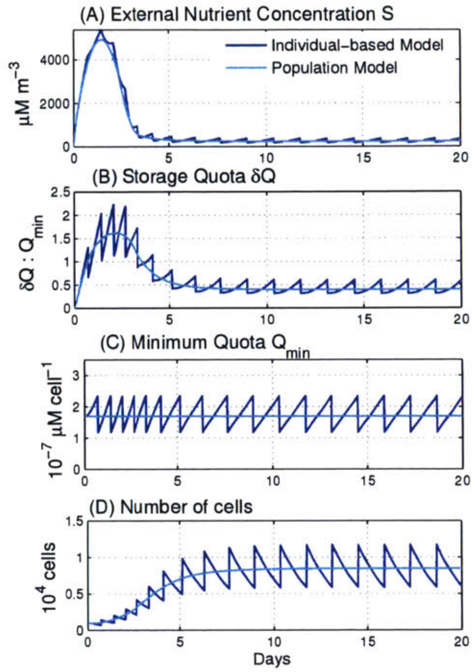

Figure A.6: Output of the population model and its individual-based model (IBM) analog for a point balance ($D = 0.5$ day^{-1}). The external nutrient concentration S (A), the internal storage quota δQ (B), the minimum quota Q_{min} (C), and the number of cells are visibly equivalent for the two models. Due to the nonlinearity from the synchronous cell growth, the steady state quota of the population model differs by 0.3% from that of the IBM.

of the IBM result from identical initial conditions, but the nonlinearity of this oscillation prohibits exact numerical equivalence.

Determining the degree of equivalence thus requires comparison of the numerical solutions. To compare the models, we quantify the departure of the population model from the mean quota of the individuals in the IBM. We calculate the error of the population model with respect to the individual model for the storage quota and for the population density (see below). In Figure A.6, the error for δQ with respect to δq of the IBM is 0.3%.

The ability to represent the population as a continuum breaks down as the population size decreases. This occurs as dilution rates approach the effective maximum growth rate of the cell population. As this happens, the steady state population size approaches zero; 'washout' in chemostat experiments. As an objective criteria for the continuum assumption, we report model output for which the IBM resulted in at least 5,000 individuals for every grid box.

Quantifying the degree of equivalence of the population and individual-based models

For the density-based population model, variables converge to fixed values at steady state. But for the IBM, the explicit cell growth and division causes the quotas to oscillate at steady state. The blending of two populations gives an unpredictable period and shape of this oscillation, and so, quantifying model equivalence required averaging model output over a period of time. Convergence to a steady state value occurred when results were averaged over at least fifteen cell cycles; all results were averaged over at least this many cycles. All model output presented here was spun up for fifty days, and then averaged over fifty days at steady state.

The storage quota δQ changes with the environment, and thus is the comparison of interest between the continuous and individual models. In the IBM, explicit cell division warrants first weighting δq by the number of individuals at each time step, producing a weighted time series, $\delta q'$, as:

$$\delta q'(t) = \delta q(t) * n(t) * \left(\frac{1}{T} \sum_{t=1}^{T} n(t) \right)^{-1} \tag{A.19}$$

where T is the total number of time steps in the fifty day period, and n is the number of individuals at a timestep t. The error between the population and individual model predictions of the storage quota is then calculated as:

$$Error = \frac{1}{T} \sum_{t=1}^{T} \left(\frac{\delta Q(t)}{\delta q'(t)} - 1 \right) \tag{A.20}$$

Considering the error in this way, as a mean, ensures that an error of zero is possible, should the median of the IBM fluctuations exactly match the population model.

The ability of the quota model to match the IBM in terms of the minimum quota serves as the underlying premise from which the two models are deemed equivalent. Thus, calculating the mean error as above for the fixed quota, Q_{min}, relative to the weighted time series of q_{min} serves as calibration of the two models. Due to nonlinearities in the IBM, this error was not exactly zero, but was assured to be 1% or less for all results.

Parameter Values

The model uses the allometric relationships for nitrogen uptake and storage published by Litchman et al. (2007) to calculate Q_{min}, ρ_{max}, and K_{ρ} from cell volume (Table 1). The theoretical purpose of this study permits the use of these empirical relationships despite uncertainties and species variance of actual cell budgets (Lourenco et al. 1998; Dortch et al. 1984; Geider and La Roche 2002). Cell volume was calculated from a prescribed diameter of 10 μm assuming a spherical shape.

In the IBM, the parameter q_{minL} determines the frequency of cell division. When q_{min} reaches q_{minL}, the cell divides, and the new cells each contain half of q_{minL}. The time average of q_{min} is thus analogous to Q_{min} in the population model. Since the time average of q_{min}

is not prescribed directly, we specify q_{minL} so that q_{min} equals Q_{min}. Theoretically, q_{minL} relates to the time average of q_{min} by a factor of $2ln(2)$, since the growth rate is defined as a doubling at an exponential rate. We thus specify:

$$q_{minL} = Q_{min} \cdot (2ln(2)) \tag{A.21}$$

The external nutrients were depleted to such low levels immediately following synchronous cell division that the rate of synthesis exceeded uptake rate, which affected the ability of the models to accurately match. To avoid this effect, quotas of cells were initialized with a range of quota values: an equal distribution from $q_{minL}/2$ to q_{minL}.

The maximum growth rate μ_∞ sets a second biological timescale in the quota model, after the maximum external nutrient uptake rate V_{max}. The two timescales are related by considering $\mu_\infty Q_{min}$ as a maximum synthesis rate. Then, the ratio $r = V_{max} : \mu_\infty Q_{min}$ represents the ratio of external nutrient uptake to biomass synthesis, and thus influences the location of the bottleneck limiting cell growth. For r greater than one, maximum synthesis is smaller than maximum uptake, and cell growth is likely to be limited by synthesis, which allows for the accumulation of nutrient storage: a larger δQ^*. For r less than one, cell growth is more likely to be limited by external uptake, minimizing δQ^*. This ratio represents a particular phytoplankton physiology. We determine this ratio r, and then calculate the corresponding μ_∞ parameter as:

$$\mu_\infty = \frac{\rho_{max}}{r\ Q_{min}} \tag{A.22}$$

We can gain more insight into our model dynamics by examining the expression for the steady state quota, Q^*, derived from Eqn. A.15:

$$\rho = \mu Q^* \tag{A.23}$$

Substituting in Eqns. 1 and 2 then gives Q^* in terms of parameters and external nutrient concentration:

$$Q^* = Q_{min}\left(1 + \frac{\rho_{max}}{\mu_\infty Q_{min}} \frac{S}{K_\rho + S}\right) \tag{A.24}$$

We can then rearrange the above to express δQ^* normalized by Q_{min}, and substituting in r, as:

$$\frac{\delta Q^*}{Q_{min}} = r \frac{S}{K_\rho + S} \tag{A.25}$$

The normalized storage quota is thus limited by the external nutrient uptake, and can reach a maximum value of r. For all results shown here, $r = 2$.

For each simulation, the model was run to equilibration with an explicit Euler forward scheme with a 0.6 hour time step. Box volume was 10^{-7} m^3 and S_0 was 20 μM.

A.A.2 Pseudocode for the numerical scheme in 2D

For point (i, j) in a 2D model, the unmodified growth rate μ is:

$$\mu_{i,j} = \mu_{\max} \frac{Q_{i,j} - Q_{min}}{Q_{i,j}} \tag{A.26}$$

For positive velocities u and v, incoming cells with quotas $Q_{i-1,j}$ and $Q_{i,j-1}$ can cause the heterogeneity. The growth rate of this incoming population, $\mu_{in,avg}$, is:

$$\mu_{in,avg} = \mu_{\max} \frac{Q_{in,avg} - Q_{min}}{Q_{in,avg}} \tag{A.27}$$

where

$$Q_{in,avg} = \frac{uX_{i-1,j}(Q_{i-1,j}) + vX_{i,j-1}(Q_{i,j-1})}{uX_{i-1,j} + vX_{i,j-1}} \tag{A.28}$$

where X is biomass concentration. The weighted average of the modification that incorporates the heterogeneity, μ_{het}, is calculated from each of the incoming quotas:

$$\mu_{in,het} = \mu_{max} \left[\frac{uX_{i-1,j}}{uX_{i-1,j} + vX_{i,j-1}} \left(\frac{Q_{i-1,j} - Q_{min}}{Q_{i-1,j}} \right) + \frac{uX_{i,j-1}}{uX_{i-1,j} + vX_{i,j-1}} \left(\frac{Q_{i,j-1} - Q_{min}}{Q_{i,j-1}} \right) \right] \tag{A.29}$$

The original growth rate calculation can then be modified to reflect ratio of these two:

$$\mu_{i,j} = \mu_{\max} \frac{Q_{i,j} - Q_{min}}{Q_{i,j}} \cdot \frac{\mu_{in,het}}{\mu_{in,avg}} \tag{A.30}$$

Results suggest applying this modification conditionally, for when error is predicted to be greater than 1%:

```
if
    $\frac{\mu_{in,avg}}{\mu_{in,het}} > 0.01$
then
    $\mu_{i,j} = \mu_{\max} \frac{Q_{i,j} - Q_{min}}{Q_{i,j}} \cdot \frac{\mu_{in,het}}{\mu_{in,avg}}$
else
    $\mu_{i,j} = \mu_{\max} \frac{Q_{i,j} - Q_{min}}{Q_{i,j}}$
end
```

References

Algar, C., and J. Vallino. 2014. Predicting microbial nitrate reduction pathways in coastal sediments. *Aquat. Microb. Ecol.*, **71**, 223–238, doi:10.3354/ame01678.

Allison, S. D., and J. B. H. Martiny. 2008. Resistance, resilience, and redundancy in microbial communities. *Proc. Natl. Acad. Sci. U. S. A.*, **105**, 11 512–9, doi:10.1073/pnas.0801925105.

Anderson, L. A.. 1995. On the hydrogen and oxygen content of marine phytoplankton. *Deep Sea Res. Part I Oceanogr. Res. Pap.*, **42 (9)**, 1675–1680, doi:10.1016/0967-0637(95)00072-E.

Anderson, T. R., V. A. Ryabchenko, M. J. R. Fasham, and V. A. Gorchakov. 2007. Denitrification in the Arabian Sea: A 3D ecosystem modelling study. *Deep Sea Res. Part I Oceanogr. Res. Pap.*, **54**, 2082–2119, doi:10.1016/j.dsr.2007.09.005.

Aristegui, J., J. M. Gasol, C. M. Duarte, and G. J. Herndl. 2009. Microbial oceanography of the dark oceans pelagic realm. *Limnol. Oceanogr.*, **54 (5)**, 1501–1529, doi:10.4319/lo.2009.54.5.1501.

Armbrust, E. V., and S. R. Palumbi. 2015. Uncovering hidden worlds of ocean biodiversity. *Science*, **348 (6237)**, 865–867, doi:10.1126/science.aaa7378.

Armstrong, R. A.. 1994. Grazing limitation and nutrient limitation in marine ecosystems: Steady state solutions of an ecosystem model with multiple food chains. *Limnol. Oceanogr.*, **39 (3)**, 597–608, doi:10.4319/lo.1994.39.3.0597.

Armstrong, R. A.. 2008. Nutrient uptake rate as a function of cell size and surface transporter density: A Michaelis-like approximation to the model of Pasciak and Gavis. *Deep. Res. Part I Oceanogr. Res. Pap.*, **55**, 1311–1317, doi:10.1016/j.dsr.2008.05.004.

Azam, F., and F. Malfatti. 2007. Microbial structuring of marine ecosystems. *Nat. Rev. Microbiol.*, **5**, 782–791, doi:10.1038/nrmicro1747.

Babbin, A. R., D. Bianchi, A. Jayakumar, and B. B. Ward. 2015. Rapid nitrous oxide cycling in the suboxic ocean. *Science*, **348 (6239)**, 1127–1129, doi:10.1126/science.aaa8380.

Babbin, A. R., R. G. Keil, A. H. Devol, and B. B. Ward. 2014. Organic matter stoichiometry, flux, and oxygen control nitrogen loss in the ocean. *Science*, **344**, 406–8, doi:10.1126/science.1248364.

Babbin, A. R., B. D. Peters, C. W. Mordy, B. Widner, K. L. Casciotti, and B. B. Ward. 2017. Novel metabolisms support the anaerobic nitrite budget in the Eastern Tropical South Pacific. *Global Biogeochem. Cycles*, **31**, 1–14, doi:10.1002/2016GB005407.

Barberán, A., E. O. Casamayor, and N. Fierer. 2014. The microbial contribution to macroecology. *Front. Microbiol.*, **5**, 1–8, doi:10.3389/fmicb.2014.00203.

Barton, A. D., S. Dutkiewicz, G. Flierl, J. Bragg, and M. J. Follows. 2010. Patterns of diversity in marine phytoplankton. *Science*, **327**, 1509–1511, doi:10.1126/science.1184961.

Bellucci, M., I. D. Ofieru, L. Beneduce, D. W. Graham, I. M. Head, and T. P. Curtis. 2015. A preliminary and qualitative study of resource ratio theory to nitrifying lab-scale bioreactors. *Microb. Biotechnol.*, **8**, 590–603, doi:10.1111/1751-7915.12284.

Bianchi, D., A. R. Babbin, and E. D. Galbraith. 2014. Enhancement of anammox by the excretion of diel vertical migrators. *Proc. Natl. Acad. Sci.*, **111**, 15 653–15 658, doi:10.1073/pnas.1410790111.

Bianchi, D., J. P. Dunne, J. L. Sarmiento, and E. D. Galbraith. 2012. Data-based estimates of suboxia, denitrification, and N2O production in the ocean and their sensitivities to dissolved O2. *Global Biogeochem. Cycles*, **26**, doi:10.1029/2011GB004209.

Biller, S. J., A. Coe, and S. W. Chisholm. 2016. Torn apart and reunited: impact of a heterotroph on the transcriptome of Prochlorococcus. *ISME J.*, **10**, 2831–2843, doi:10.1038/ismej.2016.82.

Blackford, J., J. Allen, and F. Gilbert. 2004. Ecosystem dynamics at six contrasting sites: a generic modelling study. *J. Mar. Syst.*, **52 (1-4)**, 191–215, doi:10.1016/j.jmarsys.2004.02.004.

Bonachela, J. A., M. Raghib, and S. A. Levin. 2011. Dynamic model of flexible phytoplankton nutrient uptake. *Proc. Natl. Acad. Sci.*, **108 (51)**, 20 633–20 638, doi:10.1073/pnas.1201165109.

Bott, M., and A. Niebisch. 2003. The respiratory chain of Corynebacterium glutamicum. *J. Biotechnol.*, **104**, 129–153, doi:10.1016/S0168-1656(03)00144-5.

Bouskill, N. J., J. Tang, W. J. Riley, and E. L. Brodie. 2012. Trait-based representation of biological nitrification: Model development, testing, and predicted community composition. *Front. Microbiol.*, **3**, doi:10.3389/fmicb.2012.00364.

Bowen, J. L., A. R. Babbin, P. J. Kearns, and B. B. Ward. 2014. Connecting the dots: linking nitrogen cycle gene expression to nitrogen fluxes in marine sediment mesocosms. *Front. Microbiol.*, **5**, doi:10.3389/fmicb.2014.00429.

Brandt, P., and Coauthors. 2015. On the role of circulation and mixing in the ventilation of oxygen minimum zones with a focus on the eastern tropical North Atlantic. *Biogeosciences*, **12**, 489–512, doi:10.5194/bg-12-489-2015.

Bratbak, G., and I. Dundas. 1984. Bacterial dry matter content and biomass estimations. *Appl. Environ. Microbiol.*, **48 (4)**, 755–7.

Brewer, P. G., A. F. Hofmann, E. T. Peltzer, and W. Ussler, III. 2014. Evaluating microbial chemical choices: The ocean chemistry basis for the competition between use of O2 or NO3 as an electron acceptor. *Deep Sea Res. Part I Oceanogr. Res. Pap.*, **87**, 35–42, doi:10.1016/j.dsr.2014.02.002.

Bristow, L. A., and Coauthors. 2016a. Ammonium and nitrite oxidation at nanomolar oxygen concentrations in oxygen minimum zone waters. *Proc. Natl. Acad. Sci. U. S. A.*, **113 (38)**, 10 601–6, doi:10.1073/pnas.1600359113.

Bristow, L. A., and Coauthors. 2016b. N2 production rates limited by nitrite availability in the Bay of Bengal oxygen minimum zone. *Nat. Geosci.*, doi:10.1038/ngeo2847.

Bryant, J. A., F. J. Stewart, J. M. Eppley, and E. F. DeLong. 2012. Microbial community phylogenetic and trait diversity declines with depth in a marine oxygen minimum zone. *Ecology*, **93 (7)**, 1659–73.

Bucci, V., D. Nunez-Milland, B. S. Twining, and F. L. Hellweger. 2011. Microscale patchiness leads to large and important intraspecific internal nutrient heterogeneity in phytoplankton. *Aquat. Ecol.*, **46**, 101–118, doi:10.1007/s10452-011-9384-6.

Buchwald, C., and K. L. Casciotti. 2013. Isotopic ratios of nitrite as tracers of the sources and age of oceanic nitrite. *Nat. Publ. Gr.*, **6**, 1–6, doi:10.1038/ngeo1745.

Buesseler, K. O., and P. W. Boyd. 2009. Shedding light on processes that control particle export and flux attenuation in the twilight zone of the open ocean. *Limnol. Oceanogr.*, **54 (4)**, 1210–1232, doi:10.4319/lo.2009.54.4.1210.

Buesseler, K. O., and Coauthors. 2007. Revisiting carbon flux through the ocean's twilight zone. *Science*, **316 (5824)**, 567–70, doi:10.1126/science.1137959.

Bulow, S. E., J. J. Rich, H. S. Naik, A. K. Pratihary, and B. B. Ward. 2010. Denitrification exceeds anammox as a nitrogen loss pathway in the Arabian Sea oxygen minimum zone. *Deep Sea Res. Part I Oceanogr. Res. Pap.*, **57**, 384–393, doi:10.1016/j.dsr.2009.10.014.

Burmaster, D. E.. 1979. The Unsteady Continuous Culture of Phosphate-Limited MONOCHRYSIS LUTHERI Droop: Experimental and Theoretical Analysis. *J. Exp. Mar. Bio. Ecol.*, **39**, 167–186, doi:10.1016/0022-0981(79)90012-1.

Cabré, A., I. Marinov, R. Bernardello, and D. Bianchi. 2015. Oxygen minimum zones in the tropical Pacific across CMIP5 models: Mean state differences and climate change trends. *Biogeosciences*, **12**, 5429–5454, doi:10.5194/bg-12-5429-2015.

Canfield, D. E., F. J. Stewart, B. Thamdrup, L. De Brabandere, T. Dalsgaard, E. F. Delong, N. P. Revsbech, and O. Ulloa. 2010. A cryptic sulfur cycle in oxygen-minimum-zone waters off the Chilean coast. *Science*, **330**, 1375–8, doi:10.1126/science.1196889.

Caperon, J., and J. Meyer. 1972. Nitrogen-limited growth of marine phytoplankton–I . Changes in population characteristics with steady-state growth rate*. *Deep Sea Res.*, **19**, 601–618, doi:10.1016/0011-7471(72)90089-7.

Carlson, C. A., P. A. del Giorgio, and G. J. Herndl. 2007. Microbes and the Dissipation of Energy and Respiration: From Cells to Ecosystems. *Oceanography*, 89–100.

Cavagna, A. J., and Coauthors. 2015. Production regime and associated N cycling in the vicinity of Kerguelen Island, Southern Ocean. *Biogeosciences*, **12**, 6515–6528, doi:10.5194/bg-12-6515-2015.

Chen, J., and M. Strous. 2013. Denitrification and aerobic respiration, hybrid electron transport chains and co-evolution. *Biochim. Biophys. Acta*, **1827**, 136–144, doi:10.1016/j.bbabio.2012.10.002.

Church, M. J., D. A. Hutchins, and W. Hugh. 2000. Limitation of Bacterial Growth by Dissolved Organic Matter and Iron in the Southern Ocean. *Appl. Environ. Microbiol.*, **66 (2)**, 455–466, doi:10.1128/AEM.66.2.455-466.2000.

Clark, D. R., A. P. Rees, I. Joint, S. Limnology, N. Jan, D. R. Clark, A. P. Rees, and I. Joint. 2008. Ammonium regeneration and nitrification rates in the oligotrophic Atlantic Ocean: Implications for new production estimates. *Limnol. Oceanogr.*, **53 (1)**, 52–62, doi:10.4319/lo.2008.53.1.0052.

Clayton, S., S. Dutkiewicz, O. Jahn, and M. J. Follows. 2013. Dispersal, eddies, and the diversity of marine phytoplankton. *Limnol. Oceanogr. Fluids Environ.*, **3**, 182–197, doi:10.1215/21573689-2373515.

Coles, V. J., and R. R. Hood. 2016. Approaches and Challenges for Linking Marine Biogeochemical Models with the Omics Revolution. *Aquat. Microb. Ecol. Biogeochem. A Dual Perspect.*, P. M. Glibert, and T. M. Kana, Eds., Springer, 171–183, doi:10.1007/978-3-319-30259-1.

Costa, E., J. Pérez, and J.-U. Kreft. 2006. Why is metabolic labour divided in nitrification? *Trends Microbiol.*, **14 (5)**, 213–219, doi:10.1016/j.tim.2006.03.006.

Croucher, N. J., R. Mostowy, C. Wymant, P. Turner, S. D. Bentley, and C. Fraser. 2016. Horizontal DNA Transfer Mechanisms of Bacteria as Weapons of Intragenomic Conflict. *PLoS Biol.*, **14 (3)**, doi:10.1371/journal.pbio.1002394.

Cuevas, L. A., and C. E. Morales. 2006. Nanoheterotroph grazing on bacteria and cyanobacteria in oxic and suboxic waters in coastal upwelling areas off northern Chile. *J. Plankton Res.*, **28 (4)**, 385–397, doi:10.1093/plankt/fbi124.

Daims, H., S. Lücker, and M. Wagner. 2016. A New Perspective on Microbes Formerly Known as Nitrite-Oxidizing Bacteria. *Trends Microbiol.*, **24 (9)**, 699–712, doi:10.1016/j.tim.2016.05.004.

Daims, H., and Coauthors. 2015. Complete nitrification by Nitrospira bacteria. *Nature*, **528 (7583)**, 504–509, doi:10.1038/nature16461.

Dalsgaard, T., B. Thamdrup, L. Farías, and N. Peter Revsbech. 2012. Anammox and denitrification in the oxygen minimum zone of the eastern South Pacific. *Limnol. Oceanogr.*, **57 (5)**, 1331–1346, doi:10.4319/lo.2012.57.5.1331.

Dalsgaard, T., and Coauthors. 2014. Oxygen at Nanomolar Levels Reversibly Suppresses Process Rates and Gene Expression in Anammox and Denitrification in the Oxygen. *MBio*, **5 (6)**, doi:10.1128/mBio.01966-14.

De Brabandere, L., D. E. Canfield, T. Dalsgaard, G. E. Friederich, N. P. Revsbech, O. Ulloa, and B. Thamdrup. 2014. Vertical partitioning of nitrogen-loss processes across the oxic-anoxic interface of an oceanic oxygen minimum zone. *Environ. Microbiol.*, **16 (10)**, 3041–3054, doi:10.1111/1462-2920.12255.

De Brabandere, L., B. Thamdrup, N. P. Revsbech, and R. Foadi. 2012. A critical assessment of the occurrence and extend of oxygen contamination during anaerobic incubations utilizing commercially available vials. *J. Microbiol. Methods*, **88 (1)**, 147–154, doi:10.1016/j.mimet.2011.11.001.

del Giorgio, P. A., and J. J. Cole. 1998. Bacterial Growth Efficiency in Natural Aquatic Systems. *Annu. Rev. Ecol. Syst.*, **29**, 503–541, doi:10.1146/annurev.ecolsys.29.1.503.

del Giorgio, P. A., R. Condon, T. Bouvier, K. Longnecker, C. Bouvier, E. Sherr, and J. M. Gasol. 2011. Coherent patterns in bacterial growth, growth efficiency, and leucine metabolism along a northeastern Pacific inshore-offshore transect. *Limnol. Oceanogr.*, **56 (1)**, 1–16, doi:10.4319/lo.2011.56.1.0001.

DeLong, E. F., and D. M. Karl. 2005. Genomic perspectives in microbial oceanography. *Nature*, **437 (7057)**, 336–42, doi:10.1038/nature04157.

Delong, E. F., and N. R. Pace. 2001. Environmental Diversity of Bacteria and Archaea. *Syst. Biol.*, **50 (4)**, 470–478, doi:10.1080/10635150118513, 3651.

Deutsch, C., H. Brix, T. Ito, H. Frenzel, and L. Thompson. 2011. Climate-forced variability of ocean hypoxia. *Science*, **333 (6040)**, 336–339, doi:10.1126/science.1202422.

Deutsch, C., A. Ferrel, B. Seibel, H.-O. Pörtner, and R. B. Huey. 2015. Climate change tightens a metabolic constraint on marine habitats. *Science*, **348 (6239)**, 1132–1136, doi:10.1126/science.aaa1605.

Devol, A. H.. 1978. Bacterial oxygen uptake kinetics as related to biological processes in oxygen deficient zones of the oceans*. *Deep Sea Res.*, **25**, 137–146, doi:10.1016/0146-6291(78)90001-2.

Devol, A. H.. 2008. Denitrification including Anammox. *Nitrogen Mar. Environ.*, D. G. Capone, D. A. Bronk, M. R. Mulholland, and E. J. Carpenter, Eds., 2nd ed., chap. 6, 263–301.

Dewar, R. C.. 2010. Maximum entropy production and plant optimization theories. *Philos. Trans. R. Soc. Lond. B. Biol. Sci.*, **365**, 1429–1435, doi:10.1098/rstb.2009.0293.

Dewar, R. C., and A. Maritan. 2014. A Theoretical Basis for Maximum Entropy Production. *Beyond Second Law*, R. C. Dewar, and A. Maritan, Eds., Springer-Verlag, Berlin, chap. 3, 49–71, doi:10.1007/978-3-642-40154-1-3.

Dick, J. M., and E. L. Shock. 2013. A metastable equilibrium model for the relative abundances of microbial phyla in a hot spring. *PLoS One*, **8 (9)**, doi:10.1371/journal.pone.0072395.

Dore, J. E., and D. M. Karl. 1996a. Nitrification in the euphotic zone as a source for Nitrite, Nitrate, and Nitrous oxide at Station ALOHA. *Limnol. Oceanogr.*, **41 (8)**, 1619–1628, doi:10.4319/lo.1996.41.8.1619.

Dore, J. E., and D. M. Karl. 1996b. Nitrite distributions and dynamics at Station ALOHA. *Deep. Res. II*, **43 (2-3)**, 385–402, doi:10.1016/0967-0645(95)00105-0.

Dortch, Q., J. Clayton Jr., S. Thoresen, and S. Ahmed. 1984. Species differences in accumulation of nitrogen pools in phytoplankton. *Mar. Biol.*, **81**, 237–250.

Droop, M. R.. 1973. Some Thoughts on Nutrient Limitation in Algae. *J. Phycol.*, **9**, 264–272.

Ducklow, H.. 2000. Bacterial Production and Biomass in the Oceans. *Microb. Ecol. Ocean*, D. L. Kirchman, Ed., Wiley-Liss, Inc, chap. 4, 85–120.

Dugdale, R. C., and J. J. Goering. 1967. Uptake of new and regenerated forms of nitrogen in primary productivity. *Limnol. Oceanogr.*, **12 (2)**, 196–206, doi:10.4319/lo.1967.12.2.0196.

Dunne, J. P., and Coauthors. 2012. GFDLs ESM2 global coupled climate-carbon Earth System Models Part II: Carbon system formulation and baseline simulation characteristics. *J. Clim.*, **26**, 2247–2267, doi:10.1175/JCLI-D-12-00150.1.

Dutkiewicz, S., M. Follows, J. Marshall, and W. W. Gregg. 2001. Interannual variability of phytoplankton abundances in the North Atlantic. *Deep Sea Res. Part II Top. Stud. Oceanogr.*, **48**, 2323–2344, doi:10.1016/S0967-0645(00)00178-8.

Dutkiewicz, S., J. J. Morris, M. J. Follows, J. Scott, O. Levitan, S. T. Dyhrman, and I. Berman-Frank. 2015. Impact of ocean acidification on the structure of future phytoplankton communities. *Nat. Clim. Chang.*, **5**, 1002–1006, doi:10.1038/nclimate2722.

Dutkiewicz, S., J. R. Scott, and M. J. Follows. 2013. Winners and losers: Ecological and biogeochemical changes in a warming ocean. *Global Biogeochem. Cycles*, **27**, 463–477, doi:10.1002/gbc.20042.

Dutkiewicz, S., B. A. Ward, J. R. Scott, and M. J. Follows. 2014. Understanding predicted shifts in diazotroph biogeography using resource competition theory. *Biogeosciences*, **11**, 5445–5461, doi:10.5194/bg-11-5445-2014.

Elowitz, M. B., A. J. Levine, E. D. Siggia, and P. S. Swain. 2002. Stochastic Gene Expression in a Single Cell. *Science*, **297 (5584)**, 1183–1186, doi:10.1126/science.1070919.

Eppley, R. W., and B. J. Peterson. 1979. Particulate organic matter flux and planktonic new production in the deep ocean. *Nature*, **282 (5740)**, 677–680, doi:10.1038/282677a0.

Escribano, R., P. Hidalgo, and C. Krautz. 2009. Zooplankton associated with the oxygen minimum zone system in the northern upwelling region of Chile during March 2000. *Deep Sea Res. Part II*, **56**, 1049–1060, doi:10.1016/j.dsr2.2008.09.009.

Falkowski, P. G., T. Fenchel, and E. F. Delong. 2008. The microbial engines that drive Earth's biogeochemical cycles. *Science*, **320 (5879)**, 1034–9, doi:10.1126/science.1153213.

Fasham, M. J. R., H. W. Ducklow, and S. M. McKelvie. 1990. A nitrogen-based model of plankton dynamics in the ocean mixed layer. *J. Mar. Res.*, **48**, 591–639, doi:10.1357/002224090784984678.

Fenchel, T., and B. Finlay. 1995. *Ecology and Evolution in Anoxic Worlds*. Oxford Series in Ecology and Evolution.

Fiksen, Ø., M. J. Follows, and D. L. Aksnes. 2013. Trait-based models of nutrient uptake in microbes extend the Michaelis-Menten framework. *Limnol. Oceanogr.*, **58 (1)**, 193–202, doi:10.4319/lo.2013.58.1.0193.

Flynn, K. J.. 2008. The importance of the form of the quota curve and control of non-limiting nutrient transport in phytoplankton models. *J. Plankton Res.*, **30**, 423–438, doi:10.1093/plankt/fbn007.

Follows, M. J., and S. Dutkiewicz. 2011. Modeling Diverse Communities of Marine Microbes. *Ann. Rev. Mar. Sci.*, **3**, 427–451, doi:10.1146/annurev-marine-120709-142848.

Follows, M. J., S. Dutkiewicz, S. Grant, and S. W. Chisholm. 2007. Emergent biogeography of microbial communities in a model ocean. *Science*, **315 (5820)**, 1843–6, doi:10.1126/science.1138544.

Forget, G.. 2010. Mapping Ocean Observations in a Dynamical Framework: A 200406 Ocean Atlas. *J. Phys. Oceanogr.*, **40**, 1201–1221, doi:10.1175/2009JPO4043.1.

Franks, P. J. S.. 2002. NPZ Models of Plankton Dynamics: Their Construction, Coupling to Physics, and Application. *J. Oceanogr.*, **58**, 379–387.

Frentz, Z., S. Kuehn, and S. Leibler. 2015. Strongly deterministic population dynamics in closed microbial communities. *Phys. Rev. X*, **5 (4)**, doi:10.1103/PhysRevX.5.041014.

Fripiat, F., and Coauthors. 2015. Significant mixed layer nitrification in a natural iron-fertilized bloom of the Southern Ocean. *Global Biogeochem. Cycles*, doi:10.1002/2014GB005051.

Füssel, J., P. Lam, G. Lavik, M. M. Jensen, M. Holtappels, M. Günter, and M. M. M. Kuypers. 2012. Nitrite oxidation in the Namibian oxygen minimum zone. *ISME J.*, **6**, 1200–9, doi:10.1038/ismej.2011.178.

Geider, R., and J. La Roche. 2002. Redfield revisited: variability of C:N:P in marine microalgae and its biochemical basis. *Eur. J. Phycol.*, **37**, 1–17, doi:10.1017/S0967026201003456.

Gerard, R. W.. 1931. Oxygen Diffusion Into Cells. *Biol. Bull.*, **60**, 245–268.

Gnanadesikan, A., J. P. Dunne, and J. John. 2012. Understanding why the volume of suboxic waters does not increase over centuries of global warming in an Earth System Model. *Biogeosciences*, **9**, 1159–1172, doi:10.5194/bg-9-1159-2012.

Goldman, J. C., D. a. Caron, and M. R. Dennett. 1987. Regulation of gross growth efficiency and ammonium regeneration in bacteria by substrate C:N ratio. *Limnol. Ocean.*, **32 (6)**, 1239–1252, doi:10.4319/lo.1987.32.6.1239.

Gong, X., E. Garcia-Robledo, A. Schramm, and N. P. Revsbech. 2016. Respiratory kinetics of marine bacteria exposed to decreasing oxygen concentrations. *Appl. Environ. Microbiol.*, **82**, 1412–1422, doi:10.1128/AEM.03669-15.

Gonsalves, M.-J., A. Paropkari, C. Fernandes, P. Loka Bharathi, L. Krishnakumari, V. Fernando, and G. Nampoothiri. 2011. Predominance of anaerobic bacterial community over aerobic community contribute to intensify oxygen minimum zone in the eastern Arabian Sea. *Cont. Shelf Res.*, **31**, 1224–1235, doi:10.1016/j.csr.2011.04.011.

Green, J. L., B. J. M. Bohannan, and R. J. Whitaker. 2008. Microbial biogeography: from taxonomy to traits. *Science*, **320**, 1039–1043, doi:10.1126/science.1153475.

Gruber, N., and J. N. Galloway. 2008. An Earth-system perspective of the global nitrogen cycle. *Nature*, **451 (7176)**, 293–6, doi:10.1038/nature06592.

Gruber, N., and J. L. Sarmiento. 1997. Global patterns of marine nitrogen fixation and denitrification. *Global Biogeochem. Cycles*, **11 (2)**, 235–266.

Gutknecht, E., and Coauthors. 2013. Coupled physical/biogeochemical modeling including O2-dependent processes in the Eastern Boundary Upwelling Systems: application in the Benguela. *Biogeosciences*, **10**, 3559–3591, doi:10.5194/bg-10-3559-2013.

Hawley, a. K., H. M. Brewer, a. D. Norbeck, L. Pa a Toli, and S. J. Hallam. 2014. Metaproteomics reveals differential modes of metabolic coupling among ubiquitous oxygen minimum zone microbes. *Proc. Natl. Acad. Sci.*, **111 (31)**, 11 395–11 400, doi:10.1073/pnas.1322132111.

Heijnen, J. J., and J. A. Roels. 1981. A Macroscopic Model Describing Yield and Maintenance Relationships in Aerobic Fermentation Processes. *Biotechnol. Bioeng.*, **XXIII**, 739–763.

Hellerman, S., and M. Rosenstein. 1983. Normal monthly wind stress over the world ocean with error estimates. *J. Phys. Oceanogr.*, **13**, 1093–1104, doi:10.1175/1520-0485(1983)013<1093:NMWSOT>2.0.CO;2.

Hellweger, F. L., and E. Kianirad. 2007a. Accounting for intrapopulation variability in biogeochemical models using agent-based methods. *Environ. Sci. Technol.*, **41 (8)**, 2855–60.

Hellweger, F. L., and E. Kianirad. 2007b. Individual-based modeling of phytoplankton: Evaluating approaches for applying the cell quota model. *J. Theor. Biol.*, **249**, 554–65, doi:10.1016/j.jtbi.2007.08.020.

Henson, S. A., R. Sanders, E. Madsen, P. J. Morris, F. Le Moigne, and G. D. Quartly. 2011. A reduced estimate of the strength of the ocean's biological carbon pump. *Geophys. Res. Lett.*, **38**, doi:10.1029/2011GL046735.

Hood, R. R., E. A. Laws, M. J. Follows, and D. Siegel. 2007. Modeling and prediction of marine microbial populations in the genomic era. *Oceanography*, 155–165, doi:10.5670/oceanog.2007.61.

Hug, L. A., and Coauthors. 2016. A new view of the tree and life's diversity. *Nat. Microbiol.*, **1**, doi:10.1038/nmicrobiol.2016.48.

Hutchinson, G. E.. 1961. The paradox of the plankton. *Am. Nat.*, **95 (882)**, 137–145, doi:10.1086/282171.

IPCC. 2014. Climate Change 2014: Synthesis Report. Contribution of Working Groups I, II and III to the Fifth Assessment Report of the Intergovernmental Panel on Climate Change. Tech. rep.

Jayakumar, A., G. D. O'Mullan, S. W. A. Naqvi, and B. B. Ward. 2009. Denitrifying bacterial community composition changes associated with stages of denitrification in oxygen minimum zones. *Microb. Ecol.*, **58**, 350–362, doi:10.1007/s00248-009-9487-y.

Jayakumar, A., X. Peng, and B. B. Ward. 2013. Community composition of bacteria involved in fixed nitrogen loss in the water column of two major oxygen minimum zones in the ocean. *Aquat. Microb. Ecol.*, **70**, 245–259, doi:10.3354/ame01654.

Jensen, M. M., M. M. M. Kuypers, G. Lavik, and B. Thamdrup. 2008. Rates and regulation of anaerobic ammonium oxidation and denitrification in the Black Sea. *Limnol. Oceanogr.*, **53 (1)**, 23–36, doi:10.4319/lo.2008.53.1.0023.

Jensen, M. M., P. Lam, N. P. Revsbech, B. Nagel, B. Gaye, M. S. Jetten, and M. M. Kuypers. 2011. Intensive nitrogen loss over the Omani Shelf due to anammox coupled with dissimilatory nitrite reduction to ammonium. *ISME J.*, **5**, 1660–1670, doi:10.1038/ismej.2011.44.

Jol, S. J., A. Kümmel, V. Hatzimanikatis, D. A. Beard, and M. Heinemann. 2010. Thermodynamic calculations for biochemical transport and reaction processes in metabolic networks. *Biophys. J.*, **99**, 3139–44, doi:10.1016/j.bpj.2010.09.043.

Kalvelage, T., and Coauthors. 2011. Oxygen sensitivity of anammox and coupled N-cycle processes in oxygen minimum zones. *PLoS One*, **6 (12)**, doi:10.1371/journal.pone.0029299.

Kalvelage, T., and Coauthors. 2013. Nitrogen cycling driven by organic matter export in the South Pacific oxygen minimum zone. *Nat. Geosci.*, **6**, 228–234, doi:10.1038/ngeo1739.

Kalvelage, T., and Coauthors. 2015. Aerobic microbial respiration in oceanic oxygen minimum zones. *PLoS One*, **10 (7)**, doi:10.1371/journal.pone.0133526.

Karl, D. M., G. A. Knauer, J. H. Martin, and B. B. Ward. 1984. Bacterial chemolithotrophy in the ocean is associated with sinking particles. *Nature*, **309**, 54–56, doi:10.1038/309054a0.

Kartal, B., J. T. Keltjens, and M. S. M. Jetten. 2008. The Metabolism of Anammox. *Encycl. Life Sci.*, John Wiley and Sons, doi:10.1002/9780470015902.a0021315.

Kazamia, E., K. E. Helliwell, S. Purton, A. G. Smith, and G. Fussmann. 2016. How mutualisms arise in phytoplankton communities: building eco-evolutionary principles for aquatic microbes. *Ecol. Lett.*, **19**, 810–822, doi:10.1111/ele.12615.

Keeling, R. E., A. Körtzinger, and N. Gruber. 2010. Ocean deoxygenation in a warming world. *Ann. Rev. Mar. Sci.*, **2**, 199–229, doi:10.1146/annurev.marine.010908.163855.

Key, R., and Coauthors. 2015. Global Ocean Data Analysis Project, Version 2 (GLODAPv2). Tech. rep., Carbon Dioxide Invormation Analysis Center, Oak Ridge National Laboratory, US Dept. of Energy. doi:10.3334/CDIAC/OTG.NDP093-GLODAPv2.

Kihara, S., D. a. Hartzler, and S. Savikhin. 2014. Oxygen concentration inside a functioning photosynthetic cell. *Biophys. J.*, **106**, 1882–9, doi:10.1016/j.bpj.2014.03.031.

Kirchman, D. L.. 2016. Growth Rates of Microbes in the Oceans. *Ann. Rev. Mar. Sci.*, **8**, 285–309, doi:10.1146/annurev-marine-122414-033938.

Kirchman, D. L., and P. J. l. B. Williams. 2000. Introduction. *Microb. Ecol. Ocean*, D. L. Kirchman, Ed., Wiley-Liss, Inc, chap. 1, 1–46.

Klausmeier, C. A., E. Litchman, T. Daufresne, and S. A. Levin. 2004. Optimal nitrogen-to-phosphorus stoichiometry of phytoplankton. *Nature*, **429**, 171–174, doi:1.1029/2001GL014649.

Klawonn, I., S. Bonaglia, V. Brüchert, and H. Ploug. 2015. Aerobic and anaerobic nitrogen transformation processes in N2-fixing cyanobacterial aggregates. *ISME J.*, 1456–1466, doi:10.1038/ismej.2014.232.

Kleidon, a., Y. Malhi, and P. Cox. 2010. Maximum entropy production in environmental and ecological systems. *Philos. Trans. R. Soc. Lond. B. Biol. Sci.*, **365 (1545)**, 1297–1302, doi:10.1098/rstb.2010.0018.

Koeve, W., and P. Kähler. 2010. Heterotrophic denitrification vs. autotrophic anammox - quantifying collateral effects on the oceanic carbon cycle. *Biogeosciences*, **7**, 2327–2337, doi:10.5194/bg-7-2327-2010.

Lam, P., and M. M. M. Kuypers. 2011. Microbial Nitrogen Cycling Processes in Oxygen Minimum Zones. *Ann. Rev. Mar. Sci.*, **3**, 317–348, doi:10.1146/annurev-marine-120709-142814.

Lam, P., and Coauthors. 2007. Linking crenarchaeal and bacterial nitrification to anammox in the Black Sea. *Proc. Natl. Acad. Sci.*, **104 (17)**, 7104–7109, doi:10.1073/pnas.0611081104.

LaRowe, D. E., A. W. Dale, J. P. Amend, and P. Van Cappellen. 2012. Thermodynamic limitations on microbially catalyzed reaction rates. *Geochim. Cosmochim. Acta*, **90**, 96–109, doi:10.1016/j.gca.2012.05.011.

Le Quere, C., and Coauthors. 2005. Ecosystem dynamics based on plankton functional types for global ocean biogeochemistry models. *Glob. Chang. Biol.*, **11**, 2016–2040, doi:10.1111/j.1365-2486.2005.01004.x.

Lilja, E. E., and D. R. Johnson. 2016. Segregating metabolic processes into different microbial cells accelerates the consumption of inhibitory substrates. *ISME J.*, **10**, 1568–1578, doi:10.1038/ismej.2015.243.

Lindeman, R. L.. 1942. The trophic dynamics aspect of ecology. *Ecology*, **23 (4)**, 399–417, doi:10.1017/CBO9781107415324.004.

Lipschultz, F., S. C. Wofsy, B. B. Ward, L. A. Codispoti, G. Friedrich, and J. W. Elkins. 1990. Bacterial transformations of inorganic nitrogen in the oxygen-deficient waters of the Eastern Tropical South Pacific Ocean. *Deep Sea Res. Part A, Oceanogr. Res. Pap.*, **37 (10)**, 1513–1541, doi:10.1016/0198-0149(90)90060-9.

Lipson, D. A.. 2015. The complex relationship between microbial growth rate and yield and its implications for ecosystem processes. *Front. Microbiol.*, **6**, doi:10.3389/fmicb.2015.00615.

Litchman, E., C. A. Klausmeier, O. M. Schofield, and P. G. Falkowski. 2007. The role of functional traits and trade-offs in structuring phytoplankton communities: scaling from cellular to ecosystem level. *Ecol. Lett.*, **10**, 1170–81, doi:10.1111/j.1461-0248.2007.01117.x.

Lomas, M. W., and F. Lipschultz. 2006. Forming the primary nitrite maximum: Nitrifiers or phytoplankton? *Limnol. Ocean.*, **51 (5)**, 2453–2467, doi:10.4319/lo.2006.51.5.2453.

Long, M. C., C. Deutsch, and T. Ito. 2016. Finding forced trends in oceanic oxygen. *Global Biogeochem. Cycles*, **30**, 381–397, doi:10.1002/2015GB005310.

Lourenco, S. O., E. Barbarino, U. M. L. Marquez, and E. Aidar. 1998. DISTRIBUTION OF INTRACELLULAR NITROGEN IN MARINE MICROALGAE: BASIS FOR THE CALCULATION OF SPECIFIC NITROGEN-TO-PROTEIN CONVERSION FACTORS. *J. Appl. Phycol.*, **34**, 798–811.

Mackey, K. R. M., L. Bristow, D. R. Parks, M. A. Altabet, A. F. Post, and A. Paytan. 2011. The influence of light on nitrogen cycling and the primary nitrite maximum in a seasonally stratified sea. *Prog. Oceanogr.*, **91**, 545–560, doi:10.1016/j.pocean.2011.09.001.

Madigan, M. T., J. M. Martinko, D. A. Stahl, and D. P. Clark. 2013. *Brock Biology of Microorganisms*. 13th ed., Benjamin Cummings, San Francisco.

Mahadevan, A.. 2014. Eddy effects on biogeochemistry. *Nature*, **506**, 168–169, doi:10.1038/nature13048.

Maida, I., and Coauthors. 2013. Draft Genome Sequence of the Fast-Growing Bacterium Vibrio natriegens Strain DSMZ 759. *Genome Announc.*, **1 (4)**, doi:10.1186/1471-2164-9-75.9.

Marshall, J., C. Hill, L. Perelman, and A. Adcroft. 1997. Hydrostatic, quasi-hydrostatic, and nonhydrostatic ocean modeling. *J. Geophys. Res.*, **102**, 5733–5752.

Martens-Habbena, W., P. M. Berube, H. Urakawa, J. R. de la Torre, and D. A. Stahl. 2009. Ammonia oxidation kinetics determine niche separation of nitrifying Archaea and Bacteria. *Nature*, **461 (7266)**, 976–9, doi:10.1038/nature08465.

Martin, J. H., and S. E. Fitzwater. 1988. Iron deficiency limits phytoplankton growth in the north-east Pacific subarctic. 341–343 pp., doi:10.1038/331341a0.

Martin, J. H., G. A. Knauer, D. M. Karl, and W. W. Broenkow. 1987. VERTEX: carbon cycling in the northeast Pacific. *Deep Sea Res. Part A. Oceanogr. Res. Pap.*, **34 (2)**, 267–285, doi:10.1016/0198-0149(87)90086-0.

Martiny, A. C., K. Treseder, and G. Pusch. 2013. Phylogenetic conservatism of functional traits in microorganisms. *ISME J.*, **7**, 830–8, doi:10.1038/ismej.2012.160.

Martiny, J. B. H., and Coauthors. 2006. Microbial biogeography: putting microorganisms on the map. *Nat. Rev. Microbiol.*, **4**, 102–112, doi:10.1038/nrmicro1341.

Matsumoto, K., T. Hashioka, and Y. Yamanaka. 2007. Effect of temperature-dependent organic carbon decay on atmospheric pCO 2. *J. Geophys. Res.*, **112**, doi:10.1029/2006JG000187.

Merbt, S. N., D. A. Stahl, E. O. Casamayor, E. Marti, G. W. Nicol, and J. I. Prosser. 2012. Differential photoinhibition of bacterial and archaeal ammonia oxidation. *FEMS Microbiol. Lett.*, **327**, 41–46, doi:10.1111/j.1574-6968.2011.02457.x.

Meysman, F. J. R., and S. Bruers. 2007. A thermodynamic perspective on food webs: Quantifying entropy production within detrital-based ecosystems. *J. Theor. Biol.*, **249**, 124–139, doi:10.1016/j.jtbi.2007.07.015.

Meysman, F. J. R., and S. Bruers. 2010. Ecosystem functioning and maximum entropy production: a quantitative test of hypotheses. *Philos. Trans. R. Soc. Lond. B. Biol. Sci.*, **365**, 1405–1416, doi:10.1098/rstb.2009.0300.

Mincer, T. J., M. J. Church, L. T. Taylor, C. Preston, D. M. Karl, and E. F. DeLong. 2007. Quantitative distribution of presumptive archaeal and bacterial nitrifiers in Monterey Bay and the North Pacific Subtropical Gyre. *Environ. Microbiol.*, **9 (5)**, 1162–1175, doi:10.1111/j.1462-2920.2007.01239.x.

Moore, C. M., and Coauthors. 2013. Processes and patterns of oceanic nutrient limitation. *Nat. Geosci.*, **6**, 701–710, doi:10.1038/ngeo1765.

Morris, R. L., and T. M. Schmidt. 2013. Shallow breathing: bacterial life at low O(2). *Nat. Rev. Microbiol.*, **11**, 205–12, doi:10.1038/nrmicro2970.

Mutshinda, C. M., Z. V. Finkel, C. E. Widdicombe, A. J. Irwin, and N. Norden. 2016. Ecological equivalence of species within phytoplankton functional groups. *Funct. Ecol.*, **30**, 1714–1722, doi:10.1111/1365-2435.12641.

Najjar, R. G., and Coauthors. 2007. Impact of circulation on export production, dissolved organic matter, and dissolved oxygen in the ocean: Results from Phase II of the Ocean Carbon-cycle Model Intercomparison Project (OCMIP-2). *Global Biogeochem. Cycles*, **21**, doi:10.1029/2006GB002857.

Newell, S. E., A. R. Babbin, A. Jayakumar, and B. B. Ward. 2011. Ammonia oxidation rates and nitrification in the Arabian Sea. *Global Biogeochem. Cycles*, **25 (4)**, n/a–n/a, doi:10.1029/2010GB003940.

Olsen, A., and Coauthors. 2016. The global ocean data analysis project version 2 (GLODAPv2) - An internally consistent data product for the world ocean. *Earth Syst. Sci. Data*, **8**, 297–323, doi:10.5194/essd-8-297-2016.

Paulmier, A., and D. Ruiz-Pino. 2009. Oxygen minimum zones (OMZs) in the modern ocean. *Prog. Oceanogr.*, **80**, 113–128, doi:10.1016/j.pocean.2008.08.001.

Peng, X., C. A. Fuchsman, A. Jayakumar, S. Oleynik, W. Martens-Habbena, A. H. Devol, and B. B. Ward. 2015. Ammonia and nitrite oxidation in the Eastern Tropical North Pacific. *Global Biogeochem. Cycles*, **29**, doi:10.1002/2015GB005278.

Penn, J., T. Weber, and C. Deutsch. 2016. Microbial functional diversity alters the structure and sensitivity of oxygen deficient zones. *Geophys. Res. Lett.*, **43**, 9773–9780, doi:10.1002/2016GL070438.

Pfeiffer, T., S. Schuster, and S. Bonhoeffer. 2001. Cooperation and competition in the evolution of ATP-producing pathways. *Science*, **292 (5516)**, 504–7, doi:10.1126/science.1058079.

Pirt, S. J.. 1965. The Maintenance Energy of Bacteria in Growing Cultures. *Proc. R. Soc. London. Ser. B, Biol. Sci.*, **163 (991)**, 224–231.

Preheim, S. P., and Coauthors. 2016. Surveys, simulation and single-cell assays relate function and phylogeny in a lake ecosystem. *Nat. Microbiol.*, **1**, doi:10.1038/nmicrobiol.2016.130.

Preisler, A., D. de Beer, A. Lichtschlag, G. Lavik, A. Boetius, and B. B. Jørgensen. 2007. Biological and chemical sulfide oxidation in a Beggiatoa inhabited marine sediment. *ISME J.*, **1**, 341–53, doi:10.1038/ismej.2007.50.

Qin, W., and Coauthors. 2014. Marine ammonia-oxidizing archaeal isolates display obligate mixotrophy and wide ecotypic variation. *Proc. Natl. Acad. Sci.*, **111 (34)**, 12 504–12 509, doi:10.1073/pnas.1324115111.

Reed, D. C., C. K. Algar, J. A. Huber, and G. J. Dick. 2014. Gene-centric approach to integrating environmental genomics and biogeochemical models. *Proc. Natl. Acad. Sci.*, **111 (5)**, 1879–1884, doi:10.1073/pnas.1313713111.

Revsbech, N. P., L. H. Larsen, J. Gundersen, T. Dalsgaard, O. Ulloa, and B. Thamdrup. 2009. Determination of ultra-low oxygen concentrations in oxygen minimum zones by the STOX sensor. *Limnol. Oceanogr. Methods*, **7**, 371–381, doi:10.4319/lom.2009.7.371.

Rillig, M. C., J. Antonovics, T. Caruso, A. Lehmann, J. R. Powell, S. D. Veresoglou, and E. Verbruggen. 2015. Interchange of entire communities: microbial community coalescence. *Trends Ecol. Evol.*, **30 (8)**, 470–476, doi:10.1016/j.tree.2015.06.004.

Rittman, B. E., and P. L. McCarty. 2001. *Environmental Biotechnology: Principles and Applications*. McGraw-Hill.

Robinson, C.. 2008. Heterotrophic bacterial respiration. *Microb. Ecol. Ocean.*, D. L. Kirchman, Ed., 2nd ed., Wiley-Blackwell, 299–334.

Robinson, C., and P. J. l. B. Williams. 2005. Respiration and its measurements in surface marine waters. *Respir. Aquat. Ecosyst.*, P. A. del Giorgio, and P. Williams, Eds., Oxford, chap. 9, 147–180, doi:10.1093/acprof:oso/9780198527084.001.0001.

Roden, E. E., and Q. Jin. 2011. Thermodynamics of microbial growth coupled to metabolism of glucose, ethanol, short-chain organic acids, and hydrogen. *Appl. Environ. Microbiol.*, **77 (5)**, 1907–9, doi:10.1128/AEM.02425-10.

Russell, J. B., and G. M. Cook. 1995. Energetics of bacterial growth: balance of anabolic and catabolic reactions. *Microbiol. Mol. Biol. Rev.*, **59 (1)**, 48–62, doi:10.1.1.321.8181.

Saba, V. S., and Coauthors. 2010. Challenges of modeling depth-integrated marine primary productivity over multiple decades: A case study at BATS and HOT. *Global Biogeochem. Cycles*, **24**, doi:10.1029/2009GB003655.

Santoro, A. E.. 2016. The do-it-all nitrifier. *Science*, **351 (6271)**, 342–343, doi:10.1126/science.aad9839.

Santoro, A. E., and K. L. Casciotti. 2011. Enrichment and characterization of ammonia-oxidizing archaea from the open ocean: phylogeny, physiology and stable isotope fractionation. *ISME J.*, **5**, 1796–808, doi:10.1038/ismej.2011.58.

Santoro, A. E., K. L. Casciotti, and C. A. Francis. 2010. Activity, abundance and diversity of nitrifying archaea and bacteria in the central California Current. *Environ. Microbiol.*, **12 (7)**, 1989–2006, doi:10.1111/j.1462-2920.2010.02205.x.

Santoro, A. E., and Coauthors. 2013. Measurements of nitrite production in and around the primary nitrite maximum in the central California Current. *Biogeosciences*, **10**, 7395–7410, doi:10.5194/bg-10-7395-2013.

Schlitzer, R.. 2002. Carbon export fluxes in the Southern Ocean: results from inverse modeling and comparison with satellite-based estimates. *Deep Sea Res.*, **49**, 1623–1644, doi:10.1016/S0967-0645(02)00004-8.

Shapiro, B. J., and M. F. Polz. 2014. Ordering microbial diversity into ecologically and genetically cohesive units. *Trends Microbiol.*, **22 (5)**, 235–247, doi:10.1016/j.tim.2014.02.006.

Sharples, J., and P. Tett. 1994. Modelling the effect of physical variability on the midwater chlorophyll maximum. *J. Mar. Res.*, **52**, 219–238.

Sher, D., J. W. Thompson, N. Kashtan, L. Croal, and S. W. Chisholm. 2011. Response of Prochlorococcus ecotypes to co-culture with diverse marine bacteria. *ISME J.*, **5**, 1125–1132, doi:10.1038/ismej.2011.1.

Sherr, E., and B. Sherr. 2000. Marine Microbes; An Overview. *Microb. Ecol. Ocean.*, D. L. Kirchman, Ed., Wiley-Liss, Inc, chap. 2, 13–46.

Siegel, D., K. Buesseler, S. Doney, S. Sailley, M. Behrenfeld, and P. Boyd. 2014. Global assessment of ocean carbon export by combining satellite observations and food-web models. *Global Biogeochem. Cycles*, **28**, 181–196, doi:10.1002/2013GB004743.

Siegel, D. A., and Coauthors. 2016. Prediction of the Export and Fate of Global Ocean Net Primary Production: The EXPORTS Science Plan. *Front. Mar. Sci.*, **3**, 1–10, doi:10.3389/fmars.2016.00022.

Sinsabaugh, R. L., S. Manzoni, D. L. Moorhead, and A. Richter. 2013. Carbon use efficiency of microbial communities: stoichiometry, methodology and modelling. *Ecol. Lett.*, **16**, 930–939, doi:10.1111/ele.12113.

Smith, J. M., F. P. Chavez, and C. a. Francis. 2014. Ammonium uptake by phytoplankton regulates nitrification in the sunlit ocean. *PLoS One*, **9 (9)**, e108 173, doi:10.1371/journal.pone.0108173.

Spieck, E., S. Keuter, T. Wenzel, E. Bock, and W. Ludwig. 2014. Characterization of a new marine nitrite oxidizing bacterium, Nitrospina watsonii sp. nov., a member of the newly proposed phylum "Nitrospinae". *Syst. Appl. Microbiol.*, **37**, 170–176, doi:10.1016/j.syapm.2013.12.005.

Stahl, D. A., and J. R. de la Torre. 2012. Physiology and diversity of ammonia-oxidizing archaea. *Annu Rev Microbiol*, **66**, 83–101, doi:10.1146/annurev-micro-092611-150128.

Steinberg, M. K., and Coauthors. 2011. Comparison of techniques used to count single-celled viable phytoplankton. *J. Appl. Phycol.*, **24**, 751–758, doi:10.1007/s10811-011-9694-z.

Stevens, H., and O. Ulloa. 2008. Bacterial diversity in the oxygen minimum zone of the eastern tropical South Pacific. *Environ. Microbiol.*, **10 (5)**, 1244–1259, doi:10.1111/j.1462-2920.2007.01539.x.

Stewart, P. S.. 1998. A review of experimental measurements of effective diffusive permeabilities and effective diffusion coefficients in biofilms. *Biotechnol. Bioeng.*, **59 (3)**, 261–272, doi:10.1002/(SICI)1097-0290(19980805)59:3<261::AID-BIT1>3.0.CO;2-9.

Stoecker, D. K., M. D. Johnson, C. De Vargas, and F. Not. 2009. Acquired phototrophy in aquatic protists. *Aquat. Microb. Ecol.*, **57 (3)**, 279–310, doi:10.3354/ame01340.

Stolper, D. A., N. P. Revsbech, and D. E. Canfield. 2010. Aerobic growth at nanomolar oxygen concentrations. *Proc. Natl. Acad. Sci. U. S. A.*, **107 (44)**, 18 755–60, doi:10.1073/pnas.1013435107.

Stramma, L., G. C. Johnson, J. Sprintall, and V. Mohrholz. 2008. Expanding Oxygen-Minimum Zones in the Tropical Oceans. *Science*, **320**, 655–658.

Stramma, L., S. Schmidtko, L. A. Levin, and G. C. Johnson. 2010. Ocean oxygen minima expansions and their biological impacts. *Deep. Res. Part I Oceanogr. Res. Pap.*, **57**, 587–595, doi:10.1016/j.dsr.2010.01.005.

Strom, S. L.. 2008. Microbial Ecology of Ocean Biogeochemistry: A Community Perspective. *Science*, **320 (5879)**, 1043–1045, doi:10.1126/science.1153527.

Strous, M., J. J. Heijnen, J. G. Kuenen, and M. S. M. Jetten. 1998. The sequencing batch reactor as a powerful tool for the study of slowly growing anaerobic ammonium-oxidizing microorganisms. *Appl. Microbiol. Biotechnol.*, **50**, 589–596.

Sunagawa, S., and Coauthors. 2015. Structure and function of the global ocean microbiome. *Science*, **348 (6237)**, 1261 359, doi:10.1126/science.1261359.

Suntharalingam, P., E. Buitenhuis, C. Le Quéré, F. Dentener, C. Nevison, J. H. Butler, H. W. Bange, and G. Forster. 2012. Quantifying the impact of anthropogenic nitrogen deposition on oceanic nitrous oxide. *Geophys. Res. Lett.*, **39**, doi:10.1029/2011GL050778.

Taniguchi, D. A. A., P. J. S. Franks, and F. J. Poulin. 2014. Planktonic biomass size spectra: An emergent property of size-dependent physiological rates, food web dynamics, and nutrient regimes. *Mar. Ecol. Prog. Ser.*, **514**, 13–33, doi:10.3354/meps10968.

Thamdrup, B., T. Dalsgaard, and N. P. Revsbech. 2012. Widespread functional anoxia in the oxygen minimum zone of the Eastern South Pacific. *Deep Sea Res. Part I Oceanogr. Res. Pap.*, **65**, 36–45, doi:10.1016/j.dsr.2012.03.001.

Thingstad, T. F., L. Øvreås, J. K. Egge, T. Løvdal, and M. Heldal. 2005. Use of non-limiting substrates to increase size; a generic strategy to simultaneously optimize uptake and minimize predation in pelagic osmotrophs? *Ecol. Lett.*, **8**, 675–682, doi:10.1111/j.1461-0248.2005.00768.x.

Tiano, L., E. Garcia-Robledo, T. Dalsgaard, A. H. Devol, B. B. Ward, O. Ulloa, D. E. Canfield, and N. Peter Revsbech. 2014. Oxygen distribution and aerobic respiration in the north and south eastern tropical Pacific oxygen minimum zones. *Deep Sea Res. Part I*, **94**, 173–183, doi:10.1016/j.dsr.2014.10.001.

Tikhonov, M.. 2015a. Multi-cellularity without cooperation. *arXiv*, 1506.01752.

Tikhonov, M.. 2015b. Theoretical ecology without species. *arXiv*, 1504.0255.

Tilman, D.. 1980. A Graphical-Mechanistic Approach to Competition and Predation. *Am. Nat.*, **116 (3)**, 362–393.

Tilman, D.. 1982. *Resource Competition and Community Structure*. Princeton University Press, Princeton, N.J.

Ulloa, O., D. E. Canfield, E. F. DeLong, R. M. Letelier, and F. J. Stewart. 2012. Microbial oceanography of anoxic oxygen minimum zones. *Proc. Natl. Acad. Sci. U. S. A.*, **109 (40)**, 15 996–6003, doi:10.1073/pnas.1205009109.

Vallino, J. J.. 2010. Ecosystem biogeochemistry considered as a distributed metabolic network ordered by maximum entropy production. *Philos. Trans. R. Soc. Lond. B. Biol. Sci.*, **365**, 1417–1427, doi:10.1098/rstb.2009.0272.

Vallino, J. J., and C. K. Algar. 2016. The Thermodynamics of Marine Biogeochemical Cycles: Lotka Revisited. *Ann. Rev. Mar. Sci.*, **8**, 1–24, doi:10.1146/annurev-marine-010814-015843.

Vallino, J. J., C. S. Hopkinson, and J. E. Hobbie. 1996. Modeling bacterial utilization of dissolved organic matter: Optimization replaces Monod growth kinetics. *Limnol. Oceanogr.*, **41 (8)**, 1591–1609, doi:10.4319/lo.1996.41.8.1591.

van de Leemput, I. A., A. J. Veraart, V. Dakos, J. J. M. de Klein, M. Strous, and M. Scheffer. 2011. Predicting microbial nitrogen pathways from basic principles. *Environ. Microbiol.*, **13 (6)**, 1477–87, doi:10.1111/j.1462-2920.2011.02450.x.

van den Ende, F. P., A. M. Laverman, and H. van Gemerden. 1996. Coexistence of aerobic chemotrophic and anaerobic phototrophic sulfur bacteria under oxygen limitation. *FEMS Microbiol. Ecol.*, **19**, 141–151, doi:10.1016/0168-6496(95)00082-8.

van der Heijden, M. G. A., R. D. Bardgett, and N. M. van Straalen. 2008. The unseen majority: Soil microbes as drivers of plant diversity and productivity in terrestrial ecosystems. *Ecol. Lett.*, **11**, 296–310, doi:10.1111/j.1461-0248.2007.01139.x.

van Kessel, M. A. H. J., D. R. Speth, M. Albertsen, P. H. Nielsen, H. J. M. Op den Camp, B. Kartal, M. S. M. Jetten, and S. Lücker. 2015. Complete nitrification by a single microorganism. *Nature*, **528 (7583)**, 555–559, doi:10.1038/nature16459.

VanBriesen, J. M.. 2002. Evaluation of methods to predict bacterial yield using thermodynamics. *Biodegradation*, **13**, 171–90, doi:10.1023/A:1020887214879.

Verdy, A., M. Follows, and G. Flierl. 2009. Optimal phytoplankton cell size in an allometric model. *Mar. Ecol. Prog. Ser.*, **379**, 1–12, doi:10.3354/meps07909.

Volk, T.. 2007. The properties of organisms are not tunable parameters selected because they create maximum entropy production on the biosphere scale: A by-product framework in response to Kleidon. *Clim. Change*, **85**, 251–258, doi:10.1007/s10584-007-9319-3.

Volk, T., and M. I. Hoffert. 1985. Ocean carbon pumps: analysis of relative strengths and efficiencies in ocean-driven atmospheric CO2 changes. *carbon cycle Atmos. CO2 Nat. Var. Archean to Present. Chapman Conf. Pap. 1984*, E. T. Sundquist, and W. S. Broecker, Eds., American Geophysical Union, 99–110.

Volk, T., and O. Pauluis. 2010. It is not the entropy you produce, rather, how you produce it. *Philos. Trans. R. Soc. Lond. B. Biol. Sci.*, **365**, 1317–1322, doi:10.1098/rstb.2010.0019.

Ward, B.. 1987. Nitrogen transformations in the Southern California Bight. *Deep Sea Res. Part A. Oceanogr. Res. Pap.*, **34 (5-6)**, 785–805, doi:10.1016/0198-0149(87)90037-9.

Ward, B. A., S. Dutkiewicz, and M. J. Follows. 2014. Modelling spatial and temporal patterns in size-structured marine plankton communities: Top-down and bottom-up controls. *J. Plankton Res.*, **36 (1)**, 31–47, doi:10.1093/plankt/fbt097.

Ward, B. a., S. Dutkiewicz, O. Jahn, and M. J. Follows. 2012. A size-structured food-web model for the global ocean. *Limnol. Oceanogr.*, **57 (6)**, 1877–1891, doi:10.4319/lo.2012.57.6.1877.

Ward, B. A., and M. J. Follows. 2016. Marine mixotrophy increases trophic transfer efficiency, mean organism size, and vertical carbon flux. *Proc. Natl. Acad. Sci. U. S. A.*, **113 (11)**, 2958–2963, doi:10.1073/pnas.1517118113.

Ward, B. B.. 2002. How many species of prokaryotes are there? *Proc. Natl. Acad. Sci. U. S. A.*, **99 (16)**, 10 234–10 236, doi:10.1073/pnas.162359199.

Ward, B. B.. 2005. Temporal variability in nitrification rates and related biogeochemical factors in Monterey Bay , California , USA. *Mar. Ecol. Prog. Ser.*, **292**, 97–109, doi:10.3354/meps292097.

Ward, B. B.. 2008. Nitrification in marine systems. *Nitrogen Mar. Environ.*, D. G. Capone, D. A. Bronk, M. R. Mulholland, and E. J. Carpenter, Eds., chap. 5, 199–262.

Ward, B. B.. 2013. Oceans. How nitrogen is lost. *Science*, **341 (6144)**, 352–3, doi:10.1126/science.1240314.

Ward, B. B., K. Kilpatrick, E. Renger, and R. Eppley. 1989. Biological nitrogen cycling in the nitracline. 493–513 pp., doi:10.4319/lo.1989.34.3.0493.

Watson, S. W., and J. B. Waterbury. 1971. Characteristics of two marine nitrite oxidizing bacteria, Nitrospina gracilis nov. gen. nov. sp. and Nitrococcus mobilis nov. gen. nov. sp. *Arch. Mikrobiol.*, **77**, 203–230, doi:10.1007/BF00408114.

Widder, S., and Coauthors. 2016. Challenges in microbial ecology: building predictive understanding of community function and dynamics. *ISME J.*, **10**, 2557–2568, doi:10.1038/ismej.2016.45.

Williams, P. J. l. B., and P. A. del Giorgio. 2005. Respiration in aquatic ecosystems: history and background. *Respir. Aquat. Ecosyst.*, P. A. del Giorgio, and P. J. l. B. Williams, Eds., Oxford University Press, chap. 1, 1–17.

Williams, R. G., and M. J. Follows. 2011. *Ocean Dynamics and the Carbon Cycle: Principles and Mechanisms*. Cambridge University Press.

Wishner, K. F., D. M. Outram, B. A. Seibel, K. L. Daly, and R. L. Williams. 2013. Zooplankton in the eastern tropical north Pacific: Boundary effects of oxygen minimum zone expansion. *Deep Sea Res. Part I Oceanogr. Res. Pap.*, **79**, 122–140, doi:10.1016/j.dsr.2013.05.012.

Woebken, D., B. M. Fuchs, M. M. M. Kuypers, and R. Amann. 2007. Potential interactions of particle-associated anammox bacteria with bacterial and archaeal partners in the Namibian upwelling system. *Appl. Environ. Microbiol.*, **73 (14)**, 4648–4657, doi:10.1128/AEM.02774-06.

Wright, J. J., K. M. Konwar, and S. J. Hallam. 2012. Microbial ecology of expanding oxygen minimum zones. *Nat. Rev. Microbiol.*, **10**, 381–394, doi:10.1038/nrmicro2778.

Wuchter, C., and Coauthors. 2006. Archaeal nitrification in the ocean. *Proc. Natl. Acad. Sci.*, **103 (33)**, 12 317–12 322, doi:10.1073/pnas.0600756103.

Wunsch, C., and P. Heimbach. 2007. Practical global oceanic state estimation. *Phys. D*, **230 (1-2)**, 197–208, doi:10.1016/j.physd.2006.09.040.

Yool, A., A. P. Martin, C. Fernandez, and D. Clark. 2007. The significance of nitrification for oceanic new production. *Nature*, **447**, 999–1002, doi:10.1038/nature05885.

Zafiriou, O. C., L. A. Ball, and Q. Hanley. 1992. Trace nitrite in oxic waters. *Deep Sea Res.*, **39 (7-8)**, 1329–1347, doi:10.1016/0198-0149(92)90072-2.

Zaikova, E., D. A. Walsh, C. P. Stilwell, W. W. Mohn, P. D. Tortell, and S. J. Hallam. 2010. Microbial community dynamics in a seasonally anoxic fjord: Saanich Inlet, British Columbia. *Environ. Microbiol.*, **12 (1)**, 172–191, doi:10.1111/j.1462-2920.2009.02058.x.

Zakem, E. J., and M. J. Follows. 2016. A theoretical basis for a nanomolar critical oxygen concentration. *Limnol. Oceanogr.*, **62**, 795–805, doi:10.1002/lno.10461.

Zimmerman, A. E., S. D. Allison, and A. C. Martiny. 2014. Phylogenetic constraints on elemental stoichiometry and resource allocation in heterotrophic marine bacteria. *Environ. Microbiol.*, **16 (5)**, 1398–1410, doi:10.1111/1462-2920.12329.

Zinger, L., A. Gobet, and T. Pommier. 2012. Two decades of describing the unseen majority of aquatic microbial diversity. *Mol. Ecol.*, **21**, 1878–1896, doi:10.1111/j.1365-294X.2011.05362.x.

Zubkov, M. V., and Coauthors. 2003. High Rate of Uptake of Organic Nitrogen Compounds by Rrochlorococcus Cyanobacteria as a key to their dominance in Oligortrophic oceanic waters. *Microbiology*, **69 (2)**, 1299–1304, doi:10.1128/AEM.69.2.1299.

Zumft, W. G.. 1997. Cell biology and molecular basis of denitrification. *Microbiol. Mol. Biol. Rev.*, **61 (4)**, 533–616.